DISSERTATION

Quantitative Mikrostrukturanalyse nicht-graphitischer Kohlenstoffe

–

Durchführung und Auswertung von Weitwinkelneutronenstreuung

OLIVER OSSWALD

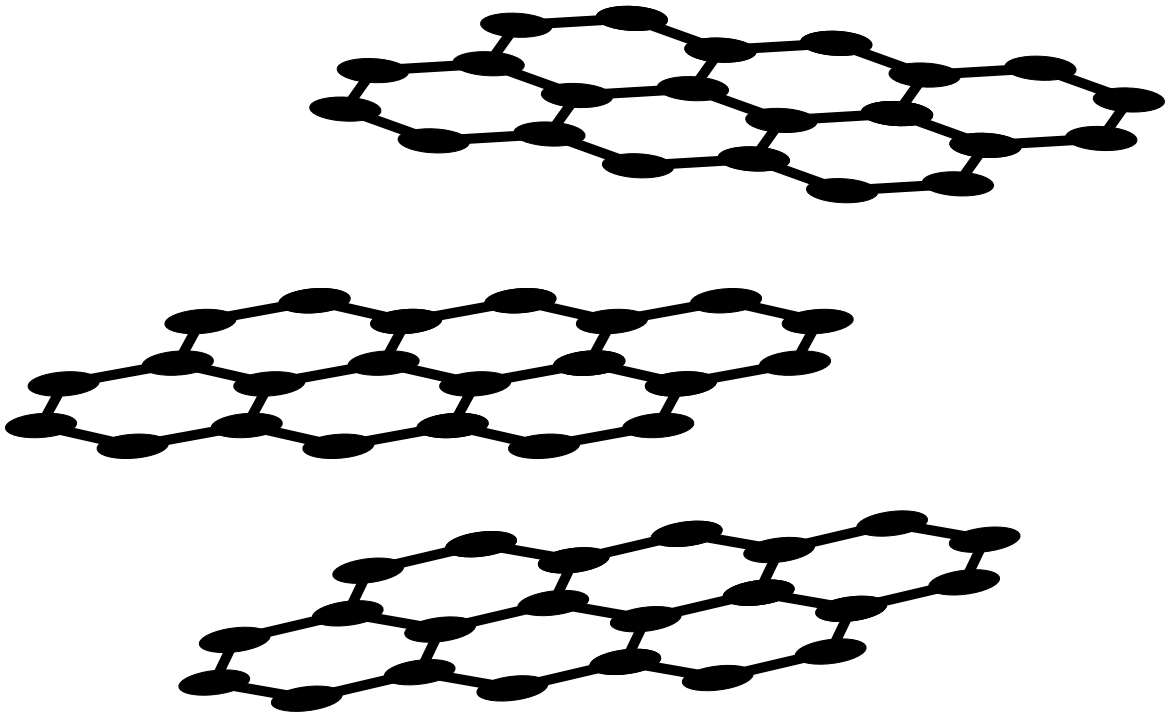

Justus-Liebig-Universität Gießen
April 2023

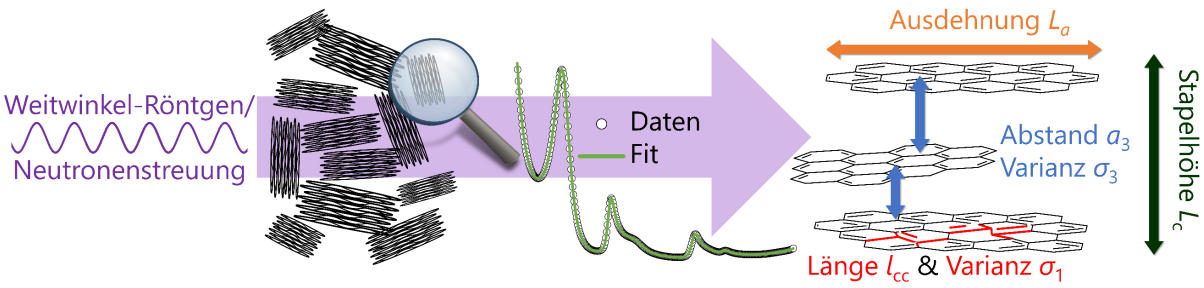

Mikrostrukturanalyse mittels Röntgen- oder Neutronenstreuung (Angelehnt an Ref. [1])

Quantitative Mikrostrukturanalyse nicht-graphitischer Kohlenstoffe

–

Durchführung und Auswertung von Weitwinkelneutronenstreuung

DISSERTATION

zur Erlangung des akademischen Grades

„doctor rerum naturalium“

– Dr. rer. nat. –

eingereicht von

Oliver Osswald

aus Gießen

am Fachbereich 08

– Biologie und Chemie –

der Justus-Liebig-Universität Gießen

Gießen, April 2023

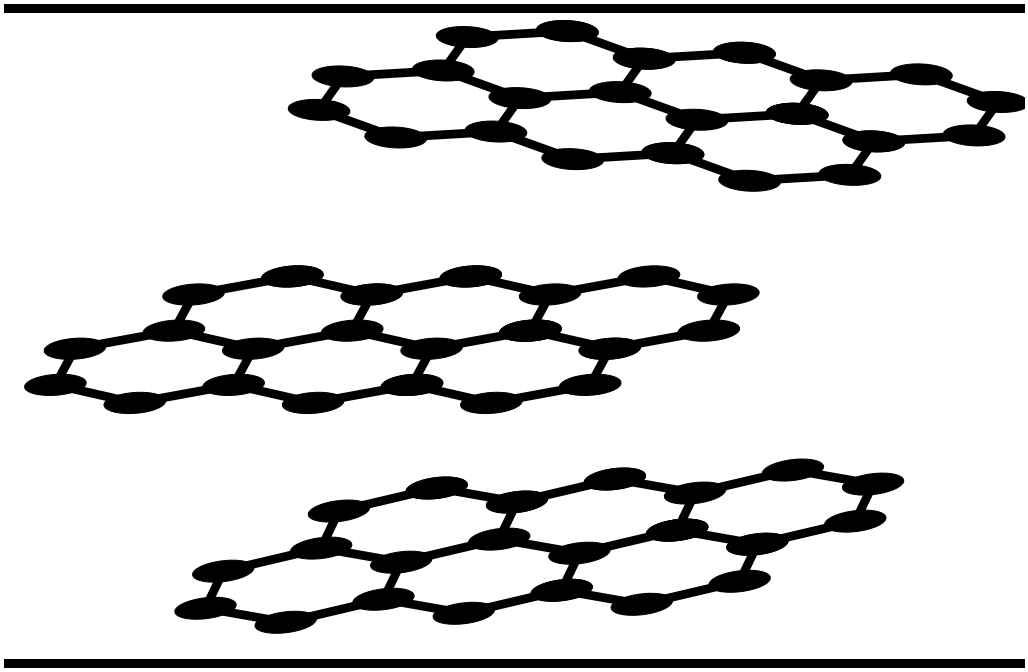

Gutachter:	Prof. Dr. Bernd Michael Smarsly
	Prof. Dr. Peter Jens Klar
Zusätzlich als Prüfer:	Apl. Prof. Dr. Dr. Dirk Walter
	Prof. Dr. Maren Lepple

Abgegeben:	28.04.2023
Angenommen:	26.07.2023
Verteidigt:	06.10.2023

Gewidmet Rosalind Franklin und Wilhelm Ruland

Do… or do not. There is no try.

Tue es… oder tue es nicht. Es gibt kein Versuchen.

Meister Yoda

(… vor langer Zeit in einer weit, weit entfernten Galaxis)

Danksagung

Ich bedanke mich bei der DEUTSCHEN FORSCHUNGSGEMEINSCHAFT E.V. (DFG), welche meine Arbeit im Rahmen des Graduiertenkollegs (GrK) 2204 „Substitutionsmaterialien für nachhaltige Energietechnologien“ finanziert hat und ohne deren Unterstützung diese Arbeit nicht hätte angefertigt werden können.

Außerdem bedanke ich mich bei allen Personen und Instituten, die mich im Laufe meiner Zeit als Doktorand unterstützt haben und mit denen ich zusammenarbeiten durfte. Mein besonderer Dank gilt dabei folgenden Personen:

- PROF. DR. BERND MICHAEL SMARSLY danke ich für die Betreuung meiner Promotion, insbesondere für die vielen anregenden und angeregten wissenschaftlichen Diskussion sowie für die insgesamt sehr schöne Zeit in seiner Arbeitsgruppe und die dazugehörigen Ausflügen. Auch hat er sich immer Zeit genommen, mir bei allen fachlichen Fragen zu den Themen Kohlenstoff, Streumethoden, Anträge, Veröffentlichungen u.v.m., aber auch bei außerfachlichen Fragen und Problemen stets zu mit Rat und Tat zur Seite zu stehen.
- Vielen Dank an PROF. DR. PETER JENS KLAR für seine Zeit als Gutachter für diese Dissertation und an APL. PROF. DR. DR. DIRK WALTER und PROF. DR. MAREN LEPPLE für ihre Bereitschaft, mich im Rahmen dieser Dissertation zu prüfen.
- Dem INSTITUT LAUE-LANGEVIN und damit natürlich auch besonders DR. HENRY FISCHER danke ich für die Messzeit am *Disordered Materials Diffractometer* (D4), aus der eine der hier vorgestellten Publikationen hervorgegangen ist sowie für die zahlreichen und ausführlichen Erklärungen rund um das Thema Weitwinkel-Neutronenstreuung.
- Mit DR. VOLKER STRAUß entstand eine sehr interessante Kooperation und Publikation zum Thema Laser-Karbonisierung. Es war sehr spannend, einmal einen anderen Ansatz zur Synthese außer dem „klassischen“ thermischen Erhitzen kennenzulernen.
- Die gesamte ARBEITSGRUPPE VON PROF. SMARSLY hat stets dafür gesorgt, dass es was zu lachen gibt und auch durch die zahlreichen Ausflüge und erheiternden abendlichen Treffen die Promotionszeit weniger stressig erscheinen lassen, sodass eine angenehme Atmosphäre entstanden ist.

- ANTONELLA D'AMBROSIO hat durch ihre Administration der AG Smarsly und ihre stetige Hilfe bezüglich Dienstreiseanträgen und -abrechnungen sowie ihre Expertise in allen organisatorischen Fragen sehr weitergeholfen.
- Großen Dank an FIONA OHSE, TANJA UND UWE OßWALD, KRISTINA SCHMIDT, MELANIE SIELAND und SEBASTIAN WERNER für die zahlreichen Korrekturen, Kommentare und Anmerkungen zu dieser Dissertation.
- DR. MARTIN GÜNGERICH hat sich um die gesamte Organisation des Graduiertenkollegs 2204 sowie die dazugehörigen Workshops, welche den Doktoranden als Fortbildungen auch seitens des ZENTRUMS FÜR MATERIALFORSCHUNG (ZfM) angeboten wurden und werden, gekümmert.
- DR. MARC OLIVER LOEH hat für die Synthese und Bereitstellung der in dieser Dissertation verwendeten Proben bei der SCHUNK KOHLENSTOFFTECHNIK GMBH in Heuchelheim gesorgt sowie sein Wissen und seine Hilfe über Kohlenstoffe im wissenschaftlich-akademischen und im industriellen Bereich gerne geteilt. Ohne seine Proben wäre diese Promotion vermutlich nicht in dieser Form zustande gekommen.
- DR. FELIX BADACZEWSKI, DR. DOMINIQUE SCHÜPFER und TORBEN PFAFF haben mir als meine direkten Vorgänger an der Universität während meiner gesamten Promotion stets alle Fragen beantwortet, sodass ich mich in das Thema Kohlenstoffe leicht einarbeiten konnte.
- DR. KEVIN TURKE hat mir beim Thema Kleinwinkelstreuung und der dazugehörigen Software sehr weitergeholfen, ohne ihn hätte ich die Daten nicht auswerten können – hoffentlich werden sie auch bald veröffentlicht.
- DR. SEBASTIAN WERNER konnte nahezu alle Fragen um das Thema Laborgeräte klären und stand für entsprechende Rückfragen immer zur Verfügung. Außerdem bin ich durch ihn dem Thema 3D-Drucker wesentlich nähergekommen.
- FABIAN SCHMITZ hat stets alle mir aufkommenden Fragen rund um Origin bereitwillig beantwortet.
- Meine gesamte FAMILIE und allen FREUNDE, besonders meine Frau KRISTINA SCHMIDT sowie unser Hund OTTO haben stets dafür gesorgt, dass ich auch einmal etwas anderes als die Arbeit im Kopf hatte und immer daran geglaubt, dass ich die Promotion auch tatsächlich schaffe.

Kurzzusammenfassung

Der Hauptinhalt dieser kumulativen Dissertation ist die Mikrostrukturanalyse nicht-graphitischer Kohlenstoffe (NGCs) mittels Weitwinkelstreuung. NGCs wie Glaskohlenstoffe und Peche bestehen aus kleinen Graphenschichten, die Stapel in turbostratischer Anordnung bilden. Da sowohl die endliche Ausdehnung der Graphene und der Stapel sowie deren intrinsische Unordnung zu einer Reflexverbreiterung bei Weitwinkelstreuexperimenten führen, ist die genaue Quantifizierung der Mikrostruktur mittels Weitwinkel-Röntgen- und Neutronenstreuung (WAXS/WANS) zwar prinzipiell möglich, aber nicht trivial. Obwohl in Laborexperimenten oftmals WAXS zur Charakterisierung genutzt wird und die Ergebnisse in vorherigen Studien oftmals auf WAXS-Daten beruhen, besitzt diese Methode gegenüber WANS einige Nachteile, z.B. die Dämpfung durch den Atomformfaktor und einen inkohärenten Untergrund.

Daher wurden für diese Arbeit WANS-Messungen an drei Arten von NGCs durchgeführt (Glaskohlenstoff aus einem Phenol-Formaldehyd-Harz, Mesophasenpech und ein Pech mit niedrigem Erweichungspunkt als Präkursoren). Der verwendete große Messbereich führte zu einer genauen Bestimmung der Schichtstruktur. Im Vergleich dazu hatten die WANS-Daten einer früheren Studie von Pfaff et al. (2019) [2] derselben Materialien zwar einen begrenzten Messbereich, eigneten sich aber gut zur Auswertung der Stapelstruktur. Eine Kombination dieser beiden Datensätze eröffnete die Möglichkeit, sowohl die Schicht- als auch die Stapelstruktur genauer als bisher möglich zu bestimmen. Die Haupterkenntnis dabei war, dass die strukturelle Ordnung der Graphenschichten bei allen Temperaturen deutlich höher ist als bisher angenommen und der von perfektem Graphen nahekommt.

Zur Analyse wurde ein kostenloses Tool (OCTCARB) für das Open-Source Programm OCTAVE entwickelt, das zur Verfeinerung von WAXS- und WANS-Daten von NGCs genutzt werden kann und auf dem Modell von RULAND & SMARSLY (2002) [3] basiert. OCTAVE und damit OCTCARB läuft auf allen gängigen Betriebssystemen (Windows, MacOS, Linux) und die Verfeinerung dauert nur wenige Minuten. Es kann auf Hochleistungsrechnern verwendet werden, um mehrere Berechnungen gleichzeitig durchzuführen. Die automatische Verfeinerung kann sowohl leicht von unerfahrenen Anwendern durchgeführt, als auch das gesamte Skript für spezielle Messgeometrien optimiert werden.

Abstract

In this cumulative dissertation, the microstructure of non-graphitic carbons (NGCs) was analysed using wide-angle scattering techniques. NGCs such as glass-like carbon and pitches consist of small graphene sheets building stacks arranged in a turbostratic order. Since the finite size as well as the intrinsic disorder of the layers and stacks cause a reflection broadening during wide-angle scattering, the precise quantification using wide-angle X-ray or neutron scattering (WAXS/WANS) is possible, but not trivial. Since WAXS is normally used for the characterization using standard laboratory equipment, the results published in previous studies are often based on WAXS-data. Unfortunately, WAXS suffers from some disadvantages like the damping by the atomic form factor and an incoherent background compared to wide-angle neutron scattering (WANS).

Therefore, for this work, powder WANS measurements were performed on three types of NGCs (glass-like carbon from a phenol-formaldehyde resin, mesophase pitch and a low-softening point pitch as precursors), where the large measurement range lead to a detailed analysis of the layer structure. Even if the WANS-data from a previous study by Pfaff et al. (2019) [2] of the same materials consist of only a small measurement range, they were used to determine the stack structure. A combination of these different WANS-data offered the possibility to determine both the layer and the stack structure more precisely than before. As a main conclusion, it was found that the intrinsic order of the graphene layers themselves is significantly higher than previously assumed for all heat-treatment temperatures and very close to that of perfect graphene.

For the analysis, a free tool (OCTCARB) was developed for the open-source software OCTAVE, which can be used to refine WAXS-and WANS-data from NGCs and is based on the model by RULAND & SMARSLY (2002). [3] OCTAVE and thus OCTCARB runs on all common operating systems (Windows, MacOS and Linux) and the entire refinement can be performed in minutes. It can even be used on high-performance computers, allowing multiple calculations to be performed simultaneously. The automatic refinement is easy to perform for inexperienced users and the entire script can be optimized for specific measurement geometries.

Inhaltsverzeichnis

1. Thematische Einführung

In diesem Kapitel wird zunächst eine thematische Einführung über die Geschichte und Vorkommen verschiedener Kohlenstoffmodifikationen (1.1), die industrielle und gesellschaftliche Relevanz (1.2.1) sowie die aktuell offenen Forschungspunkte (1.2.2) gegeben. Im weiteren Verlauf der Arbeit werden die theoretischen Grundlagen (Kapitel 2) erläutert, so auch die verschiedenen Methoden zur Mikrostrukturanalyse von nicht-graphitischen Kohlenstoffen auf atomarer Ebene (2.3), insbesondere das Modell von RULAND & SMARSLY (2.4). Die Ergebnisse der dieser Arbeit zugrunde liegenden Publikationen werden in Kapitel 3 dargestellt.

1.1. Geschichte und Vorkommen

1.1.1. Geschichte des Kohlenstoffs

Bereits vor über 30.000 Jahren nutzten Menschen in der Grotte von Chauvet in Südfrankreich Kohle für erste Höhlenmalereien, wobei dies für einige Jahrtausende die einzige Verwendung von Kohle war. [4,5] Erst in der jüngeren Geschichte ab 7.500 v. Chr. wurde Holzkohle auch zur Metallherstellung genutzt. Hierbei wurde aufgrund des niedrigen Schmelzpunktes zunächst Kupfer (T_S = 1.085 °C), später mit der Entdeckung von Zinn (T_S = 232 °C) auch Bronze (T_S = 900 – 1.000 °C) hergestellt (daher auch das Zeitalter *Bronzezeit*). [6–8] Auch machte Holzkohle die Eisengewinnung aus Eisenerz bei den Hethitern möglich (ca. 1.400 v. Chr, *Eisenzeit*). [9,10] Allerdings reichte die Temperatur von glühender Kohle nicht aus (1.200 – 1.300 °C), um Eisen (T_S = 1535 °C) zu schmelzen. Stattdessen wurde das Eisen erweicht und dann geschmiedet. [8,11]

Bis allerdings reiner Kohlenstoff erstmals industriell genutzt wurde, dauerte es nochmals einige Jahrhunderte: Die sogenannten *Silbergriffel* oder *Silberstifte* wurden ab 1558 in Keswick (Nordengland) industriell hergestellt. Das 1564 entdeckte Graphit-Vorkommen in Barrowdale in der Nähe von Keswick sorgte für einen Aufschwung der Herstellung dieser Stifte und eine schnelle Ausbreitung über ganz Europa. Dabei wurde zunächst vermutet, dass es sich bei dem Material um Bleierz handelte, woraus sich der heutige Name *Bleistift* ableitet. [12]

1772 erkannte ANTOINE LAURENT DE LAVOISIER das Element *Carboneum* und damit reinen Kohlenstoff [13,14], wobei *carbo* im Lateinischen *Kohle* bedeutet und damit bisher lediglich Kohleverbindungen (z.B. Holzkohle) gemeint waren. [15] Auch konnte LAVOISIER zeigen, dass Diamant ebenfalls aus Kohlenstoff besteht, was von den Chemikern SMITHSON TENNANT/WILLIAM HYDE WOLLASTON bzw. WILLIAM ALLEN/WILLIAM HASELDINE PEPYS unabhängig bestätigt werden konnte. [13,14,16–19] 1796 wurde ebenfalls von SMITHSON TENNANT erstmals Kohlenstoff künstlich hergestellt , indem bei Versuchen mit Phosphordämpfen und glühendem Kalk schließlich Calciumphosphat und Kohlenstoff synthetisiert wurde. [20] Das chemische Symbol *C* wurde erst 1814 von JÖNS JAKOB BERZELIUS eingeführt. [21] 1778 konnte CARL WILHELM SCHEELE nachweisen, dass Graphit ebenfalls aus reinem Kohlenstoff besteht (Abbildung 1) [22] und deckte somit den Irrtum des *Blei*stifts auf – auch wenn der Name bis heute geblieben ist

In der jüngsten Geschichte wurde zunächst 1970 die Existenz von runden, quasi-0D-Kohlenstoffmaterialien, den *Fullerenen* vorausgesagt (Abbildung 1), [23,24] bevor diese dann ab 1980 im Lichtbogen bei ~ 6000 °C im Vakuum hergestellt und die Ergebnisse 1985 veröffentlicht wurden, [25] wofür schließlich 1996 der Nobelpreis für Chemie an ROBERT F. CURL, HAROLD KROTO und RICHARD E. SMALLEY vergeben wurde. [26] SUMIO IIJIMA entdeckte 1991 mehrwandige quasi-1D-Kohlenstoffnanoröhrchen (Abbildung 1), wobei diese erst 1993 auch einwandig nachgewiesen werden konnten. [27,28] 2010 wurde der Nobelpreis „für grundlegende Experimente mit dem zweidimensionalen Material Graphen“ für die 2004 von ANDRE KONSTANTIN GEIM und KONSTANTIN SERGEJEWITSCH NOVOSELOV veröffentlichte Arbeit mit *Graphen* vergeben. [29,30]

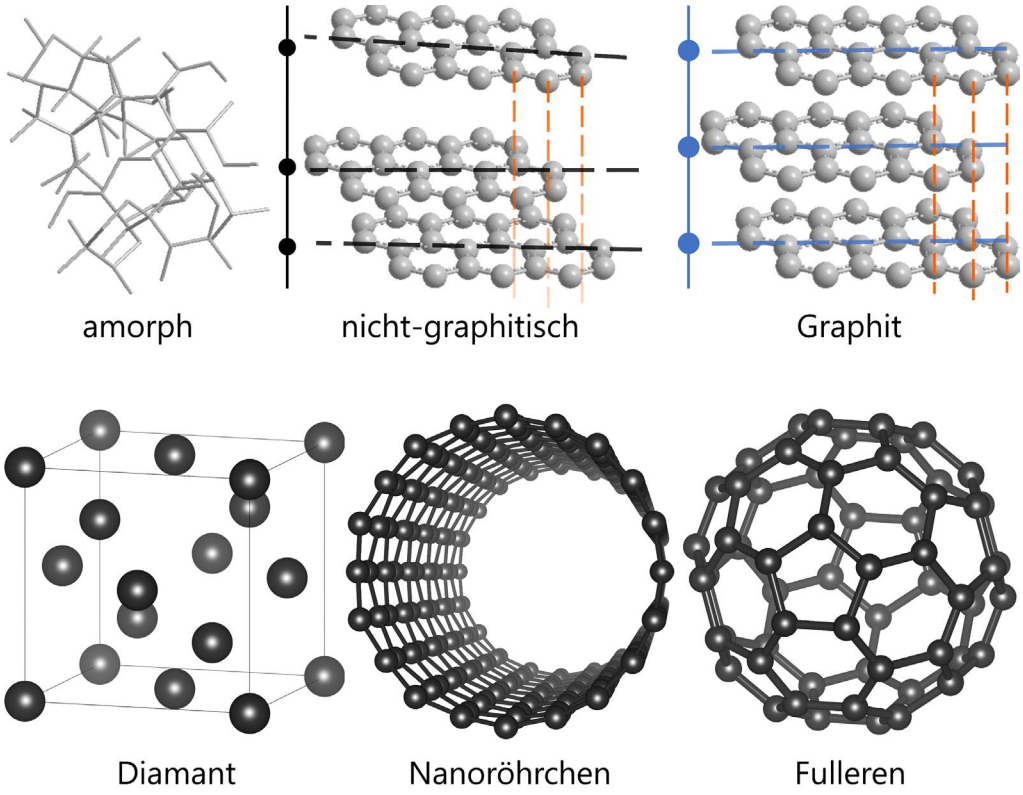

Abbildung 1. Vergleich zwischen amorphem und nicht-graphitischem Kohlenstoff sowie Graphit. Während bei Graphit die Schichten perfekt gestapelt sind, können diese bei nicht-graphitischem Kohlenstoff verkippt, verdreht, verschoben und in unterschiedlichen Abständen angeordnet sein. Bei amorphem Kohlenstoff ist keine kristallographische Fernordnung messbar. Bei der Diamantstruktur liegt Kohlenstoff in einem kubischen Gitter vor, während Nanoröhrchen aufgrund ihres geringen Durchmessers quasi-eindimensional und Fullerene quasi-nulldimensional sind.

1.1.2. Natürliche Kohlenstoff-Vorkommen

Insgesamt existiert eine große Vielzahl an verschiedenen Kohlenstoffarten: Neben Braun- und Steinkohle, welche Mischungen aus verschiedenen Kohlenstoff-Arten, flüchtigen Bestandteilen sowie Fremdstoffen sind und auch aufgrund Ihrer größtenteils amorphen Struktur (Abbildung 1) hauptsächlich als Brennstoff verwendet werden, [31,32] gibt es auch wirtschaftlich signifikant große natürliche Vorkommen von natürlichem Kohlenstoff als Graphit und Diamant (Abbildung 1).

Daneben gibt es auch noch natürliche Vorkommen von Fullerenen, z.B. im natürlichen Shungit, in Kratern von Meteoriteneinschlägen sowie im interstellaren Raum. [33–35] Allerdings sind diese Mengen nur sehr klein und damit wirtschaftlich uninteressant. Weitere in sehr kleinen Mengen natürlich vorkommende Modifikationen sind z.B. Lonsdaleit und Chaoit, welche durch Schock-Metamorphosen in sehr kleinen Mengen entstehen können. [36–38] Aufgrund der Seltenheit werden diese Modifikationen allerdings nicht weiter beleuchtet.

Größere Diamanten haben die bekannteste Verwendung als Schmuckstein, kleinere Diamanten bzw. Diamantstaub werden hingegen aufgrund der extremen Härte bei Werkzeugen, beispielsweise zum Schleifen oder Bohren, genutzt. Außerdem wird diamantartiger Kohlenstoff zur Beschichtung verwendet, um zum Beispiel die elektrische oder thermische Leitfähigkeit zu erhöhen. [39–41] In der Natur bildet sich Diamant nur unter sehr hohem Druck und hoher Temperatur und damit nur einige hundert Kilometer unter der Erdoberfläche. [42–44] Durch Eruptionen können Diamanten an die Erdoberfläche transportiert werden, wobei dieser Vorgang so schnell geht, dass keine Umwandlung in Graphit stattfindet. [45] Abgebaut wird Diamant vorwiegend in Russland, im südlichen Afrika (Botswana, D. R. Kongo, Angola, Südafrika), aber auch in Australien und Kanada. [46] Auch in Deutschland wurden bereits Diamanten gefunden, wobei diese Menge nur sehr klein war. [47,48] Künstlich können Diamanten entweder unter hohem Druck und mit hohen Temperaturen oder mittels Abscheidungsverfahren hergestellt werden. [49,50]

Bezüglich der Förderung macht Diamant lediglich einen sehr kleinen Bruchteil der Kohlenstoffförderung aus (ca. 30 t im Jahr 2017 [51]). Graphit hingegen wird in einem wesentlich größeren Maßstab gefördert: Im Jahr 2019 wurden ca. 1.670.000 t Graphit abgebaut. [52] Während weltweit in Russland die meisten Diamanten gefördert werden, macht sich bei natürlichem Graphit eine starke Abhängigkeit von China bemerkbar (Abbildung 2). [53,54] Weitere große Exporteure sind Indien und Brasilien, wobei für den Import in die EUROPÄISCHE UNION (EU) zusätzlich Simbabwe von signifikanter Bedeutung ist. In Deutschland ist die Mine in Kropfmühl (Landkreis Passau) am bedeutsamsten, welche 2012 aufgrund der steigenden Nachfrage und Preise wiedereröffnet wurde. Die Fördermenge ist aber im Vergleich zum weltweiten Abbau nur vernachlässigbar gering. [55,56] Gebildet wird Graphit ausgehend von kohlenstoffhaltigen Sedimenten über einen Zeitraum von

mehreren Millionen Jahren unter Ausschluss von Sauerstoff. [57,58] Die verschiedenen Graphitvorkommen unterscheiden sich hinsichtlich ihrer Reinheit sowie in den Größen der einzelnen Graphitpartikel, weshalb ein direkter Vergleich zwischen den unterschiedlichen Abbauregionen nur schwer möglich ist.

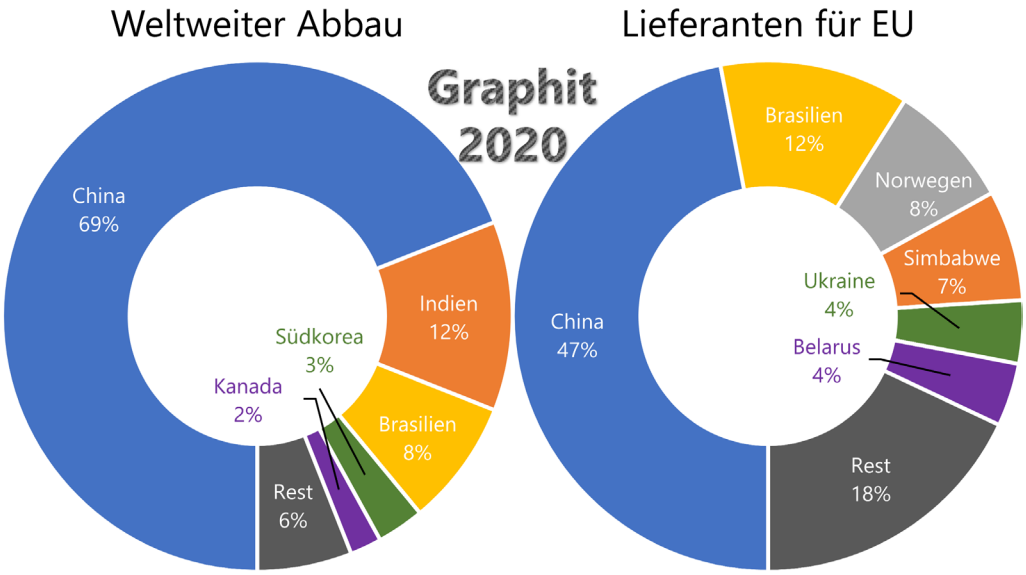

Abbildung 2. Weltweite Förderung von natürlichem Graphit sowie die Lieferanten für die Europäische Union (EU). [53]

1.2. Aktuelle Herausforderungen

1.2.1. Industrielle Relevanz und Nachhaltigkeit

Leider ist die gezeigte strukturelle Variabilität des Kohlenstoffs aber zu groß, um die gesamte Bandbreite der Eigenschaften und Probleme dieser Stoffklasse in einer einzigen Arbeit abzudecken, weshalb sich auf einzelne Aspekte beschränkt werden muss. Während dieser Promotion wurde sich hauptsächlich mit den nicht-graphitischen Kohlenstoffen beschäftigt, sodass hierauf das Hauptaugenmerk liegt. Besonders bei Vorträgen und in Kooperationen mit Projektpartnern kam es aber auch immer wieder zu Berührungspunkten mit porösen Kohlenstoffen, weshalb diese Stoffklasse im Folgenden ebenfalls noch kurz angerissen wird.

1.2.1.a. Anwendungsgebiete von Kohlenstoff

Nicht-graphitische Kohlenstoffe (NGCs) können aufgrund der intrinsischen Unordnung Mikroporen besitzen, welche durch gezielte makroporöse Templatierung (z.B. mittels Silica) vergrößert werden können. [59–64] Gleichzeitig bleibt durch die hoch geordnete Schichtstruktur weiterhin die chemische und physikalische Stabilität erhalten, weshalb NGCs eine geeignete Stoffklasse für elektrochemische Anwendungen als Trägermaterial für Katalysatoren darstellen. [65–82] Besonders die Möglichkeit, die Porengröße auf Mikro- und Makroebene gezielt zu variieren, ermöglicht es, perfekt auf die Ionengrößen abgestimmte Superkondensatoren herzustellen.

Natürlicher Graphit wird zum Beispiel in Lithium-Ionen-Akkumulatoren für die Einlagerung von Li als Anode verwendet (Abbildung 3). [83–86] Bei Natrium-Ionen-Akkumulatoren dient ungeordneter Kohlenstoff als Anode [87–91] und bei Aluminium-Ionen-Akkumulatoren kann poröser Kohlenstoff als Kathode genutzt werden (Abbildung 3). [92–95] Aufgrund der hohen Oberfläche lassen sich Kohlenstoffelektroden auch in Superkondensatoren [63,82,96] und Brennstoffzellen nutzen (Abbildung 3). [97,98]

Die porösen Derivate und die aus Carbid hergestellten Kohlenstoffe (*carbide derived carbons*, *CDCs*) werden – aufgrund der hohen Permeabilität und des geringen Preises bei gleichzeitig hoher Verfügbarkeit – oftmals als Luft- und Wasserfilter und zur Gasspeicherung und -trennung verwendet. Beispielsweise können stickstoffdotierte mesoporöse Kohlenstoffe zur Speicherung von CO_2 eingesetzt werden. [64,79,80,99–102] Direkte Anwendung finden poröse Kohlenstoffe als Aktivkohle in Luftfiltern in Autos oder Gebäuden, wobei hier die Schadstoffe adsorbiert werden, weshalb diese Filter regelmäßig ausgetauscht werden müssen. Der geringe Preis und die hohe Verfügbarkeit machen poröse Kohlenstoffe auch zu einem guten Kandidaten für nachhaltige Wasserfilter. Durch die beeinflussbare Porosität sowie die toxische Unbedenklichkeit lassen sich poröse Kohlenstoffe zur Schmutz- und Salzwasseraufbereitung nutzen. [61,62,64,103–106]

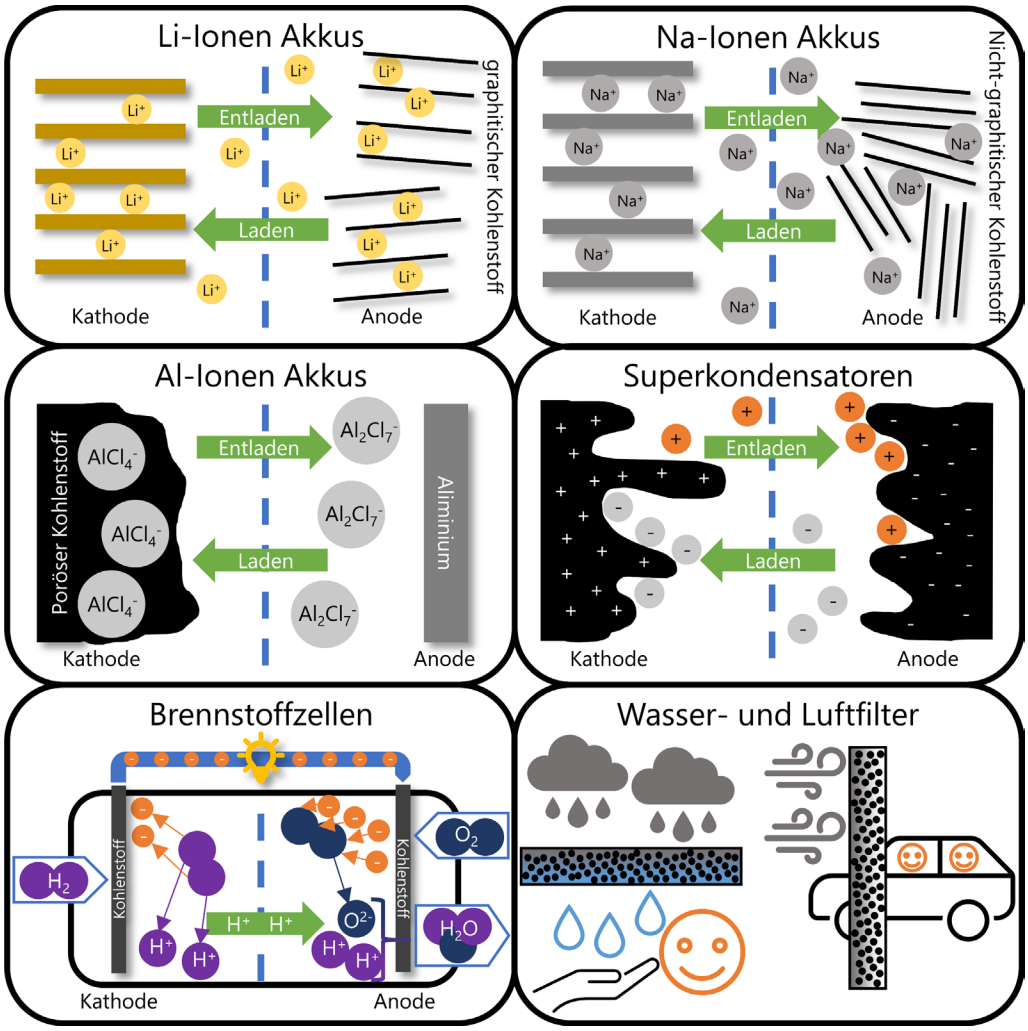

Abbildung 3. Während bei Lithium- und Natrium-Ionen-Akkumulatoren (nicht-) graphitischer Kohlenstoff als Anodenmaterial verwendet wird, kann poröser Kohlenstoff in Aluminium-Ionen-Akkumulatoren als Kathode verwendet werden. Die hohe Oberfläche der Kohlenstoffelektroden ermöglicht auch den Einsatz in Superkondensatoren. Ebenso wird Kohlenstoff als Elektrode in Brennstoffzellen und Aktivkohle als Wasser- und Luftfilter eingesetzt. Angelehnt an Ref. [64]

Auch in Zukunft wird die Optimierung und Weiterentwicklung von elektrischen Speichersystemen eine essenzielle Rolle in Hinblick auf Nachhaltigkeit spielen. Nicht nur die Endlichkeit fossiler Rohstoffe, sondern auch die globale Verteilung dieser zeigt in Zusammenhang mit den aktuellen Krisen (z.B. die Corona-Pandemie

und der Ukraine-Krieg), dass energetische Unabhängigkeit und Nachhaltigkeit unabdingbar für die europäische Zukunft sind. In den bisher genannten elektrochemischen Anwendungen wird aktuell häufig noch natürlicher Graphit als Rohstoff verwendet, wobei der Großteil aus nicht-EU Ländern importiert wird und als kritischer Rohstoff gilt (Abbildung 2 sowie Abschnitt 1.2.1.b). [53,54] Alternativen hierzu könnte die Substitution durch nicht-graphitische Kohlenstoffe sein, welche auch aus nachhaltigen organischen Vorstufen und Abfällen synthetisiert werden können. Konkret können zum Beispiel Apfel-Fallobst, Bananenschalen oder andere Bioabfälle als Anodenmaterial in Natrium- oder Kalium-Ionen-Akkumulatoren sowie in Superkondensatoren eingesetzt werden (Abbildung 3). [64,89,107–111] Für die Anwendung von Graphit in Solarzellen können bereits synthetische Produkte genutzt werden. [112,113]

1.2.1.b. Natürlicher Graphit als kritischer Rohstoff

Wie bereits beschrieben, ist Graphit wichtig für die Produktion von Akkumulatoren und Superkondensatoren. Allerdings wird für diese Produkte oft hochreiner natürlicher Graphit eingesetzt, der aber seit über 10 Jahren zu den kritischen Rohstoffen in der EU gehört und dessen Verbrauch daher signifikant gemindert werden sollte (Abbildung 4). [53,54,96,114–119] Gleichzeitig ist die Produktion von synthetischem Graphit aufgrund der hohen Temperaturen (bis zu 3000 °C) teuer und zeitaufwendig, sodass es der Industrie aktuell oft noch an Anreizen fehlt, natürlichen Graphit zu substituieren.

Dazu muss noch beachtet werden, dass verschiedene Arten an natürlichem Graphit in verschiedenen Reinheiten existieren: *Lamellengraphit* (sehr hohe Reinheit), *amorpher Graphit* (niedriger Kohlenstoffgehalt, kleine Partikel) sowie *Fasergraphit* (hochwertiger Graphit; auch Sri-Lanka-Graphit oder Ceylon-Graphit genannt, da dort die einzig signifikanten Vorkommen sind). [120] In der Elektroindustrie weit verbreitet ist auch noch der sogenannte sphärische Graphit (runde Graphitpartikel), welcher aus Lamellengraphit hergestellt wird. [111,121] Allerdings liegt hier die Produktausbeute bei nur ~ 30 %, sodass hierfür also überproportional viel natürlicher Graphit verbraucht wird. Daher ist der Anteil von ~ 55 % von Lamellengraphit am Gesamt-Graphitvorkommen umso problematischer, wenn es

um nachhaltige Energiespeicherung geht. Amorpher Kohlenstoff kommt zwar mit ~ 44 % immer noch recht häufig vor, allerdings sind hier die Partikel sehr klein und in der Regel in Braun- und Steinkohle gebunden. [111,122] Fasergraphit ist aufgrund des geringen Vorkommens (~ 1%) nicht von nachhaltiger Relevanz, zumal die resultierende Qualität trotz aufwendiger Aufreinigung zu niedrig für viele Anwendungen ist. [111,115]

Auch die EUROPÄISCHE KOMMISSION hat dieses Problem erkannt: Seit dem ersten Bericht über kritische Rohstoffe im Jahr 2011 zählt Graphit zu eben diesen kritischen Rohstoffen. [53,54,114–118] In Abbildung 4 ist das Versorgungsrisiko gegen die wirtschaftliche Bedeutung aufgetragen. Das *Versorgungsrisiko* ist ein Maß für das Risiko, dass dieser Rohstoff für die EU ausfällt: Je höher dieser Wert ist, desto höher ist das Ausfallrisiko (zum Beispiel durch Restriktionen aufgrund von Sanktionen, Handelsverträgen oder natürlicher Verfügbarkeit. Bei einem Wert > 1 wird die Verfügbarkeit als *kritisch* eingestuft). [53,54,111,114–118] Für die *wirtschaftliche Bedeutung* spielen sowohl die Relevanz für die Industrie und Anwendungen innerhalb der EUROPÄISCHEN UNION als auch die Möglichkeit für Rohstoffsubstitution eine Rolle. Hier wurde ein Wert von 2,8 als kritische Schwelle festgelegt. Sind das Versorgungsrisiko und die wirtschaftliche Bedeutung kritisch, so ist es der gesamte Rohstoff. [53,54,111,114–118]

Neben Graphit ist noch eine weitere Auswahl der von DER EUROPÄISCHEN KOMMISSION als kritisch eingestuften Rohstoffe in Abbildung 4 gezeigt. Für Lithium-Ionen-Akkumulatoren sind neben Graphit (12 – 21 Gew.-%) zusätzlich auch noch Lithium (5 – 7 Gew.-%), Kobalt (5 – 20 Gew.-%) und Nickel (5 – 10 Gew.-%) entscheidend. [123] Bis auf Nickel gehören alle Rohstoffe seit 2020 zu den kritischen Materialien. Bemerkenswert ist, dass die Kritikalität von Graphit im Gegensatz zu den anderen Stoffen in der Öffentlichkeit kaum wahrgenommen und diskutiert wird, obwohl das Versorgungsrisiko höher eingeschätzt wird.

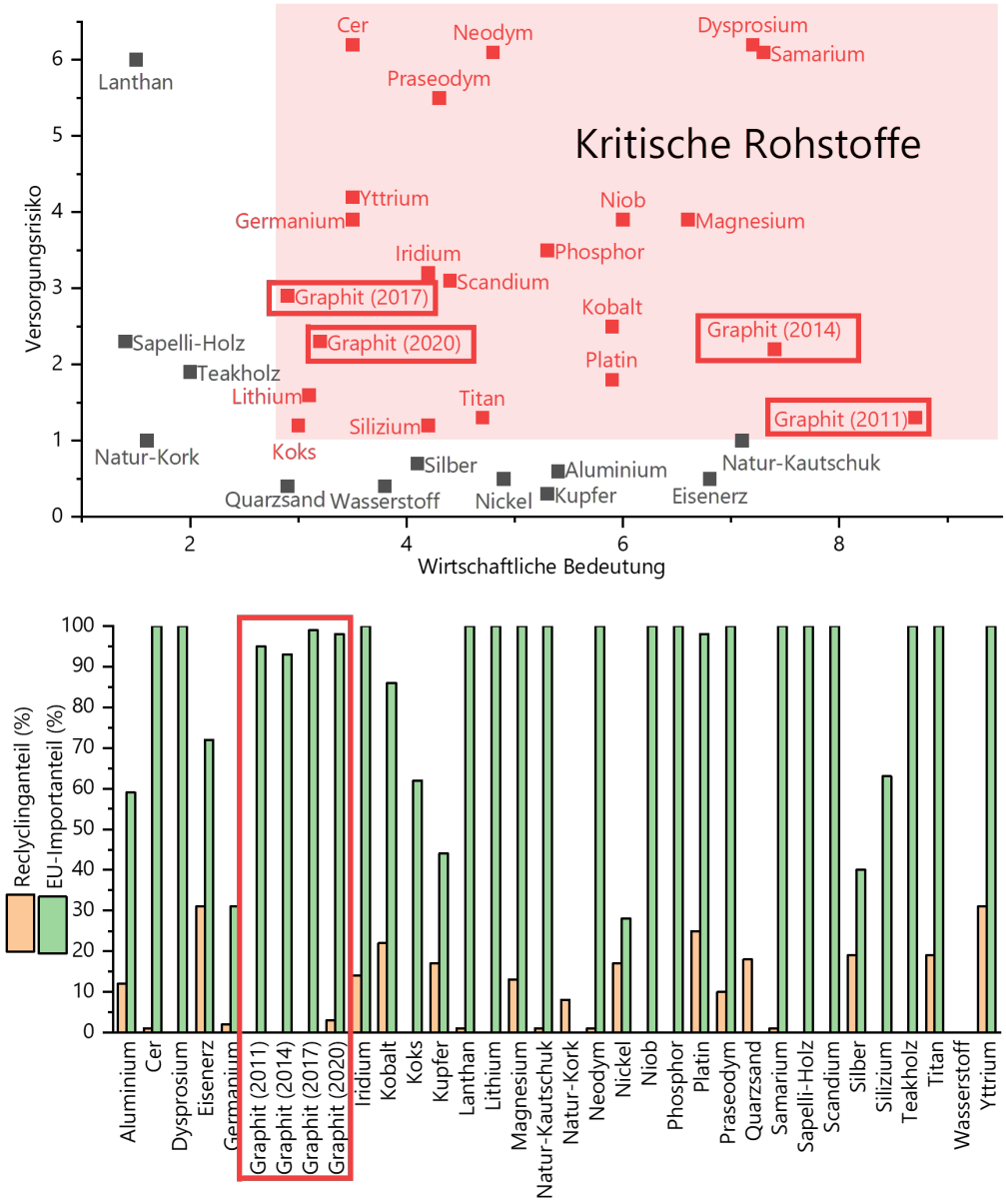

Abbildung 4. Ausgewählte von der EUROPÄISCHEN KOMMISSION als *kritisch* eingestufte Rohstoffe (rot markiert). Die gezeigten Daten beziehen sich auf den Bericht von 2020, wobei für Graphit als Vergleich auch noch die Jahre 2011 – 2017 herangezogen wurden. [53,54,114–118] 2014 ist noch synthetischer Graphit in die Berechnung mit eingeflossen, seit 2017 wird allerdings nur noch natürlicher Graphit berücksichtigt, weshalb es zu einem Sprung gekommen ist. Angelehnt an Ref. [53,54,111]

Neben der Substitution durch synthetischen Graphit ist auch die Substitution durch andere Materialien eine Möglichkeit. Für Hochtemperaturanwendungen und in Gießereien lassen sich zum Beispiel auch Beschichtungen aus Siliziumnitrid oder pyrogenem Kohlenstoff bzw. kalzinierten Petrolkoks einsetzen. [115,117,121,124–128] Bei Lithium-Ionen-Akkumulatoren lässt sich Graphit prinzipiell auch durch Lithiumtitanat ersetzen, [111,115,117,129,130] wobei hier fraglich ist, ob es sinnvoll ist, ein kritisches Material (Graphit) durch ein anderes (Lithium) zu ersetzen. Außerdem ist unklar, ob Lithium-Ionen-Akkumulatoren langfristig nicht auch durch andere Speichermöglichkeiten (Natrium-/Kalium-/Aluminium-Ionen, Redox-Fluss-Akkumulatoren, Wasserstoff-Brennstoffzellen) ersetzt werden. [87,88,90–95,97,98,131–138] Allerdings gibt es auch bei diesen Technologien Probleme bezüglich der Nachhaltigkeit, zum Beispiel die Verwendung von schnell teurer werdendem Vanadium in Redox-Flow-Batterien oder die nachhaltige Speicherung von Wasserstoff für die entsprechenden Brennstoffzellen. [97,98,131–136]

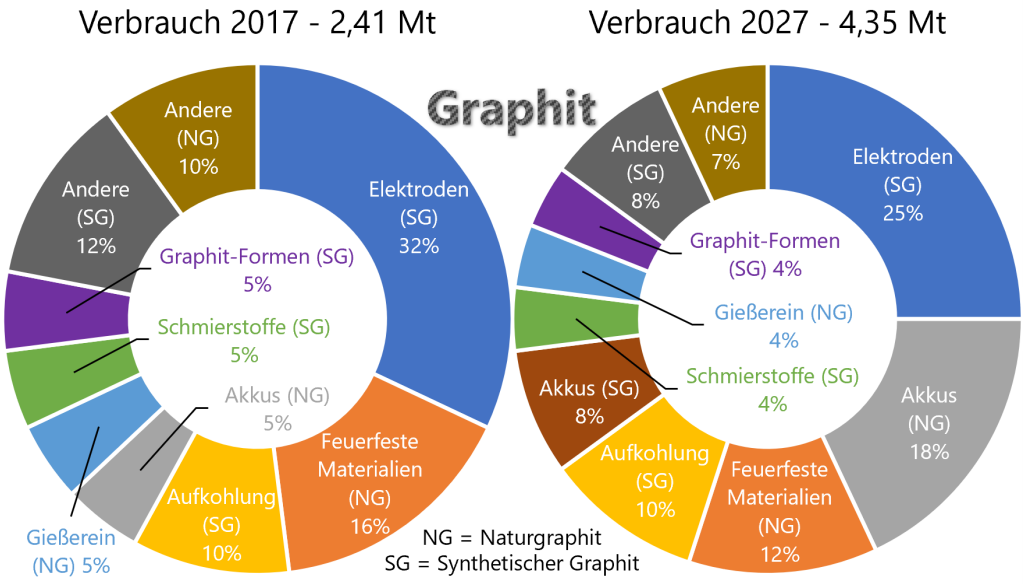

Abbildung 5. Verbrauch und Nutzung von Graphit im Jahr 2017 (2.410.000 t) sowie Vorhersage für 2027 (4.350.000 t). [139,140] Bis zum Jahr 2027 wird der Verbrauch von Graphit stark ansteigen, wobei auch ein erhöhter absoluter Verbrauch von Naturgraphit erwartet wird.

Auch ist die Recyclingrate von Graphit vernachlässigbar gering (Abbildung 4), was vor Allem an der Wirtschaftlichkeit liegt: Der Recyclingprozess ist aufwendig und das Produkt hat nicht dieselbe Reinheit und damit nicht dieselben Eigenschaften wie Naturgraphit. [141] Dazu wird zum Beispiel bei der Aluminiumherstellung bei der Schmelzflusselektrolyse Graphit in CO_2 umgewandelt, sodass hier ein direktes Recycling gar nicht möglich ist. [142] Auch wenn hierfür bereits oftmals synthetischer Graphit verwendet wird, ist der Gesamtverbrauch stark angestiegen (Abbildung 5). [139,140] Für den Gesamtverbrauch von Graphit wird eine Steigerung von 2,41 Mio. t im Jahr 2017 bis zu 4,35 Mio. t im Jahr 2027 erwartet (Abbildung 5). [139,140] Besonders problematisch ist hierbei der erhöhte Verbrauch von Naturgraphit, welcher weiterhin besonders für Akkumulatoren, feuerfeste Materialien sowie in Gießereien benötigt wird. Der Anteil von synthetischem Graphit wird voraussichtlich auch 2027 geringer als der des natürlichen Graphits sein.[143]

Zusammengefasst lässt sich festhalten, dass natürlicher Graphit aufgrund der steigenden Nachfrage bei gleichzeitig endlichen Vorkommen langfristig auf jeden Fall substituiert werden sollte. Als direkte Möglichkeit bietet sich hierfür der Einsatz von synthetischem Graphit und nicht-graphitischem Kohlenstoff an. Es wurde jedoch ebenfalls schon gezeigt, dass für die verschiedenen Anwendungen auch unterschiedliche makroskopische Eigenschaften notwendig sind. Hierfür muss insbesondere die Mikrostruktur detailliert analysiert werden, welche einen direkten Einfluss auf die makroskopischen Eigenschaften hat, um die vorhandenen Rohstoffe optimal einsetzen zu können. Im nächsten Abschnitt werden daher die aktuellen Herausforderungen bezüglich der Synthese und Charakterisierung der (nicht-)graphitischen Substituenten näher beleuchtet.

1.2.2. Offene Forschungsfragen

Da physikalische Eigenschaften wie thermische und chemische Beständigkeit und elektrische Merkmale in direktem Zusammenhang mit der Mikrostruktur von NGCs stehen, [71] ist es wichtig, diese Struktur genau zu analysieren, um NGCs auch in großem Maßstab sinnvoll einsetzen und damit kritische Rohstoffe substituieren zu können. Eine Möglichkeit ist die weit verbreitete Analyse mittels WAXS, deren Vor- und Nachteile im Folgenden kurz beschrieben werden.

Obwohl sich Weitwinkel-Röntgenstreuung (WAXS) leicht durchführen lässt und daher weit verbreitet ist, wird die Analyse von NGCs durch WAXS durch mehrere Probleme erschwert: Insbesondere die Dämpfung des Atomformfaktors und der oftmals stark begrenzte Messbereich verhindern dabei die Analyse von Reflexen höherer Ordnung, die jedoch entscheidend für die Bestimmung der Stapel-/Schichtgröße (L_a, L_c) und Unordnung (σ_1, σ_3) sind, da beide Größen in die Reflexbreite eingehen. Außerdem leidet WAXS unter einem nicht zu vernachlässigenden inkohärenten Untergrund, welcher genau berücksichtigt werden muss und bei Weitwinkel-Neutronenstreuung (WANS) einfacher zu handhaben ist (siehe auch Abbildung 6 und Abschnitt 2.4).

Die Nutzung von WANS bietet gegenüber WAXS noch weitere Vorteile, nämlich der Wegfall der Dämpfung durch den Atomformfaktor und ein großer Messbereich durch variable Wellenlänge. Allerdings zeigen bisherige Ergebnisse vom Helmholz-Zentrum in Berlin, [2] dass das in dieser Arbeit verwendete Struktur- und Anpassungsmodell von RULAND & SMARSLY [3] zwar prinzipiell auf WANS-Daten von NGCs angewendet werden kann, allerdings gibt es auch hier noch einige offene Punkte: Der in den vorangegangenen Studien verwendete Messbereich war relativ klein, sodass für diese Arbeit Proben an einem anderen Gerät mit einem größeren Messbereich am Institut Laue-Langevin in Grenoble gemessen wurden (Abbildung 6). Allerdings leiden diese WANS-Daten unter einer signifikanten Reflexverbreiterung bei kleinen Streuvektorlängen $s < 1$ Å^{-1} ($s = 2 \cdot \sin(\theta)/\lambda$), sodass sie mit den WANS-Daten von vorherigen Messungen [2] kombiniert wurden, bei denen dieses Problem nicht auftritt (Abbildung 6).

Durch die Kombination dieser beiden Datensätze konnten WANS-Daten erhalten werden, welche sowohl hoch aufgelöst sind (kleines $\Delta s/s$) als auch einen großen s-Bereich bieten. Die Mikrostruktur der Graphenschichten- und Stapel konnte damit genauer als bisher bestimmt werden. Im Verlauf der Arbeit hat sich dadurch herausgestellt, dass die Mikrostrukturquantifizierung mit den bisherigen Methoden zu ungenau war. Daneben wurden in vorherigen Arbeiten lediglich Proben einzelner Wärmebehandlungstemperaturen und keine vollständigen Temperatur-reihen analysiert. So konnten die Strukturverläufe und -entwicklungen der wärmebehandlungstemperaturabhängigen Syntheseprodukte bisher nicht exakt ausgewertet werden.

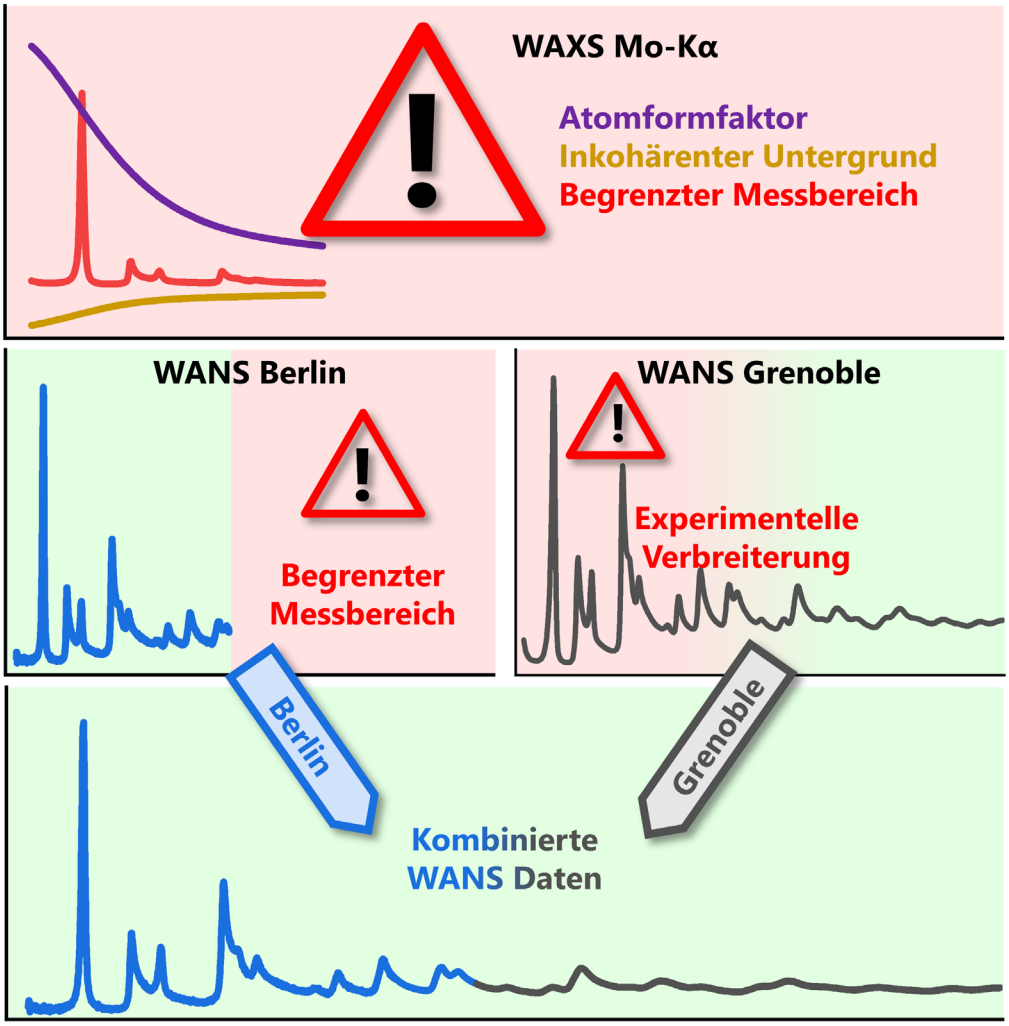

Abbildung 6. WAXS-Messungen besitzen allgemein die Nachteile der Dämpfung des Atomformfaktors, eines inkohärenten Untergrunds sowie eines begrenzten Messbereichs. WANS-Daten besitzen die ersten beiden Nachteile jedoch nicht. Allerdings haben die Daten, welche in Berlin gemessen wurden, lediglich einen begrenzten Messbereich, während die Daten, welche in Grenoble gemessen wurden, eine starke experimentelle Verbreiterung im kleinen s-Bereich aufweisen. Somit können nur kombinierte WANS-Messungen die Vorteile eines hohen Messbereiches bei gleichzeitig hoher Datenqualität bieten. Reproduziert mit Genehmigung von Oliver Osswald; veröffentlicht bei MDPI, *C*, 2023.

Die aktuell gängigste und vielversprechendste Methode zur Quantifizierung der Mikrostrukturparameter ist zwar die Verwendung von Weitwinkel-Röntgen- und Neutronenstreuung (*wide-angle X-ray/neutron scattering*, WAXS/WANS), [2,3,61,62,96,99,100,137,144–179] allerdings sind aufgrund der breiten, überlappenden und asymmetrischen Reflexe [146,176] klassische Auswertungs-Ansätze wie zum Beispiel die SCHERRER-Analyse, [180] die auf der Analyse der Breite von getrennten WAXS/WANS-Maxima basieren, für die Mikrostrukturanalyse von WAXS/WANS-Daten von NGCs ungeeignet. [169] Daher ist die Auswertung von solchen Streudaten nicht trivial, weshalb spezielle Software zur Anpassung benötigt wird (mehr dazu in Abschnitt 2.3.1). Leider erfüllt die bisher verfügbare Software nicht alle gewünschten Anforderungen. [148,149,153–156,161,167,174]

Daher bestand noch vor der eigentlich Datenanalyse das erste Ziel dieser Arbeit darin, eine geeignete Software zu entwickeln, welche sowohl WAXS- als auch WANS-Daten unter Berücksichtigung verschiedener Geräte- und Untergrundparameter anpassen kann und gleichzeitig vollständig auf kostenloser Drittsoftware basiert. Dazu sollte die Anpassung möglichst auf verschiedenen Betriebssystemen vollkommen automatisch funktionieren und möglichst einfach zu handhaben sein. Auch musste zunächst sichergestellt werden, dass sich das theoretische Modell von Ruland & Smarsly [3] überhaupt auf WANS-Daten anwenden lässt.

2. Theoretische Grundlagen

2.1. Begriffsdefinitionen

Sowohl in der Literatur als auch in wissenschaftlichen Vorträgen kommen immer wieder Unstimmigkeiten und Widersprüche zur Verwendung der Begriffe *amorpher*, *nicht-graphitischer*, *graphitischer Kohlenstoff* und *Graphit* zum Vorschein. Daher soll an dieser Stelle zunächst eine detaillierte Begriffsdefinition ergänzend zu Abbildung 1, welche bereits schematische Darstellungen zu den verschiedenen Strukturen gezeigt hat, erfolgen.

Laut der INTERNATIONALEN UNION FÜR REINE UND ANGEWANDTE CHEMIE (engl. **I**NTERNATIONAL **U**NION OF **P**URE AND **A**PPLIED **C**HEMISTRY, kurz IUPAC) ist *amorpher Kohlenstoff* „ein Kohlenstoffmaterial ohne kristalline Fernordnung", auf „Materialien mit lokalisierten π-Elektronen beschränkt" und „nicht anwendbar auf Kohlenstoffmaterialien mit zweidimensionalen Strukturelementen […] mit einem nahezu idealen interatomaren Abstand von a = 142 pm und einer Ausdehnung von mehr als 1000 pm". [181]

Nicht-graphitischer Kohlenstoff ist laut IUPAC-Definition ein Festkörper „mit zweidimensionaler Fernordnung der Kohlenstoffatome in planaren hexagonalen Netzwerken, jedoch ohne messbare kristallographische Ordnung in der dritten Richtung (c-Richtung) abgesehen von mehr oder weniger paralleler Stapelung". [182] Im Gegensatz zum amorphen Kohlenstoff liegt bei diesen Stoffen also eine messbare Fernordnung in den Schichten vor, wobei die Schichten gestapelt sind. Eine solche Ordnung, bei der die Schichten zwar parallel angeordnet, aber gegeneinander verschoben und/oder verkippt sind, wird auch als *turbostratisch* bezeichnet.

Graphit ist von der IUPAC als Kohlenstoff mit einer perfekten Kristallstruktur definiert, wobei „die Schichten […] in einer dreidimensionalen kristallinen Fernordnung parallel zueinander gestapelt" sind. [183] Als *graphitischer Kohlenstoff* werden „alle Arten von Stoffen, die aus dem Element Kohlenstoff in der allotropen Form von Graphit" bezeichnet, wobei die Abgrenzung zu Graphit durch das Fehlen einer „perfekten Graphitstruktur" gezogen wird. [183,184]

Bei genauer Betrachtung könnte man auch die bereits angesprochene Verschiebung und Verkippung der turbostratischen Kohlenstoffe als einen solchen strukturellen Defekt ansehen, sodass bei einer wörtlichen Auslegung der IUPAC-Definition ein nicht-graphitischer Kohlenstoff eigentlich auch ein graphitischer Kohlenstoff ist. Allerdings wird zur Klärung dieses Widerspruchs weiter ausgeführt, dass „die Verwendung des Begriffs graphitischer Kohlenstoff" lediglich dann gerechtfertigt ist, wenn „durch Beugungsmethoden dreidimensionale hexagonale kristalline Fernordnung im Material nachgewiesen werden kann. Andernfalls sollte der Begriff nicht-graphitischer Kohlenstoff verwendet werden". [184] Bemerkenswert hierbei ist, dass zur genauen Definition von nicht-graphitischem Kohlenstoff und zur Abgrenzung zum graphitischen Kohlenstoff eine Messmethode herangezogen wird, um den eigentlich fließenden Übergang wieder scharf abgrenzen zu können.

Als *Graphitierung* wird wiederum „eine Festkörperumwandlung von thermodynamisch instabilem nicht-graphitischem Kohlenstoff in Graphit durch Wärmebehandlung" bezeichnet. [185] Nicht-graphitische Kohlenstoffe, die „sich bei der […] Wärmebehandlung in graphitischen Kohlenstoff" umwandeln, werden *graphitierbarer Kohlenstoff* genannt, das Produkt ist dann *graphitierter Kohlenstoff*. [186,187] Im Gegensatz dazu ist ein *nicht-graphitierbarer Kohlenstoff* „ein nicht-graphitischer Kohlenstoff, der allein durch Hochtemperaturbehandlung […] nicht in graphitischen Kohlenstoff umgewandelt werden kann". [188] Er bleibt also weiterhin nicht-graphitisch, wobei als Ergebnis *glasartiger Kohlenstoff* (*glass-like carbon*) mit „einer sehr geringen Durchlässigkeit für Flüssigkeiten und Gase", bei dem „die Originalflächen und die Bruchflächen […] ein pseudoglasartiges Aussehen" haben, erhalten wird. [189] Der häufig verwendete Begriffe *glassy carbon* wurde jedoch „als Warenzeichen eingeführt und sollte daher nicht verwendet werden". [189]

Zuletzt sollte auch darauf geachtet werden, dass Graphitierung und Karbonisierung unterschiedliche Vorgänge sind. Bei der *Karbonisierung* werden „aus organischem Material meist durch Pyrolyse in inerter Atmosphäre feste Rückstände mit steigendem Gehalt des Elements Kohlenstoff gebildet" [190], welche wiederum später graphitiert werden können.

2.2. Struktur und Synthese von NGCs

2.2.1. Kristallstruktur

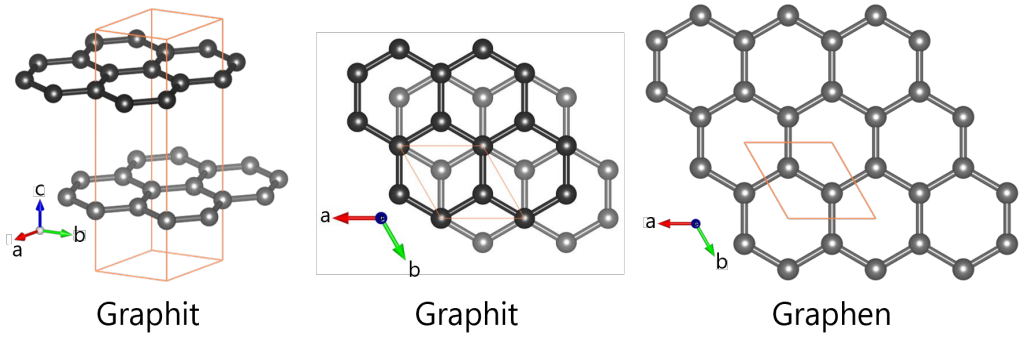

Abbildung 7. Einheitszellen von Graphit und Graphen. Beide Strukturen besitzen hexagonale Einheitszellen mit denselben Gitterparametern *a* und *b*.

Graphit und nicht-graphitische Kohlenstoffe bestehen aus mehreren Schichten von hexagonal angeordneten Kohlenstoffatomen (Abbildung 7). In diesen Schichten bilden jeweils drei Elektronen aus den 2*s*-, 2p_x- und 2p_y-Orbitalen der Atome eine σ-Bindung zu Nachbaratomen aus, sodass in der gesamten Schicht eine sp^2-Hybridisierung vorliegt. [64,111,191–194] Die zu den Schichten senkrecht stehenden 2p_z-Orbitale bilden π-Bindungen mit delokalisierten Elektronen zu den jeweiligen nächsten Nachbarn aus, was die hohe elektrische Leitfähigkeit von Graphenschichten erklärt. Die Gitterparameter betragen in Schichtrichtung

$$a = b = \sqrt{3} \cdot l_{cc} = \sqrt{3} \cdot 1{,}42\ \text{Å} = 2{,}46\ \text{Å} \qquad (1)$$

und der Winkel zwischen den Gittervektoren bzw. zwei C-C Bindungen ist 120 °.

In Stapelrichtung beträgt der Schichtabstand a_3 = 3,35 Å und der Gitterparameter somit c = 2a_3 = 6,7 Å. [37,195–197] Allerdings liegen zwischen den Schichten keine kovalenten Bindungen, sondern lediglich schwache van-der-Waals-Wechselwirkungen vor. Die Schichten können nicht nur hexagonal (ABABAB; JOHN DESMOND BERNAL [198]), sondern auch rhomboedrisch (ABCABC; HENRY SOLOMON LIPSON & ALEXAN-DER RAWSON STOKES [199]) angeordnet sein, wobei die hexagonale Modifikation aufgrund der thermodynamischen Stabilität wesentlich häufiger vorkommt. [64,192]

Kohlenstoffe, welche aus Stapeln parallel geschichteter sp^2-hybridisierter Kohlenstofflagen ohne dreidimensionale kristalline Fernordnung bestehen, werden als *nicht-graphitische Kohlenstoffe* (engl. *non-graphitic carbons*, NGCs) bezeichnet. [182] Fälschlicherweise werden solche turbostratischen Strukturen in der Literatur oft als *synthetischer Graphit* bezeichnet. Dieser Terminus meint aber i.d.R. nicht-graphitischen Kohlenstoff und nicht *Graphit* im kristallographischen Sinn.

Im Gegensatz zu Graphit, bei dem die Struktur perfekt geordnet ist, besitzen nicht-graphitische Kohlenstoffe unterschiedliche Stapelabstände (a_3), welche zusätzlich noch voneinander abweichen können (Varianz σ_3). Auch variiert die Stapelhöhe (L_c) abhängig von dem Präkursor sowie der Wärmebehandlungstemperatur bei der Graphitierung. Gleichzeitig besitzen auch die Schichten eine endliche Ausdehnung (L_a) und die durchschnittliche Kohlenstoff-Bindungslänge (l_{cc}) unterliegt ebenfalls einer gewissen Unordnung (σ_1). [3,151,152,161,163–165] 2002 haben WILHELM RULAND & BERND MICHAEL SMARSLY ein erweitertes mathematisches Modell entwickelt, welches den Einfluss verschiedener Strukturparameter auf die Weitwinkelstreuung beschreibt. [3] Wie von RULAND & SMARSLY beschrieben und in Abbildung 8 gezeigt, lässt sich die Struktur klar in Schicht- und Stapelparameter differenzieren. Die Theorie bezüglich der Streuung wird in Abschnitt 2.4 näher erläutert.

Graphitierbare Kohlenstoffe können bei hohen Behandlungstemperaturen eine graphitähnliche Struktur mit dreidimensionaler Fernordnung bilden (Abbildung 8) – bei nicht-graphitierbaren Kohlenstoffen ist dies nicht der Fall. Diese bleiben auch bei hohen Behandlungstemperaturen im gewissen Maße ungeordnet und bilden *glasartige Kohlenstoffe*. [200,201] Trotz dieser prinzipiellen strukturellen Unterschiede besitzen die graphitierbaren und nicht-graphitierbaren nicht-graphitischen Kohlenstoffe auch einige Gemeinsamkeiten: Die thermische Stabilität und chemische Inertheit ist bis zur Höhe der Behandlungstemperatur weiterhin gegeben und auch die Mikrostruktur lässt sich mit ähnlichen Parametern beschreiben. [3,71,77,202]

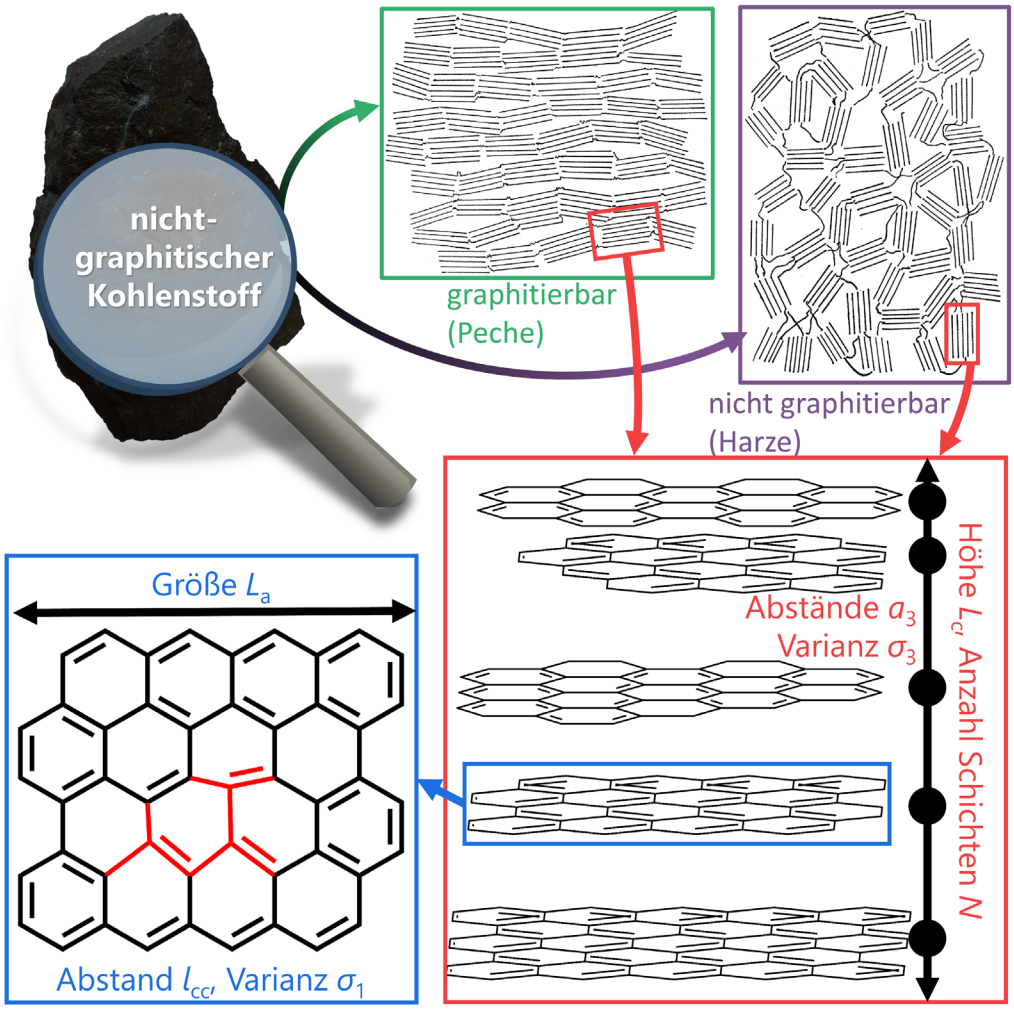

Abbildung 8. Prinzipieller Aufbau von graphitierbaren und nicht graphitierbaren nicht-graphitischen Kohlenstoffen: Die sp^2-hybridisierten Graphenschichten sind übereinandergestapelt, allerdings gegeneinander verdreht und verschoben, sodass keine dreidimensionale Fernordnung entsteht. Die Mikrostruktur lässt sich durch verschiedene Parameter, hauptsächlich über die Abstände, Schicht-/Stapelgrößen sowie die Unordnungsparameter beschreiben (mehr dazu in Abschnitt 2.4). Angelehnt an Ref. [152].

2.2.2. NGC-Synthese durch thermische Behandlung

Die bereits genannte thermische Behandlung ist prinzipiell in drei Bereiche gegliedert, wobei für die jeweiligen Bereiche aber keine starren Temperaturgrenzen existieren. Zunächst werden die synthetischen Präkursoren oder die verwendeten Biomasseabfälle pyrolysiert und dann bei höheren Temperaturen zunächst karbonisiert und – je nach Präkursor – graphitiert. [64,111,200,203]

Bei der Pyrolyse (~ 1.000 – 1.500 °C) reagieren zunächst die Vorläuferverbindungen untereinander und bilden Polymere bzw. isomerieren/aromatisieren. Dabei werden oftmals flüchtige Moleküle wie Kohlenstoffdioxid, Methan, Wasser oder andere kleine organische Verbindungen frei. [64,70,111,145,192,203–206] In diesem Temperaturbereich liegt neben dem gewünschten sp^2-hybridisierten Kohlenstoff oftmals auch noch Kohlenstoff mit sp^1- oder sp^3-Hybridisierung vor. [70,111,203,205–208] Allerdings sind konkrete Aussagen über die Anteile und den genauen Temperaturbereich stark von den jeweiligen Vorläuferverbindungen abhängig, sodass es sich hierbei mehr um Richtwerte als um absolute Werte handelt. Insgesamt liegen in diesem Bereich aber schon sp^2-hybridisierte Graphenschichten mit messbarer Ausdehnung vor. Diese Schichten sind auch parallel angeordnet, sodass die turbostratische Struktur mittels Weitwinkelstreuung entsprechend gemessen und analysiert werden kann. [1,3,209]

Bei höheren Temperaturen bis ~ 2.500 °C spricht man vom Bereich der Graphitierung. In diesem Temperaturbereich erfolgt ein weiteres Lagen- und Stapelwachstum. Hierbei wird nicht nur die Größe der einzelnen Schichten oder der Stapel, sondern auch deren intrinsische Ordnung erhöht. Allerdings liegt in der Regel noch keine dreidimensionale Fernordnung vor und die Struktur ist weiter turbostratisch. [210] Bei noch höheren Temperaturen (bis zu 3.000 °C) muss zwischen graphitierbaren und nicht-graphitierbaren Kohlenstoffen bzw. Präkursoren unterschieden werden. Bei graphitierbaren Vorläufern wie zum Beispiel bei polyzyklischen aromatischen Kohlenstoffen liegen bereits bei Raumtemperaturen zum Großteil sp^2-hybridisierte Kohlenstoffatome vor. Daher ist bei diesen Präkursoren das bereits genannte Schichtwachstum im Vergleich zu Phenol-Formaldehyd-Harzen schneller. Auch ordnen sich die einzelnen Schichten bei sehr hohen Temperaturen graphitähnlich an, sodass eine dreidimensionale Fernordnung

messbar ist. Allerdings entspricht die Struktur hier immer noch nicht der von perfektem Graphit, sondern es liegt noch eine gewisse Unordnung vor (Abbildung 9). [210]

Nicht-graphitierbare Präkursoren wie zum Beispiel Phenol-Formaldehyd-Resolharz bilden zunächst Polymere, welche aber immer noch einen signifikanten Anteil an Fremdatomen wie zum Beispiel Sauerstoff enthalten. Daher ist hier das Lagen- und Stapelwachstum wesentlich langsamer. Daraus folgen glasartige Kohlenstoffe mit geordneter Graphen- aber ungeordneter Stapelstruktur mit Mikroporen im Nanometerbereich (Abbildung 9). [210]

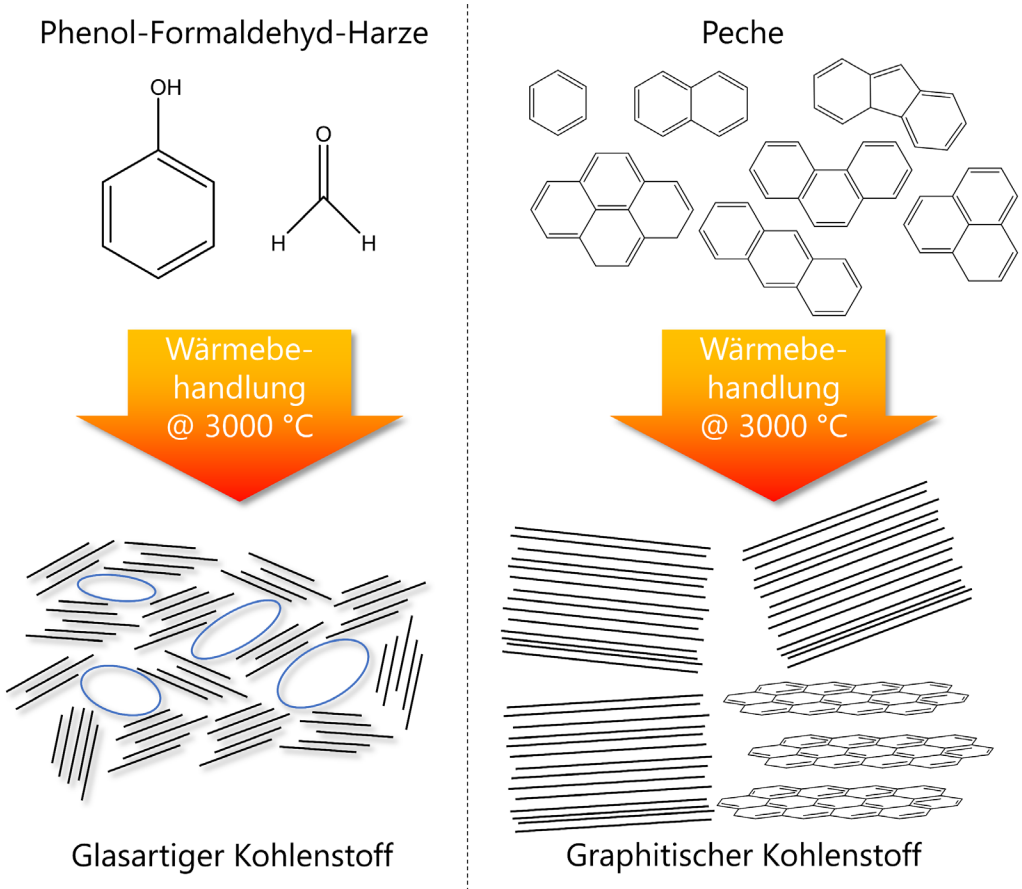

Abbildung 9. Schematische Darstellung der verschiedenen Präkursoren. Phenol-Formaldehyd-Harze bilden bei hohen Temperaturen leicht poröse glasartige Kohlenstoffe, während Peche, insbesondere Peche mit niedrigem Erweichungspunkt, bei sehr hohen Temperaturen Graphit oder zumindest hochgeordneten graphitähnlichen Kohlenstoff bilden können. Reproduziert mit Genehmigung von Oliver Osswald; veröffentlicht bei MDPI, *C*, 2023.

2.3. Analysemethoden

Für die Mikrostrukturanalyse von NGCs werden aktuell üblicherweise drei Ansätze angewendet: Transmissionselektronenmikroskopie (TEM), [61,100,145,152,159,169,204,211] Raman-Spektroskopie [5,99,111,179,212–221] sowie Weitwinkel-Röntgen-/Neutronenstreuung (WAXS/WANS). [1,2,61,62,100,145,147–150,153–157,170,172–174,176–178,204,209,217,222] Hierbei können die entsprechenden Daten zum Teil auch simuliert werden (Abbildung 10). Daneben kann auch Kleinwinkelstreuung für die Strukturanalyse von porösen Kohlenstoffen genutzt werden. Mittels Kleinwinkelstreuung lässt sich jedoch nicht die Mikrostruktur auf atomarer Ebene bestimmen. Stattdessen kann diese Methode für die Analyse von Porensystemen genutzt werden, [223–228] weshalb sie hier auch nicht weiter ausgeführt wird.

Mittels TEM lassen sich zwar die Stapel- und Schichtgrößen bestimmen und auch quantitativ messen, allerdings lässt sich die Schichtunordnung bislang nicht und die Stapelunordnung nur sehr schwer quantifizieren. Raman-Spektroskopie kann verwendet werden, um die durchschnittliche Schichtausdehnung L_a quantitativ und die Schicht- und Stapelordnung qualitativ zu bestimmen, allerdings wird hier immer noch diskutiert, wie genau L_a berechnet werden muss und inwiefern diese Daten vergleichbar zu den Ergebnissen aus WAXS/WANS-Messungen sind. [111,209,217,222]

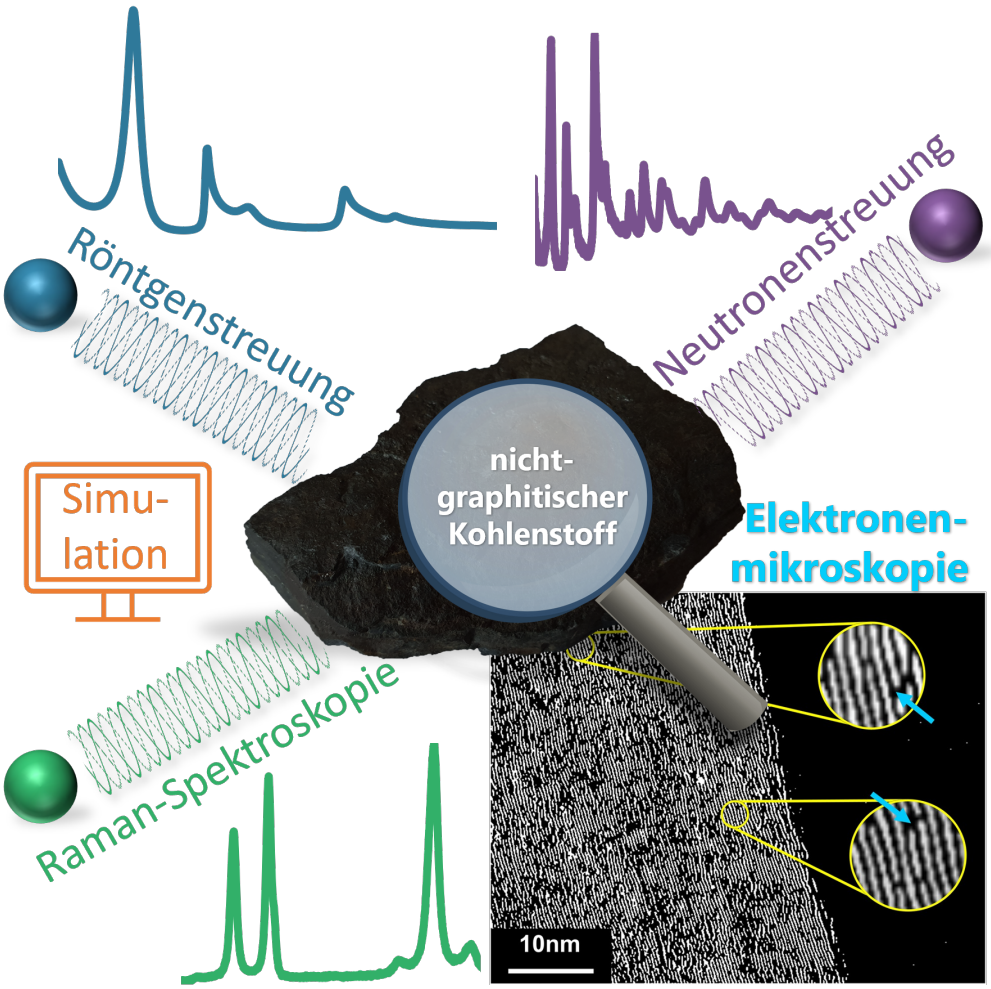

Abbildung 10. Vergleich von verschiedenen Messmethoden für die Charakterisierung von NGCs. Die Mikrostruktur von NGCs lässt sich mittels Röntgen-, Neutronenstreuung, Raman-Spektroskopie und Elektronenmikroskopie bestimmen. TEM-Bild entnommen von Ref. [229] (Creative-Commons-Lizenz: http://www.creativecommons.org/licenses/by/4.0).

2.3.1. Weitwinkelstreuung

Da die Strukturaufklärung von nicht-graphitischen Kohlenstoffen in dieser Arbeit hauptsächlich mittels Weitwinkelstreuung erfolgte, wird dieses Verfahren näher beschrieben. Der genutzte Effekt wurde zunächst von MAX VON LAUE entdeckt (Nobelpreis für Physik 1914 „für seine Entdeckung der Beugung von Röntgenstrahlen durch Kristalle“), [230–232] aber erst von WILLIAM HENRY und WILLIAM LAWRENCE BRAGG korrekt erklärt und für Strukturanalyse verwendet (Nobelpreis für Physik 1915 „für ihre Verdienste bei der Analyse der Kristallstruktur mittels Röntgenstrahlen“). [233–238]

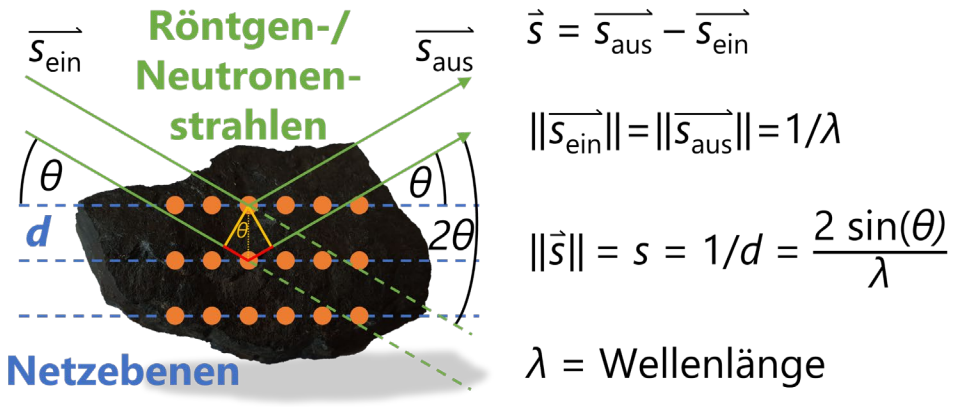

Abbildung 11. Schematische Darstellung des Streueffekts an Kristallgittern: Die eingehenden Strahlen streuen an den einzelnen Atomen, was phänomenologisch auch als Beugung am (Kristall-)Gitter beschrieben werden kann. Dadurch kommt es bei bestimmten Winkel-/Wellenlänge-/Gitterabstandverhältnissen zu konstruktiver Interferenz, welche beim Experiment gemessen wird.

Bei kristallinen Stoffen sind die Atome periodisch in einem Gitter angeordnet, sodass es abhängig von der Wellenlänge bei bestimmten Ein- und Ausfallswinkeln zu konstruktiver Interferenz kommt (Abbildung 11). Durch die gemessene Intensität bzw. Interferenz in Abhängigkeit des Messwinkels entsteht ein Diffraktogramm, bei dem die gemessenen Interferenzen den Kristall-Gitterebenen entsprechen. So lassen sich die gewünschten Informationen bezüglich der Mikrostruktur ermitteln.

Photonen werden an der Elektronenhülle als Kugel und Neutronen am Nukleus als Punktzentrum gestreut. Es kommt genau dann zu konstruktiver Interferenz, wenn der Gangunterschied zwischen zwei (oder mehreren) Strahlen genau ein Vielfaches (n) der Wellenlänge (λ) ist (Abbildung 11). Dieser Gangunterschied (rot in Abbildung 11) hängt auch vom Beugungswinkel (θ) und dem Gitterebenenabstand (d) ab, sodass sich die BRAGG-Gleichung ergibt:

$$n\,\lambda = 2\,d\sin(\theta) \tag{2}$$

Alternativ lässt sich die Interferenz auch über den ein- und ausfallenden Streuvektor ($\overrightarrow{s_{ein}}$ bzw. $\overrightarrow{s_{aus}}$) bzw. deren Länge beschreiben:

$$\|\overrightarrow{s_{ein}}\| = \|\overrightarrow{s_{aus}}\| = 1/\lambda \tag{3}$$

$$\|\vec{s}\| = \|\overrightarrow{s_{ein}} - \overrightarrow{s_{aus}}\| = s = \frac{2\sin(\theta)}{\lambda} \tag{4}$$

Während 1924 die Struktur von Graphit mittels Röntgen-Weitwinkelstreuung aufgeklärt wurde [198] und es auch in den 1930ern und 1940ern von WARREN, BISCOE, HOUSKA et al. weitere Studien zur Strukturaufklärung von Kohlenstoffen gab, [146,176,177] hat besonders ROSALIND ELSIE FRANKLIN zur Strukturaufklärung nicht-graphitischer Kohlenstoffe beigetragen. [151,152,210,239–253] Nach dieser Pionierarbeit von WARREN, BISCOE, HOUSKA und FRANKLIN hat sich besonders WILHELM RULAND mit der Strukturaufklärung von (nicht-)graphitischen Kohlenstoffen mittels Röntgenstreuung beschäftigt. [3,78,160,163–166,227] Grund hierfür war unter anderem, dass WAXS grundlegende Vorteile, insbesondere die unkomplizierte experimentelle Analyse mit Standard-Laborgeräten sowie die Analyse eines Durchschnitts der gesamten Probenmenge im Gegensatz zu punktuellen Ausschnitten, bietet.

Anstelle der Analyse einzelner Reflexe ist es aufgrund der Asymmetrie der (hk)-Interferenzen und Überlappung sinnvoller, die gesamte WAXS/WANS-Kurve mit einer geeigneten Modellfunktion anzupassen. 2002 veröffentlichten RULAND & SMARSLY ein Modell für die Analyse von WAXS- und WANS-Daten, was sich besonders durch die Berücksichtigung der turbostratischen Struktur sowie der Vielfalt der verwendeten Struktur- und Unordnungsparameter auszeichnet. [3]

Im Laufe der Promotion wurde das Modell von RULAND & SMARSLY [3] verwendet und auf WANS-Daten übertragen, um ein neues Softwaretool zur automatischen Analyse von WAXS/WANS-Daten von NGCs zu entwickeln. Dies beinhaltet auch die qualitative Behandlung des inkohärenten Untergrunds bei WANS-Daten. Die theoretische Ausführung dazu erfolgt im nächsten Abschnitt. Dieses Modell wurde bereits 2018 in CARBX von PFAFF et al. verwendet, um Streudaten möglichst automatisiert mittels einer graphischen Oberfläche anpassen zu können. [161] Dieser theoretische Ansatz ist zwar vielversprechend und auch in der Praxis mehrfach erfolgreich erprobt, [2,61,62,100,145,150,204] muss aber weiter ausgebaut werden, um den gewünschten Anforderungen gerecht zu werden: Aktuell ist die Software nur für Microsoft Windows, nicht aber für andere Betriebssysteme verfügbar und benötigt Wolfram Mathematica [254] als kommerzielle Software für die automatische Anpassung. Weitere Einzelheiten zu diesem neuen Tool sind in Kapitel 3.1 zu finden.

2.3.2. Modell von RULAND & SMARSLY

In diesem Abschnitt wird das theoretische Modell von RULAND & SMARSLY [3] erläutert, welches die Weitwinkelstreuung von nicht-graphitischem Kohlenstoff beschreibt. Das Modell basiert auf der von WARREN beschriebenen turbostratischen Struktur, [177] bei der Graphenschichten parallel zueinander gestapelt sind, sonst aber keine dreidimensionale Fernordnung besitzen. Es werden überlappende (*hk*)- und (00*l*)-Interferenzen gemessen, welche mit geeigneten Funktionen modelliert werden können. [a]

Die Streuintensität (normalisiert auf Elektroneneinheiten pro Kohlenstoffatom) $I_{e.u.}$ ist gegeben als eine Superposition der kohärenten Streuung der Struktur (I_{coh} von engl. *coherent*) und inkohärenter Streuung (I_{incoh} von engl. *incoherent*) (Abbildung 12):

$$I_{e.u.} = I_{coh} + I_{incoh} \quad (5)$$

[a] Die Indizierung in Klammern bezeichnet zwar streng genommen Netzebenen und einzelne Reflexe müssten ohne Klammern indiziert werden, jedoch werden zur besseren Lesbarkeit in dieser Arbeit Klammern für beide Bedeutungen synonym verwendet.

Die inkohärente Streuung besteht aus der COMPTON- Streuung (I_{com}), korrigiert um den Breit-Dirac Rückstoß-Faktor (*recoil*), den spezifischen Absorptionsfaktor (Q_{abs}) sowie einem optionalen Faktor für einen Sekundärmonochromator (Q):

$$I_{incoh} = I_{com} \cdot recoil \cdot Q_{abs} \cdot Q \quad (6)$$

Die genauen Formeln für die einzelnen Faktoren bzw. der Berechnung der Compton- Streuung anzugeben, würde an dieser Stelle zu weit führen, stattdessen wird auf die entsprechenden Einzelpublikationen von RULAND et al. [163,164,255–257] bzw. der Arbeit von PFAFF et al. [161] und Kapitel 6.4.2 dieser Arbeit verwiesen.

Die kohärente Streuung setzt sich aus der Interferenz(-intensität) innerhalb der einzelnen Schichten (I_{intra} von engl. *intralayer*) sowie der Interferenz(-intensität) durch die Stapelbindung zwischen den Schichten (I_{inter} von engl. *interlayer*) sowie dem Atomformfaktor von Kohlenstoff (f_C) zusammen (Abbildung 12 A/C):

$$I_{coh} = f_C^2 \cdot (I_{inter} + I_{intra}) \quad (7)$$

Im Falle von Röntgenstreuung ist f_C eine Funktion abhängig vom Messwinkel bzw. der Streuvektorlänge (Abbildung 12B). Die Näherungen für die Berechnung [258–260] sind ebenfalls im Anhang in Kapitel 6.4.2 gezeigt. Bei Neutronenstreuung wird für f_C die konstante Streulängendichte von Kohlenstoff verwendet, welche allerdings nicht extra berechnet werden muss, da diese Größe indirekt über die Normalisierungskonstante k erfasst wird (siehe Seite 32). [261–263] Für die Berechnung von $I_{inter} + I_{intra}$ wird an dieser Stelle auf die Originalpublikation von RULAND & SMARSLY verwiesen. [3]

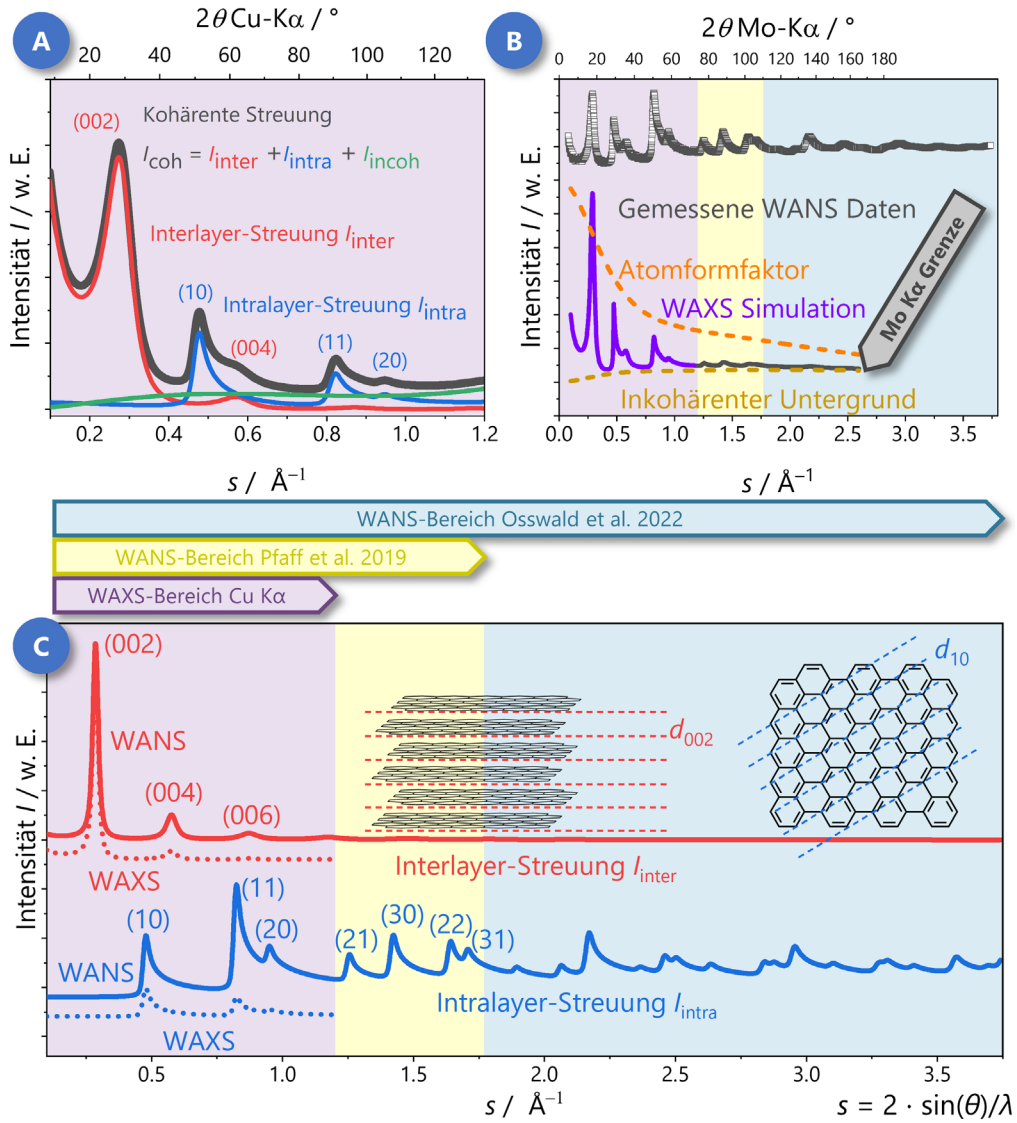

Abbildung 12. A) Repräsentatives Beispiel für experimentelle WAXS-Daten eines NGC, die durch eine Überlagerung von symmetrischen Stapel-Reflexen (00*l*), asymmetrischen Schicht-Reflexen (*hk*) und der inkohärenten Streuung (I_{incoh}) gegeben sind. B) Während WAXS-Daten unter der durch den atomaren Formfaktor induzierten Dämpfung leiden, können durch die Verwendung von WANS-Daten besser unterscheidbare Reflexe erhalten und sinnvoll analysiert werden. C) Simulation von WAXS/WANS-Daten eines NGC (ohne Untergrundstreuung): Mit Neutronenstrahlung anstelle von Röntgenstrahlen können mehr (*hk*)-Reflexe gemessen und damit insbesondere die Schicht-/Graphenstruktur genauer bestimmt werden. Reproduziert mit Genehmigung von Oliver Osswald; veröffentlicht bei MDPI, *C*, 2023.

Wenn nicht alle Kohlenstoffatome im hexagonalen Gitter angeordnet sind, sondern zum Beispiel sp^3-hybridisiert als Verunreinigung an den Rändern oder als Defekte innerhalb des Gitters vorliegen, kann nach den Arbeiten von FRANKLIN [151,152] angenommen werden, dass diese Atome eine Untergrundstreuung ohne weitere Interferenz verursachen. Mit der Konzentration an nicht-organisiertem Kohlenstoff (C_{un}) ergibt sich für die Gesamtintensität von Kohlenstoff folgender Zusammenhang:

$$I_{e.u.,\,c,\,WAXS} = (I_{coh} + I_{incoh}) = \\ (1 - c_{un}) \cdot f_C^2 \cdot (I_{inter} + I_{intra}) + c_{un} \cdot f_C^2 + I_{com} \cdot recoil \cdot Q_{abs} \cdot Q \tag{8}$$

Während Gleichung (8) so nur für Röntgenstreuung gilt, wird die inkohärente Streuung für Neutronenstreuung nicht analytisch berechnet, sondern als eine von der Streuvektorlänge s abhängige Funktion angegeben angepasst. Da für Neutronenstreuung f_C konstant ist, wird dies in Gleichung (9) durch den Faktor a und in Gleichung (12) auch durch den allgemeinen Normalisierungsfaktor k berücksichtigt. Die inkohärente Streuung wird bei Neutronenstreuung durch den Ausdruck $b(s)$ beschrieben und in der praktischen Anwendung nicht analytisch berechnet, sondern vor der eigentlichen Verfeinerung numerisch angepasst. Das genaue Vorgehen für die Untergrundbetrachtung für WANS ist sowohl in den Originalpublikationen [264,265] als auch im Anhang in Kapitel 6.4.2 beschrieben. Insgesamt ergibt sich für WANS folgender Zusammenhang:

$$I_{e.u.\ C\ WANS} = (I_{coh} + I_{incoh}) = (1 - c_{un}) \cdot f_C^2 \cdot (I_{inter} + I_{intra}) + c_{un} \cdot f_C^2 + I_{incoh} \\ = \quad a \quad \cdot (I_{inter} + I_{intra}) + \quad b(s) \tag{9}$$

Auch bei WANS lässt sich die Gesamtintensität weiterhin nach Stapel- und Schichtstruktur aufteilen (Abbildung 12 C). Die Intensität ist aber nicht durch den Atomformfaktor gedämpft, wodurch deutlich mehr (hk)-Reflexe sichtbar werden, was eine genauere Bestimmung der Schichtstruktur erlaubt. Die Stapelunordnung führt hingegen generell zu einer großen Dämpfung der (00l)-Reflexe, sodass WANS für die Bestimmung der Stapelstruktur nur geringe Vorteile bringt.

Während die vorherigen Gleichungen die Streuung an Kohlenstoff beschreiben, müssen auch die in den Proben vorliegenden Verunreinigungen durch Fremdatome (in der Regel Wasserstoff, Stickstoff, Sauerstoff und Schwefel) berücksichtigt

werden. Für diese Atome wird angenommen, dass diese vollständig unorganisiert vorliegen und nicht zur kohärenten Streuung beitragen. Deren Streuintensität wird bei Neutronenstreuung ebenfalls durch den Term $b(s)$ berücksichtigt, für Röntgenstreuung allerdings analytisch berechnet:

$$I_{\text{e.u., X}} = I_{\text{coh, X}} + I_{\text{incoh, X}} = f^2_{\text{X}} + I_{\text{com, X}} \cdot recoil \cdot Q_{\text{abs}} \qquad (10)$$

Dabei wird die Intensität $I_{\text{e.u., x}}$ für jedes Element (x = H, N, O, S) mit seiner Konzentration gewichtet (c_{H}, c_{O}, c_{N}, c_{S} und $c_{\text{C}} = 1 - c_{\text{H}} - c_{\text{O}} - c_{\text{N}} - c_{\text{S}}$) und die insgesamt resultierende Streuung aller Atome $I_{\text{e.u.}}$ wie folgt berechnet:

$$I_{\text{e.u.}} = c_{\text{C}} \cdot I_{\text{e.u., c}} + c_{\text{H}} \cdot I_{\text{e.u., H}} + c_{\text{N}} \cdot I_{\text{e.u., N}} + c_{\text{O}} \cdot I_{\text{e.u., O}} + c_{\text{S}} \cdot I_{\text{e.u., S}} \qquad (11)$$

Um die gemessene Intensität vollständig zu erhalten (I_{obs} von engl. *observed*), wird $I_{\text{e.u.}}$ noch um weitere Faktoren korrigiert: Die Polarisation P, die Absorption A und eine Normierungskonstante k. [3,266] Außerdem werden zwei Konstanten für die Berücksichtigung eines unbekannten linearen und nicht-linearen Untergrunds ($const_1$, $const_2$) genutzt. Daneben kann ein exponentieller Dämpfungsfaktor verwendet werden, welcher einen möglichen Anteil einer Kleinwinkelstreuung poröser Kohlenstoffe beschreiben kann (*gFact*). Auch wird ein Faktor zur Umrechnung von einer variablen zu einer festen Divergenzblende (*AutoColl*) genutzt. Dazu hat es sich als nützlich erwiesen, eine logarithmische Darstellung zu verwenden, da diese Anpassungsfunktion zuverlässigere Ergebnisparameter liefert als ohne Logarithmierung. Die anschließende Potenzierung dient dazu, die korrekten (gemessenen) Intensitäten zu erhalten. Insgesamt ergibt sich für die gemessene Streuintensität dann folgender Zusammenhang:

$$I_{\text{obs}} = 10\text{^}[\log_{10}((1/AutoColl) \cdot gFact \cdot k \cdot A \cdot P \cdot (I_{\text{e.u.}})) + const_1) + const_2] \qquad (12)$$

Diese theoretischen Überlegungen wurden genutzt, um das bereits angesprochenen Tool zur automatischen Analyse von WAXS- und WANS-Daten zu erstellen und die Daten aus Berlin und Grenoble damit auszuwerten. In Kapitel 3 werden die Ergebnisse aus diesen Publikationen kurz vorgestellt.

3. Ergebnisse

In diesem Abschnitt werden die Ergebnisse der zwei dieser Arbeit zugrundeliegenden Publikationen vorgestellt. [1,209] Die Ergebnisse werden getrennt nach Publikation vorgestellt, wobei sich auf eine kurze Motivation und die wichtigsten Erkenntnisse beschränkt wird. Genauere Ausführungen können direkt den Publikationen entnommen werden.

3.1. Ergebnisse der ersten Publikation

Während bereits ausführlich gezeigt wurde, dass sich die Mikrostruktur von nicht-graphitischen Kohlenstoffen mittels WAXS/WANS-Messungen bestimmen lässt und durch die Arbeit von RULAND & SMARSLY [3] bereits ein Modell zur Auswertung solcher Daten vorliegt, gab es noch keine Software, welche die gewünschten Anforderungen (kostenlos, open-source, schnell, leicht anpassbar, Verfügbarkeit für verschiedene Betriebssysteme, Analyse von WANS-Daten) vollständig erfüllt. Daher wurde in dieser Publikation [1] eine erste Version eines Skripts zur Verfeinerung von WAXS- und WANS-Daten vorgestellt, das den von RULAND & SMARSLY vorgestellten Ansatz [3] in Kombination mit GNU OCTAVE [267] sowie des dazugehörigen OPTIM-Pakets [268] als freie Open-Source-Software verwendet, die unter der GNU General Public License steht. [269] Durch die Verwendung dieses Scripts („OCTCARB“) ergeben sich wichtige Vorteile: OCTAVE und damit auch OCTCARB ist komplett kostenlos und quelloffen, für verschiedene Betriebssysteme verfügbar und benötigt keine weitere Software.

Eine Hauptverbesserung gegenüber früherer Software (CARBX) [161] ist die Möglichkeit, Pulver-Weitwinkelneutronenstreudaten (WANS) zu verfeinern. Zusätzlich ist es auch möglich, OCTAVE für fast alle Linux-Distributionen zu kompilieren, sodass OCTCARB mit den meisten High-Performance-Computing-Clustern verwendet werden kann. Gleichzeit ist OCTCARB aber auch so ressourcenschonend in Bezug auf die CPU-Auslastung, dass nicht der gesamte Computer blockiert wird und noch weitere Programme parallel ausgeführt werden können, wobei die Analyse einer WAXS/WANS-Kurve dennoch in zufriedenstellender Zeit, also innerhalb von Minuten, durchgeführt werden kann.

Neben der automatischen und GUI-basierten Verfeinerung kann das Verfeinerungsskript auch leicht für andere Messgeometrien, Blenden-konfigurationen und andere individuelle Bedürfnisse modifiziert bzw. angepasst werden. Dies macht den vorgestellten Ansatz nicht nur für Anwender nutzbar, die eine unkomplizierte, automatisierte Verfeinerung von WAXS/WANS-Daten von NGCs anstreben, sondern auch für fortgeschrittene Anwender, die den gesamten Verfeinerungsprozess für ihre individuellen Bedürfnisse optimieren möchten.

Als zusätzliche Verbesserung können nun auch die inkohärenten Streuintensitäten von Wasserstoff und Schwefel als ungeordnete Fremdatome berechnet werden (zusätzlich zu Stickstoff und Sauerstoff, welche schon vorher implementiert waren), um einen physikalisch sinnvollen und detaillierten inkohärenten Untergrund berücksichtigen zu können. Auch werden die statistischen, experimentellen Fehler im Sinne der etablierten Theorie der Fehlerfortpflanzung ermittelt und anhand der Kovarianzmatrix berechnet, d. h. es werden nun die Standardabweichungen der verfeinerten Parameter ausgegeben. In einigen Fällen sind die Daten am Beginn und Ende des zugänglichen Datenbereichs nicht nutzbar, z.B. wegen starker Kleinwinkelstreubeiträge. OCTCARB enthält eine einfache Möglichkeit, solche Daten zu überspringen und so die Analyse zu verbessern.

Insgesamt wurde ein zuverlässiges, kostenloses, schnelles und quelloffenes Verfahren zur Auswertung der Weitwinkel-Röntgen-/Neutronenstreuung (WAXS/WANS) nicht-graphitischer Kohlenstoffe entwickelt, das bekannte Anpassungsroutinen (LEVENBERG-MARQUARDT-Algorithmus) verwendet. [1,270–272] Mit OCTCARB können WAXS/WANS-Daten unter Verwendung des theoretischen Modells von RULAND & SMARSLY [3] verfeinert und physikalisch aussagekräftige Parameter erlangt werden, welche die Stapel- und Schichtstruktur inklusive der intrinsischen Unordnung beschreiben.

3.2. Ergebnisse der zweiten Publikation

Die zweite dieser Arbeit zugrundeliegende Publikation [209] beschäftigte sich mit der grundlegenden Frage nach der Unordnung in nicht-graphitischen Kohlenstoffen (NGCs), besonders innerhalb der einzelnen Graphenschichten. Da neben der strukturellen Unordnung (σ_1) selbst auch die endliche Ausdehnung (L_a) der Schichten zu einer Reflexverbreiterung führt, besteht die Herausforderung in der Unterscheidung zwischen Unordnung und Größe anhand von WAXS/WANS-Daten. Die Idee in dieser Arbeit bestand darin, WANS-Daten von zwei verschiedenen Einrichtungen (Helmholtz-Zentrum in Berlin (HBZ) [273] und Institute Laue-Langevin in Grenoble (ILL) [274,275]) von denselben Proben zu erhalten und im Anschluss zu kombinieren. Die Daten aus Berlin haben zwar nur einen kleineren Messbereich ($\sim 0{,}40\ \text{Å}^{-1} < s < 1{,}7\ \text{Å}^{-1}$), dafür aber eine sehr gute $\Delta s/s$-Auflösung. Die Daten aus Grenoble besitzen einen wesentlich größeren Messbereich ($0{,}052\ \text{Å}^{-1} < s < 3{,}76\ \text{Å}^{-1}$), sind allerdings im kleinen s-Bereich aufgrund der experimentellen Verbreiterung schlechter aufgelöst. Durch eine Kombination beider Daten kann ein großer Messbereich der Streuvektorlängen s ($= 2 \cdot \sin(\theta)/\lambda$) erhalten werden, welcher von den unterschiedlichen Auflösungen der Experimente im kleinen (Berlin) und großen (Grenoble) s-Bereich profitiert (Abbildung 13) und so zu eine detaillierten Analyse der Stapel- und der Schichtstruktur genutzt werden kann.

Dabei wurde auch gezeigt, dass WANS-Daten im Allgemeinen aus mehreren Gründen WAXS-Daten überlegen sind: Erstens kommt es zu keiner Dämpfung durch einen Atomformfaktor im Bereich großer Streuvektorlängen. Zweitens kann der inkohärente Untergrund einfacher berücksichtigt werden. Drittens ist der verfügbare Messbereich im Vergleich zu Labor-WAXS-Aufbauten wesentlich größer, was den zugänglichen Bereich von Reflexen erhöht. Auch hat sich gezeigt, dass hochwertige WANS-Daten im großen s-Bereich tatsächlich die Möglichkeit bieten, zwischen L_a und σ_1 zu unterscheiden. Dies führte zu einer aussagekräftigen und detaillierten Überprüfung des aktuellen Wissens über die Mikrostruktur, insbesondere über die Schichtstruktur und deren Entwicklung bei unterschiedlichen Wärmebehandlungstemperaturen.

Es wurde dabei nachgewiesen, dass lediglich WANS-Daten mit einem hohen *s*-Bereich zu einer zuverlässigen und reproduzierbaren Bestimmung der Unordnung und Größe der Graphenschichten führen. WAXS-Daten und WANS-Daten mit einem kleinen *s*-Bereich, insbesondere auch typische Laborinstrumente mit Cu-K_α Röntgenquellen, führen lediglich zu einer unzuverlässigen Bestimmung von L_a und σ_l und sind somit für die exakte Quantifizierung ungeeignet. Allerdings bleiben die semiquantitativen Verhältnisse der Werte für verschiedene Proben nahezu gleich.

Grundlegend wurde nachgewiesen, dass das Modell von RULAND & SMARSLY [3] eine hervorragende Anpassung von WANS-Daten bis hin zu großen *s*-Werten ermöglicht, was überhaupt die Möglichkeit einer präzisen Bestimmung der Mikrostrukturparameter bezüglich der Graphenstruktur ermöglicht.

Als wichtigstes strukturelles Ergebnis sind scheinbar „ungeordnete" Kohlenstoffe (insbesondere Phenol-Formaldehyd-Harze) wesentlich geordneter als bisher angenommen. Die Graphenschichten für solche Kohlenstoffproben sind kleiner (in der Größenordnung von höchstens einigen Nanometern), aber intrinsisch geordneter als in früheren Studien postuliert (Abbildung 13). [2,145,204] Insgesamt wurde bei den vorherigen Studien die Schichtausdehnung und Unordnung systematisch überschätzt. Diese Erkenntnisse stellen einen grundlegenden Fortschritt bezüglich der Sicht auf die Struktur dieser Materialien dar. Sie sind keineswegs „amorph", sondern das Gegenteil ist der Fall: Die Graphene in NGCs besitzen eine Ordnung, die einem idealen Graphen sehr nahekommt. Dieses Ergebnis könnte zukünftig zum Verständnis der Graphitierung, also der Entstehung von Graphit, beitragen.

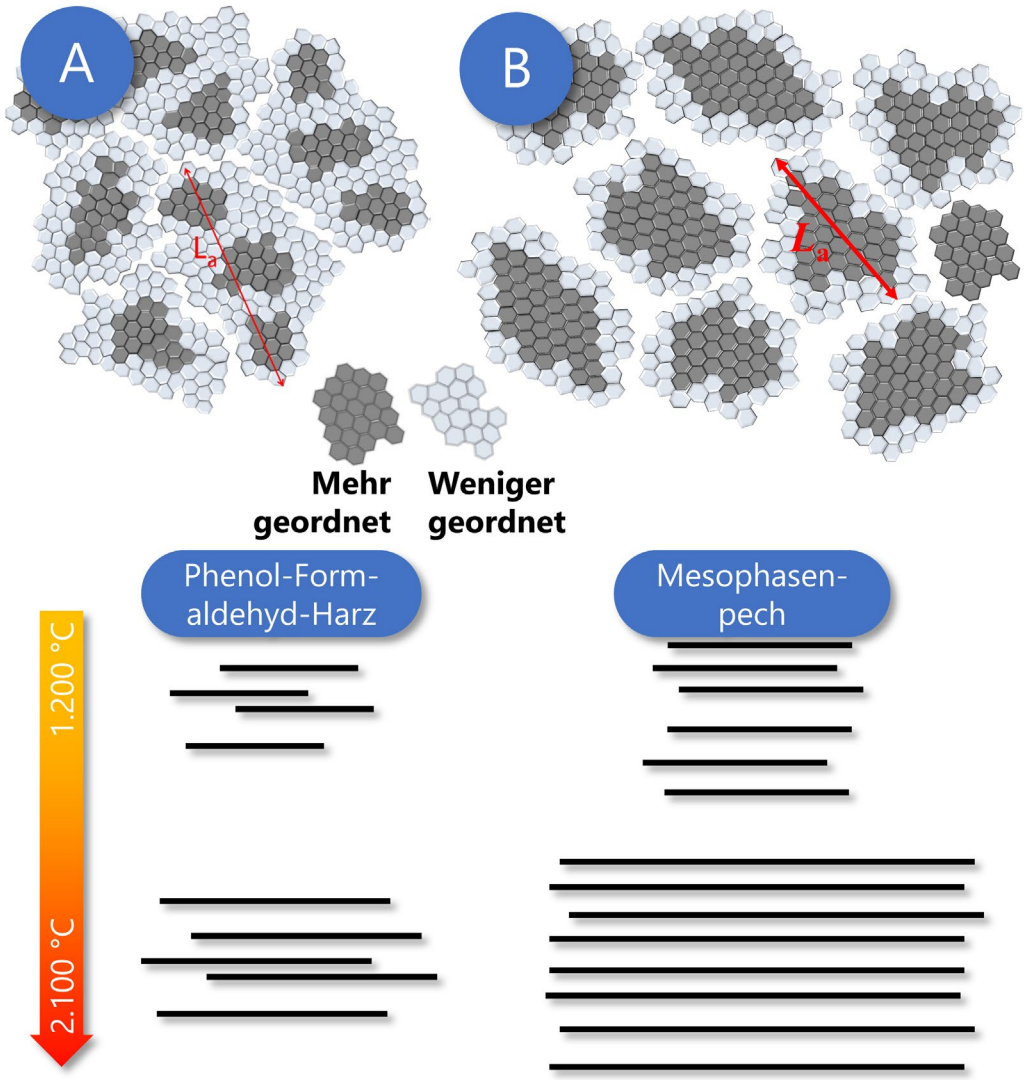

Abbildung 13. Neue Einblicke in die Mikrostruktur von nicht-graphitischem Kohlenstoff: Im Vergleich zu früheren Studien [2] (A) liefern die aktuellen Ergebnisse (B) ein verfeinertes Bild von kleineren, aber hochgeordneten Graphenschichten. Während beim Phenol-Formaldehyd-Harz die Stapelgröße mit steigender Wärmebehandlungstemperatur nur unwesentlich zunimmt, werden die Stapel beim Mesophasenpech signifikant größer und geordneter. Nachdruck (angepasst) mit freundlicher Genehmigung von Ref. [2] Copyright 2019 American Chemical Society. Nachweis siehe Kapitel 6.3.

4. Fazit und Ausblick

4.1. Fazit

Zusammenfassend wurde im Rahmen der Promotion ein kostenloses Software-Skript (OCTCARB) entwickelt, das in dem Open-Source Programm OCTAVE Weitwinkel-Röntgen- und Neutronenstreuungsdaten (WAXS/WANS) von nicht-graphitischen Kohlenstoffen (NGCs) verfeinert und auf dem Modell von RULAND & SMARSLY (2002) basiert. [3] Als Ergebnis werden bis zu 14 strukturell sinnvolle Parameter wie die Schichtausdehnung, Stapelhöhe und der Grad der Unordnung der Graphene und ihrer Stapelung erhalten. Zusätzlich können die Untergrundstreuung basierend auf bestimmten physikalischen Phänomenen und verschiedene Korrekturparameter wie Polarisation und Absorption berücksichtigt werden. Die Software ist so konzipiert, dass sie auch von erstmaligen Benutzern verwendet, aber auch jederzeit angepasst und optimiert werden kann. Als weiteres wesentliches Feature läuft OCTAVE und damit OCTCARB auf allen gängigen Betriebssystemen (Windows, MacOS und Linux). Außerdem kann die gesamte Verfeinerung innerhalb von Minuten durchgeführt werden.

Sowohl die einzelnen Graphenschichten als auch die Stapel weisen eine strukturelle Unordnung auf, welche mittels WAXS- und WANS-Messungen analysiert werden können. Auch wenn WANS-Daten von NGCs bereits bekannt und in verschiedenen Studien ausgewertet worden sind, gibt es noch offene Fragen in Bezug auf die Validierung von WAXS-Daten, welche normalerweise für die routinemäßige Charakterisierung verwendet werden, allerdings diverse Nachteile gegenüber WANS-Messungen besitzen. Die bisherigen WANS-Daten aus einer früheren Studie von Pfaff et al. im Jahr 2019 [2] haben einen kleinen *s*-Bereich, was die genaue Bestimmung der Schichtstruktur erschwert. Daher wurden in dieser Studie Pulver-WANS-Daten derselben Proben bei einer Messzeit am Institut Laue-Langevin (ILL) in Grenoble aufgenommen. Da diese Daten einen größeren Messbereich besitzen, im kleinen *s*-Bereich aber schlechter aufgelöst sind, hat eine Kombination dieser beiden WANS-Daten die einzigartige Gelegenheit eröffnet, sowohl die Schicht- als auch die Stapelstruktur so genau wie möglich zu bestimmen. Es wurde dabei festgestellt, dass die Graphenschichten deutlich geordneter als bisher angenommen sind und der von perfekten Graphenschichten sehr

nahekommen. Diese Studie hat eine fortschrittliche Methodik zur Untersuchung von Kohlenstoffen auf turbostratischer Graphenbasis erarbeitet und auch den Blick auf die Struktur wichtiger Klassen von nicht-graphitischem Kohlenstoff erweitert.

4.2. Ausblick

Aus WANS-Daten lässt sich die sogenannte *pair-distribution-function* (*PDF*) mittels einer Furier-Transformation berechnen (Abbildung 14), aus der sich ebenfalls Mikrostrukturparameter bestimmen lassen. [2,276–283] Hierfür können nicht nur WANS, sondern auch qualitativ hochwertige WAXS-Daten mit einem hohen Messbereich genutzt werden (z.B. XPDF-Experimente an der Diamond-Lichtquelle in Oxford). Diese sind generell leichter verfügbar als WANS-Daten, da hier ein Synchrotron als Strahlenquelle genutzt werden kann. Allerdings wurde hierfür in der Literatur noch nicht ausreichend diskutiert, wie genau die PDF von NGCs sinnvoll interpretiert und ausgewertet werden müssen, um die notwendigen und wichtigen Mikrostrukturparameter zu erhalten. Genauer gesagt muss ermittelt werden, wie sich die Schichtgröße (L_a) und deren Unordnung (σ_l) auf die resultierenden PDF auswirkt, wie beide Werte aus einer PDF ermittelt werden können und ob sich die Stapelstruktur überhaupt quantitativ aus PDFs ermitteln lässt. Zusätzlich sollte untersucht werden, ob das für WAXS/WANS-Daten verwendete Modell von RULAND & SMARSLY [3] auch zum Anpassen von PDFs verwendet werden kann. Hierfür soll sowohl auf bestehende Software [284–287] zurückgegriffen, aber auch die beschriebene selbst entwickelte Software der ersten Publikation entsprechend weiterentwickelt werden.

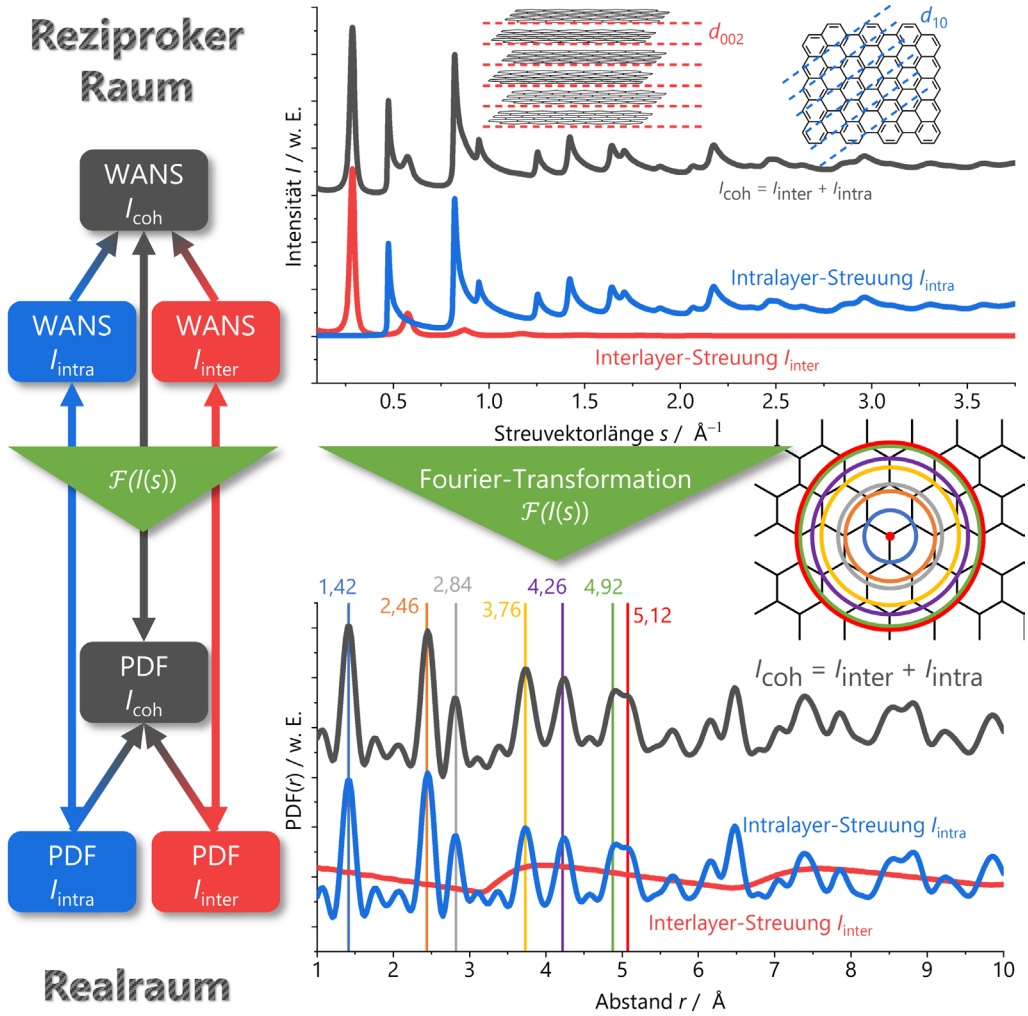

Abbildung 14. Berechnung der *pair-distribution-function* (*PDF*) mittels einer Fourier-Transformation aus WANS-Daten. Die berechneten Maxima stimmen mit den theoretischen Abständen der nächste-Nachbar-Verteilung in Graphen überein. Analog zu WAXS/WANS-Daten kann aus einer Überlagerung der einzelnen Funktionen für Schichten (*intra*) und Stapeln (*inter*) die Gesamt-PDF erhalten werden. Allerdings lässt sich aus diesen „Gesamtdaten“ analytisch nicht ohne Weiteres auf die einzelnen Anteile der Schicht- und Stapelbeiträge schließen. Die Pfeile im linken Teil beschreiben die Wege, für die eine Umrechnung möglich ist.

Als weitere Arbeit könnte außerdem das bisherige Modell von RULAND & SMARSLY [3] weiterentwickelt werden, um nicht nur die Streuintensität turbostratischer nicht-graphitischer Kohlenstoffe zu beschreiben, sondern auch den Übergangsbereich zu Graphit. Hierbei entspricht die Mikrostruktur noch nicht vollständig der von Graphit, jedoch bildet sich langsam eine dreidimensionale Fernordnung aus, sodass (*hkl*)-Reflexe sichtbar werden. Dies ist zum Beispiel bei Pechen bei einer Behandlungstemperatur von über 2.500 °C der Fall, welche mit den bisherigen Methoden nur unzureichend charakterisiert werden können. [204,209] Ein Modell dazu lieferte WILHELM RULAND bereits 1965, [288] allerdings wurde dieses noch nicht in die bisher verfügbare Computersoftware integriert.

Generell gehören Harze und (Steinkohleteer-)Peche zu den weitverbreitetsten Präkursoren, allerdings ist die große Mehrheit der Harze nicht-graphitierbar. [289] Dagegen sind besonders Peche graphitierbar und eignen sich sehr gut als Bindemittel für die Darstellung höherstrukturierter Graphitmaterialien. Allerdings sind diese Peche bzw. die in den Pechen enthaltenen polyaromatischen Kohlenwasserstoffe oftmals toxisch, weshalb Alternativstoffe für diese Peche wünschenswert wären. Hierbei könnte einerseits die Graphitierung bzw. die Graphitierbarkeit von herkömmlichen Harzen verbessert werden bzw. müssten graphitierbare Harze entwickelt werden. Eine Idee stellt dabei ein neues, petrolstämmiges Kohlenwasserstoffharz dar. Anders als z.B. Phenol-Formaldehyd-Harze gilt dieses neue Harz als graphitierbar und soll somit eventuell als Alternativmaterial zu Pechen verwendet werden. Zur Analyse der Produkte aus solchen Präkursoren kann das in ersten Publikation [1] vorgestellte OCTCARB verwendet werden.

5. Literatur

(1) Osswald, O.; Smarsly, B. M. OctCarb — A GNU Octave Script for the Analysis and Evaluation of Wide-Angle Scattering Data of Non-Graphitic Carbons. *C* **2022**, *8(4)* (78). DOI: 10.3390/c8040078.

(2) Pfaff, T.; Badaczewski, F. M.; Loeh, M. O.; Franz, A.; Hoffmann, J.-U.; Reehuis, M.; Zeier, W. G.; Smarsly, B. M. Comparative Microstructural Analysis of Nongraphitic Carbons by Wide-Angle X-ray and Neutron Scattering. *J. Phys. Chem. C* **2019**, *123* (33), 20532–20546. DOI: 10.1021/acs.jpcc.9b03590.

(3) Ruland, W.; Smarsly, B. M. X-ray scattering of non-graphitic carbon: an improved method of evaluation. *J Appl Crystallogr* **2002**, *35* (5), 624–633. DOI: 10.1107/S0021889802011007.

(4) Pigeaud, R. J. Clottes, (Sous la dir. de), 2001. La grotte Chauvet. L'art des origines. Paris, Éditions du Seuil, collection « Arts rupestres », 225 p., 206 fig., ill. couleur, notes bibl., nbr. réf. bibl. *L'Anthropologie* **2002**, *106* (4), 649–650. DOI: 10.1016/S0003-5521(02)01130-5.

(5) Pimenta, M. A.; Dresselhaus, G.; Dresselhaus, M. S.; Cançado, L. G.; Jorio, A.; Saito, R. Studying disorder in graphite-based systems by Raman spectroscopy. *Physical chemistry chemical physics : PCCP* **2007**, *9* (11), 1276–1291. DOI: 10.1039/b613962k. Online veröffentlicht: 11.01.2007.

(6) Pernicka, E. Gewinnung und Verbreitung der Metalle in prähistorischer Zeit. 21-129 Seiten / Jahrbuch des Römisch-Germanischen Zentralmuseums Mainz, Bd. 37 Nr. 1 (1990) **2020.** DOI: 10.11588/JRGZM.1990.1.72999.

(7) Esin, U., Ed. *Die Anfänge der Metallverwendung und Bearbeitung in Anatolien*; Les Debuts de la Metallurgie, Colloque XXIII, 1976.

(8) Lide, D. R.; Bruno, T. J. *CRC handbook of chemistry and physics:A ready-reference book of chemical and physical data*, 2015-2016, 96th Edition; CRC Press, 2015.

(9) Cornelius, F. *Geistesgeschichte der Frühzeit:Teil I: Von der Eiszeit bis zur Erfindung der Keilschrift*; Leiden, 1960.

(10) Beck, H., Ed. *Reallexikon der germanischen Altertumskunde*, 2. völlig neu bearb. u. stark erw. Aufl.; De Gruyter, 2006.

(11) Henneberg, I.; Ingo Henneberg, R. R. *www.die-roemer-online.de --- Das Forum rund um die "Römer"*. http://www.die-roemer-online.de/index.html?/eisenherstellung/eisenherstellung.html (Zugriff am 31.05.2022).

(12) Petroski, H. *Der Bleistift:Die Geschichte eines Gebrauchsgegenstands*; Birkhäuser, 1995.

(13) Lavoisier, A. L. *Mémoire sur la nature du principle qui se combine avec les métaux pendant leur calcination, & qui en augmente le poids*, 1775.

(14) Morris, R. J.; Guerlac, H. Lavoisier on Fire and Air: The Memoir of July 1772. *Isis* **1969**, *60* (3), 374–382. DOI: 10.1086/350506.

(15) PONS GmbH. *carbo - Latein-Deutsch Übersetzung | PONS*. https://de.pons.com/%C3%BCbersetzung/latein-deutsch/carbo (Zugriff am 30.05.2022).

(16) Information Technology Associates. *Smithson Tennant - Encyclopedia*. https://www.theodora.com/encyclopedia/t/smithson_tennant.html (Zugriff am 30.05.2022).

(17) Pötsch, W. R.; Fischer, A.; Müller, W.; Cassebaum, H. *Lexikon bedeutender Chemiker*; Bibliographisches Institut, 1988.

(18) Weeks, M. E. The chemical contributions of William Allen. *J. Chem. Educ.* **1958**, *35* (2), 70. DOI: 10.1021/ed035p70.

(19) Allen, W.; Pepys, W. H. XVII. On the changes produced in atmospheric air, and oxygen gas, respiration. *Phil. Trans. R. Soc.* **1808**, *98*, 249–281. DOI: 10.1098/rstl.1808.0018.

(20) Crell, L. *Chemische Annalen für die Freunde der Naturlehre, Arzneigelehrtheit, Haushaltungskunst und Manufakturen*:*Erster Teil*, Nachdruck der Ausgabe von 1789; Hansebooks GmbH, 2016.
(21) Berzelius, J. J. *Lehrbuch der Chemie*; Arnold, 1843.
(22) Walden, P. Carl Wilhelm Scheele. Ein Gedenkblatt zu seinem 200. Geburtstage. *Z. anorg. allg. Chem.* **1943**, *250* (3-4), 230–235. DOI: 10.1002/zaac.19432500302.
(23) Hargittai, I. *The road to Stockholm*:*Nobel Prizes, science, and scientists*, Reprinted 2003; Oxford Univ. Press, 2003.
(24) Boyd, D. B.; Slanina, Z. Introduction and foreword to the special issue commemorating the thirtieth anniversary of Eiji Osawa's C60 paper. *Journal of Molecular Graphics and Modelling* **2001**, *19* (2), 181–184. DOI: 10.1016/S1093-3263(00)00106-6.
(25) Kroto, H. W.; Heath, J. R.; O'Brien, S. C.; Curl, R. F.; Smalley, R. E. C60: Buckminsterfullerene. *Nature* **1985**, *318* (6042), 162–163. DOI: 10.1038/318162a0.
(26) NobelPrize.org. *The Nobel Prize in Chemistry 1996*. https://www.nobelprize.org/prizes/chemistry/1996/summary/ (Zugriff am 30.05.2022).
(27) Iijima, S. Helical microtubules of graphitic carbon. *Nature* **1991**, *354* (6348), 56–58. DOI: 10.1038/354056a0.
(28) Iijima, S.; Ichihashi, T. Single-shell carbon nanotubes of 1-nm diameter. *Nature* **1993**, *363* (6430), 603–605. DOI: 10.1038/363603a0.
(29) NobelPrize.org. *The Nobel Prize in Physics 2010*. https://www.nobelprize.org/prizes/physics/2010/summary/ (Zugriff am 30.05.2022).
(30) Novoselov, K. S.; Geim, A. K.; Morozov, S. V.; Jiang, D.; Zhang, Y.; Dubonos, S. V.; Grigorieva, I. V.; Firsov, A. A. Electric field effect in atomically thin carbon films. *Science* **2004**, *306* (5696), 666–669. DOI: 10.1126/science.1102896.
(31) AG Energiebilanzen. *Energieverbrauch in Deutschland im Jahr 2021*. https://ag-energiebilanzen.de/wp-content/uploads/2022/03/AGEB_Jahresbericht2020_20220325_dt.pdf (Zugriff am 31.05.2022).
(32) Bundesministerium für Wirtschaft und Klimaschutz. *Kohle*. https://www.bmwk.de/Redaktion/DE/Artikel/Energie/kohlepolitik.html (Zugriff am 31.05.2022).
(33) Cordiner, M. A.; Linnartz, H.; Cox, N. L. J.; Cami, J.; Najarro, F.; Proffitt, C. R.; Lallement, R.; Ehrenfreund, P.; Foing, B. H.; Gull, T. R.; Sarre, P. J.; Charnley, S. B. Confirming Interstellar C 60+ Using the Hubble Space Telescope. *ApJ* **2019**, *875* (2), L28. DOI: 10.3847/2041-8213/ab14e5.
(34) Dettmann, J. *Fullerene*; Birkhäuser Basel, 1994. DOI: 10.1007/978-3-0348-5705-5.
(35) Mineralienatlas. *Mineralienatlas - Fossilienatlas*. https://www.mineralienatlas.de/lexikon/index.php/Fulleren?lang=de (Zugriff am 31.05.2022).
(36) Schroecke, H.; Weiner, K. L. *Mineralogie*:*Ein Lehrbuch auf systematischer Grundlage*; De Gruyter, 1981.
(37) Strunz, H.; Nickel, E. H. *Strunz mineralogical tables*:*Chemical-structural mineral classification system, with 226 figures*, 9e éd; E. Schweizerbart'sche, 2001.
(38) Goresy, A. E.; Donnay, G. A new allotropic form of carbon from the ries crater. *Science (New York, N.Y.)* **1968**, *161* (3839), 363–364. DOI: 10.1126/science.161.3839.363.
(39) Bender, O. *Die Härte der Edelsteine*. http://www.gold-uhren-schmuck.de/edelstein-haerte.html (Zugriff am 31.05.2022).

(40) Schumann, W. *Edelsteine und Schmucksteine*:*Alle Arten und Varietäten der Welt*, 13., überarb. und erw. Aufl., Neuausg; BLV Verlagsgesellschaft, 2002.
(41) Wort, C. J.; Balmer, R. S. Diamond as an electronic material. *Materials Today* **2008**, *11* (1-2), 22–28. DOI: 10.1016/S1369-7021(07)70349-8.
(42) Harte, B.; Richardson, S. Mineral inclusions in diamonds track the evolution of a Mesozoic subducted slab beneath West Gondwanaland. *Gondwana Research* **2012**, *21* (1), 236–245. DOI: 10.1016/j.gr.2011.07.001.
(43) Smith, E. M.; Shirey, S. B.; Nestola, F.; Bullock, E. S.; Wang, J.; Richardson, S. H.; Wang, W. Large gem diamonds from metallic liquid in Earth's deep mantle. *Science (New York, N.Y.)* **2016**, *354* (6318), 1403–1405. DOI: 10.1126/science.aal1303.
(44) Löffler, G.; Voßmerbäumer, H. *Mit unserer Erde leben*:*Beiträge der Fakultät für Geowissenschaften der Universität Würzburg ; im Rahmen der Ringvorlesung im WS 2000/2001*; Königshausen & Neumann, 2002.
(45) Evans, A. M. *Erzlagerstättenkunde*; Ferdinand Enke, 1992.
(46) Diamanten Infos. *Produktion von Rohdiamanten: 2009*. https://www.diamanten-infos.com/rohdiamant/jahr-produktion-2009.html (Zugriff am 31.05.2022).
(47) Mineralienatlas. *Mineralienatlas - Fossilienatlas*. https://www.mineralienatlas.de/lexikon/index.php/MineralDataShow?mineralid=927&sections=12 (Zugriff am 31.05.2022).
(48) Mindat. *Diamond*. https://www.mindat.org/show.php?id=1282&ld=1#themap (Zugriff am 31.05.2022).
(49) Diamant Agentur. Synthetische Diamanten - endlich leicht verständlich. *Diamant Agentur GmbH,* Mar 16, 2021. https://diamantagentur.de/fachwissen/synthetische-diamanten/ (Zugriff am 31.05.2022).
(50) Krefting, M. Diamanten: Wie sich echte von synthetischen abheben. *geo.de,* Feb 15, 2022. https://www.geo.de/wissen/diamanten--wie-sich-echte-von-synthetischen-abheben-31629054.html (Zugriff am 31.05.2022).
(51) Bundeszentrale für politische Bildung. *Diamantenabbau*:*Krieg und Frieden*. https://sicherheitspolitik.bpb.de/de/m4/layers/mineral-deposits-and-their-distribution/fossil-and-mineral-resources/diamond-mining#1/13/17 (Zugriff am 31.05.2022).
(52) Damm, S. *Rohstoffrisikobewertung - Graphit*, Datenstand: November 2021; DERA Rohstoffinformationen, Vol. 51; DERA, 2021.
(53) Blengini, G. A.; El Latunussa, C.; Eynard, U.; Torres de Matos, C.; Wittmer, D. M. A. G.; Georgitzikis, K.; Pavel, C. C.; Carrara, S.; Mancini, L.; Unguru, M.; Blagoeva, D.; Mathieux, F.; Pennington, D. W. *Study on the EU's list of critical raw materials (2020)*:*Final report*; Publications Office of the European Union, 2020. DOI: 10.2873/11619.
(54) Europäische Kommission. *MITTEILUNG DER KOMMISSION AN DAS EUROPÄISCHE PARLAMENT, DEN RAT, DEN EUROPÄISCHEN WIRTSCHAFTS- UND SOZIALAUSSCHUSS UND DEN AUSSCHUSS DER REGIONEB*:*Widerstandsfähigkeit der EU bei kritischen Rohstoffen: Einen Pfad hin zu größerer Sicherheit und Nachhaltigkeit abstecken*. https://eur-lex.europa.eu/legal-content/DE/TXT/PDF/?uri=CELEX:52020DC0474&from=DE (Zugriff am 31.05.2022).
(55) Graphit Kropfmühl AG. *Über uns*. https://www.gk-graphite.com/de/ueber-uns/ (Zugriff am 31.05.2022).
(56) Graphit Kropfmühl AG. *Wiederaufnahme des Graphitabbaus in Kropfmühl*, 2012.

(57) Purle, T. *Graphit - Eigenschaften, Verwendung und Entstehung*. https://www.steine-und-minerale.de/atlas.php?f=1&l=G&name=Graphit (Zugriff am 31.05.2022).
(58) Regelous, A.; Holzförster, F. *Die drei Schätze im Passauer Land*. https://hausamstrom.de/wp-content/uploads/2018/12/K-Regelous_Holzf%C3%B6rster_2018-Kap_6-Rohstoff-Graphit.pdf (Zugriff am 31.05.2022).
(59) Adelhelm, P.; Cabrera, K.; Smarsly, B. M. On the use of mesophase pitch for the preparation of hierarchical porous carbon monoliths by nanocasting. *Science and Technology of Advanced Materials* **2012**, *13* (1), 15010. DOI: 10.1088/1468-6996/13/1/015010.
(60) Hu, Y.-S.; Adelhelm, P.; Smarsly, B. M.; Hore, S.; Antonietti, M.; Maier, J. Synthesis of Hierarchically Porous Carbon Monoliths with Highly Ordered Microstructure and Their Application in Rechargeable Lithium Batteries with High-Rate Capability. *Adv. Funct. Mater.* **2007**, *17* (12), 1873–1878. DOI: 10.1002/adfm.200601152.
(61) Loeh, M. O.; Badaczewski, F. M.; Lehr, M. von der; Ellinghaus, R.; Dobrotka, S.; Metz, J.; Smarsly, B. M. Hard-templating of carbon using porous SiO2 monoliths revisited - Quantitative impact of spatial confinement on the microstructure evolution. *Carbon* **2018**, *129*, 552–563. DOI: 10.1016/j.carbon.2017.12.044.
(62) Badaczewski, F. M.; Loeh, M. O.; Pfaff, T.; Wallacher, D.; Clemens, D.; Smarsly, B. M. An advanced structural characterization of templated meso-macroporous carbon monoliths by small- and wide-angle scattering techniques. *Beilstein journal of nanotechnology* **2020**, *11*, 310–322. DOI: 10.3762/bjnano.11.23.
(63) Pandolfo, A. G.; Hollenkamp, A. F. Carbon properties and their role in supercapacitors. *Journal of Power Sources* **2006**, *157* (1), 11–27. DOI: 10.1016/j.jpowsour.2006.02.065.
(64) Badaczewski, F. *Charakterisierung der Mikro- und Porenstruktur von nicht-graphitischen Kohlenstoffen mittels Streumethoden*; Justus-Liebig-Universität Gießen, 2020.
(65) Spradling, D. M.; Guth, R. A. Carbon foams. *Advanced materials & processes* **2003**, *161* (11), 29–31.
(66) Manthiram, A.; Fu, Y.; Chung, S.-H.; Zu, C.; Su, Y.-S. Rechargeable lithium-sulfur batteries. *Chemical reviews* **2014**, *114* (23), 11751–11787. DOI: 10.1021/cr500062v.
(67) Oschatz, M.; Kockrick, E.; Rose, M.; Borchardt, L.; Klein, N.; Senkovska, I.; Freudenberg, T.; Korenblit, Y.; Yushin, G.; Kaskel, S. A cubic ordered, mesoporous carbide-derived carbon for gas and energy storage applications. *Carbon* **2010**, *48* (14), 3987–3992. DOI: 10.1016/j.carbon.2010.06.058.
(68) Nishihara, H.; Kyotani, T. Templated nanocarbons for energy storage. *Advanced materials (Deerfield Beach, Fla.)* **2012**, *24* (33), 4473–4498. DOI: 10.1002/adma.201201715. Online veröffentlicht: 16.07.2012.
(69) Doherty, C. M.; Caruso, R. A.; Smarsly, B. M.; Adelhelm, P.; Drummond, C. J. Hierarchically Porous Monolithic LiFePO 4 /Carbon Composite Electrode Materials for High Power Lithium Ion Batteries. *Chem. Mater.* **2009**, *21* (21), 5300–5306. DOI: 10.1021/cm9024167.
(70) Oberlin, A. Carbonization and graphitization. *Carbon* **1984**, *22* (6), 521–541. DOI: 10.1016/0008-6223(84)90086-1.
(71) Kumar, R.; Dhakate, S. R.; Mathur, R. B. The role of ferrocene on the enhancement of the mechanical and electrochemical properties of coal tar

pitch-based carbon foams. *J Mater Sci* **2013**, *48* (20), 7071–7080. DOI: 10.1007/s10853-013-7518-z.

(72) Dash, R.; Chmiola, J.; Yushin, G.; Gogotsi, Y.; Laudisio, G.; Singer, J.; Fischer, J.; Kucheyev, S. Titanium carbide derived nanoporous carbon for energy-related applications. *Carbon* **2006**, *44* (12), 2489–2497. DOI: 10.1016/j.carbon.2006.04.035.

(73) Oschatz, M.; Borchardt, L.; Pinkert, K.; Thieme, S.; Lohe, M. R.; Hoffmann, C.; Benusch, M.; Wisser, F. M.; Ziegler, C.; Giebeler, L.; Rümmeli, M. H.; Eckert, J.; Eychmüller, A.; Kaskel, S. Hierarchical Carbide-Derived Carbon Foams with Advanced Mesostructure as a Versatile Electrochemical Energy-Storage Material. *Adv. Energy Mater.* **2014**, *4* (2), 1300645. DOI: 10.1002/aenm.201300645.

(74) Wang, J.; Sugita, S.; Nagayama, K.; Matsumoto, T. OS18-3 Spatiotemporal Dynamics of Actin during Adhesion Process of MC3T3-E1 Cells to Substrate(Cell and Tissue mechanics 1,OS18 Cell and tissue mechanics,BIOMECHANICS). *ATEM* **2015**, *2015.14* (0), 237. DOI: 10.1299/jsmeatem.2015.14.237.

(75) Kim, Y.-S.; Guo, X.-F.; Kim, G.-J. Synthesis of carbon monolith with bimodal meso/macroscopic pore structure and its application in asymmetric catalysis. *Catalysis Today* **2010**, *150* (1-2), 91–99. DOI: 10.1016/j.cattod.2009.09.005.

(76) Zhang, S.; Chen, L.; Zhou, S.; Zhao, D.; Wu, L. Facile Synthesis of Hierarchically Ordered Porous Carbon via in Situ Self-Assembly of Colloidal Polymer and Silica Spheres and Its Use as a Catalyst Support. *Chem. Mater.* **2010**, *22* (11), 3433–3440. DOI: 10.1021/cm1002274.

(77) Tzeng, S.-S.; Chr, Y.-G. Evolution of microstructure and properties of phenolic resin-based carbon/carbon composites during pyrolysis. *Materials Chemistry and Physics* **2002**, *73* (2-3), 162–169. DOI: 10.1016/S0254-0584(01)00358-3.

(78) Perret, R.; Ruland, W. X-ray small-angle scattering of glassy carbon. *J Appl Crystallogr* **1972**, *5* (3), 183–187. DOI: 10.1107/S0021889872009161.

(79) Goel, C.; Bhunia, H.; Bajpai, P. K. Synthesis of nitrogen doped mesoporous carbons for carbon dioxide capture. *RSC Adv.* **2015**, *5* (58), 46568–46582. DOI: 10.1039/C5RA05684E.

(80) Li, J.; Lu, R.; Dou, B.; Ma, C.; Hu, Q.; Liang, Y.; Wu, F.; Qiao, S.; Hao, Z. Porous graphitized carbon for adsorptive removal of benzene and the electrothermal regeneration. *Environmental science & technology* **2012**, *46* (22), 12648–12654. DOI: 10.1021/es303069j.

(81) Silvestre-Albero, A.; Rico-Frances, S.; Rodríguez-Reinoso, F.; Kern, A. M.; Klumpp, M.; Etzold, B. J.; Silvestre-Albero, J. High selectivity of TiC-CDC for CO2/N2 separation. *Carbon* **2013**, *59*, 221–228. DOI: 10.1016/j.carbon.2013.03.012.

(82) Inagaki, M.; Konno, H.; Tanaike, O. Carbon materials for electrochemical capacitors. *Journal of Power Sources* **2010**, *195* (24), 7880–7903. DOI: 10.1016/j.jpowsour.2010.06.036.

(83) An, S. J.; Li, J.; Daniel, C.; Mohanty, D.; Nagpure, S.; Wood, D. L. The state of understanding of the lithium-ion-battery graphite solid electrolyte interphase (SEI) and its relationship to formation cycling. *Carbon* **2016**, *105*, 52–76. DOI: 10.1016/j.carbon.2016.04.008.

(84) Buqa, H.; Goers, D.; Holzapfel, M.; Spahr, M. E.; Novák, P. High Rate Capability of Graphite Negative Electrodes for Lithium-Ion Batteries. *J. Electrochem. Soc.* **2005**, *152* (2), A474. DOI: 10.1149/1.1851055.

(85) Forgez, C.; Vinh Do, D.; Friedrich, G.; Morcrette, M.; Delacourt, C. Thermal modeling of a cylindrical LiFePO4/graphite lithium-ion battery. *Journal of Power Sources* **2010**, *195* (9), 2961–2968. DOI: 10.1016/j.jpowsour.2009.10.105.

(86) Nie, M.; Chalasani, D.; Abraham, D. P.; Chen, Y.; Bose, A.; Lucht, B. L. Lithium Ion Battery Graphite Solid Electrolyte Interphase Revealed by Microscopy and Spectroscopy. *J. Phys. Chem. C* **2013**, *117* (3), 1257–1267. DOI: 10.1021/jp3118055.

(87) Delmas, C. Sodium and Sodium-Ion Batteries: 50 Years of Research. *Adv. Energy Mater.* **2018**, *8* (17), 1703137. DOI: 10.1002/aenm.201703137.

(88) Hwang, J.-Y.; Myung, S.-T.; Sun, Y.-K. Sodium-ion batteries: present and future. *Chemical Society Reviews* **2017**, *46* (12), 3529–3614. DOI: 10.1039/C6CS00776G.

(89) Lotfabad, E. M.; Ding, J.; Cui, K.; Kohandehghan, A.; Kalisvaart, W. P.; Hazelton, M.; Mitlin, D. High-density sodium and lithium ion battery anodes from banana peels. *ACS nano* **2014**, *8* (7), 7115–7129. DOI: 10.1021/nn502045y. Online veröffentlicht: 06.06.2014.

(90) Slater, M. D.; Kim, D.; Lee, E.; Johnson, C. S. Sodium-Ion Batteries. *Adv. Funct. Mater.* **2013**, *23* (8), 947–958. DOI: 10.1002/adfm.201200691.

(91) Yabuuchi, N.; Kubota, K.; Dahbi, M.; Komaba, S. Research development on sodium-ion batteries. *Chemical reviews* **2014**, *114* (23), 11636–11682. DOI: 10.1021/cr500192f. Online veröffentlicht: 12.11.2014.

(92) Das, S. K.; Mahapatra, S.; Lahan, H. Aluminium-ion batteries: developments and challenges. *J. Mater. Chem. A* **2017**, *5* (14), 6347–6367. DOI: 10.1039/C7TA00228A.

(93) Lin, M.-C.; Gong, M.; Lu, B.; Wu, Y.; Wang, D.-Y.; Guan, M.; Angell, M.; Chen, C.; Yang, J.; Hwang, B.-J.; Dai, H. An ultrafast rechargeable aluminium-ion battery. *Nature* **2015**, *520* (7547), 325–328. DOI: 10.1038/nature14340. Online veröffentlicht: 06.04.2015.

(94) Sun, H.; Wang, W.; Yu, Z.; Yuan, Y.; Wang, S.; Jiao, S. A new aluminium-ion battery with high voltage, high safety and low cost. *Chem. Commun.* **2015**, *51* (59), 11892–11895. DOI: 10.1039/C5CC00542F.

(95) Wang, D.-Y.; Wei, C.-Y.; Lin, M.-C.; Pan, C.-J.; Chou, H.-L.; Chen, H.-A.; Gong, M.; Wu, Y.; Yuan, C.; Angell, M.; Hsieh, Y.-J.; Chen, Y.-H.; Wen, C.-Y.; Chen, C.-W.; Hwang, B.-J.; Chen, C.-C.; Dai, H. Advanced rechargeable aluminium ion battery with a high-quality natural graphite cathode. *Nat Commun* **2017**, *8* (1), 14283. DOI: 10.1038/ncomms14283. Online veröffentlicht: 13.02.2017.

(96) Krüner, B.; Schreiber, A.; Tolosa, A.; Quade, A.; Badaczewski, F.; Pfaff, T.; Smarsly, B. M.; Presser, V. Nitrogen-containing novolac-derived carbon beads as electrode material for supercapacitors. *Carbon* **2018**, *132*, 220–231. DOI: 10.1016/j.carbon.2018.02.029.

(97) Trimm, D. L.; Önsan, Z. I. ONBOARD FUEL CONVERSION FOR HYDROGEN-FUEL-CELL-DRIVEN VEHICLES. *Catalysis Reviews* **2001**, *43* (1-2), 31–84. DOI: 10.1081/CR-100104386.

(98) Manoharan, Y.; Hosseini, S. E.; Butler, B.; Alzhahrani, H.; Senior, B. T. F.; Ashuri, T.; Krohn, J. Hydrogen Fuel Cell Vehicles; Current Status and Future Prospect. *Applied Sciences* **2019**, *9* (11), 2296. DOI: 10.3390/app9112296.

(99) Härmas, R.; Palm, R.; Kurig, H.; Puusepp, L.; Pfaff, T.; Romann, T.; Aruväli, J.; Tallo, I.; Thomberg, T.; Jänes, A.; Lust, E. Carbide-Derived Carbons: WAXS and Raman Spectra for Detailed Structural Analysis. *C* **2021**, *7* (1), 29. DOI: 10.3390/c7010029.

(100) Faber, K.; Badaczewski, F. M.; Oschatz, M.; Mondin, G.; Nickel, W.; Kaskel, S.; Smarsly, B. M. In-Depth Investigation of the Carbon Microstructure of Silicon Carbide-Derived Carbons by Wide-Angle X-ray Scattering. *J. Phys. Chem. C* **2014**, *118* (29), 15705–15715. DOI: 10.1021/jp502832x.

(101) Oschatz, M.; Borchardt, L.; Thommes, M.; Cychosz, K. A.; Senkovska, I.; Klein, N.; Frind, R.; Leistner, M.; Presser, V.; Gogotsi, Y.; Kaskel, S. Carbide-derived carbon monoliths with hierarchical pore architectures. *Angewandte Chemie (International ed. in English)* **2012**, *51* (30), 7577–7580. DOI: 10.1002/anie.201200024.

(102) Wang, L.; Sun, F.; Gao, J.; Pi, X.; Qu, Z.; Zhao, G. Adjusting the Porosity of Coal-Based Activated Carbons Based on a Catalytic Physical Activation Process for Gas and Liquid Adsorption. *Energy Fuels* **2018**, *32* (2), 1255–1264. DOI: 10.1021/acs.energyfuels.7b03211.

(103) Bolisetty, S.; Mezzenga, R. Amyloid-carbon hybrid membranes for universal water purification. *Nature nanotechnology* **2016**, *11* (4), 365–371. DOI: 10.1038/nnano.2015.310. Online veröffentlicht: 25.01.2016.

(104) Gusain, R.; Kumar, N.; Ray, S. S. Recent advances in carbon nanomaterial-based adsorbents for water purification. *Coordination Chemistry Reviews* **2020**, *405*, 213111. DOI: 10.1016/j.ccr.2019.213111.

(105) Sweetman, M.; May, S.; Mebberson, N.; Pendleton, P.; Vasilev, K.; Plush, S.; Hayball, J. Activated Carbon, Carbon Nanotubes and Graphene: Materials and Composites for Advanced Water Purification. *C* **2017**, *3* (4), 18. DOI: 10.3390/c3020018.

(106) Wingender, J.; Achten, C. *Aktivkohle:RD-01-01229*. https://roempp.thieme.de/lexicon/RD-01-01229 (Zugriff am 09.06.2022).

(107) Wu, L.; Buchholz, D.; Vaalma, C.; Giffin, G. A.; Passerini, S. Apple-Biowaste-Derived Hard Carbon as a Powerful Anode Material for Na-Ion Batteries. *ChemElectroChem* **2016**, *3* (2), 292–298. DOI: 10.1002/celc.201500437.

(108) Liu, Y.; Huang, B.; Lin, X.; Xie, Z. Biomass-derived hierarchical porous carbons: boosting the energy density of supercapacitors via an ionothermal approach. *J. Mater. Chem. A* **2017**, *5* (25), 13009–13018. DOI: 10.1039/C7TA03639F.

(109) Marino, C.; Cabanero, J.; Povia, M.; Villevieille, C. Biowaste Lignin-Based Carbonaceous Materials as Anodes for Na-Ion Batteries. *J. Electrochem. Soc.* **2018**, *165* (7), A1400-A1408. DOI: 10.1149/2.0681807jes.

(110) Vaalma, C.; Giffin, G. A.; Buchholz, D.; Passerini, S. Non-Aqueous K-Ion Battery Based on Layered K 0.3 MnO 2 and Hard Carbon/Carbon Black. *J. Electrochem. Soc.* **2016**, *163* (7), A1295-A1299. DOI: 10.1149/2.0921607jes.

(111) Schüpfer, D. B. *Strukturelle Umwandlungsprozesse in Kohlenstoffmaterialien:Korrelation von Raman-Spektren und Strukturanalysedaten*; Justus-Liebig-Universität Gießen, 2021.

(112) Bogachuk, D.; Tsuji, R.; Martineau, D.; Narbey, S.; Herterich, J. P.; Wagner, L.; Suginuma, K.; Ito, S.; Hinsch, A. Comparison of highly conductive natural and synthetic graphites for electrodes in perovskite solar cells. *Carbon* **2021**, *178*, 10–18. DOI: 10.1016/j.carbon.2021.01.022.

(113) Lamberti, F.; Schmitz, F.; Chen, W.; He, Z.; Gatti, T. The Non-Innocent Role of Hole-Transporting Materials in Perovskite Solar Cells. *Sol. RRL* **2021**, *5* (10), 2100514. DOI: 10.1002/solr.202100514.

(114) Godlewska, L.; Grohol, M. *Study on the review of the list of critical raw materials:Final report*; Publications Office of the European Union, 2017.

(115) Europäische Kommission. *REPORT ON CRITICAL RAW MATERIALS FOR THE EU*:*Report of the Ad hoc Working Group on defining critical raw materials*, 2014.
(116) Europäische Kommission. *MITTEILUNG DER KOMMISSION AN DAS EUROPÄISCHE PARLAMENT, DEN RAT, DEN EUROPÄISCHEN WIRTSCHAFTS- UND SOZIALAUSSCHUSS UND DEN AUSSCHUSS DER REGIONEB*:*GRUNDSTOFFMÄRKTE UND ROHSTOFFE: HERAUSFORDERUNGEN UND LÖSUNGSANSÄTZE* (Zugriff am 31.05.2022).
(117) Europäische Kommission. *MITTEILUNG DER KOMMISSION AN DAS EUROPÄISCHE PARLAMENT, DEN RAT, DEN EUROPÄISCHEN WIRTSCHAFTS- UND SOZIALAUSSCHUSS UND DEN AUSSCHUSS DER REGIONEB*:*über die Überprüfung der Liste kritischer Rohstoffe für die EU und die Umsetzung der Rohstoffinitiative* (Zugriff am 31.05.2022).
(118) Europäische Kommission. *MITTEILUNG DER KOMMISSION AN DAS EUROPÄISCHE PARLAMENT, DEN RAT, DEN EUROPÄISCHEN WIRTSCHAFTS- UND SOZIALAUSSCHUSS UND DEN AUSSCHUSS DER REGIONEB*:*über die Liste kritischer Rohstoffe für die EU 2017* (Zugriff am 31.05.2022).
(119) Weingarth, D.; Zeiger, M.; Jäckel, N.; Aslan, M.; Feng, G.; Presser, V. Graphitization as a Universal Tool to Tailor the Potential-Dependent Capacitance of Carbon Supercapacitors. *Adv. Energy Mater.* **2014**, *4* (13), 1400316. DOI: 10.1002/aenm.201400316.
(120) Ceylon Graphite. *Vein Graphite | Graphite in Sri Lanka | Ceylon Graphite*. https://www.ceylongraphite.com/about/vein-graphite/ (Zugriff am 02.06.2022).
(121) Roberts, J.; Elliott, J.; Lismore-Scott, S. *Industrial Minerals*. https://www.indmin.com/Article/2950761/Channel/19575/Graphite-juniors-should-not-ignore-traditional-marketspanel.html (Zugriff am 02.06.2022).
(122) Fastmarkets IM. *Industrial Minerals*:*Graphite Market Brief*. https://www.indmin.com/Graphite.html (Zugriff am 02.06.2022).
(123) Moradi, B.; Botte, G. G. *Recycling of graphite anodes for the next generation of lithium ion batteries*. https://link-springer-com.ezproxy.uni-giessen.de/article/10.1007/s10800-015-0914-0 (Zugriff am 02.06.2022).
(124) Resorbent. *Kalzinierter Petrolkoks*. https://www.resorbent.de/kalzinierter-petrolkoks (Zugriff am 02.06.2022).
(125) Schiermeier, Q. Putting the carbon back: the hundred billion tonne challenge. *Nature* **2006**, *442* (7103), 620–623. DOI: 10.1038/442620a.
(126) Ratner, B. D. *Biomaterials science*:*An introduction to materials in medicine*, 2. ed., transferred to digital print; Elsevier, Acad. Press, 2011.
(127) Riley, F. L. Silicon Nitride and Related Materials. *J American Ceramic Society* **2000**, *83* (2), 245–265. DOI: 10.1111/j.1151-2916.2000.tb01182.x.
(128) Bourrat, X.; Fillion, A.; Naslain, R.; Chollon, G.; Brendlé, M. Regenerative laminar pyrocarbon. *Carbon* **2002**, *40* (15), 2931–2945. DOI: 10.1016/S0008-6223(02)00230-0.
(129) Ohzuku, T.; Ueda, A.; Yamamoto, N. Zero-Strain Insertion Material of Li [Li1 / 3Ti5 / 3] O 4 for Rechargeable Lithium Cells. *J. Electrochem. Soc.* **1995**, *142* (5), 1431–1435. DOI: 10.1149/1.2048592.
(130) Gao, J.; Jiang, C.; Ying, J.; Wan, C. Preparation and characterization of high-density spherical Li4Ti5O12 anode material for lithium secondary batteries.

Journal of Power Sources **2006**, *155* (2), 364–367. DOI: 10.1016/j.jpowsour.2005.04.008.

(131) Tokuda, N.; Kanno, T.; Hara, T.; Shigematsu, T.; Tsutsui, Y.; Ikeuchi, A.; Itou, T.; Kumamoto, T. *Development of a redox flow battery system*, 1998.

(132) Parasuraman, A.; Lim, T. M.; Menictas, C.; Skyllas-Kazacos, M. Review of material research and development for vanadium redox flow battery applications. *Electrochimica Acta* **2013**, *101*, 27–40. DOI: 10.1016/j.electacta.2012.09.067.

(133) Wang, W.; Luo, Q.; Li, B.; Wei, X.; Li, L.; Yang, Z. Recent Progress in Redox Flow Battery Research and Development. *Adv. Funct. Mater.* **2013**, *23* (8), 970–986. DOI: 10.1002/adfm.201200694.

(134) Weber, A. Z.; Mench, M. M.; Meyers, J. P.; Ross, P. N.; Gostick, J. T.; Liu, Q. Redox flow batteries: a review. *J Appl Electrochem* **2011**, *41* (10), 1137–1164. DOI: 10.1007/s10800-011-0348-2.

(135) Cheng, X.; Shi, Z.; Glass, N.; Zhang, L.; Zhang, J.; Song, D.; Liu, Z.-S.; Wang, H.; Shen, J. A review of PEM hydrogen fuel cell contamination: Impacts, mechanisms, and mitigation. *Journal of Power Sources* **2007**, *165* (2), 739–756. DOI: 10.1016/j.jpowsour.2006.12.012.

(136) Ross, D. K. Hydrogen storage: The major technological barrier to the development of hydrogen fuel cell cars. *Vacuum* **2006**, *80* (10), 1084–1089. DOI: 10.1016/j.vacuum.2006.03.030.

(137) Einert, M.; Wessel, C.; Badaczewski, F.; Leichtweiß, T.; Eufinger, C.; Janek, J.; Yuan, J.; Antonietti, M.; Smarsly, B. M. Nitrogen-Doped Carbon Electrodes: Influence of Microstructure and Nitrogen Configuration on the Electrical Conductivity of Carbonized Polyacrylonitrile and Poly(ionic liquid) Blends. *Macromol. Chem. Phys.* **2015**, *216* (19), 1930–1944. DOI: 10.1002/macp.201500169.

(138) Ou, M.; Zhang, Y.; Zhu, Y.; Fan, C.; Sun, S.; Feng, J.; Sun, X.; Wei, P.; Xu, J.; Peng, J.; Wu, X.; Jiang, G.; Li, Q.; Fang, C.; Han, J. Local Structures of Soft Carbon and Electrochemical Performance of Potassium-Ion Batteries. *ACS applied materials & interfaces* **2021**, *13* (24), 28261–28269. DOI: 10.1021/acsami.1c06303. Online veröffentlicht: 09.06.2021.

(139) Roskill. *Natural and Synthetic Graphite Report 2017*.

(140) Hebestreit, C. *THE IMPORTANCE OF CRITICAL RAW MATERIALS THROUGH THE EYES OF ORGANISED CIVIL SOCIETY:THE CASE OF GRAPHITE*. https://www.eesc.europa.eu/sites/default/files/files/hebestreit.pdf (Zugriff am 02.06.2022).

(141) Natarajan, S.; Aravindan, V. An Urgent Call to Spent LIB Recycling: Whys and Wherefores for Graphite Recovery. *Adv. Energy Mater.* **2020**, *10* (37), 2002238. DOI: 10.1002/aenm.202002238.

(142) Seilnacht, T. *Schmelzfluss-Elektrolyse zur Aluminiumgewinnung*. https://www.seilnacht.com/Lexikon/schmelzf.html (Zugriff am 02.06.2022).

(143) Matthias Rapf; Klaus Waizenegger; Martin Kranert. *Untersuchungen zur Elimination schwerabbaubarer Stoffe (organische Spurenstoffe) in Abwasser mit einem mikrobiologisch regenerierenden Adsorptions-Scheibentauchkörper – Abschlußbericht zum F+E-Projekt, gefördert von der Willy-Hager-Stiftung.*

(144) Azuma, H. A New Structural Model for Nongraphitic Carbons. *J Appl Crystallogr* **1998**, *31* (6), 910–916. DOI: 10.1107/S0021889898008085.

(145) Badaczewski, F. M.; Loeh, M. O.; Pfaff, T.; Dobrotka, S.; Wallacher, D.; Clemens, D.; Metz, J.; Smarsly, B. M. Peering into the structural evolution of glass-like carbons derived from phenolic resin by combining small-angle

neutron scattering with an advanced evaluation method for wide-angle X-ray scattering. *Carbon* **2019**, *141*, 169–181. DOI: 10.1016/j.carbon.2018.09.025.
(146) Biscoe, J.; Warren, B. E. An X-Ray Study of Carbon Black. *Journal of Applied Physics* **1942**, *13* (6), 364–371. DOI: 10.1063/1.1714879.
(147) Diamond, R. X-ray studies of some carbonized coals. *Phil. Trans. R. Soc. Lond. A* **1960**, *252* (1008), 193–223. DOI: 10.1098/rsta.1960.0004.
(148) Dopita, M.; Emmel, M.; Salomon, A.; Rudolph, M.; Matěj, Z.; Aneziris, C. G.; Rafaja, D. Temperature evolution of microstructure of turbostratic high melting coal-tar synthetic pitch studied using wide-angle X-ray scattering method. *Carbon* **2015**, *81*, 272–283. DOI: 10.1016/j.carbon.2014.09.058.
(149) Dopita, M.; Rudolph, M.; Salomon, A.; Emmel, M.; Aneziris, C. G.; Rafaja, D. Simulations of X-Ray Scattering on Two-Dimensional, Graphitic and Turbostratic Carbon Structures. *Adv. Eng. Mater.* **2013**, *15* (12), 1280–1291. DOI: 10.1002/adem.201300157.
(150) Faber, K.; Badaczewski, F. M.; Ruland, W.; Smarsly, B. M. Investigation of the Microstructure of Disordered, Non-graphitic Carbons by an Advanced Analysis Method for Wide-Angle X-ray Scattering. *Z. anorg. allg. Chem.* **2014**, *640* (15), 3107–3117. DOI: 10.1002/zaac.201400210.
(151) Franklin, R. E. The interpretation of diffuse X-ray diagrams of carbon. *Acta Cryst* **1950**, *3* (2), 107–121. DOI: 10.1107/S0365110X50000264.
(152) Franklin, R. E. Crystallite growth in graphitizing and non-graphitizing carbons. *Proc. R. Soc. Lond. A* **1951**, *209* (1097), 196–218. DOI: 10.1098/rspa.1951.0197.
(153) Fujimoto, H. Theoretical X-ray scattering intensity of carbons with turbostratic stacking and AB stacking structures. *Carbon* **2003**, *41* (8), 1585–1592. DOI: 10.1016/S0008-6223(03)00116-7.
(154) Fujimoto, H. A new estimation method for the degree of graphitization for random layer lattices. *Carbon* **2010**, *48* (12), 3446–3453. DOI: 10.1016/j.carbon.2010.05.041.
(155) Fujimoto, H. *Carbon Analyzer*, 2022. http://www.asahi-net.or.jp/~qn6h-fjmt (Zugriff am 01.11.2022).
(156) Fujimoto, H.; Shiraishi, M. Characterization of unordered carbon using Warren–Bodenstein's equation. *Carbon* **2001**, *39* (11), 1753–1761. DOI: 10.1016/S0008-6223(00)00308-0.
(157) Houska, C. R.; Warren, B. E. X-Ray Study of the Graphitization of Carbon Black. *Journal of Applied Physics* **1954**, *25* (12), 1503–1509. DOI: 10.1063/1.1702373.
(158) Keating, D. T.; Vineyard, G. H. The complete incoherent scattering function for carbon. *Acta Cryst* **1956**, *9* (11), 895–896. DOI: 10.1107/S0365110X56002539.
(159) Kovalevski, V.; Buseck, P. R.; Cowley, J. Comparison of carbon in shungite rocks to other natural carbons: An X-ray and TEM study. *Carbon* **2001**, *39* (2), 243–256. DOI: 10.1016/S0008-6223(00)00120-2.
(160) Perret, R.; Ruland, W. Profile analysis of random-layer lines. *J Appl Crystallogr* **1968**, *1* (4), 257–262. DOI: 10.1107/S0021889868005455.
(161) Pfaff, T.; Simmermacher, M.; Smarsly, B. M. CarbX : a program for the evaluation of wide-angle X-ray scattering data of non-graphitic carbons. *J Appl Crystallogr* **2018**, *51* (1), 219–229. DOI: 10.1107/S1600576718000195.
(162) Puech, P.; Dabrowska, A.; Ratel-Ramond, N.; Vignoles, G. L.; Monthioux, M. New insight on carbonisation and graphitisation mechanisms as obtained

from a bottom-up analytical approach of X-ray diffraction patterns. *Carbon* **2019**, *147*, 602–611. DOI: 10.1016/j.carbon.2019.03.013.

(163) Ruland, W. X-ray determination of crystallinity and diffuse disorder scattering. *Acta Cryst* **1961**, *14* (11), 1180–1185. DOI: 10.1107/S0365110X61003429.

(164) Ruland, W. The separation of coherent and incoherent Compton X-ray scattering. *Br. J. Appl. Phys.* **1964**, *15* (11), 1301–1307. DOI: 10.1088/0508-3443/15/11/306.

(165) Ruland, W. X-ray studies on the carbonization and graphitization of acenaphthylene and bifluorenyl. *Carbon* **1965**, *2* (4), 365–378. DOI: 10.1016/0008-6223(65)90007-2.

(166) Ruland, W. Fourier transform methods for random-layer line profiles. *Acta Cryst* **1967**, *22* (5), 615–623. DOI: 10.1107/S0365110X67001252.

(167) Saenko, N. S. The X-ray diffraction study of three-dimensional disordered network of nanographites: Experiment and theory. *Physics Procedia* **2012**, *23*, 102–105. DOI: 10.1016/j.phpro.2012.01.026.

(168) Salmon, P. S.; Petri, I. Structure of glassy and liquid GeSe 2. *J. Phys.: Condens. Matter* **2003**, *15* (16), S1509-S1528. DOI: 10.1088/0953-8984/15/16/301.

(169) Sharma, A.; Kyotani, T.; Tomita, A. Comparison of structural parameters of PF carbon from XRD and HRTEM techniques. *Carbon* **2000**, *38* (14), 1977–1984. DOI: 10.1016/S0008-6223(00)00045-2.

(170) Shi, H.; Reimers, J. N.; Dahn, J. R. Structure-refinement program for disordered carbons. *J Appl Crystallogr* **1993**, *26* (6), 827–836. DOI: 10.1107/S0021889893003784.

(171) Shi, L.; Rohringer, P.; Suenaga, K.; Niimi, Y.; Kotakoski, J.; Meyer, J. C.; Peterlik, H.; Wanko, M.; Cahangirov, S.; Rubio, A.; Lapin, Z. J.; Novotny, L.; Ayala, P.; Pichler, T. Confined linear carbon chains as a route to bulk carbyne. *Nature materials* **2016**, *15* (6), 634–639. DOI: 10.1038/nmat4617. Online veröffentlicht: 04.04.2016.

(172) Tsui, L. *CarbonXS GUI*. https://lktsui.github.io/carbon_xs_gui/tutorial.html (Zugriff am 04.01.2021).

(173) Tsui, L.; Garzon, F. CarbonXS GUI : a graphical front-end for CarbonXS. *J Appl Crystallogr* **2017**, *50* (6), 1830–1833. DOI: 10.1107/S1600576717015035.

(174) Ungár, T.; Gubicza, J.; Ribárik, G.; Pantea, C.; Zerda, T. Microstructure of carbon blacks determined by X-ray diffraction profile analysis. *Carbon* **2002**, *40* (6), 929–937. DOI: 10.1016/S0008-6223(01)00224-X.

(175) Wang, H.; Delacroix, S.; Osswald, O.; Anderson, M.; Heil, T.; Lepre, E.; Lopez-Salas, N.; Kaner, R. B.; Smarsly, B.; Strauss, V. Laser-carbonization: Peering into the formation of micro-thermally produced (N-doped)carbons. *Carbon* **2021**, *176*, 500–510. DOI: 10.1016/j.carbon.2021.01.145.

(176) Warren, B. E. X-Ray Diffraction Study of Carbon Black. *The Journal of Chemical Physics* **1934**, *2* (9), 551–555. DOI: 10.1063/1.1749528.

(177) Warren, B. E. X-Ray Diffraction in Random Layer Lattices. *Phys. Rev.* **1941**, *59* (9), 693–698. DOI: 10.1103/PhysRev.59.693.

(178) Warren, B. E.; Bodenstein, P. The diffraction pattern of fine particle carbon blacks. *Acta Cryst* **1965**, *18* (2), 282–286. DOI: 10.1107/S0365110X65000609.

(179) Zickler, G. A.; Smarsly, B.; Gierlinger, N.; Peterlik, H.; Paris, O. A reconsideration of the relationship between the crystallite size La of carbons determined by X-ray diffraction and Raman spectroscopy. *Carbon* **2006**, *44* (15), 3239–3246. DOI: 10.1016/j.carbon.2006.06.029.

(180) Scherrer, P. Bestimmung der inneren Struktur und der Größe von Kolloidteilchen mittels Röntgenstrahlen. In *Kolloidchemie Ein Lehrbuch*; Zsigmondy, R., Ed.; Springer Berlin Heidelberg, 1912; pp 387–409. DOI: 10.1007/978-3-662-33915-2_7.
(181) IUPAC. amorphous carbon. In *The IUPAC Compendium of Chemical Terminology*; Gold, V., Ed.; International Union of Pure and Applied Chemistry (IUPAC), 2019. DOI: 10.1351/goldbook.A00294.
(182) IUPAC. non-graphitic carbon. In *The IUPAC Compendium of Chemical Terminology*; Gold, V., Ed.; International Union of Pure and Applied Chemistry (IUPAC), 2019. DOI: 10.1351/goldbook.N04193.
(183) IUPAC. graphite. In *The IUPAC Compendium of Chemical Terminology*; Gold, V., Ed.; International Union of Pure and Applied Chemistry (IUPAC), 2019. DOI: 10.1351/goldbook.G02684.
(184) IUPAC. graphitic carbon. In *The IUPAC Compendium of Chemical Terminology*; Gold, V., Ed.; International Union of Pure and Applied Chemistry (IUPAC), 2019. DOI: 10.1351/goldbook.G02689.
(185) IUPAC. graphitization. In *The IUPAC Compendium of Chemical Terminology*; Gold, V., Ed.; International Union of Pure and Applied Chemistry (IUPAC), 2019. DOI: 10.1351/goldbook.G02691.
(186) IUPAC. graphitizable carbon. In *The IUPAC Compendium of Chemical Terminology*; Gold, V., Ed.; International Union of Pure and Applied Chemistry (IUPAC), 2019. DOI: 10.1351/goldbook.G02690.
(187) IUPAC. graphitized carbon. In *The IUPAC Compendium of Chemical Terminology*; Gold, V., Ed.; International Union of Pure and Applied Chemistry (IUPAC), 2019. DOI: 10.1351/goldbook.G02693.
(188) IUPAC. non-graphitizable carbon. In *The IUPAC Compendium of Chemical Terminology*; Gold, V., Ed.; International Union of Pure and Applied Chemistry (IUPAC), 2019. DOI: 10.1351/goldbook.N04194.
(189) IUPAC. glass-like carbon. In *The IUPAC Compendium of Chemical Terminology*; Gold, V., Ed.; International Union of Pure and Applied Chemistry (IUPAC), 2019. DOI: 10.1351/goldbook.G02639.
(190) IUPAC. carbonization. In *The IUPAC Compendium of Chemical Terminology*; Gold, V., Ed.; International Union of Pure and Applied Chemistry (IUPAC), 2019. DOI: 10.1351/goldbook.C00840.
(191) Aoki, H.; S. Dresselhaus, M. *Physics of Graphene*; Springer International Publishing, 2014. DOI: 10.1007/978-3-319-02633-6.
(192) Pierson, H. O. *Handbook of carbon, graphite, diamond, and fullerenes*:*Properties, processing, and applications*; Materials science and process technology series : Electronic materials and process technology; Noyes Publications, 2001.
(193) Ulbricht, G. *2-dimensionaler Ladungsträgertransport in Graphen und einkristallinen organischen Halbleitern*.
(194) Krueger, A. *Carbon materials and nanotechnology*; Wiley-Blackwell, 2010.
(195) Holleman, A. F.; Wiberg, E.; Wiberg, N.; Fischer, G. *Anorganische Chemie*, 103. Auflage; De Gruyter, 2017.
(196) Holleman, A. F.; Wiberg, N. *Anorganische Chemie*, Aufl. 103; De Gruyter, 2016.
(197) Strunz, H. *Strunz Mineralogical Tables. Ninth Edition*:*Chemical-Structural Mineral Classification System*, 9th ed.; Schweizerbart, 2020.
(198) Bernal, J. D. The structure of graphite. *Proc. R. Soc. Lond. A* **1924**, *106* (740), 749–773. DOI: 10.1098/rspa.1924.0101.
(199) Lipson, H. S.; Stokes, A. R. The structure of graphite. *Proc. R. Soc. Lond. A* **1942**, *181* (984), 101–105. DOI: 10.1098/rspa.1942.0063.

(200) Fitzer, E.; Kochling, K.-H.; Boehm, H. P.; Marsh, H. Recommended terminology for the description of carbon as a solid (IUPAC Recommendations 1995). *Pure and applied chemistry* **1995**, *67* (3), 473–506. DOI: 10.1351/pac199567030473.

(201) Vieira, L. d. S. A review on the use of glassy carbon in advanced technological applications. *Carbon* **2022**, *186*, 282–302. DOI: 10.1016/j.carbon.2021.10.022.

(202) Liu, Z.-J.; Guo, Q.-G.; Liu, L.; Shi, J.-L.; Zhai, G.-T. Influence of filler type on the performance and microstructure of a carbon/graphite material. *New Carbon Materials* **2010**, *25* (4), 313–316. DOI: 10.1016/S1872-5805(09)60035-4.

(203) Marsh, H.; Edwards, I. A. S.; Menendez, R. *Introduction to carbon science*; Butterworths, 1989.

(204) Loeh, M. O.; Badaczewski, F. M.; Faber, K.; Hintner, S.; Bertino, M. F.; Mueller, P.; Metz, J.; Smarsly, B. M. Analysis of thermally induced changes in the structure of coal tar pitches by an advanced evaluation method of X-ray scattering data. *Carbon* **2016**, *109*, 823–835. DOI: 10.1016/j.carbon.2016.08.031.

(205) Emmerich, F. G. Evolution with heat treatment of crystallinity in carbons. *Carbon* **1995**, *33* (12), 1709–1715. DOI: 10.1016/0008-6223(95)00127-8.

(206) Martín, Y.; García, R.; Keating, P.; Snape, C. E.; Moinelo, S. R. A Study of the Polymerization and Condensation Reactions during the Heat Treatment of Pitches under Gas-Blowing Conditions. *Energy Fuels* **2000**, *14* (2), 380–392. DOI: 10.1021/ef9901443.

(207) Joseph, D.; Oberlin, A. Oxidation of carbonaceous matter—I. *Carbon* **1983**, *21* (6), 559–564. DOI: 10.1016/0008-6223(83)90239-7.

(208) Oberlin, A.; Bonnamy, S.; Rouxhet, P. G. Colloidal and supramolecular aspects of carbon. *Chemistry and physics of carbon* **1999**, *26*, 1–148.

(209) Osswald, O.; Loeh, M. O.; Badaczewski, F. M.; Pfaff, T.; Fischer, H. E.; Franz, A.; Hoffmann, J.-U.; Reehuis, M.; Klar, P. J.; Smarsly, B. M. On the Highly Ordered Graphene Structure of Non-Graphitic Carbons (NGCs)-A Wide-Angle Neutron Scattering (WANS) Study. *C* **2023**, *9* (1), 27. DOI: 10.3390/c9010027.

(210) Franklin, R. E. Graphitizing and non-graphitizing carbons, their formation, structure and properties. *Angewandte Chemie* **1953**, *13* (65), 353.

(211) Sumiya, H.; Yusa, H.; Inoue, T.; Ofuji, H.; Irifune, T. Conditions and mechanism of formation of nano-polycrystalline diamonds on direct transformation from graphite and non-graphitic carbon at high pressure and temperature. *High Pressure Research* **2006**, *26* (2), 63–69. DOI: 10.1080/08957950600765863.

(212) Ferrari, A. C.; Meyer, J. C.; Scardaci, V.; Casiraghi, C.; Lazzeri, M.; Mauri, F.; Piscanec, S.; Jiang, D.; Novoselov, K. S.; Roth, S.; Geim, A. K. Raman spectrum of graphene and graphene layers. *Physical review letters* **2006**, *97* (18), 187401. DOI: 10.1103/PhysRevLett.97.187401. Online veröffentlicht: 30.10.2006.

(213) Ferrari, A. C.; Robertson, J. Interpretation of Raman spectra of disordered and amorphous carbon. *Phys. Rev. B* **2000**, *61* (20), 14095–14107. DOI: 10.1103/PhysRevB.61.14095.

(214) Ferrari, A. C.; Basko, D. M. Raman spectroscopy as a versatile tool for studying the properties of graphene. *Nature nanotechnology* **2013**, *8* (4), 235–246. DOI: 10.1038/nnano.2013.46.

(215) Jorio, A.; Dresselhaus, M. S.; Saito, R.; Dresselhaus, G. *Raman Spectroscopy in Graphene Related Systems*; John Wiley & Sons, 2011.
(216) Mallet-Ladeira, P.; Puech, P.; Weisbecker, P.; Vignoles, G. L.; Monthioux, M. Behavior of Raman D band for pyrocarbons with crystallite size in the 2–5 nm range. *Applied Physics A: Materials Science & Processing* **2014**, *114* (3), 759–763. DOI: 10.1007/s00339-013-7671-x.
(217) Schüpfer, D. B.; Badaczewski, F. M.; Guerra-Castro, J. M.; Hofmann, D. M.; Heiliger, C.; Smarsly, B. M.; Klar, P. J. Assessing the structural properties of graphitic and non-graphitic carbons by Raman spectroscopy. *Carbon* **2020**, *161*, 359–372. DOI: 10.1016/j.carbon.2019.12.094.
(218) Tuinstra, F.; Koenig, J. L. Raman Spectrum of Graphite. *The Journal of Chemical Physics* **1970**, *53* (3), 1126–1130. DOI: 10.1063/1.1674108.
(219) Vinado, R.; Fischbach, D. B. New Lines in the Raman Spectra of Carbons and Graphite. *J American Ceramic Society* **1978**, *61* (1-2), 13–17. DOI: 10.1111/j.1151-2916.1978.tb09219.x.
(220) Nemanich, R. J.; Solin, S. A.; Gúerard, D. Raman scattering from intercalated donor compounds of graphite. *Phys. Rev. B* **1977**, *16* (6), 2965–2972. DOI: 10.1103/PhysRevB.16.2965.
(221) Nemanich, R. J.; Solin, S. A. First- and second-order Raman scattering from finite-size crystals of graphite. *Phys. Rev. B* **1979**, *20* (2), 392–401. DOI: 10.1103/PhysRevB.20.392.
(222) Schüpfer, D. B.; Badaczewski, F. M.; Peilstöcker, J.; Guerra-Castro, J. M.; Shim, H.; Firoozabadi, S.; Beyer, A.; Volz, K.; Presser, V.; Heiliger, C.; Smarsly, B. M.; Klar, P. J. Monitoring the thermally induced transition from sp3-hybridized into sp2-hybridized carbons. *Carbon* **2021**, *172*, 214–227. DOI: 10.1016/j.carbon.2020.09.063.
(223) Härk, E.; Ballauff, M. Carbonaceous Materials Investigated by Small-Angle X-ray and Neutron Scattering. *C* **2020**, *6* (4), 82. DOI: 10.3390/c6040082.
(224) Härk, E.; Petzold, A.; Goerigk, G.; Risse, S.; Tallo, I.; Härmas, R.; Lust, E.; Ballauff, M. Carbide derived carbons investigated by small angle X-ray scattering: Inner surface and porosity vs. graphitization. *Carbon* **2019**, *146*, 284–292. DOI: 10.1016/j.carbon.2019.01.076.
(225) Olds, D. P.; Duxbury, P. M. Efficient algorithms for calculating small-angle scattering from large model structures. *J Appl Crystallogr* **2014**, *47* (3), 1077–1086. DOI: 10.1107/S1600576714005925.
(226) Porod, G. Die Röntgenkleinwinkelstreuung von dichtgepackten kolloiden Systemen. *Kolloid-Zeitschrift* **1951**, *124* (2), 83–114. DOI: 10.1007/BF01512792.
(227) Ruland, W. Small-angle scattering of two-phase systems: determination and significance of systematic deviations from Porod's law. *J Appl Crystallogr* **1971**, *4* (1), 70–73. DOI: 10.1107/S0021889871006265.
(228) Smarsly, B. M.; Antonietti, M.; Wolff, T. Evaluation of the small-angle x-ray scattering of carbons using parametrization methods. *The Journal of Chemical Physics* **2002**, *116* (6), 2618–2627. DOI: 10.1063/1.1433463.
(229) Ghazinejad, M.; Holmberg, S.; Pilloni, O.; Oropeza-Ramos, L.; Madou, M. Graphitizing Non-graphitizable Carbons by Stress-induced Routes. *Scientific reports* **2017**, *7* (1), 16551. DOI: 10.1038/s41598-017-16424-z. Online veröffentlicht: 29.11.2017.
(230) Eckert, M. Max von Laue and the discovery of X-ray diffraction in 1912. *Ann. Phys.* **2012**, *524* (5), A83-A85. DOI: 10.1002/andp.201200724.

(231) NobelPrize.org. *The Nobel Prize in Physics 1914*. https://www.nobelprize.org/prizes/physics/1914/summary/ (Zugriff am 15.06.2022).
(232) Laue, M. von; Wagner, E. H. *Roentgenstrahl-interferenzen*, 3rd ed.; Akademische Verlagsgesellschaft, 1941.
(233) Bragg, W. H. The reflection of X-rays by crystals. (II.). *Proc. R. Soc. Lond. A* **1913**, *89* (610), 246–248. DOI: 10.1098/rspa.1913.0082.
(234) Bragg, W. L. The structure of some crystals as indicated by their diffraction of X-rays. *Proc. R. Soc. Lond. A* **1913**, *89* (610), 248–277. DOI: 10.1098/rspa.1913.0083.
(235) Bragg, W. H. X-rays and Crystals. *Nature* **1913**, *90* (2256), 572. DOI: 10.1038/090572c0.
(236) Bragg, W. H.; Bragg, W. L. The reflection of X-rays by crystals. *Proc. R. Soc. Lond. A* **1913**, *88* (605), 428–438. DOI: 10.1098/rspa.1913.0040.
(237) Bragg, W. H.; Bragg, W. L. The structure of the diamond. *Proc. R. Soc. Lond. A* **1913**, *89* (610), 277–291. DOI: 10.1098/rspa.1913.0084.
(238) NobelPrize.org. *The Nobel Prize in Physics 1915*. https://www.nobelprize.org/prizes/physics/1915/summary/ (Zugriff am 15.06.2022).
(239) Bacon, G. E.; Franklin, R. E. The alpha dimension in graphite. *Acta Crystallogr.* **1951** (4).
(240) Bangham, D. H.; Franklin, R. E. Thermal expansion of coals and carbonised coals. *Trans. Faraday Soc.* **1946**, *42*, B289. DOI: 10.1039/TF946420B289.
(241) Bangham, D. H.; Franklin, R. E.; Hirst, W.; Maggs, F. A. P. A structural model for coal substance. *Fuel* **1949**, *10* (28), 231–237.
(242) Franklin, R. E. Graphitizable and nongraphitizable carbons. *Compt. rend.*, *1951* (232).
(243) Franklin, R. E. A note on the true density, chemical composition and structure of coals and carbonized coals. *Fuel* **1948**, *2* (27), 46–49.
(244) Franklin, R. E. A study of the fine structure of carbonaceous solids by measurements of true and apparent densities. Part I. Coals. *Trans. Faraday Soc.* **1949**, *45*, 274. DOI: 10.1039/TF9494500274.
(245) Franklin, R. E. Note sur la structure colloidale des houilles carbonisees. *Bulletin de la societe chimiqze de france* **1949** (16), D53-D54.
(246) Franklin, R. E. A rapid approximate method for correcting low-angle scattering measurements for the influence of the finite height of the X-ray beam. *Acta Cryst* **1950**, *3* (2), 158–159. DOI: 10.1107/S0365110X50000343.
(247) Franklin, R. E. Influence of the bonding electrons on the scattering of X-rays by carbon. *Nature* **1950**, *165* (4185), 71. DOI: 10.1038/165071a0.
(248) Franklin, R. E. On the structure of carbon. *J. Chim. Phys.* **1950**, *47*, 573–575. DOI: 10.1051/jcp/1950470573.
(249) Franklin, R. E. Les carbones graphitisables et non-graphitisables. *Comptes rendus hebdomadaires des seances de l academie des sciences* **1951**, *3* (232), 232–234.
(250) Franklin, R. E. The structure of graphitic carbons. *Acta Cryst* **1951**, *4* (3), 253–261. DOI: 10.1107/S0365110X51000842.
(251) Franklin, R. E. Homogeneous and Heterogeneous Graphitization of Carbon. *Nature* **1956**, *177* (4501), 239. DOI: 10.1038/177239a0.
(252) Watt, J. D.; Franklin, R. E. Changes in the Structure of Carbon during Oxidation. *Nature* **1957**, *180* (4596), 1190–1191. DOI: 10.1038/1801190a0.
(253) Harris, P. J.; Suarez-Martinez, I. Rosalind Franklin, carbon scientist. *Carbon* **2021**, *171*, 289–293. DOI: 10.1016/j.carbon.2020.09.022.
(254) *Mathematica, Version 12.1*; Wolfram Research, Inc., 2020. https://www.wolfram.com/mathematica.

(255) Cromer, D. T. Compton Scattering Factors for Aspherical Free Atoms. *The Journal of Chemical Physics* **1969**, *50* (11), 4857–4859. DOI: 10.1063/1.1670980.
(256) James, R. W. *The optical principles of the diffraction of X-rays*, Repr. with addendum, London, 1962.
(257) Milberg, M. E.; Brailsford, A. D. The atomic incoherent scattering intensities of boron, oxygen and carbon. *Acta Cryst* **1958**, *11* (10), 672–673. DOI: 10.1107/S0365110X58001808.
(258) Prince, E.; Fuess, H.; Hahn, T.; Wondratschek, H.; Müller, U.; Shmueli, U.; Authier, A.; Kopský, V.; Litvin, D. B.; Rossmann, M. G.; Arnold, E.; Hall, S.; McMahon, B. *International Tables for Crystallography*, C; International Union of Crystallography, 2006. DOI: 10.1107/97809553602060000103.
(259) Stephens, P. W. *International Tables for Crystallography 8v Set 4e (Updated Sept 2014)*; John Wiley & Sons Inc, 2014.
(260) Fox, A. G.; O'Keefe, M. A.; Tabbernor, M. A. Relativistic Hartree–Fock X-ray and electron atomic scattering factors at high angles. *Acta Crystallogr A Found Crystallogr* **1989**, *45* (11), 786–793. DOI: 10.1107/S0108767389007567.
(261) NIST Center for Neutron Research. *Neutron scattering lengths and cross sections*. https://www.ncnr.nist.gov/resources/n-lengths/ (Zugriff am 22.12.2020).
(262) Sears, V. F. Neutron scattering lengths and cross sections. *Neutron News* **1992**, *3* (3), 26–37. DOI: 10.1080/10448639208218770.
(263) Sivia, D. S. *Elementary scattering theory:For X-ray and neutron users*, Reprinted.; Oxford University Press, 2017.
(264) Fischer, H. E.; Barnes, A. C.; Salmon, P. S. Neutron and x-ray diffraction studies of liquids and glasses. *Rep. Prog. Phys.* **2006**, *69* (1), 233–299. DOI: 10.1088/0034-4885/69/1/R05.
(265) Placzek, G. The Scattering of Neutrons by Systems of Heavy Nuclei. *Phys. Rev.* **1952**, *86* (3), 377–388. DOI: 10.1103/PhysRev.86.377.
(266) Buerger, M. J. The Correction of X-Ray Diffraction Intensities for Lorentz and Polarization Factors. *Proceedings of the National Academy of Sciences of the United States of America* **1940**, *26* (11), 637–642. DOI: 10.1073/pnas.26.11.637.
(267) Eaton, J. W.; Bateman, D.; Hauberg, S.; Wehbring, R. *GNU Octave version 5.2.0 manual: a high-level interactive language for numerical computations*, 2020. https://docs.octave.org/v5.2.0/ (Zugriff am 01.11.2022).
(268) The Octave Forge Community. *The 'optim' package*. https://octave.sourceforge.io/optim/ (Zugriff am 23.06.2022).
(269) Free Software Foundation, Inc. *GNU General Public License:Version 3*. https://www.gnu.org/licenses/gpl-3.0.html (Zugriff am 21.10.2020).
(270) Levenberg, K. A method for the solution of certain non-linear problems in least squares. *Quart. Appl. Math.* **1944**, *2* (2), 164–168. DOI: 10.1090/QAM/10666.
(271) Moré, J. J. The Levenberg-Marquardt algorithm: Implementation and theory. In *Numerical Analysis*; Watson, G. A., Ed.; Lecture Notes in Mathematics; Springer Berlin Heidelberg, 1978; pp 105–116. DOI: 10.1007/BFb0067700.
(272) Marquardt, D. W. An Algorithm for Least-Squares Estimation of Nonlinear Parameters. *Journal of the Society for Industrial and Applied Mathematics* **1963**, *11* (2), 431–441. DOI: 10.1137/0111030.
(273) Hoffmann, J.-U.; Reehuis, M. E2: The Flat-Cone Diffractometer at BER II. *JLSRF* **2018**, *4*. DOI: 10.17815/jlsrf-4-110.
(274) Fischer, H. E.; Cuello, G. J.; Palleau, P.; Feltin, D.; Barnes, A. C.; Badyal, Y. S.; Simonson, J. M. D4c: A very high precision diffractometer for disordered

materials. *Applied Physics A: Materials Science & Processing* **2002**, *74* (0), s160-s162. DOI: 10.1007/s003390101087.

(275) Smarsly, B. M.; Badaczewski, F.; Fischer, H. E.; Loeh, M.; Osswald, O.; Pfaff, T. Analysis of the wide-angle neutron scattering of non-graphitic carbon - testing of an advanced evaluation approach. DOI: 10.5291/ILL-DATA.5-26-218.

(276) Gilbert, B. Finite size effects on the real-space pair distribution function of nanoparticles. *J Appl Crystallogr* **2008**, *41* (3), 554–562. DOI: 10.1107/S0021889808007905.

(277) Howell, R. C.; Proffen, T.; Conradson, S. D. Pair distribution function and structure factor of spherical particles. *Phys. Rev. B* **2006**, *73* (9). DOI: 10.1103/PhysRevB.73.094107.

(278) Masson, O.; Thomas, P. Exact and explicit expression of the atomic pair distribution function as obtained from X-ray total scattering experiments. *J Appl Crystallogr* **2013**, *46* (2), 461–465. DOI: 10.1107/S0021889812051357.

(279) Olds, D.; Wang, H.-W.; Page, K. DShaper : an approach for handling missing low- Q data in pair distribution function analysis of nanostructured systems. *J Appl Crystallogr* **2015**, *48* (6), 1651–1659. DOI: 10.1107/S1600576715016581.

(280) Peterson, P. F.; Božin, E. S.; Proffen, T.; Billinge, S. J. L. Improved measures of quality for the atomic pair distribution function. *J Appl Crystallogr* **2003**, *36* (1), 53–64. DOI: 10.1107/S0021889802018708.

(281) Weisbecker, P.; Leyssale, J.-M.; Fischer, H. E.; Honkimäki, V.; Lalanne, M.; Vignoles, G. L. Microstructure of pyrocarbons from pair distribution function analysis using neutron diffraction. *Carbon* **2012**, *50* (4), 1563–1573. DOI: 10.1016/j.carbon.2011.11.035.

(282) Willinger, E. *Analysis of Local Structure by Atomic Pair Distribution Function*; Modern Methods in Heterogeneous Catalysis Research, 2017.

(283) Szczygielska, A.; Burian, A.; Dore, J. C.; Duber, S.; Hannon, A. Paracrystalline nature of saccharose- and anthracene-based carbons studied by wide-angle scattering. In *Narrow-gap semiconductor photodiodes*; Rutkowski, J., Rogalski, A., Eds.; SPIE, 2012; pp 288–294. DOI: 10.1117/12.519677.

(284) Billinge, S. J. L. *diffpy/libdiffpy*. https://github.com/diffpy/libdiffpy (Zugriff am 20.05.2021).

(285) Billinge, S. J. L. *diffpy/diffpy.pdfgui*. https://github.com/diffpy/diffpy.pdfgui/releases/download/svn3067/diffpy-1.0-r3067.exe (Zugriff am 01.06.2021).

(286) Farrow, C. L.; Juhas, P.; Liu, J. W.; Bryndin, D.; Bozin, E. S.; Bloch, J.; Proffen, T.; Billinge, S. J. L. PDFgui user guide **2016**.

(287) Farrow, C. L.; Juhas, P.; Liu, J. W.; Bryndin, D.; Božin, E. S.; Bloch, J.; Proffen, T.; Billinge, S. J. L. PDFfit2 and PDFgui: computer programs for studying nanostructure in crystals. *Journal of physics. Condensed matter : an Institute of Physics journal* **2007**, *19* (33), 335219. DOI: 10.1088/0953-8984/19/33/335219. Online veröffentlicht: 04.07.2007.

(288) Ruland, W. X-ray studies on the structure of graphitic carbons. *Acta Cryst* **1965**, *18* (6), 992–996. DOI: 10.1107/S0365110X65002414.

(289) Marsh, H.; Latham, C. S. The Chemistry of Mesophase Formation. In *Petroleum-Derived Carbons*; Bacha, J. D., Newman, J. W., White, J. L., Eds.; ACS Symposium Ser, No. 303; American Chemical Society, 1986; pp 1–28. DOI: 10.1021/bk-1986-0303.ch001.

6. Anhang

6.1. Abkürzungsverzeichnis

6.1.1. Allgemeine Abkürzungen

DFG	**D**eutsche **F**orschungs**g**emeinschaft
GrK	**Gr**aduierten**k**olleg
GUI	Graphische Benutzeroberfläche (engl. ***g**raphical **u**ser **i**nterface*)
IUPAC	Internationale Union für reine und angewandte Chemie (engl. ***I**nternational **U**nion of **P**ure and **A**pplied **C**hemistry*)
NGC(s)	Nicht-graphitische(r) Kohlenstoff(e) (engl. ***n**on-**g**raphitic **c**arbon(**s**)*)
NG	**N**atürlicher **G**raphit
SG	**S**ynthetischer **G**raphit

6.1.2. Messmethoden

PDF	Paar-Verteilungs-Funktion (engl. **p**air-**d**istribution-**f**unction)
TEM	**T**ransmissions**e**lektronen**m**ikroskopie
WAXS	Weitwinkelröntgenstreuung (engl. ***w**ide-**a**ngle **X**-ray **s**cattering*)
WANS	Weitwinkelneutronenstreuung (engl. ***w**ide-**a**ngle **n**eutron **s**cattering*)
XRD	Röntgenstreuung (engl. ***X**-**r**ay **d**iffraction*)

6.1.3. Chemische Komponenten

CO_2	Kohlenstoffdioxid
Li	Lithium
CDC	Von Karbid abgeleiteter Kohlenstoff (engl. **c**arbide-**d**erived **c**arbon)

6.1.4. Strukturparameter

L_a	Schichtausdehnung
l_{cc}	C-C Bindungslänge
σ_1	Standardabweichung der nächste-Nachbar-Verteilung
N	Anzahl der Schichten pro Stapel
L_c	Stapelhöhe
a_3	Durchschnittlicher Schichtabstand
$a_{3\,min}$	Minimaler Schichtabstand
σ_3	Standardabweichung des Schichtabstandes (Stapelunordnung)

6.2. Wissenschaftliche Beiträge

6.2.1. Zugrunde liegende Publikationen

(1) **Oliver Osswald**, Bernd M. Smarsly. OctCarb — A GNU Octave Script for the Analysis and Evaluation of Wide-Angle Scattering Data of Non-Graphitic Carbons. *C* 2022, 8(4) (78). DOI: 10.3390/c8040078.

(2) **Oliver Osswald**, Marc O. Loeh, Felix M. Badaczewski, Torben Pfaff, Henry E. Fischer, Alexandra Franz, Jens-Uwe Hoffmann, Manfred Reehuis, Peter J. Klar, Bernd M. Smarsly. On the Highly Ordered Graphene Structure of Non-Graphitic Carbons (NGCs)-A Wide-Angle Neutron Scattering (WANS) Study. *C* 2023, 9 (1), 27. DOI: 10.3390/c9010027.

6.2.2. Sonstige Publikationen

Huize Wang, Simon Delacroix, **Oliver Osswald**, Mackenzie Anderson, Tobias Heil, Enrico Lepre, Nieves Lopez-Salas, Richard B. Kaner, Bernd Smarsly, Volker Strauss. Laser-carbonization: Peering into the formation of micro-thermally produced (N-doped)carbons. *Carbon* 2021 (176), 500-510. DOI: 10.1016/j.carbon.2021.01.145

6.2.3. Konferenzbeiträge / wissenschaftliche Reisen

Mai 2019: Messzeit am „Very Small Angle Neutron Scattering (VSANS) Diffractometer" (Sehr-Kleinwinkel-Neutronenstreudiffraktometer) V16 am Neutronenreaktor BER III des Helmholtz-Zentrum in Berlin-Wannsee.

August 2019: Messzeit am „Disordered Materials Diffractometer" ("Diffraktometer für ungeordnete Materialien") D4 am Neutronenreaktor des Institut Laue-Langevin Grenoble (Frankreich).

August 2019: Postervortrag zum Thema „Automation of microstructure analysis of non-graphitic carbons" (Automatisierung der

Mikrostrukturanalyse von nicht-graphitischen Kohlenstoffen) im Rahmen des Graduiertenkollegs 2204 „Substitutionsmaterialien für nachhaltige Energietechnologien".

September 2019: Vortrag und Poster zum Thema „Microstructure analysis of non-graphitic carbons" („Mikrostrukturanalyse von nicht-graphitischen Kohlenstoffen") beim 7. Deutsch-Japanischen Kohlenstoff-Symposium/Tagung des Arbeitskreis Kohlenstoff der Deutschen Forschungsgemeinschaft in Würzburg.

Oktober 2019: Vortrag zum Thema „Microstructure analysis of non-graphitic carbons" („Mikrostrukturanalyse von nicht-graphitischen Kohlenstoffen") im Rahmen des Graduiertenkollegs 2204 „Substitutionsmaterialien für nachhaltige Energietechnologien" in Gießen.

Oktober 2019: Postervortrag zum Thema „Microstructure analysis of non-graphitic carbons" („Mikrostrukturanalyse von nicht-graphitischen Kohlenstoffen") im Rahmen des Graphene und Co. Konferenz in Bad Herrenalb.

Dezember 2019: Nutzertreffen des Neutronenreaktors HZB II des Helmholtz-Zentrum in Berlin-Wannsee.

Juli 2020: Messzeit am „Small angle X-ray Scattering Diffractometer" („Kleinwinkel-Röntgenstreudiffraktometer") V16 am „Elettra Sinctrotrone" (Elektronen-Synchrotron) in Triest (Italien).

September 2020: Vortrag zum Thema „Microstructure analysis of non-graphitic carbons" („Mikrostrukturanalyse von nicht-graphitischen Kohlenstoffen)" im Rahmen des „Materials Science and Engineering Congress" (Kongress für Materialwissenschaft und -technik) in Darmstadt.

Juni 2021: Messzeit am „Spectroscopy Applied to Material Based on Absorption" („Auf Material angewendete Spektroskopie basierend auf Absorption") Experiment SAMBA am „Soleil Synchrotron" (Synchrotron *Sonne*) bei Paris (Frankreich).

Oktober 2021:	Teilnahme an der „Graphene“ Konferenz in Grenoble (Frankreich).
Mai 2022	Vorträge zu den Themen „Acetylen über Partielle Oxidation von Erdgas: Koks und Ruß - XRD Untersuchungen“ und „Blick in die atomare Struktur von sp^2-Kohlenstoffmaterialien durch Röntgen- und Neutronenstreuung - eine verbesserte Software zur Auswertung“ bei der Tagung des Arbeitskreis Kohlenstoff der Deutschen Forschungsgemeinschaft (online).
Juli 2022:	Posterbeitrag zum Thema „On The Surprisingly High Order Of The Graphene Structure Of Non-Graphitic Carbons (NGCs) Determined By Wide-Angle Neutron Scattering (WANS)” („Über die überraschend hohe Ordnung der Graphenstruktur von nicht-graphitischen Kohlenstoffen (NGCs), bestimmt durch Weitwinkel-Neutronenstreuung (WANS)“) bei der „Carbon” (Kohlenstoff) Konferenz in London (Großbritannien).

6.3. Publikationen Haupttexte

6.3.1. Publikation 1 [1]

Reproduziert mit Genehmigung von Oliver Osswald; veröffentlicht bei MDPI, *C*, 2022.

Article

OctCarb—A GNU *Octave* Script for the Analysis and Evaluation of Wide-Angle Scattering Data of Non-Graphitic Carbons

Oliver Osswald * and Bernd M. Smarsly *

Institute of Physical Chemistry, Justus-Liebig-University Giessen, Heinrich-Buff-Ring 17, 35392 Giessen, Germany
* Correspondence: carbon@oss-wald.de (O.O.); bernd.smarsly@phys.chemie.uni-giessen.de (B.M.S.)

Abstract: We present a free software script operating in GNU *Octave* for the refinement of wide-angle X-ray and neutron scattering (WAXS/WANS) data of non-graphitic carbons (NGCs). The refinement script (*OctCarb*) is based on the evaluation approach of Ruland and Smarsly (2002). As result, up to 14 physically meaningful parameters such as the layer extension L_a, the stack height L_c, as well as the degree of disorder of the graphenes and their stacking are obtained through a well-established fitting routine. In addition, background scattering based on specific physical phenomena and different correction parameters such as polarization and absorption can be considered. Since the complex mathematical calculations are implemented and performed in the background, with only a few settings to be made, the software was designed to be usable by inexperienced users. As another key feature, *Octave* and thus *OctCarb* run on all common operating systems (Windows, MacOS and Linux), and can even be used on high-performance computing clusters (HPCs) to perform multiple calculations at once. In addition to this, the whole refinement can be performed within minutes, and it is possible to tweak and optimize it for special purposes and measuring geometries. These features make *OctCarb* useful for all scientists dealing with the characterization of NGCs by X-ray or neutron scattering techniques.

Keywords: non-graphitic carbon; wide-angle scattering; open-source software

check for updates

Citation: Osswald, O.; Smarsly, B.M. *OctCarb*—A GNU *Octave* Script for the Analysis and Evaluation of Wide-Angle Scattering Data of Non-Graphitic Carbons. *C* **2022**, *8*, 78. https://doi.org/10.3390/c8040078

Academic Editor: Cédric Pardanaud

Received: 3 November 2022
Accepted: 29 November 2022
Published: 9 December 2022

Publisher's Note: MDPI stays neutral with regard to jurisdictional claims in published maps and institutional affiliations.

1. Introduction

Non-graphitic carbons (NGCs) are an important class of sp^2-based carbon materials, comprising a wide variety of ton-scale natural and synthetic carbons such as charcoal, activated carbon, glassy carbon, and soot, as well as research-oriented materials such as carbide-derived carbons (CDC). They also represent a promising and sustainable class of materials that are studied and applied in current research, industrial development, and commercial applications. The bulk material can be used for different electrical and low-friction applications [1–3], whereas the porous derivates and CDCs are used in gas storage/separation [4–8], as electrodes in sulfur–lithium-batteries [7,9,10] and supercapacitors [11–13], and as catalyst support [14,15]. Carbons made of phenol–formaldehyde resins (PF-R), the so-called glassy carbons, serve as containers in high-temperature applications [16] as they maintain a pronounced chemical resistance [17].

Per IUPAC definition [18], NGCs "are all varieties of solids consisting mainly of the element carbon with two-dimensional long-range order of the carbon atoms in planar hexagonal networks, but without any measurable crystallographic order in the third direction (*c*-direction) apart from more or less parallel stacking." Thus, NGCs are defined by characteristic features in wide-angle X-ray and neutron scattering. The general basic structure as well as typical wide-angle X-ray scattering (WAXS) data are shown in Figures 1 and 2, respectively.

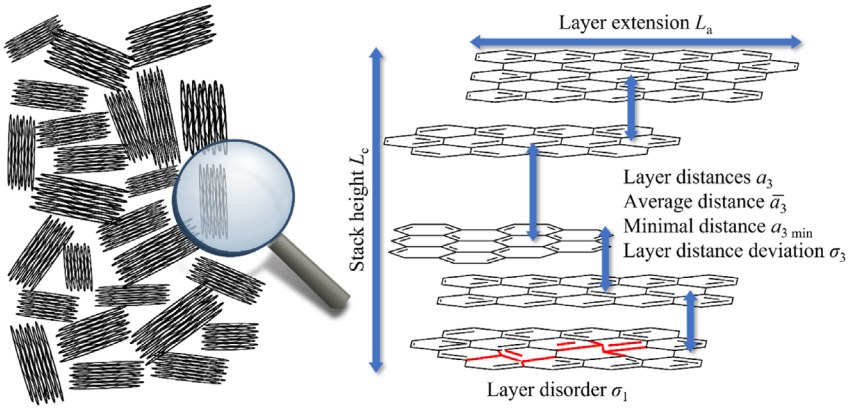

Figure 1. Sketch of the structural make-up of non-graphitic carbons (NGCs) containing a turbostratic stacking of graphenes. Detailed information about all parameters can be found in Section 2.2.

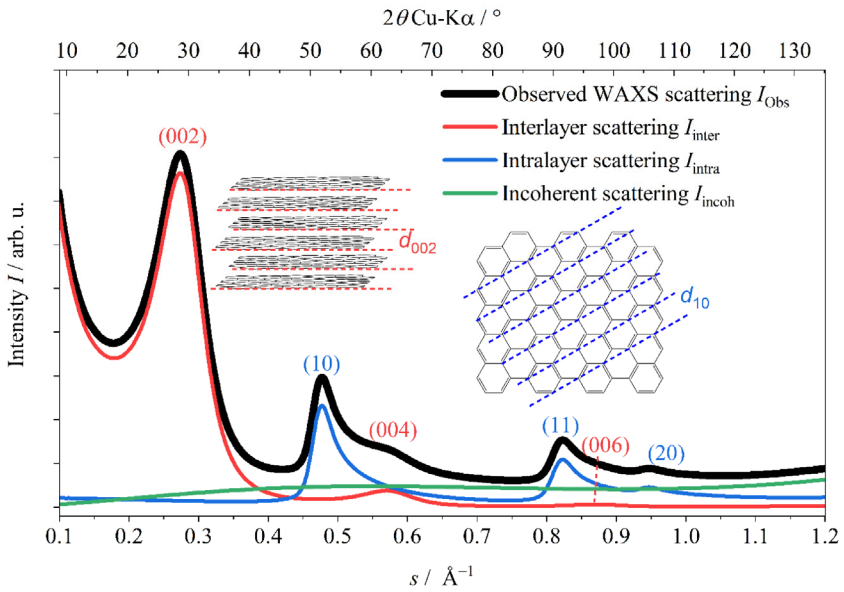

Figure 2. Representative example for an experimental wide-angle X-ray scattering (WAXS) data set of a NGC, which is given by a superposition of interlayer reflections (00*l*), asymmetric intralayer reflections (*hk*) and the incoherent scattering (I_{incoh}). s is the modules of the scattering vector ($s = 2/\lambda \cdot \sin(\theta)$). It should be noted that the indexing shown with parentheses, strictly speaking, denotes lattice planes, and that reflections would have to be indexed without parentheses. However, brackets are coherently used in this publication for both meanings, for improving readability.

Physical properties such as thermal and chemical resistance and electrical features are directly related to the microstructure of NGCs [2], the characterization of which is chal-

lenging. Electron microscopy (TEM, HRTEM) only reveals a small section of the sample. Hence, Raman spectroscopy and wide-angle X-ray/neutron scattering (WAXS/WANS) are commonly used to obtain quantitative structural parameters of NGCs. While Raman spectroscopy is mainly used to determine the average extension L_a of the graphene layers, WAXS/WANS allows for precisely determining a significant number of different structural parameters describing the NGC microstructure [19–28]. Recently, we discussed and compared the determination of L_a by these two methods, applied on a systematic series of carbons, and a procedure was presented for thorough characterization of NGCs based on Raman spectroscopy only [29,30].

However, in spite of the potential of refining WAXS/WANS data to determine the turbostratic microstructure of different carbon materials, the currently available software for the analysis of such data suffers from certain limitations. The most common approaches and their respective features (advantages and disadvantages) are summarized in the following.

CarbonXS introduced by Shi et al. featuring a corresponding graphical user interface (GUI) [31–33] is one of the most commonly used software tools. To the best of our knowledge, this program only allows to refine X-ray, but not neutron scattering data. In addition, *CarbonXS* uses a straightforward polynomial to account for the incoherent background, which however has no specific underlying physical model. Nevertheless, this approach is certainly useful and applicable to many different samples. The work of Fujimoto et al. [34–36] based on the approach of Warren and Bodenstein [37] is also only available for WAXS and not for WANS, and the software is currently not available in English [38]. The method of Saenko [39] uses the crystallite size as the only effect causing signal broadening, thus supposing that the material does not possess any disorder, which is not meaningful for NGC samples. The approach developed by Dopita et al. [40,41] uses MathWorks *Matlab* [42] as the programming language, which is a commercial software tool. In this approach, the graphite crystal structure is used as a model to refine the WAXS data, which is only meaningful for highly ordered carbon materials, but not for NGCs, because the turbostratic structure does not exhibit 3D periodicity. Ungár et al. also assume a 3-dimensional ordered hexagonal structure [43], which is only applicable to graphite-like materials, i.e., for high temperature-treated pitches but not for carbons with disorder in the graphene-based stacks. In 2002, Ruland and Smarsly introduced an evaluation method [44] based on the turbostratic structure of the NGCs and particularly takes into account the disorder of the layers and stacks to refine the WAXS data [44]. This model is used in *CarbX* [25], another software using a GUI, developed by our group, which currently does not allow for refining neutron scattering data either. Furthermore, it is only available for Microsoft Windows but not for other operation systems and needs Wolfram *Mathematica* [45] as backend for certain advanced mathematical calculations. Hence, by this option *CarbX*, it is not free of charge and also not entirely open-source. Furthermore, it so far suffers from a quite long calculation time up to multiple hours, especially for a larger number of measurement points. Hence, the approach by Ruland and Smarsly represents on one hand a reasonable structural make-up of NGCs but is on the other hand handicapped by the mathematical complexity of the underlying theoretical scattering functions.

Therefore, this study presents a first version of a script (*OctCarb*) for refining WAXS and WANS data on the basis of the approach introduced by Ruland and Smarsly [44], using GNU *Octave* [46] as free open-source software, which is under the GNU General Public License [47]. Although *Octave* does not feature an extended graphical user interface (GUI), there are important benefits by using *Octave*: *Octave* is completely free and open-source and available for different operating systems and it does not need any further software. It is also possible to compile *Octave* for MacOS and nearly all Linux distributions, and therefore *Octave* can also be used with most high-performance computing clusters. In addition to the automatic and GUI-based refinement, *OctCarb* can be modified and customized easily for special purposes. This makes the presented approach not only usable for users aiming at a straightforward refinement of WAXS/WANS data of NGCs in an automated fashion,

but also for advanced scientists and users, who would like to customize and optimize the whole refinement process for their individual needs.

In the following sections, the model of Ruland and Smarsly [44] is briefly summarized, and subsequently the implementation of *OctCarb* in *Octave* and its installation and operation will be explained in detail. The provided refinement method and structural parameters derived thereof are compared with published evaluations of WAXS/WANS data of previous studies. Additionally, a detailed description of the options for automatic and manual refinement and their advantages as well as the possibility to refine WANS data are provided. In particular, we describe criteria for a satisfactory analysis and provide video tutorials on how to refine WAXS/WANS data using GNU Octave.

2. Materials and Methods

In this section, first a brief description of the evaluation approach is given (2.1). In the second part, the microstructure parameters are explained (2.2), and in 2.3, an overview of the improvements using *Octave*/*OctCarb* is provided. In Section 2.4, technical details and the installation progress are explained.

2.1. WAXS/WANS of Non-Graphitic Carbons (NGCs)

The microstructure, i.e., the basic structure unit, of NGCs generally consists of two-dimensional sp^2-layers, e.g., graphene layers, that are stacked on top of each other (Figure 1). Since the stacks suffer from transitional and rotational disorder [48], NGCs do not exhibit three-dimensional crystallographic long-range order [44], which is equivalent to the IUPAC definition of NGCs [18]. In addition, the layer dimension and the C-C bond length, e.g., the sp^2-structure itself, exhibit non-uniformity (disorder) to be considered when analyzing the microstructure of NGCs. The resulting broad asymmetric (*hk*) reflections in the WAXS/WANS powder pattern, which are caused by the turbostratic structure [48,49], as well as the strong overlap of the signals, make the use of the full-width-at-half-maximum (FWHM) and in particular a Scherrer-type analysis [50] unsuitable to evaluate WAXS/WANS data [51]. Therefore, several approaches for fitting single (*hk*) [52–55] and (00*l*) [56] reflections were already developed more than 50 years ago. Yet, because of the pronounced overlapping, analyzing single (*hk*) or (00*l*) reflections [48,49] possesses inherent shortcomings. Shi et al. developed a software tool to refine the microstructure data of NGCs based on fitting the entire range of a WAXS curve [31]. In 2002, Ruland and Smarsly refined the profile functions for the (00*l*) and (*hk*) reflections and proposed a further developed approach to treat the complete WAXS curve of NGC powder materials [44]. This theoretical approach represents the basis for the *CarbX* software tool, which can be used to refine experimental WAXS data of powder materials and derive physically meaningful parameters [25]. It should be noted that the indexing shown with parentheses strictly denotes lattice planes, and reflections would have to be indexed without parentheses. However, brackets are used in this publication for both meanings, to improve readability.

Here, only a short summary of the used WAXS/WANS model [44] is given. A more detailed description can be found in previous studies [22,25]. In this approach, the normalized WAXS or WANS intensity in electron units per carbon atom ($I_{\mathrm{e.u.}}$) is modified by a normalization constant (k), the polarization (P) and an absorption factor (A):

$$I_{\mathrm{obs}} = k \cdot A \cdot P \cdot I_{\mathrm{e.u.}} \tag{1}$$

Note that the Lorentz factor is already considered in $I_{\mathrm{e.u.}}$ [44]. In addition, the reflections are usually so broad that the influence of device broadening is negligible. A more detailed description of all these correction parameters is given in the SI File (part B) in S16. I_{obs} is the observed (or theoretically calculated) wide-angle scattering, and $I_{\mathrm{e.u.}}$ contains the

coherent scattering I_{coh} originating from the NGC, and the incoherent scattering (I_{incoh}), which is assumed as modified Compton scattering of carbon ($I_{com,\,c}$):

$$I_{e.u.} = I_{coh} + I_{incoh} \tag{2}$$

The incoherent scattering (I_{incoh}) as well as the influence of foreign atoms (H, N, O, S) will be described in the SI File (part B) in section S14.

I_{coh} is given by the superposition of the scattering of the single graphenes (intralayer scattering I_{intra}; (hk) reflections) and the interferences of their stacking (interlayer scattering I_{inter}; (00l) reflections), modulated by the atomic form factor of carbon (f_c):

$$I_{coh,\,c} = {f_c}^2 \cdot (I_{inter} + I_{intra}) \tag{3}$$

It should be noted that this equation applies to both X-ray and neutron radiation, with only one important difference: while f_c features a specific course for X-ray radiation and needs to be suitably interpolated, it is a constant for neutron radiation. Hence, a fixed value of 1 can be assumed for f_c in case of WANS, since it is adjusted by the normalization constant k anyway. I_{coh} can also be expanded to include the concentration of foreign atoms such as hydrogen (c_H), nitrogen (c_N), oxygen (c_O), sulfur (c_S) and non-organized carbon (c_{un}), following the works of Franklin [57,58]. In addition, an anisotropy factor (Δ_{an}) for the different atomic form factors parallel ($f_{c,\,perp}$) and perpendicular ($f_{c,\,perp}$) to the layers can be considered [25,44]. For the proportion of scattering that results from "non-organized" carbon [44], the following equation applies:

$$I_{e.u.,\,c}\,(\text{WAXS}) = (I_{coh,\,c} + I_{incoh,\,c}) = (1 - c_{un}) \cdot (f^2_{c,\,perp} \cdot I_{inter} + f^2_{c,\,para} \cdot I_{intra}) + c_{un} \cdot f^2_{c,\,para} + I_{com,\,c} \cdot recoil \cdot Q_{abs} \cdot Q \tag{4}$$

$$\begin{aligned} I_{e.u.,\,c}\,(\text{WANS}) = (I_{coh,\,c} + I_{incoh,\,c}) &= (1 - c_{un}) \cdot (f^2_c \cdot I_{inter} + f^2_c \cdot I_{intra}) + c_{un} \cdot f^2_c + I_{incoh,\,c} \\ &= a \cdot (I_{inter} + I_{intra}) + b(s) \end{aligned} \tag{5}$$

Note that (4) holds for WAXS, while (5) is valid for WANS. In (4), $f_{c,\,para}$ is used because the difference between $f_{c,\,para}$ and $f_{c,\,perp}$ is very small, and therefore, it is more practical to use this atomic form factor instead introducing a third (mixed) atomic form factor, which would also have no significant effect on the result. a in (5) is a normalization factor constant, which is included in the scaling factor k in equation (6), and b is a non-constant background. Hence, for WANS equation (5) is applied, separating the coherent and incoherent background b(s) differently compared with WAXS (see S19 in the SI File (part B)).

Regarding experimental effects additional multiplicative factors considering a fixed irradiated length or a fixed divergence slit ($AutoColl$), an exponential damping factor ($gFact$) for taking the possibility of a small-angle scattering contribution at low s values, and two constants ($const_1$, $const_2$) for considering a non-linear background, can be used to adapt the calculated WAXS/WANS pattern (I_{obs}) to a particular instrumental setup:

$$I_{obs} = 10\hat{}[\log_{10}((1/AutoColl) \cdot gFact \cdot k \cdot A \cdot P \cdot (I_{e.u.})) + const_1) + const_2] \tag{6}$$

This logarithmic representation was used as we found that the fitting refinement worked more reliably. The subsequent exponentiation was used to obtain the correct (measured) intensities. In principle, this equation contains all factors entering the theoretical WAXS/WANS, especially the impact of the device and background scattering. Further information about these parameters, their calculation and their background can be found in the SI File (part B) in S16 and in the SI of previous works [25,44].

2.2. Refined Microstructural Parameters

The physically meaningful microstructure parameters can be distinguished into three sets: layer structure, stacking structure and impurities. A more detailed overview of all

parameters including the microstructure parameters as well as the parameters used by *OctCarb* is given in the SI File (part A) in S1.

2.2.1. Layer Structure

In our approach, the most important parameters for describing the layer structure, i.e., also the intralayer scattering, are the average layer extension (L_a), its polydispersity (κ_a), the average C-C bond length (l_{cc}) and disorder in the layers (i.e., stress and strain) (σ_1), see (Ruland & Smarsly, 2002), Table 1.

Table 1. Microstructure parameters describing the layer structure. Note that L_a, l_m and κ_a are mathematically dependent on each other and calculated from a gamma distribution with the shape factors ν and α.

Parameter	Description	Explanation
L_a	Average graphene layer size	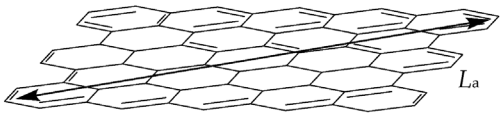
l_m κ_a	Average chord length of layers Polydispersity of layers	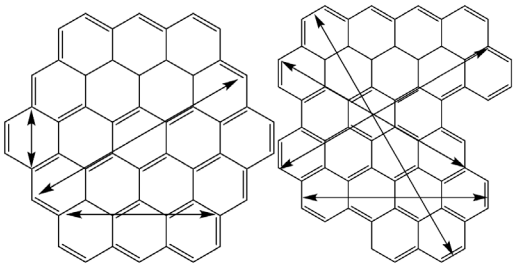
l_{cc} σ_1	Average C-C bond length Intralayer disorder	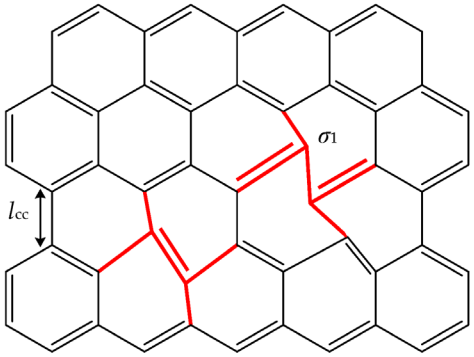

Adapted from Faber et al. [21].

2.2.2. Interlayer Stacking Structure

Analogous to the intralayer parameters, an average stacking height (L_c), its polydispersity (κ_c), an average layer distance ($\overline{a_3}$) and the standard deviation (σ_3) can be defined for describing the interlayer stacking. In addition, the minimal layer distance ($a_{3\,min} = \overline{a_3} - d a_3$), the average number of graphene layers per stack ($N = L_c/\overline{a_3}$) and the homogeneity of the stacks (η) are physically meaningful parameters [44]. Additionally, the thermal motion (u_3), i.e., in principle the Debye–Waller factor, and the anisotropy of the atomic

form factor of carbon (Δ_{an}) can be refined but have in most cases only a small influence on the analysis. The preferred orientation parameter (q) might also be refined, it also depends on the experimental setup, Table 2.

Table 2. Microstructural parameters describing the graphene stacking (interlayer scattering I_{inter}). L_c, κ_c and N are mathematically dependent on each other and calculated from a gamma distribution $n(N)$. N being the number of layers per stack, with the parameters μ and β [44] and is also dependent on $\overline{a_3}$.

Parameter	Description	Explanation
L_c κ_c	Average stack height Polydispersity of stack height	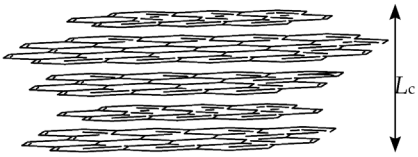
$\overline{a_3}$ $a_{3\,\min}$ σ_3 N	Average layer distance Minimal layer distance Standard deviation of layer distances Average number of layers per Stack	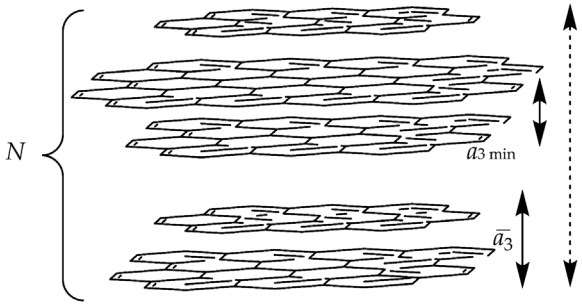
η	Homogeneity of the stacks	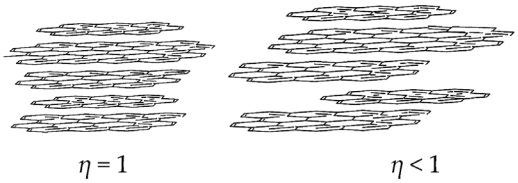
q	Preferred orientation	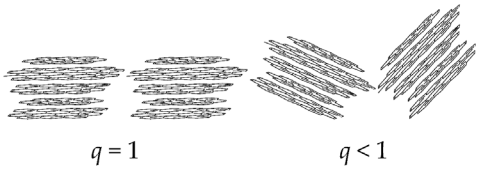
Δ_{an}	Anisotropy for the atomic form factor of carbon	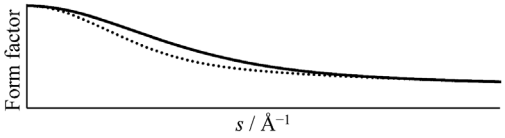

Adapted from Faber et al. [21].

2.2.3. Impurities

In addition to the microstructural parameters related to I_{coh}, the concentration of disordered sp^3 carbon (c_{un}) and the concentration of disordered hydrogen (c_H), nitrogen (c_N), oxygen (c_O) and sulfur (c_S) can also be considered, which might be needed to evaluate WAXS data in terms of the background scattering. However, especially for hydrogen in a WANS experiment, this approach is insufficient. For $c_H > 0.5\%$ a Voigt-function showed satisfactory results to determine the background of WANS data as shown in the SI File (part B) in S19, Table 3.

Table 3. NGCs can contain non-organized carbon (sp^3 hybridized) or foreign atoms (e.g., H, N, O, S). It must be assumed that these atoms are also non-organized and cause only background scattering.

Parameter	Description	Explanation
c_{un}	Concentration of unorganized carbon	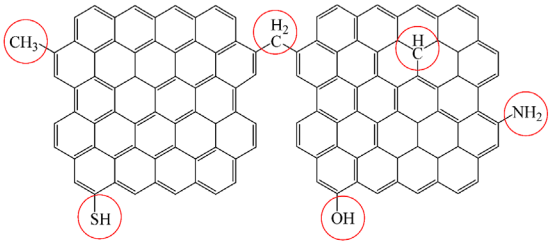
c_H	Concentration of unorganized hydrogen	
c_N	Concentration of unorganized nitrogen	
c_O	Concentration of unorganized oxygen	
c_S	Concentration of unorganized sulfur	

Adapted from Faber et al. [21].

2.3. Improvements and Implementation in OctCarb

The Ruland and Smarsly approach [44] as used by Pfaff et al. [25] can be implemented in different programming languages. At the current state, it is implemented in the tool *CarbX*, based on C++ and Wolfram *Mathematica* [25]. Here, in *OctCarb* we modified the refinement routine used in *CarbX* for several reasons. First, in *CarbX* external files were needed for the computation of the atomic form factors and incoherent scattering. In detail, published values for the atomic form factors and the incoherent scattering (WAXS) were tabulated in a text file, which was read during the refinement, and the in-between values needed to be interpolated. As a shortcoming, the necessary interpolation was time-inefficient, and the values could not be calculated outside the range of the tabulated values. For this reason, here the atomic form factors for nitrogen (f_N) and oxygen (f_O) as well as the Compton scattering of carbon ($I_{com,C}$) were fitted by suitable spline functions and could then be calculated with an analytical function. Moreover, for carbon (including the form factor anisotropy Δ_{an} ($f_{c,para}$)), the approximation function for calculating the atomic form factor (f_c) was improved, being closer to the theoretical values given in [59]. A more detailed description of these parameters can be found in the SI File (part B) S14. Additionally, in *CarbX* the atomic form factor of carbon is not correct for high s values ($s > 3$ Å^{-1}). For Cu-K$_\alpha$ radiation, this shortcoming is irrelevant, since the maximum value is $s_{max} \approx 1.2$ Å^{-1}. However, for small wavelengths ($\lambda < 0.5$ Å), another interpolation function has to be used [59] to calculate the correct atomic form factor for higher values of s to make it suitable also for synchrotron experiments with small wavelengths.

Second, in *OctCarb* two additional parameters were added for the ability to consider the concentrations of non-organized hydrogen (c_H) and sulfur (c_S) atoms, in addition to nitrogen and oxygen. Similarly, it was assumed that hydrogen and sulfur are spatially statistically distributed and contribute only by diffuse scattering. Third, separately calculating the coherent or the incoherent scattering is another improvement, which might be a useful feature to judge the order of the graphenes themselves and the impact of background. Another difference in the code used in this study compared with Pfaff et al. [25] is the

implementation of ν, which together with α serves for modeling the intralayer scattering I_{intra}. Since this is a very special feature, it is described in the SI File (part B) in S15.

Advancements in computing:

- *OctCarb* is an entirely free software tool, also with respect to automatic data fitting;
- The data analysis can be performed on average personal computers, i.e., the analysis of one WAXS/WANS curve can be performed within a satisfactory time, i.e., within minutes;
- The tool is resource-efficient in terms of CPU usage, which means that other programs can be run simultaneously;
- *Octave* and therefore *OctCarb* is available for Windows, MacOS and Linux;
- *Octave* provides an option for batch compilation (important for parallel data fitting);
- The program is—in practical details—more convenient than *CarbX*, e.g., the fitting results (parameters) are now automatically stored;
- No other third-party software tool is needed.

Advancements in the structural characterization based on WAXS/WANS:

- Wide-angle neutron scattering data can be analyzed;
- A rigorous background treatment (and fitting) for WAXS and WANS, based on the corresponding theoretical contributions (Compton scattering, non-organized carbon, etc.), is included;
- The treatment of impurity atoms (sulfur, nitrogen, etc.) in terms of a contribution to the background scattering was improved;
- The incorporation/treatment of the atomic form factors was optimized;
- The statistical, experimental errors are treated in terms of the well-established theory of error propagation, and calculated based on the covariance matrix, i.e., the standard deviations of the refined parameters are calculated;
- In some cases, the data at the left and right end of the accessible data range are not useable, e.g., because of strong small-angle scattering contributions. The tool contains a comfortable option to skip such data.

2.4. Technical Details and Installation

GNU *Octave* is a free and open-source software that was "originally intended to be companion software for an undergraduate-level textbook on chemical reactor design written by James B. Rawlings of the University of Wisconsin-Madison and John G. Ekerdt of the University of Texas" [60]. Meanwhile, *Octave* is a high-end software for solving mathematical problems in an analytical and/or numerical way. A script language is used to define and perform the needed calculations. The scripts are comparable and compatible with the commercial software *MatLab* from MathWorks [42]. While *Octave* is pre-compiled for Microsoft Windows, it can be also installed or compiled for MacOS, nearly all Linux distributions such as *Debian*, *Ubuntu*, or *CentOS*, and distribution-independent software such as *Docker* or *Flatpak*; in principle, *Octave* can also be compiled for *Android* or *BSD* systems. Overall, *Octave* can be used for nearly all operating systems and hardware. System requirements and links for downloading and instructions for compiling are in the next sections.

2.4.1. Third-Party Plugins

Even if GNU *Octave* has already included a lot of mathematical functions and operations, it can be extended by several plugins. For the present purposes of refining a theoretical function to measured data points, the *optim* package is needed to perform all mathematical operations. Generally, if the *Octave-GUI* is used, all other dependencies, which in turn are required for the use of *optim*, are automatically installed. If the *Octave-CLI* (command line interface) is used, all other dependencies, which in turn are required for the use of *optim*, might be installed manually. Hence, *struct* and *statistics* (which need *io* itself) must be installed before installing *optim*.

2.4.2. Refinement Algorithm

In the *optim* package, different algorithms for optimization, data fitting and data refinement are available. However, taking a look at the source code, most of these functions use the Levenberg–Marquardt algorithm developed for non-linear refinement [61–63]. In this work, the function *nonlin_curvefit* is applied for the refinement since it can be used with additional refinement parameters such as the weighting of the points or minimum and maximum values of the structure parameters. In addition, the function *curvefit_stat* is used to obtain additional statistical information such as the accuracy of the fit and standard deviations of the refined parameters.

2.4.3. System Requirements and Installation

Overall, there are no special system requirements for installing and using *Octave*. Since the calculations can take a long time, especially with large data sets, at least 4 GB RAM and a fast CPU (speed per core) are recommended, but not essential. The refinement was also tested with a Raspberry Pi running *Linux Raspbian* (Based on *Debian Bullseye*), and although it takes more time than on a "classic" tower PC, it does work. However, *Octave* only uses one CPU core by default, so that the computing speed per core is crucial for the total computing time. In the end, calculations can also be performed on high-performance computing clusters under Linux.

To use the *iObs* algorithm in C++ or to compile an *.oct file by your own, the "numerical recipes in C" as a third-party library is needed. Since this product is only commercially and not open-source available, the needed files cannot be shared as SI and must be purchased instead [64].

An instruction including a video explaining the installations and initial setups is available in the SI File (part A) in S8, in the GitHub (https://github.com/osswaldo/NGCs/tree/master/Instruction%20Videos (accessed on 2 November 2022)) and at YouTube (English: https://www.youtube.com/playlist?list=PLTlnYDX5g1FylWfH8cSM_ZQUQpn3dSp6M (accessed on 2 November 2022)), (German: https://www.youtube.com/playlist?list=PLTlnYDX5g1FwaOQkLXTxrpvHW9CRUwBrk (accessed on 2 November 2022)).

3. Results

3.1. Usage of OctCarb

To use *OctCarb* for the refinement of the WAXS/WANS data of non-graphitic carbons, first *Octave* and the *optim* package must be installed. During the installation of *Octave*, the chosen installation path should not contain empty spaces (" "), otherwise, problems during the installation of the *optim* package might occur. For example, a safe path would be "C:/Octave/Octave-6.3.0". Next, the *iObs.oct* file must be downloaded (or self-compiled) as described in the SI File (part A) in S7 and in the GitHub (https://github.com/osswaldo/NGCs/tree/master/Octave/oct-files (accessed on 2 November 2022)). Third, the file *FitRoutine.m* must be downloaded and modified for the required purpose, e.g., with respect to the sample name and measurement data path. An example for starting the algorithm and the operations can be found in the "Excerpt from GitHub" (SI). After opening *Octave*, the example script can be loaded either using *File* → *Open* or the shortcut in the upper toolbar. In Figure 3, the basic graphical user interface (GUI), and in Figure 4, the results of a typical refinement using *OctCarb* are shown: In addition to the microstructure parameters in text form, *Octave/OctCarb* plots the experimental data, the refined fitting curve as well as their deviation, and saves all these data in a CSV file.

If you have never worked with *Octave* so far, it is highly recommended to watch an instruction video. Due to the high distribution and availability of *Octave*, there are a lot of instruction videos available, e.g., under YouTube (https://www.youtube.com/watch?v=sHGqwF2s-tM (accessed on 2 November 2022)). For this reason, no further basic instruction into *Octave* is given here. More details about the installation and setup as well as the typical refinement steps including an exemplary refinement can be found in the SI File (part A) in

section S9. Additionally, a detailed tutorial for the fitting of WAXS/WANS data of NGCs with pictures for every step can be found in the SI File (part A) in S9.

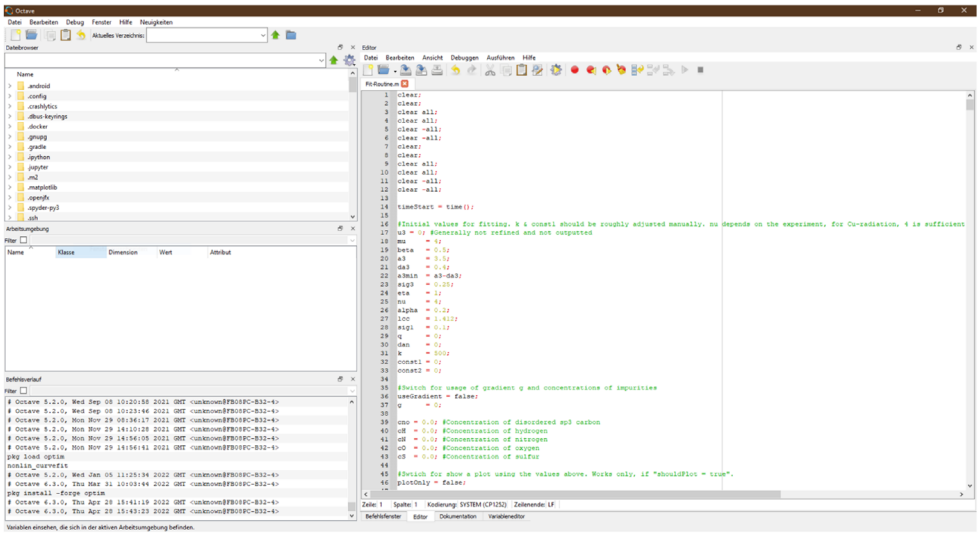

Figure 3. Main graphical user interface (GUI) of *Octave* and the *OctCarb* refinement script (main window). On the top bar, the *Octave* files (*.m) can be opened and saved, and various windows can be activated and deactivated. On the left side, the current working directory can be changed, and the currently used variables and executed commands are shown. On the lower side, one can switch between the *Command Window* (e.g., the *Octave* Command User Interface), the *Editor* (to edit the script files) and the *Variable Editor* and *Documentation*.

3.2. Verification and Application

In general, nonlinear fitting procedures, as used in our *Octave*-based refinement, can suffer from various complications, e.g., a reasonable fitting might be achieved by different sets of the parameter values. Hence, in *OctCarb* particular emphasis was put on the validity of the refinement and the structural parameters obtained thereof. First, we demonstrated the general functionality of *OctCarb* for refining typical WAXS data (3.2.1). In 3.2.2, the impact of data noise and the number of data points are discussed. Validation was performed by applying *OctCarb* on the same WAXS and WANS data as previously published, comparing the fits and the parameter values (3.2.3) [19,23,25,26]. Second, in order to perform a self-consistency test, theoretical WAXS/WANS data were computed and artificially blurred with different levels of data noise (3.2.4). These "new experimental" data were then used as input for *OctCarb* to verify if the fitting algorithm yields the original parameters. All fit results/microstructure parameters including the standard deviation as well as exemplary calculation times can be found in Table S2.

Figure 5 shows an exemplary WAXS pattern and a reasonable fitting result, proving the applicability of *OctCarb* to typical experimental data. However, in some cases a refinement might not fit the data over the entire range of WAXS/WANS data, in particular with respect to two issues, namely, the course of the data curve at small s and the background scattering. Yet we found that a meaningful and precise determination of the main structural parameters such as the average stack height (L_c) or the average layer extension (L_a) does not require a reasonable fitting of the entire data set, i.e., a deviation between the data and the fitting function in certain parts is tolerable. Figure 5 highlights the importance of the

various parts along the *s*-axis in assessing the quality of a fitting, which is valid for most samples studied. In plain terms: even if the red regions (Figure 5) are not well fitted, still the structural parameters are reliably determined. On the other side, the green regions must be well fitted in order to obtain reliable and meaningful parameter values.

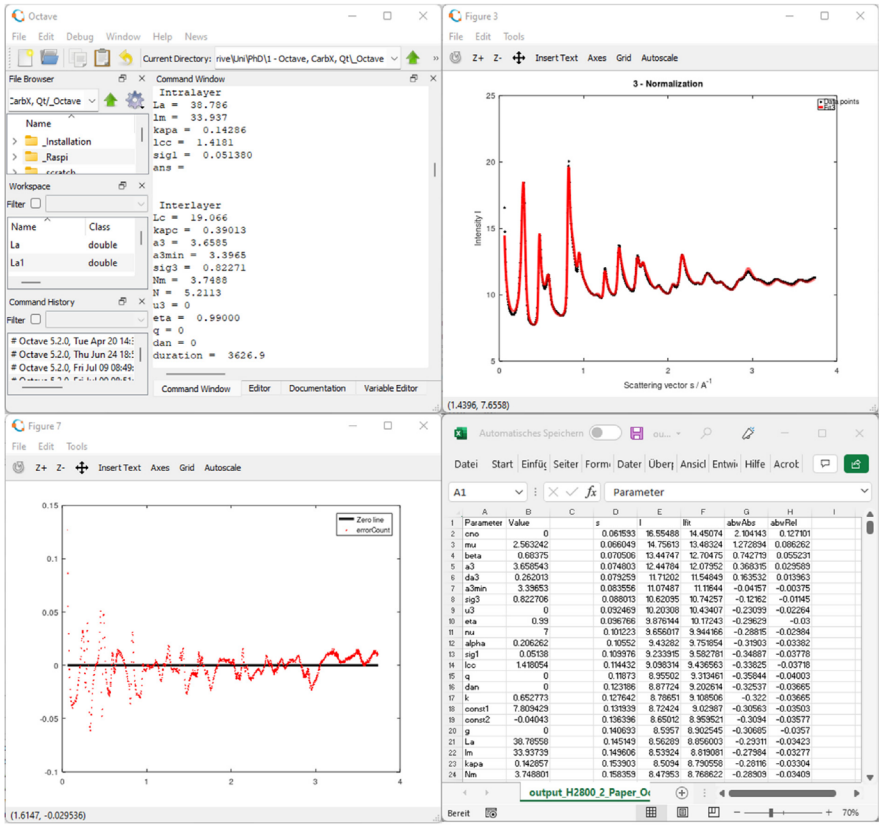

Figure 4. Results of the wide-angle neutron scattering (WANS) refinement using *OctCarb* (upper left): In addition to the microstructural parameters in text form categorized by interlayer and intralayer parameters, *Octave* plots the measurement data and the fit as well as the deviation, and saves all in a CSV file.

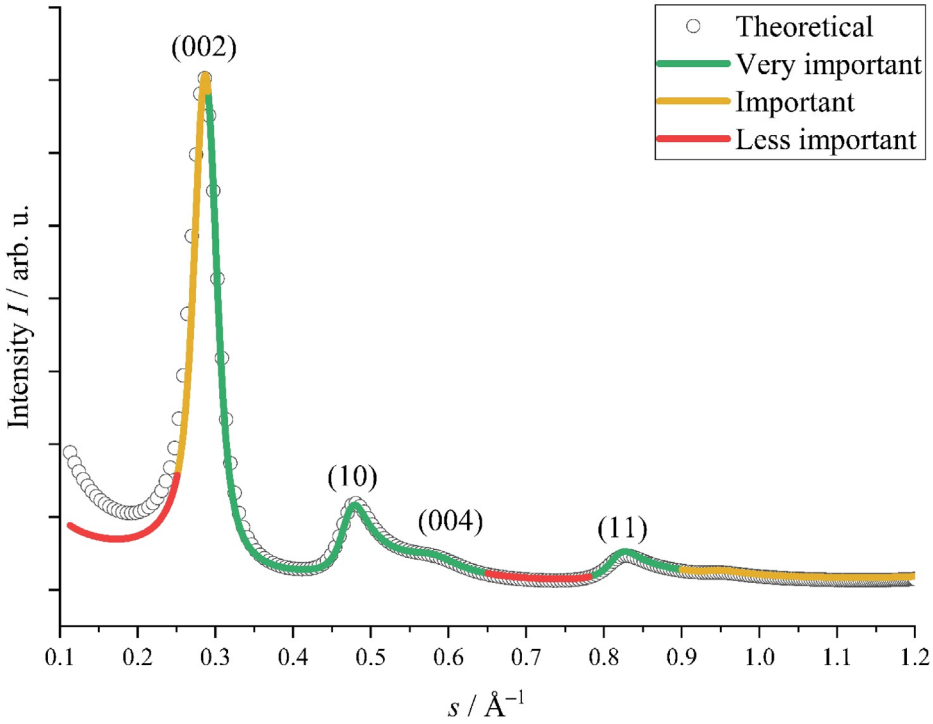

Figure 5. Theoretical WAXS data of NGCs and a typical, reasonable fit. Green: Most important regions for fitting, which are strongly influenced by the NGC microstructural parameters. These parts must be refined as well as possible. Based on our experience, the yellow regions are significantly influenced by foreign atoms, the measurement geometry and factors contributing to the incoherent scattering. Overall, the green regions should have a higher priority in judging the quality of a fitting result. While micropores influence the lower *s*-range of the red region, the range around $s = 0.7$ Å^{-1} can be influenced by amorphous carbon with a bond length of around $d_{C\text{-}C} \sim 1.42$ Å and $s_{C\text{-}C} = 1/d_{c\text{-}c} \sim 0.7$ Å. As another point, only low amounts (<5–10%) of unorganized carbon or foreign atoms such as nitrogen or oxygen can be considered well by the present model. Higher amounts can significantly influence the data at lower values of *s*, e.g., the red region. Our approach cannot model such higher concentrations of impurities, as it assumes that these atoms are isolated and show no mutual correlation in their position. Hence, a reasonable fitting of these specific regions might be impossible using *OctCarb* because these additive scattering contributions are not considered by our approach.

3.2.1. Software Validation on WAXS Data and General Issues

Octave and thus also *OctCarb* use the Levenberg–Marquardt non-linear fitting algorithm to perform the refinement ("fitting"). In *CarbX*, in the standard mode, a manual modeling of the WAXS data is performed, using a qualitative criterion in the form of a reasonable fit upon parameter variation, as determined by visual perception. In contrast, as a main advantage, *OctCarb* provides the values of the structural parameters and the calculation of their error bars based on a well-defined mathematical procedure, using the covariance matrix. A more detailed discussion of the refinement procedure, especially the determination of the error bars, is found in the SI File (part A) in Section S3.

For the verification of the refinement method using *OctCarb*, four WAXS data sets were used, taken from Faber et al. [22], i.e., a coal tar pitch carbonized at 800 °C (CTP-800), an activated carbon (AC Type H), a carbonized furfuryl alcohol treated at 850 °C (FA-850) and a poly(ionic liquid)-derived carbon fiber (PIL) from Einert et al. [65]. These samples were chosen since they were already used in the study of Pfaff et al. [25] for the verification of *CarbX*, our previously introduced software tool used for the evaluation of WAXS data of NGCs (Figures 6 and S1). Indeed, *OctCarb* is also able to achieve a reasonable fitting, showing the applicability to typical experimental WAXS data (Figures 6 and S1). The resulting parameters for the aforementioned samples, in comparison to the modelling by *CarbX*, are found in the SI File (part A) in Table S3.

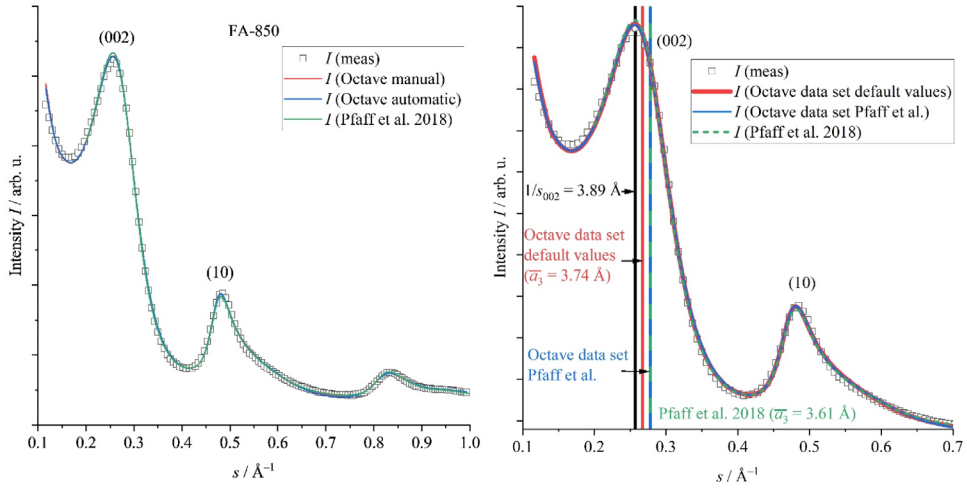

Figure 6. Validation of *OctCarb* using WAXS data of FA-850 (furfuryl alcohol-based carbon). Automatic refinements using different starting parameters were performed in order to analyze the impact of the initial values on the final fitting result during the non-linear fitting procedures. **Green**: Final refinement of Pfaff et al. [25]: red: automatic fitting by *OctCarb* using the refined microstructural values from Pfaff et al. [25] as initial parameters (*Octave data set* Pfaff et al. see Figure S1), blue: automatic fit with our default starting parameters as described in the SI File (part A) in Table S7 (*Octave data set default values*, see Figure S1). A first analysis using the already refined microstructure parameters from Pfaff et al. [25] served to validate if the general refinement works in principle and leads to comparable results. The second analysis using the default starting parameters aimed to validate if the numerical refinement/minimalization of *OctCarb* works well and leads to the same (or similar) results. These default starting values are in principle means of the aforementioned structural parameters of common NGCs. Additionally, in this study and in the model of Ruland and Smarsly [44], $\overline{a_3}$ is defined as the mean value of the layer distances, whereas calculating the average layer distance by $1/s_{(002)}$ does not provide a mean, but the modal value. Therefore, these values are different, and in conclusion, an average layer distance $\overline{a_3}$ (mean) can only be calculated by a refinement of the whole (002) reflection and not only from the position of the maximum. Note: only every second measurement point is shown for better visibility. For plots of the other samples, see Figure S1 in the SI File (part A).

Overall, the automized non-linear fitting algorithm of *Octave/OctCarb* provides reasonable fitting for all samples over the entire range of the dataset (Figures 6 and S1), which corresponds to a standard XRD setup with Cu-K_α wavelength. We would like to emphasize that *OctCarb* performs the fitting in a fully automated fashion, with a significant number

(typically 12) of structural parameters typically being fitted: the average and minimal layer distance, its standard deviation and polydispersity (a_3, $a_{3\,min}$, σ_3 & κ_c), the average stack height and the number of layers per stack (L_c & N), the homogeneity of the stacks (η), the average C-C bond length (l_{cc}), the average layer extension, and the disorder and polydispersity of it (L_a, σ_1 & κ_a) and a possible preferred orientation (q) are usually varied and, hence, obtained in a mathematical refinement algorithm.

The resulting parameters of fitting using *OctCarb* are in the same range as in the reference studies [25,26]; thus, both approaches provide reasonable results. However, for several of the parameters the deviation can be up to 20% (see L_a, L_c, for sample FA-850, Figure 6 and Table S3). Based on the systematic fitting in *Octave*, we consider the *OctCarb*-derived values more reliable.

In detail, we now compare the evaluation of WAXS data by *Octave* and the study of Pfaff et al. [25] by the closer inspection of the sample FA-850 as an exemplary case (Figure 6). As already mentioned, there are significant differences in the resulting parameters (Table S3), which can be correlated to the quality of the fit in this case. The fitting curve of Pfaff et al. [25] is shifted slightly, but systematically to higher intensities than the data points in the region of the (002) reflection, and a little lower in the range of the (10) reflection (Figure 6), which might explain the significant differences seen in L_a and L_c. By contrast, fitting by *OctCarb* provides an almost perfect fit in these regions, demonstrating the superiority of a rigorous mathematical fitting algorithm.

Here, we would also like to take this example to illustrate that a simple analysis generates misleading values for structural parameters: calculating the average layer distance ($\overline{a_3}$) simply by $a_3 = 1/s_{(002)}$ yields about 3.9 Å. However, this calculation ignores the variation of a_3, which is taken into consideration by Ruland and Smarsly (2002), providing $\overline{a_3}$ ~ 3.6 Å (Pfaff et al. [25]) and $\overline{a_3}$ ~ 3.75 Å (*OctCarb*), which are quite disparate from the simple calculation "$\overline{a_3} = 1/s_{(002)}$". Even if the absolute difference in these two values is only 0.15 Å (4%), it must be considered that for structural reasons, $\overline{a_3}$ lies normally in the range of 3.3 Å up to 4.0 Å (in some cases also lower or higher), and therefore, 0.15 Å is a significant difference. More precisely, 3.6 Å is much closer to the theoretical layer distance of perfect graphite (3.35 Å) [66,67] and could therefore lead to the false assumption that the stacks are more highly ordered as they actually are.

This example underlines the necessity for using advanced evaluation and software for WAXS/WANS data of NGCs, especially when physical properties should be related to the microstructure data (for example Li-intercalation properties/possibility in batteries). Only systematic refinement can lead to precise microstructural data and thus to meaningful interpretation in regard to physical properties.

3.2.2. Influence of the Amount/Noise of Data Points and Start Parameters on the Fitting Routine

Generally, the influence of the number of data points and the noise must be considered in a differentiated manner. Evidently, data noise should be as low as possible, especially for the parts of low scattering intensities in a WAXS/WANS curve. Further information about this feature and the general influence of the amount/noise of data points and start parameters on the fitting routine can be found in the SI File (part A) in S11.

3.2.3. Software Validation Using WANS Data

For testing the functionality of *OctCarb* for WANS data, we applied it to the WANS data published by Pfaff et al. [26]. Two different classes of carbons had been studied, namely carbon obtained from phenol formaldehyde resorcinol (PF-R) and heat-treated at 2100 °C and 2800 °C (H-2100/H-2800), and a low-softening point pitch heat-treated at 1200 °C (LSPP-1200). These samples were chosen to determine whether *OctCarb* is able to depict fine differences from high-quality WANS data in the structural parameters upon treating at temperatures close to graphitization, as well as a function of the precursor. The WANS data were acquired at the E2 flat-cone diffractometer at the BER II reactor of Helmholtz-Zentrum

Berlin using a Debye–Scherrer geometry [68]. The refinement by *OctCarb* uses the default starting parameters from Table S7 in the SI File (part A) and the normalization based on absolute WANS intensities.

It is seen (Figure 7) that an excellent refinement is obtained by *OctCarb* for all of these chemically quite different samples, also taking into account that the s range is significantly larger (three times) than the WAXS data obtained with a typical lab setup (Cu-K_α). Based on this exceptional functional capability of *OctCarb*, in the following, we compare the refinement of these samples with the previous analysis [25] with respect to the reliability and validity in determining the relevant structural parameters (L_a, σ_3, ...).

In general, the relative error for each parameter is in the range of 10–15% for a manual refinement [25], while for the automatic refinement (*OctCarb*), the errors for each parameter are smaller, on the order of 5% (see Table S5). Overall, all mean parameters refined using *OctCarb* fit well to the values already determined by Pfaff et al. [26], except for L_a and σ_3 for LSPP-1200, which is caused by a poor refinement of the (004)-reflection (Figure 7). Here, a manual parameter variation allowed for a better data refinement, which will be explained below. In case of H-2800, the agreement in the values is excellent, showing that the excellent fitting of WANS data spanning a large range of s yields meaningful structural information. An interesting feature is seen for sample H-2100: the *OctCarb* fit yields a lower value for σ_1 compared with Pfaff et al. [26], and at the same time, the average layer size (L_a) is also lower. Since a smaller degree of disorder correlates in principle with sharper reflections and, on the other hand, a smaller layer L_a to a broadening of (hk) reflections, the two effects can possibly cancel out each other in the fitting.

Notably, for both H-2100 and LSPP-1200, the (004) reflection is quite broad and thus appears only as a "shoulder" of the (10) reflection, which the automatic fitting routine of *OctCarb* is not able to handle appropriately. This undesired fitting behavior can be understood in terms of the underlying fitting algorithm: *OctCarb* tries to fit the entire scattering curve, containing various single reflections. The region around the (004)-reflection is comparably small and therefore a relative unimportant part in its relevance for the fitting process. The feet/valleys right and left in the vicinity of the (10)/(004) reflections are well fitted by *OctCarb* using the automatic refinement, since overall, there are a lot more relevant data points available for this range than for the (004) reflection, so that *Octave* (i.e., the Levenberg–Marquardt algorithm) weights these feet/valleys higher than the (004) reflection itself. On the other hand, these feet/valleys cannot be well fitted by the manual refinement, if the (004) reflection is well fitted manually. Thus, in such cases, one has to compromise, which part of the WAXS/WANS curve is considered more relevant for the analysis. This example illustrates that in the end, it is up to the user to set priorities with regard to the quality of the fit and how to deal with a potential discrepancy between automatic (purely mathematical) and manual (experience-based) refinement. More details about such cases, i.e., fitting the parts of a scattering curve, can be found in the SI File (part A) in S6.

In order to establish a reasonable fitting for the (004) reflection, the WANS data of the low-softening-point pitch sample LSPP-1200 were refined manually in *OctCarb* after the automatic refinement. Here, "manual refinement" means that after the automatic refinement, the resulting parameters were variated manually, and the quality of the fit was judged by the user. Overall, it can be concluded that WANS data can be well refined and evaluated using *Octave* in combination with the model of Ruland and Smarsly [44] to obtain meaningful microstructural parameters of NGC.

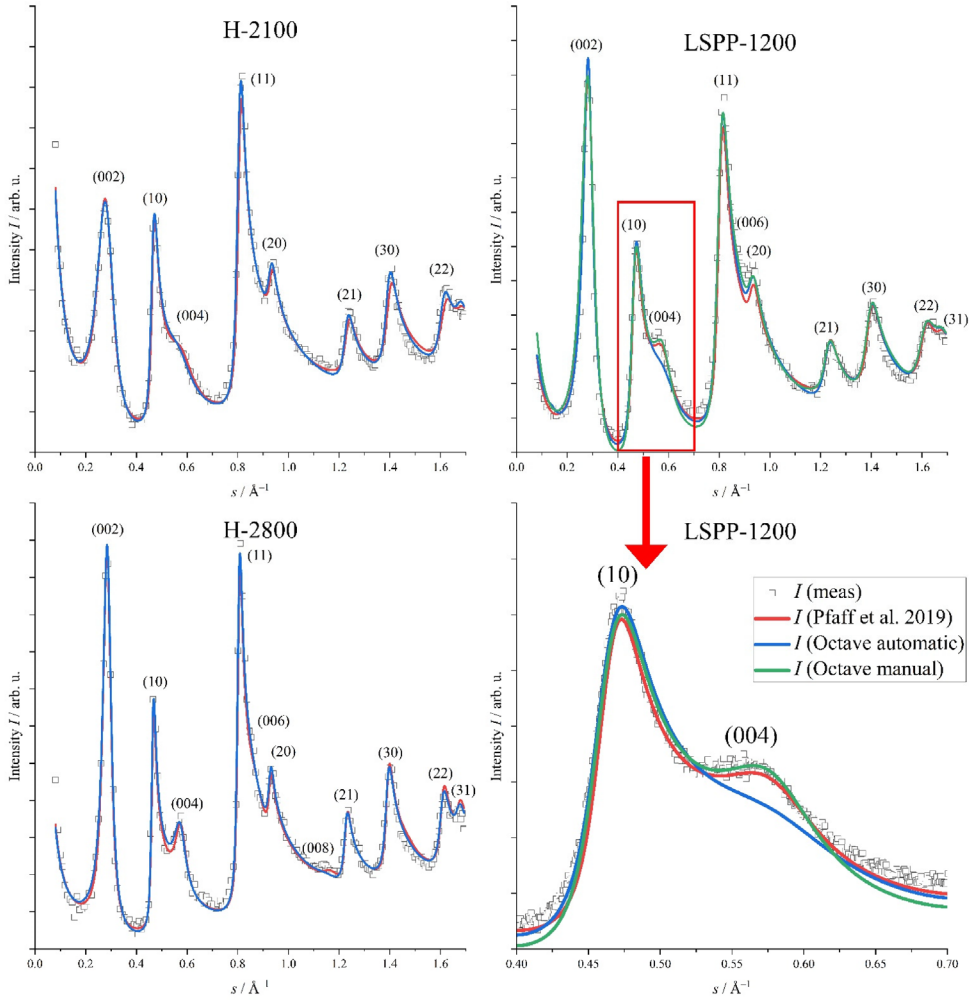

Figure 7. Refinement of previously reported wide-angle neutron scattering (WANS) data by Pfaff et al. [26]. The measured WANS data (black; every 10th point (except for the last plot)) were fitted automatically (red) and the result manually refined (blue). For H-2800, no manual refinement was needed. For LSPP-1200, the interlayer parameters had to be adjusted to fit better the (004) reflection.

3.2.4. Noise Level Test on WAXS and WANS Data

For the noise level test, common average WAXS/WANS patterns were simulated, and the simulated points were noised by a random Gaussian deviation with a standard deviation of σ_{noise} = 0.05. For WAXS, in addition to the coherent scattering (I_{coh}), the incoherent scattering (I_{incoh}) was simulated analytically, where for WANS, only I_{coh} was calculated. Both the unperturbed data (absence of noise) and the noised WAXS/WANS data were refined using *OctCarb* as an automatic fit. Table 4 summarizes the input values

for the data simulation and the resulting parameters using the automatic fit function. In Figure 8, the blurred WAXS and WANS data as well as the refinements for the perfect data (blue) and the noisy data (red) are shown. Overall, the fitting as well as the individual parameters are very close to the initial data for both, the unperturbed and the noisy data. This excellent match means that the refinement leads to reliable fitting parameters also for noisy data, and thus the structural parameters obtained from the fitting routine can be considered meaningful.

Table 4. Overview of the refinement of simulated WAXS data, which were blurred by statistical noise generated by a Gaussian distribution. The results indicate that *OctCarb* can evaluate reproducibly microstructural parameters from given WAXS and WANS data. Since the influence of σ_1 on WAXS (for typical Cu-K$_\alpha$ lab setups) and the influence of σ_3 on WANS data is only small, these parameters cannot always be determined exactly. Therefore, the resulting values for σ_1 (WAXS) and σ_3 (WANS) deviate significantly from the input value.

		Perf. WAXS Data		Noisy WAXS Data		Perf. WANS Data		Noisy WANS Data	
Parameter	**Input**	**Fit**	**Error**	**Fit**	**Error**	**Fit**	**Error**	**Fit**	**Error**
	3.70	3.70	0.0%	3.69	−0.3%	3.70	0.0%	3.69	−0.3%
σ_3	0.50	0.50	0.0%	0.49	−2.0%	0.50	0.0%	0.46	−8.0%
N	3.0	3.0	0.0%	3.0	0.0%	3.0	0.0%	3.0	0.0%
L_c	11.1	11.1	0.0%	11.1	0.0%	11.1	0.0%	11.10	0.0%
κ_c	0.50	0.50	0.0%	0.50	0.0%	0.50	0.0%	0.52	4.0%
L_a	20.0	20.0	0.0%	20.0	0.0%	20.0	0.0%	20.00	0.0%
l_{cc}	1.420	1.420	0.0%	1.419	−0.1%	1.420	0.0%	1.420	0.0%
σ_1	0.025	0.030	20.0%	0.016	−36.0%	0.025	0.0%	0.025	0.0%

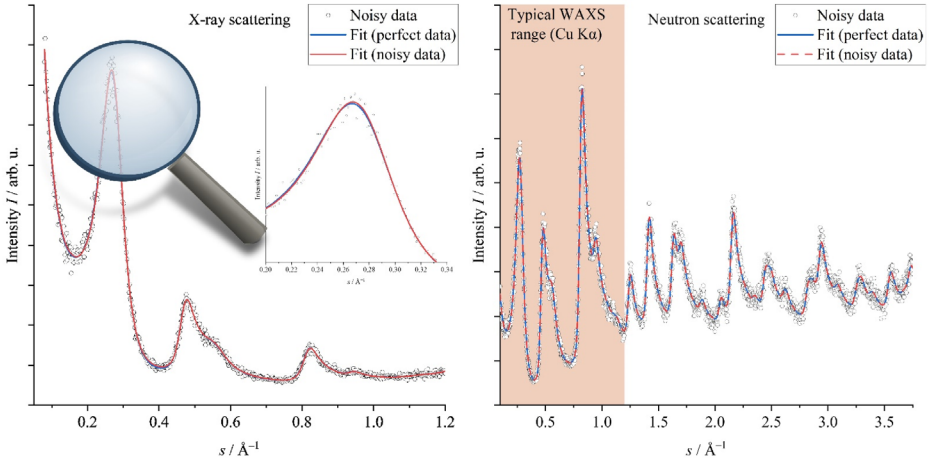

Figure 8. Noise level test using simulated WAXS (left) and WANS (right) data, which were blurred by statistical noise according to a Gaussian distribution (σ = 0.05) (black). The range of s values and the used noise level correspond to that of a typical laboratory instrument using Cu K$_\alpha$ radiation, especially for WAXS. The resulting fit of the noised data (red) is close to the fit for the perfect data (blue). The deviations are only small, implying that such noise level does not exert significant influence on the resulting structural parameters (Table 4). The data are simulated corresponding to a resin treated at medium heat-treatment temperatures (1800–2500 °C) or a pitch at lower temperatures (1200–2000 °C).

Looking at the disorder parameters for the stacks (interlayer, σ_3) and the layers (intralayer, σ_1), the accuracy of σ_3 is not improved using WANS data. In contrast, the intralayer disorder parameter σ_1 can be determined with significant higher accuracy if the WANS data extend until such large s values. This interesting result can be attributed to the degree of disorder in the intra- and interlayer structure, in combination with different accessible ranges of s: at higher values of s the interlayer reflections are usually dampened out because of the significant disorder in the stacking, and thus the (004) or, at best, (006) reflection appears at least as a shoulder. Hence, using WAXS/WANS data ranging to high s values does not provide higher accuracy in determining the degree of the disorder in the layer stacking. By contrast, usually a much larger number of intralayer reflections appears, and consequently, the evaluation of σ_1 benefits from an extended range of s.

4. Discussion

A main improvement compared with our previously introduced package (*CarbX*) is the ability to analyze powder wide-angle neutron scattering (WANS) data, and in particular the integration into the well-established *Octave* software. Additionally, *OctCarb* is open-source and can be modified to adapt it for individual needs. Compared with other software tools and our predecessor software (*CarbX*), the new program *OctCarb* provides an all-in-one tool for data processing and refinement for different radiation types (WAXS/WANS) and measurement geometries and without the usage of any external software. The main progress compared with *CarbX* is the usage of an open-source tool for a standardized fitting procedure (Levenberg–Marquardt algorithm), which is included in the *Octave* package. As a further improvement, the concentrations of foreign atoms of hydrogen, nitrogen, oxygen, and sulfur are also considered, and an incoherent background scattering is accurately taken into account. Another important improvement is the simplified handling of the parameter for the polydispersity of the graphenes (ν), which had originally been introduced by Ruland and Smarsly [44], and the refinement of which had complicated the procedure. Fixing this parameter in a well-defined procedure now leads to the possibility of significantly tweaking the amount of time for a single refinement, which can be reduced now to the order of some minutes only. Moreover, in our opinion, the possibility of refining WANS data as well as the possibility to use *OctCarb* and the whole refinement algorithm on all common operating systems (Windows, MacOS and Linux) and therefore also on high-performance computing systems are relevant and useful improvements. While using an HPC is certainly advantageous for refining several samples simultaneously, we found that for one single dataset, even standard computers evaluate with similar speed.

In contrast to other provided software for the WAXS analysis of NGCs, the calculation of (*hk*)-profiles and thus also L_a in the approach of Ruland and Smarsly [44] is based on the concept of the chord-length distribution (CLD), i.e., single-atom positions are not used for the graphenes, as is the case in the Debye scattering function. It uses an analytical expression based on a Gaussian distribution as described in Ruland and Tompa (1967) [69]. As L_a is thus calculated from a CLD, the used approach is valid also for small L_a values on the Ångstrom scale. Additionally, due to the calculation of the whole profile shape and not only a simple single-peak or peak-position analysis, the peak-maximum shift mentioned by Warren and Bodenstein (1966) [70] is intrinsically considered in the approach of Ruland and Smarsly [44] and thus also in *OctCarb*.

5. Conclusions

Here we presented a reliable, free, comfortable and fully open-source software tool (*OctCarb*) for evaluating the wide-angle X-ray/neutron scattering (WAXS/WANS) of non-graphitic carbon powder materials. *OctCarb* enables the refinement of WAXS/WANS data using the theoretical model of Ruland and Smarsly [44] and provides physically meaningful parameters describing the stacking and layer structure including intrinsic structural disorder. While the underlying theoretical scattering model is complex, we

would like to emphasize that *OctCarb* is usable also by non-XRD experts for a profound analysis of experimental WAXS/WANS data.

As an outlook, it is planned to use the algorithm and *OctCarb* for the refinement of pair-distribution-function (PDF) data of NGCs, which can be obtained from WANS as well as from low-wavelength WAXS experiments, e.g., from synchrotron measurements [71,72]. Another option is the distribution of a *.mex file in order to make the calculation in iObs and *OctCarb* usable in MathWorks *MatLab*, another mathematical software tool similar to *Octave*. [42] Even if MathWorks *MatLab* is not free of charge, it might be a good alternative since it is widely spread and has well-working parallel computing functions implemented. Even if this part is not provided in this study, it is still possible to create the needed *.mex file using the C/C++ data from GitHub (https://github.com/osswaldo/NGCs/tree/master/Octave/oct-files (accessed on 2 November 2022)) and compile the iObs.mex analogous to iObs.oct.

Supplementary Materials: The following supporting information can be downloaded at: https://www.mdpi.com/article/10.3390/c8040078/s1, SI part A—Octave installation and examples, SI part B—Correction/fine treatment of WAXS/WANS data and mathematical background, Excerpt from GitHub, OctCarb Test Data [73–89].

Author Contributions: Conceptualization, O.O. and B.M.S.; methodology, O.O.; software, O.O.; validation, O.O.; formal analysis, O.O.; investigation, O.O. and B.M.S.; resources, O.O. and B.M.S.; data curation, O.O.; writing—original draft preparation, B.M.S.; writing—review and editing, B.M.S.; visualization, O.O.; supervision, B.M.S.; project administration, B.M.S.; funding acquisition, B.M.S. All authors have read and agreed to the published version of the manuscript.

Funding: Financial support is provided by the DFG via the GRK (Research Training Group) 2204 "Substitute Materials for Sustainable Energy Technologies".

Data Availability Statement: The data presented in this study are available in the SI File "OctCarb Test Data.zip".

Acknowledgments: We acknowledge Torben Pfaff for programming the basic calculation routine in C++, and Henry E. Fischer for assistance in the inelastic neutron scattering experiments, data preparation and beamtime support. We would also like to thank Torben Pfaff and Felix Badaczewski for performing the WANS measurements and Marc Oliver Loeh for synthesizing the samples. We also acknowledge computational resources provided by the HPC Core Facility and the HRZ of the Justus-Liebig University Giessen. We thank Christian Bauer and Felix Badaczewski for testing and evaluating *OctCarb*.

Conflicts of Interest: The authors declare no conflict of interest.

References

1. Doherty, C.M.; Caruso, R.A.; Smarsly, B.M.; Adelhelm, P.; Drummond, C.J. Hierarchically Porous Monolithic LiFePO 4/Carbon Composite Electrode Materials for High Power Lithium Ion Batteries. *Chem. Mater.* **2009**, *21*, 5300–5306. [CrossRef]
2. Kumar, R.; Dhakate, S.R.; Mathur, R.B. The role of ferrocene on the enhancement of the mechanical and electrochemical properties of coal tar pitch-based carbon foams. *J. Mater. Sci.* **2013**, *48*, 7071–7080. [CrossRef]
3. Oberlin, A. Carbonization and graphitization. *Carbon* **1984**, *22*, 521–541. [CrossRef]
4. Goel, C.; Bhunia, H.; Bajpai, P.K. Synthesis of nitrogen doped mesoporous carbons for carbon dioxide capture. *RSC Adv.* **2015**, *5*, 46568–46582. [CrossRef]
5. Li, J.; Lu, R.; Dou, B.; Ma, C.; Hu, Q.; Liang, Y.; Wu, F.; Qiao, S.; Hao, Z. Porous graphitized carbon for adsorptive removal of benzene and the electrothermal regeneration. *Environ. Sci. Technol.* **2012**, *46*, 12648–12654. [CrossRef]
6. Oschatz, M.; Borchardt, L.; Thommes, M.; Cychosz, K.A.; Senkovska, I.; Klein, N.; Frind, R.; Leistner, M.; Presser, V.; Gogotsi, Y.; et al. Carbide-derived carbon monoliths with hierarchical pore architectures. *Angew. Chem. Int. Ed. Engl.* **2012**, *51*, 7577–7580. [CrossRef]
7. Oschatz, M.; Kockrick, E.; Rose, M.; Borchardt, L.; Klein, N.; Senkovska, I.; Freudenberg, T.; Korenblit, Y.; Yushin, G.; Kaskel, S. A cubic ordered, mesoporous carbide-derived carbon for gas and energy storage applications. *Carbon* **2010**, *48*, 3987–3992. [CrossRef]
8. Silvestre-Albero, A.; Rico-Frances, S.; Rodríguez-Reinoso, F.; Kern, A.M.; Klumpp, M.; Etzold, B.J.; Silvestre-Albero, J. High selectivity of TiC-CDC for CO2/N2 separation. *Carbon* **2013**, *59*, 221–228. [CrossRef]

9. Dash, R.; Chmiola, J.; Yushin, G.; Gogotsi, Y.; Laudisio, G.; Singer, J.; Fischer, J.; Kucheyev, S. Titanium carbide derived nanoporous carbon for energy-related applications. *Carbon* **2006**, *44*, 2489–2497. [CrossRef]
10. Manthiram, A.; Fu, Y.; Chung, S.-H.; Zu, C.; Su, Y.-S. Rechargeable lithium-sulfur batteries. *Chem. Rev.* **2014**, *114*, 11751–11787. [CrossRef]
11. Inagaki, M.; Konno, H.; Tanaike, O. Carbon materials for electrochemical capacitors. *J. Power Sources* **2010**, *195*, 7880–7903. [CrossRef]
12. Oschatz, M.; Borchardt, L.; Pinkert, K.; Thieme, S.; Lohe, M.R.; Hoffmann, C.; Benusch, M.; Wisser, F.M.; Ziegler, C.; Giebeler, L.; et al. Hierarchical Carbide-Derived Carbon Foams with Advanced Mesostructure as a Versatile Electrochemical Energy-Storage Material. *Adv. Energy Mater.* **2014**, *4*, 1300645. [CrossRef]
13. Wang, J.; Sugita, S.; Nagayama, K.; Matsumoto, T. OS18-3 Spatiotemporal Dynamics of Actin during Adhesion Process of MC3T3-E1 Cells to Substrate(Cell and Tissue mechanics 1,OS18 Cell and tissue mechanics, BIOMECHANICS). *ATEM* **2015**, *14*, 237. [CrossRef]
14. Kim, Y.-S.; Guo, X.-F.; Kim, G.-J. Synthesis of carbon monolith with bimodal meso/macroscopic pore structure and its application in asymmetric catalysis. *Catal. Today* **2010**, *150*, 91–99. [CrossRef]
15. Zhang, S.; Chen, L.; Zhou, S.; Zhao, D.; Wu, L. Facile Synthesis of Hierarchically Ordered Porous Carbon via in Situ Self-Assembly of Colloidal Polymer and Silica Spheres and Its Use as a Catalyst Support. *Chem. Mater.* **2010**, *22*, 3433–3440. [CrossRef]
16. Tzeng, S.-S.; Chr, Y.-G. Evolution of microstructure and properties of phenolic resin-based carbon/carbon composites during pyrolysis. *Mater. Chem. Phys.* **2002**, *73*, 162–169. [CrossRef]
17. Perret, R.; Ruland, W. X-ray small-angle scattering of glassy carbon. *J. Appl. Crystallogr.* **1972**, *5*, 183–187. [CrossRef]
18. Fitzer, E.; Kochling, K.-H.; Boehm, H.P.; Marsh, H. Recommended terminology for the description of carbon as a solid (IUPAC Recommendations 1995). *Pure Appl. Chem.* **1995**, *67*, 473–506. [CrossRef]
19. Badaczewski, F.M.; Loeh, M.O.; Pfaff, T.; Dobrotka, S.; Wallacher, D.; Clemens, D.; Metz, J.; Smarsly, B.M. Peering into the structural evolution of glass-like carbons derived from phenolic resin by combining small-angle neutron scattering with an advanced evaluation method for wide-angle X-ray scattering. *Carbon* **2019**, *141*, 169–181. [CrossRef]
20. Badaczewski, F.M.; Loeh, M.O.; Pfaff, T.; Wallacher, D.; Clemens, D.; Smarsly, B.M. An advanced structural characterization of templated meso-macroporous carbon monoliths by small- and wide-angle scattering techniques. *Beilstein J. Nanotechnol.* **2020**, *11*, 310–322. [CrossRef]
21. Faber, K.; Badaczewski, F.M.; Oschatz, M.; Mondin, G.; Nickel, W.; Kaskel, S.; Smarsly, B.M. In-Depth Investigation of the Carbon Microstructure of Silicon Carbide-Derived Carbons by Wide-Angle X-ray Scattering. *J. Phys. Chem. C* **2014**, *118*, 15705–15715. [CrossRef]
22. Faber, K.; Badaczewski, F.M.; Ruland, W.; Smarsly, B.M. Investigation of the Microstructure of Disordered, Non-graphitic Carbons by an Advanced Analysis Method for Wide-Angle X-ray Scattering. *Z. Anorg. Allg. Chem.* **2014**, *640*, 3107–3117. [CrossRef]
23. Loeh, M.O.; Badaczewski, F.M.; Faber, K.; Hintner, S.; Bertino, M.F.; Mueller, P.; Metz, J.; Smarsly, B.M. Analysis of thermally induced changes in the structure of coal tar pitches by an advanced evaluation method of X-ray scattering data. *Carbon* **2016**, *109*, 823–835. [CrossRef]
24. Loeh, M.O.; Badaczewski, F.M.; von der Lehr, M.; Ellinghaus, R.; Dobrotka, S.; Metz, J.; Smarsly, B.M. Hard-templating of carbon using porous SiO2 monoliths revisited—Quantitative impact of spatial confinement on the microstructure evolution. *Carbon* **2018**, *129*, 552–563. [CrossRef]
25. Pfaff, T.; Simmermacher, M.; Smarsly, B.M. CarbX: A program for the evaluation of wide-angle X-ray scattering data of non-graphitic carbons. *J. Appl. Crystallogr.* **2018**, *51*, 219–229. [CrossRef]
26. Pfaff, T.; Badaczewski, F.M.; Loeh, M.O.; Franz, A.; Hoffmann, J.-U.; Reehuis, M.; Zeier, W.G.; Smarsly, B.M. Comparative Microstructural Analysis of Nongraphitic Carbons by Wide-Angle X-ray and Neutron Scattering. *J. Phys. Chem. C* **2019**, *123*, 20532–20546. [CrossRef]
27. Ou, M.; Zhang, Y.; Zhu, Y.; Fan, C.; Sun, S.; Feng, J.; Sun, X.; Wei, P.; Xu, J.; Peng, J.; et al. Local Structures of Soft Carbon and Electrochemical Performance of Potassium-Ion Batteries. *ACS Appl. Mater. Interfaces* **2021**, *13*, 28261–28269. [CrossRef]
28. Härmas, R.; Palm, R.; Kurig, H.; Puusepp, L.; Pfaff, T.; Romann, T.; Aruväli, J.; Tallo, I.; Thomberg, T.; Jänes, A.; et al. Carbide-Derived Carbons: WAXS and Raman Spectra for Detailed Structural Analysis. *C* **2021**, *7*, 29. [CrossRef]
29. Schüpfer, D.B.; Badaczewski, F.M.; Guerra-Castro, J.M.; Hofmann, D.M.; Heiliger, C.; Smarsly, B.M.; Klar, P.J. Assessing the structural properties of graphitic and non-graphitic carbons by Raman spectroscopy. *Carbon* **2020**, *161*, 359–372. [CrossRef]
30. Schüpfer, D.B.; Badaczewski, F.M.; Peilstöcker, J.; Guerra-Castro, J.M.; Shim, H.; Firoozabadi, S.; Beyer, A.; Volz, K.; Presser, V.; Heiliger, C.; et al. Monitoring the thermally induced transition from sp3-hybridized into sp2-hybridized carbons. *Carbon* **2021**, *172*, 214–227. [CrossRef]
31. Shi, H.; Reimers, J.N.; Dahn, J.R. Structure-refinement program for disordered carbons. *J. Appl. Crystallogr.* **1993**, *26*, 827–836. [CrossRef]
32. Tsui, L. CarbonXS GUI. Available online: https://lktsui.github.io/carbon_xs_gui/tutorial.html (accessed on 4 January 2021).
33. Tsui, L.; Garzon, F. CarbonXS GUI: A graphical front-end for CarbonXS. *J. Appl. Crystallogr.* **2017**, *50*, 1830–1833. [CrossRef]
34. Fujimoto, H.; Shiraishi, M. Characterization of unordered carbon using Warren–Bodenstein's equation. *Carbon* **2001**, *39*, 1753–1761. [CrossRef]

35. Fujimoto, H. Theoretical X-ray scattering intensity of carbons with turbostratic stacking and AB stacking structures. *Carbon* **2003**, *41*, 1585–1592. [CrossRef]
36. Fujimoto, H. A new estimation method for the degree of graphitization for random layer lattices. *Carbon* **2010**, *48*, 3446–3453. [CrossRef]
37. Warren, B.E.; Bodenstein, P. The diffraction pattern of fine particle carbon blacks. *Acta Cryst.* **1965**, *18*, 282–286. [CrossRef]
38. Fujimoto, H. Carbon Analyzer, 2022. Available online: http://www.asahi-net.or.jp/~{}qn6h-fjmt (accessed on 2 November 2022).
39. Saenko, N.S. The X-ray diffraction study of three-dimensional disordered network of nanographites: Experiment and theory. *Phys. Procedia* **2012**, *23*, 102–105. [CrossRef]
40. Dopita, M.; Rudolph, M.; Salomon, A.; Emmel, M.; Aneziris, C.G.; Rafaja, D. Simulations of X-Ray Scattering on Two-Dimensional, Graphitic and Turbostratic Carbon Structures. *Adv. Eng. Mater.* **2013**, *15*, 1280–1291. [CrossRef]
41. Dopita, M.; Emmel, M.; Salomon, A.; Rudolph, M.; Matěj, Z.; Aneziris, C.G.; Rafaja, D. Temperature evolution of microstructure of turbostratic high melting coal-tar synthetic pitch studied using wide-angle X-ray scattering method. *Carbon* **2015**, *81*, 272–283. [CrossRef]
42. *MATLAB*, Version 9.9.0 (R2020b); The MathWorks Inc.: Natick, MA, USA, 2020.
43. Ungár, T.; Gubicza, J.; Ribárik, G.; Pantea, C.; Zerda, T. Microstructure of carbon blacks determined by X-ray diffraction profile analysis. *Carbon* **2002**, *40*, 929–937. [CrossRef]
44. Ruland, W.; Smarsly, B.M. X-ray scattering of non-graphitic carbon: An improved method of evaluation. *J. Appl. Crystallogr.* **2002**, *35*, 624–633. [CrossRef]
45. Wolfram Research, Inc. Mathematica, Version 12.1, 2020. Available online: https://www.wolfram.com/mathematica (accessed on 2 November 2022).
46. Eaton, J.W.; Bateman, D.; Hauberg, S.; Wehbring, R. {GNU Octave} Version 5.2.0 Manual: A High-Level Interactive Language for Numerical Computations, 2020. Available online: https://www.gnu.org/software/octave/doc/v5.2.0/ (accessed on 2 November 2022).
47. Free Software Foundation, Inc. GNU General Public License: Version 3. Available online: https://www.gnu.org/licenses/gpl-3.0.html (accessed on 21 October 2020).
48. Warren, B.E. X-Ray Diffraction in Random Layer Lattices. *Phys. Rev.* **1941**, *59*, 693–698. [CrossRef]
49. Biscoe, J.; Warren, B.E. An X-Ray Study of Carbon Black. *J. Appl. Phys.* **1942**, *13*, 364–371. [CrossRef]
50. Scherrer, P. Bestimmung der inneren Struktur und der Größe von Kolloidteilchen mittels Röntgenstrahlen. In *Kolloidchemie ein Lehrbuch*; Zsigmondy, R., Ed.; Springer: Berlin/Heidelberg, Germany, 1912; pp. 387–409. ISBN 978-3-662-33517-8.
51. Sharma, A.; Kyotani, T.; Tomita, A. Comparison of structural parameters of PF carbon from XRD and HRTEM techniques. *Carbon* **2000**, *38*, 1977–1984. [CrossRef]
52. Diamond, R. X-ray studies of some carbonized coals. *Phil. Trans. R. Soc. Lond. A* **1960**, *252*, 193–223. [CrossRef]
53. Perret, R.; Ruland, W. Profile analysis of random-layer lines. *J. Appl. Crystallogr.* **1968**, *1*, 257–262. [CrossRef]
54. Ruland, W. X-ray studies on the carbonization and graphitization of acenaphthylene and bifluorenyl. *Carbon* **1965**, *2*, 365–378. [CrossRef]
55. Ruland, W. Fourier transform methods for random-layer line profiles. *Acta Cryst.* **1967**, *22*, 615–623. [CrossRef]
56. Houska, C.R.; Warren, B.E. X-Ray Study of the Graphitization of Carbon Black. *J. Appl. Phys.* **1954**, *25*, 1503–1509. [CrossRef]
57. Franklin, R.E. The interpretation of diffuse X-ray diagrams of carbon. *Acta Cryst.* **1950**, *3*, 107–121. [CrossRef]
58. Franklin, R.E. Crystallite growth in graphitizing and non-graphitizing carbons. *Proc. R. Soc. Lond. A* **1951**, *209*, 196–218. [CrossRef]
59. Prince, E.; Fuess, H.; Hahn, T.; Wondratschek, H.; Müller, U.; Shmueli, U.; Authier, A.; Kopský, V.; Litvin, D.B.; Rossmann, M.G.; et al. *International Tables for Crystallography*; International Union of Crystallography: Chester, UK, 2006; ISBN 978-1-4020-5259-0.
60. octave.org. Preface (GNU Octave (Version 5.2.0)). Available online: https://octave.org/doc/v5.2.0/Preface.html (accessed on 2 November 2021).
61. Levenberg, K. A method for the solution of certain non-linear problems in least squares. *Quart. Appl. Math.* **1944**, *2*, 164–168. [CrossRef]
62. Marquardt, D.W. An Algorithm for Least-Squares Estimation of Nonlinear Parameters. *J. Soc. Ind. Appl. Math.* **1963**, *11*, 431–441. [CrossRef]
63. Moré, J.J. The Levenberg-Marquardt algorithm: Implementation and theory. In *Numerical Analysis*; Watson, G.A., Ed.; Springer: Berlin/Heidelberg, Germany, 1978; pp. 105–116. ISBN 978-3-540-08538-6.
64. Vetterling, W.T. *Numerical Recipes*, 3rd ed.; Cambridge University Press: Cambridge, UK, 2007; ISBN 0521880688.
65. Einert, M.; Wessel, C.; Badaczewski, F.; Leichtweiß, T.; Eufinger, C.; Janek, J.; Yuan, J.; Antonietti, M.; Smarsly, B.M. Nitrogen-Doped Carbon Electrodes: Influence of Microstructure and Nitrogen Configuration on the Electrical Conductivity of Carbonized Polyacrylonitrile and Poly(ionic liquid) Blends. *Macromol. Chem. Phys.* **2015**, *216*, 1930–1944. [CrossRef]
66. Holleman, A.F.; Wiberg, E.; Wiberg, N.; Fischer, G. *Anorganische Chemie*; 103. Auflage; De Gruyter: Berlin, Boston, 2017; ISBN 978-3-11-051854-2.
67. Strunz, H. *Strunz Mineralogical Tables. Ninth Edition: Chemical-Structural Mineral Classification System*, 9th ed.; Schweizerbart: Stuttgart, Germany, 2020; ISBN 9783510654529.
68. Hoffmann, J.-U.; Reehuis, M. E2: The Flat-Cone Diffractometer at BER II. *JLSRF* **2018**, *4*, A129. [CrossRef]

69. Ruland, W.; Tompa, H. The effect of multiple scattering on structural parameters determined from X-ray small-angle scattering. *J. Appl. Crystallogr.* **1972**, *5*, 1–7. [CrossRef]
70. Warren, B.E.; Bodenstein, P. The shape of two-dimensional carbon black reflections. *Acta Cryst.* **1966**, *20*, 602–605. [CrossRef]
71. Masson, O.; Thomas, P. Exact and explicit expression of the atomic pair distribution function as obtained from X-ray total scattering experiments. *J. Appl. Crystallogr.* **2013**, *46*, 461–465. [CrossRef]
72. Olds, D.P.; Duxbury, P.M. Efficient algorithms for calculating small-angle scattering from large model structures. *J. Appl. Crystallogr.* **2014**, *47*, 1077–1086. [CrossRef]
73. HKHLR—HPC Hessen. justHPC Gießen. Available online: https://www.hkhlr.de/de/cluster/justhpc-giessen (accessed on 21 July 2022).
74. Placzek, G. The Scattering of Neutrons by Systems of Heavy Nuclei. *Phys. Rev.* **1952**, *86*, 377–388. [CrossRef]
75. Fischer, H.E.; Barnes, A.C.; Salmon, P.S. Neutron and x-ray diffraction studies of liquids and glasses. *Rep. Prog. Phys.* **2006**, *69*, 233–299. [CrossRef]
76. Milberg, M.E.; Brailsford, A.D. The atomic incoherent scattering intensities of boron, oxygen and carbon. *Acta Cryst.* **1958**, *11*, 672–673. [CrossRef]
77. Keating, D.T.; Vineyard, G.H. The complete incoherent scattering function for carbon. *Acta Cryst.* **1956**, *9*, 895–896. [CrossRef]
78. Ruland, W. X-ray determination of crystallinity and diffuse disorder scattering. *Acta Cryst.* **1961**, *14*, 1180–1185. [CrossRef]
79. James, R.W. *The Optical Principles of the Diffraction of X-rays*; George Bell & Sons: London, UK, 1962; Volume 2.
80. Ruland, W. The separation of coherent and incoherent Compton X-ray scattering. *Br. J. Appl. Phys.* **1964**, *15*, 1301–1307. [CrossRef]
81. Buerger, M.J. The Correction of X-Ray Diffraction Intensities for Lorentz and Polarization Factors. *Proc. Natl. Acad. Sci. USA* **1940**, *26*, 637–642. [CrossRef]
82. Schulz, L.G. A Direct Method of Determining Preferred Orientation of a Flat Reflection Sample Using a Geiger Counter X-Ray Spectrometer. *J. Appl. Phys.* **1949**, *20*, 1030–1033. [CrossRef]
83. Sivia, D.S. *Elementary Scattering Theory: For X-ray and Neutron Users*; Reprinted; Oxford University Press: Oxford, UK, 2017; ISBN 9780199228683.
84. Hubbell, J.H.; Seltzer, S. Tables of X-Ray Mass Attenuation Coefficients and Mass Energy-Absorption Coefficients 1 keV to 20 MeV for Elements Z = 1 to 92 and 48 Additional Substances of Dosimetric Interest. 1995. Available online: https://www.semanticscholar.org/paper/Tables-of-X-Ray-Mass-Attenuation-Coefficients-and-1-Hubbell-Seltzer/2098301d7be3283817f2567a2c5ca4553b5b41a8 (accessed on 2 November 2022).
85. NIST Center for Neutron Research. Neutron Scattering Lengths and Cross Sections. Available online: https://www.ncnr.nist.gov/resources/n-lengths/ (accessed on 2 November 2022).
86. Fox, A.G.; O'Keefe, M.A.; Tabbernor, M.A. Relativistic Hartree–Fock X-ray and electron atomic scattering factors at high angles. *Acta Crystallogr. A Found Crystallogr.* **1989**, *45*, 786–793. [CrossRef]
87. Sears, V.F. Neutron scattering lengths and cross sections. *Neutron News* **1992**, *3*, 26–37. [CrossRef]
88. Cromer, D.T. Compton Scattering Factors for Aspherical Free Atoms. *J. Chem. Phys.* **1969**, *50*, 4857–4859. [CrossRef]
89. Salmon, P.S.; Petri, I. Structure of glassy and liquid GeSe 2. *J. Phys. Condens. Matter* **2003**, *15*, S1509–S1528. [CrossRef]

6.3.2. Publikation 2 [209]

Reproduziert mit Genehmigung von Oliver Osswald; veröffentlicht bei MDPI, *C*, 2023.

Journal of Carbon Research

MDPI

Article

On the Highly Ordered Graphene Structure of Non-Graphitic Carbons (NGCs)—A Wide-Angle Neutron Scattering (WANS) Study

Oliver Osswald [1,*], Marc O. Loeh [2], Felix M. Badaczewski [2], Torben Pfaff [3], Henry E. Fischer [4], Alexandra Franz [5], Jens-Uwe Hoffmann [5], Manfred Reehuis [5], Peter J. Klar [6] and Bernd M. Smarsly [1,*]

[1] Institute of Physical Chemistry, Justus-Liebig-University Giessen, Heinrich-Buff-Ring 17, 35392 Giessen, Germany
[2] Schunk Kohlenstofftechnik GmbH, Rodheimer Strasse 59, 35452 Heuchelheim, Germany
[3] Lang GmbH & Co. KG, Dillstrasse 4, 35625 Hüttenberg, Germany
[4] Institut Laue-Langevin, 71 Avenue des Martyrs, CS 20156, CEDEX 9, 38042 Grenoble, France
[5] Helmholtz-Zentrum Berlin für Materialien und Energie, Hahn-Meitner-Platz 1, 14109 Berlin, Germany
[6] Institute of Experimental Physics I, Justus-Liebig-University Giessen, Heinrich-Buff-Ring 16, 35392 Giessen, Germany
* Correspondence: carbon@oss-wald.de (O.O.); bernd.smarsly@phys.chemie.uni-giessen.de (B.M.S.)

Abstract: Non-graphitic carbons (NGCs), such as glass-like carbons, pitch cokes, and activated carbon consist of small graphene layer building stacks arranged in a turbostratic order. Both structure features, including the single graphene sheets as well as the stacks, possess structural disorder, which can be determined using wide-angle X-ray or neutron scattering (WAXS/WANS). Even if WANS data of NGCs have already been extensively reported and evaluated in different studies, there are still open questions with regard to their validation with WAXS, which is usually used for routine characterization. In particular, using WAXS for the damping of the atomic form factor and the limited measured range prevent the analysis of higher-ordered reflections, which are crucial for determining the stack/layer size (L_a, L_c) and disorder (σ_1, σ_3) based on the reflection widths. Therefore, in this study, powder WANS was performed on three types of carbon materials (glass-like carbon made out of a phenol-formaldehyde resin (PF-R), a mesophase pitch (MP), and a low softening-point pitch (LSPP)) using a beamline at ILL in Grenoble, providing a small wavelength and thus generating WANS data covering a large range of scattering vectors (0.052 Å^{-1} < s < 3.76 Å^{-1}). Merging these WANS data with WANS data from previous studies, possessing high resolution in the small s range, on the same materials allowed us to determine both the interlayer and the interlayer structure as accurately as possible. As a main conclusion, we found that the structural disorder of the graphene layers themselves was significantly smaller than previously assumed.

Keywords: non-graphitic carbon; wide-angle scattering; disorder-determination

check for updates

Citation: Osswald, O.; Loeh, M.O.; Badaczewski, F.M.; Pfaff, T.; Fischer, H.E.; Franz, A.; Hoffmann, J.-U.; Reehuis, M.; Klar, P.J.; Smarsly, B.M. On the Highly Ordered Graphene Structure of Non-Graphitic Carbons (NGCs)—A Wide-Angle Neutron Scattering (WANS) Study. *C* **2023**, *9*, 27. https://doi.org/10.3390/c9010027

Academic Editor: Cédric Pardanaud

Received: 23 December 2022
Revised: 15 February 2023
Accepted: 16 February 2023
Published: 27 February 2023

1. Introduction

Carbon occurs in many forms, of which diamonds (made up of sp^3 hybridized carbon) and graphite (made up of sp^2-hybridized carbon) are the most common ones. Among the sp^2-hybridized carbon materials, the so-called "non-graphitic carbons (NGCs)" represent a million-ton-scale class and are of significant relevance for applications. NGCs comprise a plurality of carbons, such as activated carbon, glass-like carbon, and bio chars such as charcoal. As a bulk material, it can be used for different electrical and low friction applications [1–3], whereas the porous derivates and the carbide derived carbons (CDCs) are commonly used in gas storage/separation, e.g., in carbon molecular sieves (CMS) [4–8], as electrodes in sulfur lithium batteries [6,9,10] and super capacitors [11–13], and as catalyst supports in different syntheses [14,15]. Also the so called "glass-like" carbons, which are

available from phenol formaldehyde (PF) precursors, are part of the NGC family and are commercially used due to their excellent thermal and chemical stability [16], e.g., to produce carbon fiber reenforced carbons for high-temperature applications [17].

In general, NGCs consist of sp2-hybridized (graphene) layers (Figure 1), which are stacked parallel on top of each other, but are randomly arranged by rotation perpendicularly to the layer ("turbostratic" structure), as already proposed by Warren [18]. The graphenes and the stacks have nanometer dimensions and possess substantial structural disorder, both in the graphenes themselves as well as in the stacking, i.e., the stacking distance between adjacent graphenes exhibits a broad distribution (Figure 1). This absence of long-range crystallographic order causes broad and overlapping scattering maxima in WAXS and WANS. It is important to note that this feature constitutes the definition of NGCs by the IUPAC [19]. The main structural dimensions of these stacks are described by the parameters L_a and L_c, which are the average lateral extension and the stack height, respectively. Further important and relevant parameters are the C-C bond length (l_{cc}), the average distance $\overline{a_3}$ between the layers, and parameters quantifying the substantial degree of disorder (strain) within the layers themselves and their stacking (σ_1 and σ_3).

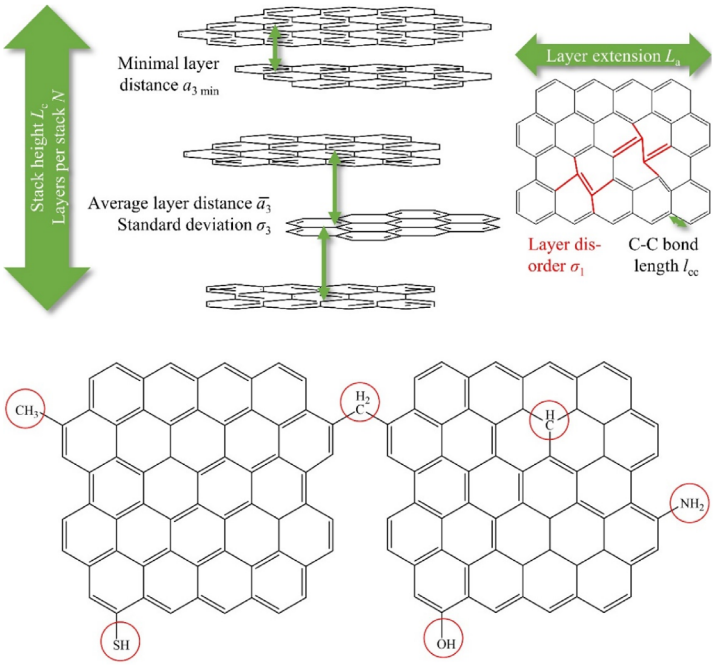

Figure 1. Principle structure of non-graphitic carbons (NGCs) containing a turbostratic stacking arrangement of single (disordered) graphene layers. Also, NGCs can contain unorganized carbon (sp^3-hybridized) or foreign atoms (e.g., H, N, O, S). Adapted from [20,21].

Given the broad industrial application of NGCs, a quantitative determination of the aforementioned microstructure based on experimentally accessible structural parameters is crucial for the tuning of production processes and fundamental understanding of the linkage between the microstructure and macroscopic material properties. The latter comprises

hardness, chemical stability, thermal properties, and electrical conductivity, which hence defines the final application.

Three main approaches are usually applied for the microstructural characterization of NGCs, which are transmission electron microscopy (TEM) [22,23], Raman scattering [24–26], and wide-angle X-ray scattering (WAXS), is the latter being used as one of the first methods to characterize such carbons [25,27–30]. Among them, WAXS offers fundamental advantages, particularly in the straightforward experimental analysis using standard X-ray powder diffraction laboratory setups. Raman scattering is used as a routine method that provides the lateral extension of the graphene layers and a qualitative overview on structural order, but is especially useful for small graphene dimensions and disordered layers, yet the analysis needs further validation with respect to other structural features [25]. Instead, WAXS or wide-angle neutron scattering (WANS) can provide a larger number of structural parameters, especially regarding structural disorder. The main features of WAXS/WANS data are the superposition of the scattering from the single graphenes ("intralayer scattering") and their stacking ("interlayer scattering"), as well as the large width of the corresponding reflections (see Figure 2). It is important to emphasize that the two essential structural features of NGCs, the graphenes and the stacks, both possess a small dimension of a few nm, as well as structural disorder. Understanding the changes in the graphene dimension and the disorder upon chemical or thermal treatment are, however, desirable and crucial in unraveling the fundamentals of carbonization and graphitization. Importantly, the nanometer-sized dimension and the structural disorder both result in a significant broadening of the interlayer and intralayer reflections. It is thus challenging to separate these effects from WAXS/WANS data to obtain accurate and reliable values for the size-related parameters (L_a, L_c) and their respective disorders (σ_1 & σ_3). Since finite crystallite size and disorder result in a different dependence of the width of reflections with increasing modulus of the scattering vector s ($s = 2\sin(\theta)/\lambda$), the most suitable strategy to disentangle size and disorder is the acquisition of as many reflections as possible, which is equivalent to acquiring WAXS/WANS data up to a large s. Unraveling the exact degree of disorder of the graphenes and their stacking, which are quantified by the parameters σ_1 and σ_3, constitutes the main motivation of this present study.

However, owing to the broad, overlapping, and asymmetrical reflections, classic evaluation approaches based on analyzing the width of separated WAXS/WANS maxima are inappropriate for the microstructural analysis of NGCs based on WAXS/WANS. In contrast, it is recommended to fit the entire WAXS/WANS curve using a suitable model function. A widely used approach for WAXS was proposed by Shi et al. in 1993 [31], followed by other procedures by Azuma in 1998 [32] and Fujimoto and Shiraishi in 2001 [33]. Finally, in 2002, Ruland and Smarsly published an advanced approach for analyzing the WAXS of NGCs [34] that has already been successfully used in several studies [20,35–42]. Typical WAXS/WANS data and the general idea of the approach of Ruland and Smarsly are shown in Figure 2.

C **2023**, *9*, 27

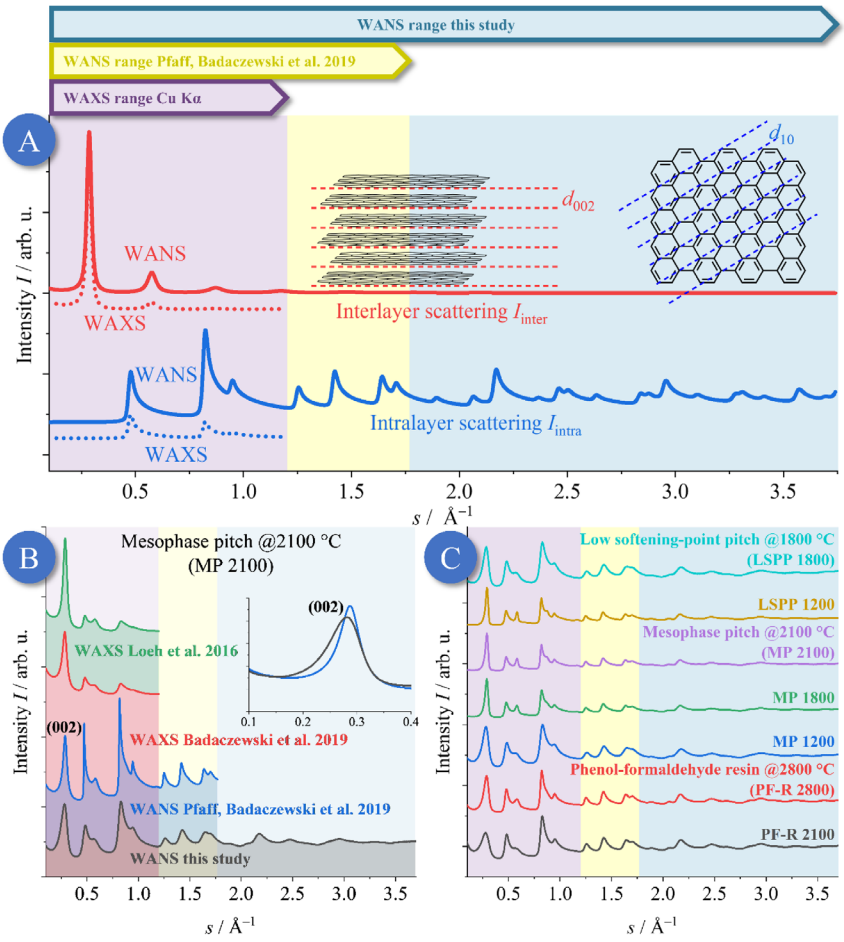

Figure 2. (**A**): Simulation of WAXS/WANS data of a representative NGC (without background scattering), which is given by a superposition of symmetric interlayer reflections (00*l*) and asymmetric intralayer reflections (*hk*). By using neutron radiation instead of X-rays, much more intralayer reflections can be measured, and, therefore, the intralayer graphene structure in particular can be determined more accurately. (**B**): One particular sample (mesophase pitch; MP @2100 °C, i.e., treated at 2100 °C) was studied four times, namely using WAXS measurements in the study of Loeh et al. (2016) [40], WAXS measurements in the work of Badaczewski et al. (2019) [37], WANS analysis performed by Pfaff et al. (2019) [43], and WANS measurements, the latter of which were performed in this study. In the present WANS study, a much lower wavelength was used compared to Badaczewski et al. (2019) [43]. While both WAXS measurements are very similar, there are differences between the two WANS measurements (performed at the Berlin and Grenoble facilities) due to the different instrumental resolutions. (**C**): Overview of the WANS data of samples, which were measured two times (2019 and in this study) and combined to get one merged WANS curve with high *s*-space

resolution, and also an extended *s*-range. Here, *s* means the modulus of the scattering vector *s* ($s = 2\sin(\theta)/\lambda$). It should be noted that the indexing shown with parentheses strictly denotes lattice planes, and reflections would have to be indexed without parentheses. However, brackets are used in this publication for both meanings to improve readability.

While evaluation approaches such as the one of Ruland and Smarsly provide meaningful structural characterization, the analysis of NGCs by WAXS and thus their validity generally suffers from the following features (Figure 3):

1. Atomic form factors result in the damping of WAXS data at larger *s* values. This effect is significant for typical XRD setups using a CuK_α wavelength.
2. The Compton scattering has to be exactly taken into account, but has a complex dependence on *s*.
3. The limited range of *s* ($s = 2/\lambda \sin(\theta)$) commonly available in standard lab XRD setups reduces the number of accessible WAXS reflections. A large number of reflections is, however, crucial to quantitatively disentangle size (L_a and L_c) and disorder effects (σ_1 and σ_3 in our approach), which both influence the significant width of the NGC reflections.

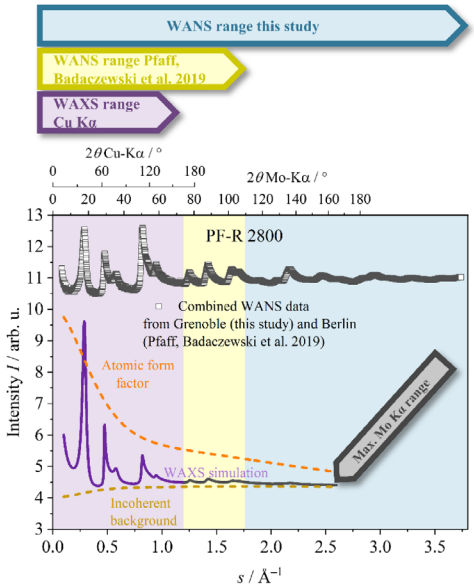

Figure 3. Illustration of the shortcomings of X-rays in the analysis of NGCs and the advantage of WANS. The merged WANS data shown (sample PF-R 2800, a phenol-formaldehyde resin) were obtained from a beamtime at Grenoble (this study) and from an HZB (Berlin) beamtime, see Pfaff et al. [43]. While WAXS data suffer from the damping induced by the atomic form factor, by using WANS data more distinguishable reflections can be obtained and analyzed. Also, WAXS measurements with, e.g., Mo-Kα radiation, which makes high values of the *s* accessible too, may not significantly improve the evaluation, since the atomic form factor leads to a substantial damping in this case. Additionally, when using X-ray radiation, the incoherent background must be taken into account and calculated exactly for a quantitative analysis.

Thus, WANS performed up to large s values provides fundamental advantages in the study of NGCs when compared to WAXS. Recently, our experiments performed at the Flat-Cone Diffractometer (E2 at BER II, HZB, Berlin) [44] revealed that, with a few specific modifications, the approach by Ruland and Smarsly can indeed be applied to the WANS data of NGCs. However, due to wavelength restrictions, the observable range of s was not significantly larger compared to typical lab WAXS experiments. Hence, the full potential of WANS (see points 1–3 above) was not accessible. In particular, the accurate determination of the disorder parameter remained unsatisfactory.

Thus, in the present study WANS data were collected at the D4 wide-angle neutron diffractometer at the Institute Laue–Langevin (ILL) in Grenoble on the very same samples [45,46], complementing the HZB data, based on these considerations:

1. While the WANS data acquired in our previous study featured high precision particularly at low s (Berlin; Pfaff et al., 2019 [43]), the facility at Grenoble featured advantageous resolution at high s (0.052 $Å^{-1} < s < 3.76$ $Å^{-1}$). However, the Berlin HZB WANS data (0.400 $Å^{-1} < s < 1.44$ $Å^{-1}$) possessed better resolution in the region of the (002) reflection compared to the WANS data acquired in Grenoble. Thus, combining both data sets for the very same sample was intended to test if a valid deconvolution of the effects of finite size and disorder in both the interlayer and intralayer structure was possible.
2. The noise of the Grenoble WANS beam line was very low; therefore, the refinement quality and the resulting microstructure parameters were superior. In particular, the analysis of the higher-order reflections, possessing decreasing intensity, benefited from a low background and noise.
3. The high neutron flux available at the D4 in Grenoble allowed for the acquisition of high-quality data for a substantial number of materials. In particular, in this study, extensive temperature series were possible for materials exposed to a lot of temperature steps. Together with the high data quality, fine changes in the evolution of the microstructure upon temperature treatment were thus accessible.

Based on performing WANS experiments at the Grenoble facility and merging them with the HZB WANS data, which were performed on the very same NGC materials, we therefore aimed at a precise quantification and, thus, interpretation of the disorder of the graphenes and their stacking. Moreover, by applying the quite basic structural model underlying the approach of Ruland and Smarsly, we addressed the question as to whether the concomitant refinement approach is indeed able to fit WANS data up to quite large s values, in the light of the relatively small number of relevant structural parameters (L_a, L_c, σ_1, σ_3) which also act as refinement parameters in this fitting approach. Moreover, the structural analysis was compared with Raman scattering analysis, especially using a novel approach by Schüpfer et al. [25], which could thus result in the verification of the state-of-the-art analysis in this field as well, as identical samples were compared [24–26]. Further, the results were compared to elemental analysis. Based on this method validation, our study is intended to gain further insights into the evaluation of the NGC graphene structure upon temperature treatment up to temperatures that are close to the onset of graphitization.

2. Materials and Methods

2.1. Sample Preparation

For our studies, we used different NGCs made from different precursors and that were heat treated at different temperatures from 1000 °C to 3000 °C. The precursors were mesophase pitches (MP), low softening point pitches (LSPP/WP) and phenol-formaldehyde resole resins (PF-R). The different precursors were heat-treated to different temperatures between 1000 °C and 3000 °C in an inert gas atmosphere. Each sample was kept for 2 h at the given temperature. The resin was cured in ambient atmosphere at different temperatures (70 °C, 140 °C, 220 °C) for 12 h. After ball milling and washing with deionized water (for resin), all samples (including the pitches) were carbonized in nitrogen atmosphere at 800 °C

for 2 h using a heating rate of 240 °C/h. Additionally, further graphitization (1000 °C up to 3000 °C) was done using a heating rate of 300 °C/h and a residence time of 2 h. The heat treatment at 3000 °C was carried out using an Acheson furnace. Note that the WANS experiments were performed at room temperature.

The samples in Table 1 were measured and evaluated:

Table 1. Overview of the refinement of simulated WAXS data, which were blurred by statistical noise generated by a Gaussian distribution. The results indicate that *OctCarb* can evaluate reproducibly microstructural parameters from given WAXS and WANS data. Since the influence of σ_1 on WAXS (for typical Cu-K$_\alpha$ lab setups) and the influence of σ_3 on WANS data is small, these parameters cannot always be determined exactly. Therefore, the resulting values for σ_1 (WAXS) and σ_3 (WANS) deviated significantly from the input value.

Heat Treatment Temperature	Long Name	Short Name	WANS This Study	WAXS Ref. [40]	WAXS Ref. [37]	WANS Ref. [43]
Phenol-formaldehyde resin (PF-R)						
1000 °C	PF-R 1000	H 1000	X	-	X	-
1200 °C	PF-R 1200	H 1200	X	-	X	-
1500 °C	PF-R 1500	H 1500	X	-	X	-
1800 °C	PF-R 1800	H 1800	X	-	X	-
2100 °C	PF-R 2100	H 2100	X	-	X	X
2300 °C	PF-R 2300	H 1300	X	-	X	-
2800 °C	PF-R 2800	H 2800	X	-	X	X
3000 °C	PF-R 3000	H 3000	X	-	X	-
Mesophase pitch (MP)						
1200 °C	MP 1200	MP 1200	X	X	X	X
1500 °C	MP 1500	MP 1500	X	X	X	-
1800 °C	MP 1800	MP 1800	X	X	X	X
2100 °C	MP 2100	MP 2100	X	X	X	X
Low softening-point pitch (LSPP)						
1200 °C	LSPP 1200	WP 1200	X	X	-	X
1800 °C	LSPP 1800	WP 1800	X	-	-	X
2500 °C	LSPP 2500	WP 2500	X	-	-	X
2800 °C	LSPP 2800	WP 2800	X	-	-	X
3000 °C	LSPP 3000	WP 3000	X	-	X	X

2.2. Wide-Angle Scattering

Wide-angle X-ray scattering was measured using a PANalytical X'Pert Pro powder diffractometer at a wavelength of 1.5418 Å (Cu-Kα radiation). As sample holder, a no-background silicon crystal was used. Wide-angle neutron scattering was carried out at the D4 disordered materials diffractometer at the Institut Laue–Langevin (ILL) in Grenoble [46]. The samples were loaded in an approx. 6mm diameter cylindrical vanadium cell at ambient conditions. Three identical cells were used to collect the data as efficiently as possible. The monochromator generated wavelength was about 0.5 Å (refined λ = 0.4975 Å), which generated a neutron flux about 5.0×10^7 cm^{-2} s^{-1} and a quite high s_{max} = 3.76 Å^{-1} (s_{min} = 0.05 Å^{-1}) with a resolution of about Δs_{min} = 0.005 Å^{-1}. The data collecting time for all samples was approx. 100 min. The measurements [45,46] were performed at room temperature and in vacuum with $p < 10^{-3}$ mbar. Measurements were performed on the empty cells, the instrument background, a standard vanadium sample for intensity normalization, and a nickel powder sample for wavelength calibration. The CORRECT program was then used to normalize the data to arns/str/atom, as well as to make attenuation (i.e., absorption) and multiple-scattering corrections.

Background correction was done in a similar way to the method of Osswald and Smarsly [21]. For five samples containing a significant amount of hydrogen (c(H) > 0.2%), a

C 2023, 9, 27

pseudo-Voigt correction was used as described by Fischer et al. [47] and in 2.2 (PF-R 1000, 1200, 1500 and MP 1200, 1500). For all other samples, a Placzek correction [48] was used to determine the background scattering in a meaningful way. Since the measured s-range is quite high, it can be assumed that the scattering curve oscillates around a constant value and, to be more precise, the intensity must oscillate around $I = 1$ in order to calculate the scattering intensity S of the q ($S(q)$) curve ($q = 2\pi s$), from which the pair distribution function ($PDF(r)$) can be calculated by a Fourier transform (Equation (1)) [49–53]. This pair distribution function was calculated but will be presented in detail in a following work.

$$PDF(r) = 2/\pi \int_0^{q_{max}} q\,(S(q) - 1)\sin(q\,r)\mathrm{d}q \quad (1)$$

2.3. Elemental Analysis

A Vario EL from Elementar was used to determine the carbon and hydrogen contents, whereas for oxygen and nitrogen, an Eltra OHN2000 was used. The results are shown in Section 3.5).

2.4. Raman Spectroscopy

For the PF-R and LSPP series, the data from Schüpfer et al. in 2020/2021 [24,25] were used. These data were measured with a Renishaw inVia Raman microscope system using backscattering geometry at ambient conditions with a 532 nm laser and a 50× objective. For the PF-R, the integral exposure time was 3 accumulations of 30 s with a laser power of 0.6 mW, using a resolution of ~1.5 cm^{-1} and a range of 1000–3200 cm^{-1}. For the LSPP, a 1.5 mW laser was used with an exposure time of 30 s (20 s for LSPP 2500). A total of 10 accumulations were performed for the LSPP 1200 and 3000, 7 accumulations for the LSPP 1800 and 2800, and 15 accumulations for the LSPP 2500. The MP series was measured by a Senterra Raman microscope system from Bruker with 200 accumulations of 5 s in a range of 1000–3200 cm^{-1} using a 50× objective and a wavelength of 532 nm with a 2 mW laser under ambient conditions.

2.5. Data Treatment

2.5.1. Background Correction

For the background correction of the WANS data, the models of Placzek [48] or Fischer et al. [47] should be used, where the background scattering can be calculated by fitting by a cubic polynomial or a pseudo-Voigt function. The samples treated at moderate temperatures, i.e., PF-R 1000 and PF-R 1200, contain a significant concentration of hydrogen, which leads to a non-constant background scattering in the WANS data, especially due to hydrogen (see Section 3.5), which possesses a high incoherent scattering cross section. This pronounced non-constant background scattering can dominate the WANS data. Details about these corrections will also be given in the SI file in S1.

2.5.2. WANS Data Combination

Generally, the interlayer parameters were mainly determined using the (002) and the (004) reflections. While the (002) reflection was clearly visible, the (004) reflection was broad and often appeared as only a shoulder of the (10) reflection, and, therefore, it was difficult to determine L_c and σ_3 values accurately. By using WANS measurements, the (006) reflection can also be used for the analysis because of the absence of damping by a non-constant atomic form factor. However, the instrumental resolution in the s-space ($\Delta s/s$) for the present (Grenoble) WANS data was not as good as in our previous experiments at HZB (Berlin). Therefore, the WANS data from Pfaff et al. measured at the HZB in Berlin were combined with the WANS data measured at Grenoble (Figure 4). This led to merged WANS data with high resolution for small (Berlin) as well as high (Grenoble) s-values and, therefore, both inter- and intralayer parameters could be determined with high accuracy. A

more detailed description, regarding how this combination was performed, can be found in the SI file under S3.

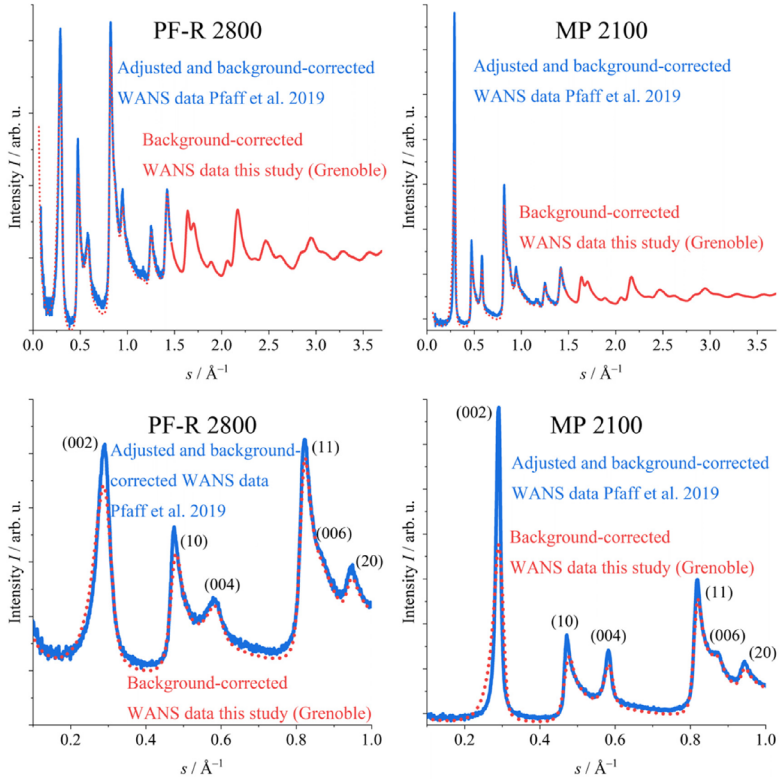

Figure 4. The WANS data from Pfaff et al. (2019) [43] (blue) were combined with WANS data from this study (red). In the range of lower *s*-values, the WANS data from this study (red dotted) were only slightly different for PF-R 2800 (disordered glass-like carbon). For MP 2100 (graphitizable mesophase pitch), the differences were more pronounced, since this sample was more ordered and showed sharper reflections. In addition, the *s*-space resolution of the WANS data acquired at the Grenoble facility was lower than that of Pfaff et al. As a result, the reflections in the anterior *s*-region were broader and had lower intensity. Overall, by combining the different WANS data, both the interlayer and intralayer parameters could be accurately determined.

In total, for the 7 samples, WANS data acquired from two different facilities in each of the cases were measured and combined (PF-R 2100/2800, MP 1200/1800/2100, LSPP 1200/1800). Figure 4 shows the combination of the two different samples, namely, the non-graphitizable phenol-formaldehyde resin heat-treated at 2800 °C and the graphitizable mesophase pitch heat-treated at 2100 °C. The significant width of the (002) reflection indicated a quite disordered stacking for PF-R 2800. For MP 2100, the width of the (002) reflection was much smaller, and therefore, the experimental resolution ($\Delta s/s$) exhibited a higher influence on this reflection. The WANS data from Pfaff et al. measured in Berlin [43] did not suffer from such a broadening, and therefore the two sets of WANS data were

combined to get as reliable an analysis as possible. In the following, the figures and tables (as well as the SI file) show both the results obtained from the combined and from the original WANS data of this present study (Grenoble facility).

2.5.3. WANS Data Refinement

The results of the data refinement using the algorithm of Ruland and Smarsly [34] and the Octave refinement script (*OctCarb*) of Osswald and Smarsly [21] are shown in Section 3.2 (only PF-R), Table S1 (all samples) and Figures S1–S4 (comparison to previous studies). The figures contain the most relevant parameters obtained in this study and our previous ones [37,40,43]. A detailed comparison for each structural parameter is given in Tables S3–S35.

For LSPPs 2500/2800/3000, i.e., for high treatment temperatures, mixed (*hkl*) reflections, e.g., (101) and (102) at s = 0.493 Å^{-1} and s = 0.557 Å^{-1}, respectively, were visible (Figure S7 in the SI). Therefore, the approach by Ruland and Smarsly [34] could not be used for these samples. Instead, the Scherrer analysis [54] was applied based on the full width at half maximum (*FWHM*), as described by ref. [24,37,40,41,43] for such materials.

The basic equation used was the following:

$$L_c = \frac{0.93}{FWHM} \frac{\lambda}{\cos(\theta_{center})} \quad (2)$$

It was used for the background-corrected WANS data for (002) reflections for some of the LSPP samples (2.500 °C and above) using the FWHM of a Gauss-type profile, which is meaningful for such powder diffraction experiments [43,55]. Here, 0.93 was chosen as factor, as described to be meaningful for small and disordered stacks [56]. The θ_{center} is the position of the Bragg signal in units of radians. The parameter L_c was calculated using Equation (2), and $\overline{a_3}$ and l_{cc} were calculated directly from the positions of the (002) and (10) reflections, respectively, in this case. Additionally, it must be assumed that no further disorder was present in the samples, i.e., σ_3 = 0 Å.

3. Results

3.1. Qualitative Discussion of the WANS Data

The background-corrected WANS data of the NGCs from the phenol-formaldehyde resin (PF-R) are shown in Figure 5, and the corresponding data for the low-softening point pitch (LSPP) and mesophase pitch (MP) samples can be found in Figures S6 and S8, respectively. The WAXS/WANS of NGCs is the superposition of interlayer scattering caused by the stacking, and the intralayer scattering caused by the graphene layers themselves. Assuming that a higher temperature results in growth and higher order in both, the graphene layers and in the layer stacking [20,37–43], overall, the reflections of samples get sharper with higher treatment temperature. For instance, PF-R 1000 showed broad reflections, while PF-R 3000 exhibits sharper reflections (Figure 5).

Additionally, the influence of the precursor can be studied for these two types of carbon: the PF-R-based carbon was prepared from phenol and formaldehyde, but the pitches consisted mainly of different aromatic molecules as building blocks (Figure 6). Therefore, the amount of foreign atoms, especially of hydrogen and oxygen, which prevents the formation of highly ordered graphene layers [37], was higher in the PF-R precursor than in the pitches. Moreover, PF-R polymerized in a first step without building sp^2-hybridized layers. By contrast, in pitch-based carbons, the dimensions and order of the graphene stacks increase faster with increasing heat treatment temperature, as is qualitatively seen in Figure 2B,C. In the following chapters, we address the question as to whether structural parameters and the evolution of the graphene structure can be correlated with differences in the content of foreign atoms, assuming that a high amount of hydrogen hinders the formation of well-defined and highly ordered sp^2 layers. Evidently, the significant width of the reflections of the PF-R samples at higher s-values speaks to a relationship between the

C 2023, 9, 27

impurities and the degree of disorder, especially for the lower temperatures of this series (1000 °C and 1200 °C).

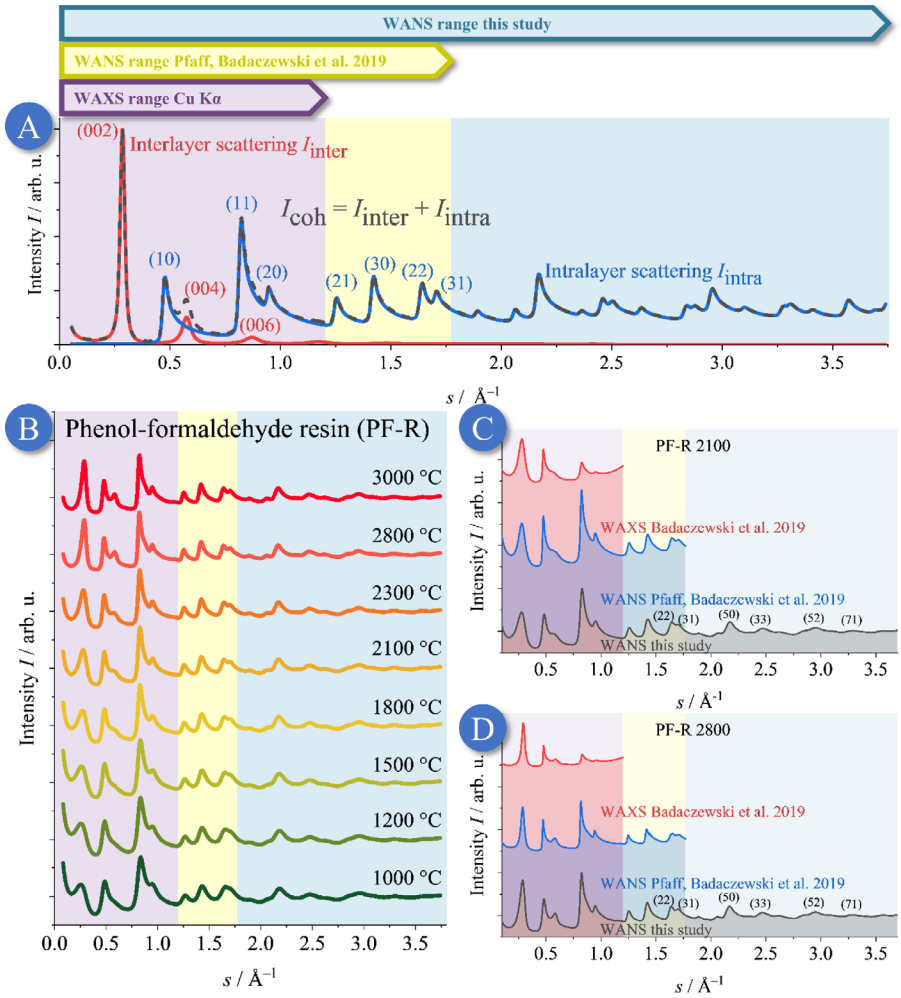

Figure 5. (**A**): The theoretical WANS intensity normalized per carbon (in electron units) $I_{e.u.}$ is given by a superposition of the interlayer (I_{inter}) and intralayer (I_{intra}) scattering. (**B**): WANS data of the phenol-formaldehyde resin (PF-R) carbon samples, including the previous WAXS (purple), the WANS (yellow) data, and the additional WANS range of the present study (blue). The temperature values represent the respective maximum heat treatment temperature. All these WANS data were already corrected for incoherent scattering using the procedure shown in Section S1 in the SI. (**C**,**D**): Comparison between the previously published WAXS (blue) and WANS (red) data from Pfaff et al. (2019) (blue), and the WANS measurements of this study, acquired at the Grenoble facility (black).

C 2023, 9, 27

Since in this present study, the accessible s-range was much larger than in Pfaff et al. (2019) [43] and Badaczewski et al. (2019) [37], the intralayer structure could be determined more accurately. By contrast, for the stacking, no improvements were possible, as the widths of the (00l) reflections for these carbons increased so strongly with increasing s that these reflections were dampened out at moderate s-values. The WANS data for the temperature series of the LSPP and MP samples (pitches) can be found in the SI file (Figures S6 and S8).

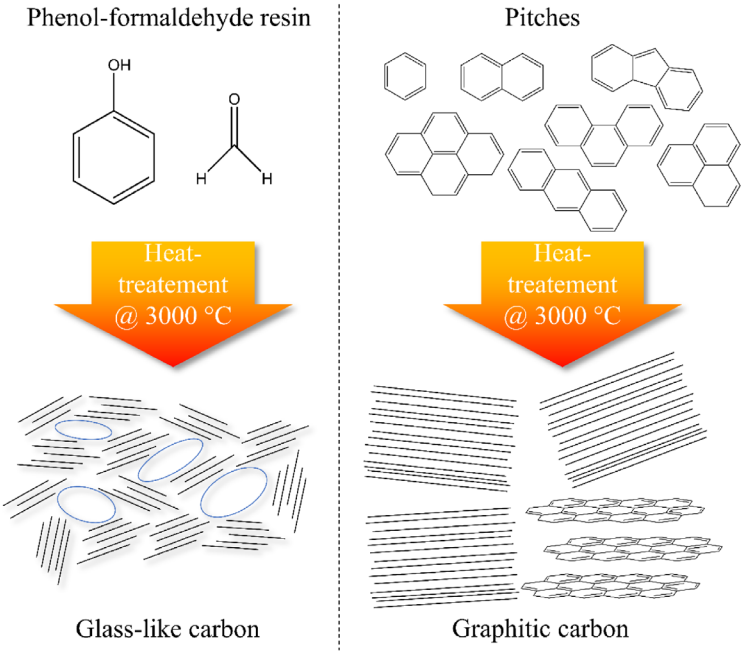

Figure 6. Schematic representation of the two types of precursors used. Phenol-formaldehyde resins form slightly porous glass-like carbons at high temperatures, while pitches, especially low softening-point pitches, can form graphite at very high temperatures.

The main advancement of this study using a beamline at the Grenoble neutron facility, when compared to our previous WANS measurements at HZB (Berlin), is the acquisition of reflections of up to quite high s-values, where mainly (hk) reflections contribute to the WANS pattern. Therefore, more reflections were used, allowing accurately determining the layer extent (L_a) and disorder (σ_1) from the (hk) reflections, using the Grenoble WANS data. Nevertheless, these WANS data suffered from a lower resolution for lower s-values. Since, however, the low-s-range is necessary to precisely determine the interlayer stacking, the evaluation of the WANS data from Pfaff et al. (2019) [43] was assumed to be more accurate at small s values, i.e., for determining the interlayer parameters (L_c, σ_3). Therefore, to achieve a maximum precision in quantifying the interlayer as well as the intralayer parameters, we combined the data of the two WANS measurements acquired from identical samples, the procedure of which is described in the SI file (S3). It should be noted that the indexing shown with parentheses strictly denotes lattice planes, and reflections would have to be indexed without parentheses. However, brackets are used in this publication for both meanings to improve readability.

3.2. Non-Graphitic Carbons from Phenol-Formaldehyde Resin (PF-R)

Here, the results for the phenol-formaldehyde resin (PF-R) temperature series will be discussed (Figure 7). Overall, the stack height (L_c) and layer extension (L_a) increased with increasing heat treatment temperature, while the disorder parameters in the stacking and layers (σ_3 and σ_1, respectively) decreased. Additionally, the average layer distance ($\overline{a_3}$) decreased, while the minimal layer distance ($a_{3\,\mathrm{min}}$) increased as well. These changes were in conformity with the assumption that the degree of order, as well as the dimension of the graphene stacks, raises with increasing temperatures. PF-R 1000 contained a significant amount of hydrogen, which generated a substantial background scattering in WANS and required suitable correction. We found that this procedure rendered the determination of the average layer distance $\overline{a_3}$ to be uncertain, but all other parameters did not seem to be influenced by the high hydrogen content. In the following, the parameters and trends upon temperature treatment are discussed and compared to our previous WANS/WAXS series for these samples.

3.2.1. Graphene Stacks of the PF-R Carbons Temperature Series

Notably, our previous and current WAXS/WANS studies (Figure 7) yielded similar trends in the structural parameters as a function of treatment temperature, even with the absolute values being different (beside PF-R 1000, as described above). While the L_c values were similar, this was not the case for the stacking disorder (σ_3). Note that a higher value of σ_3 indicates a higher degree of disorder. As found by Badaczewski et al. [37], the parameter value decreased from ~0.5 to 0.15 Å, whereas, in this study, the value decreases from 1 (upper limit) to ~0.8 Å. These different absolute values thus suggested a higher degree of disorder, but such straightforward interpretation ignores another fitting parameter, which is the minimal layer distance ($a_{3\,\mathrm{min}}$), which had been reported in previous studies of such carbon materials [20,37,39–41,43]. Based on the excellent data quality in this present study, we found that the dimension of refined $a_{3\,\mathrm{min}}$ values was reasonable, in the range of the ideal layer distance in graphite. However, the uncertainty in $a_{3\,\mathrm{min}}$ as obtained from the refinement was so high that no convincing relationship to the treatment could be deduced. Additionally, the average layer distance ($\overline{a_3}$) is directly linked to the position of the reflection using Bragg's law and should, therefore, not change [57]. Iinterestingly, the L_c value slightly decreased in the temperature range of 500 °C 1000 °C, and then continuously increased. This decrease can be attributed to the release of pyrolysis gases in this temperature range, which results in a certain disruption of the graphene stacks, as has been reported previously [37].

The uncertainty for $\overline{a_3}$ as a refined parameter was between 5% and 10%, which decreased with higher heat treatment temperature. This tendency can be explained by the interplay of ($a_{3\,\mathrm{min}}$) and the standard deviation of the layer distance (σ_3). Regarding to the work of Ruland and Smarsly [34], all these parameters contribute to the profile shape of the (00*l*) reflections, and $a_{3\,\mathrm{min}}$ has an especially significant influence on the peak position. Therefore, the refined values for $a_{3\,\mathrm{min}}$ and σ_3 in this study might be different compared to the references. However, the values of σ_3 possess a lower uncertainty and can thus be used to compare the samples with respect to this type of translational disorder.

Details about the analysis of the polydispersity of the stacks (κ_c) and the homogeneity (η) can be found in the SI file in S1.

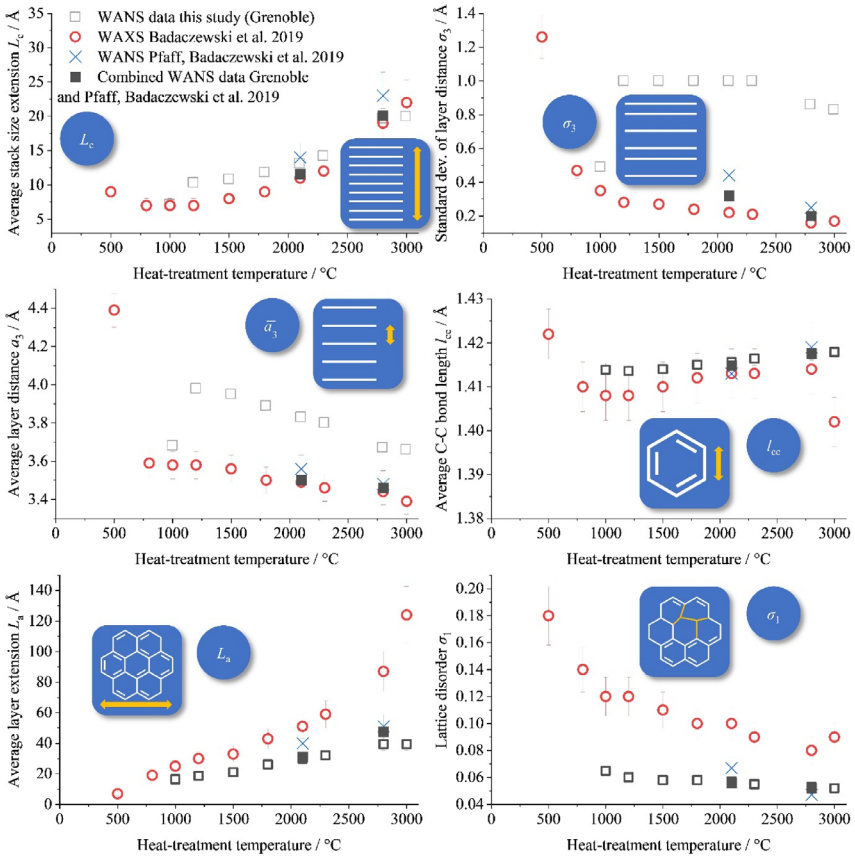

Figure 7. Microstructural parameters obtained from WANS refinement for the carbons derived from phenol-formaldehyde resin (PF-R) as precursor (black border only: this study (WANS Grenoble), red: Badaczewski et al. (WAXS) [37], blue: Pfaff et al. (WANS Berlin) [43], black filled: combined WANS data from Grenoble and Berlin). More information about the meaning of the absolute value of σ_1 can be found in the SI file in S6. The decrease in L_c for temperatures between 500 °C and 1000 °C might have been caused by the release of pyrolysis gases in this temperature range, as already described previously [37]. This interpretation is supported by the quite high values of σ_3 for 500 °C.

3.2.2. Layer Structure of the Phenol-Formaldehyde Resin (PF-R) Temperature Series

For the microstructural parameters specifying the graphene layers, similar conclusions can be made as for the stacking with regard to the comparison with our previous studies. While the average C-C bond length (l_{cc}) was nearly identical to the results of Badaczewski et al. [37], the values for the layer disorder (σ_1) and the average layer extension (L_a), obtained in this study, were significantly lower. Additionally, the polydispersity of the layer extension ($\kappa_a = 1/\nu$) was smaller, since ν was set to seven to follow the work of Osswald and Smarsly [21], and, therefore, κ_a was systematically smaller. However, the influence of κ_a on the WAXS/WANS data is only small; it is rather L_a and σ_1 that determine the (hk) profiles.

Smaller layer dimensions (L_a) lead to broader reflections; a smaller value of σ_1 causes the opposite, i.e., sharper (hk) reflections. As a difference, the layer dimension L_a influenced all (hk) reflections identically with respect to the width, while—for fundamental reasons - the impact of σ_1 on reflections width continuously increases at higher s values [34]. Since the measured s-range was much higher for our WANS data than for the WAXS data, and due to the absence of the damping of the atomic form factor, the intralayer parameters for the layer structure were determined much more reliably in this study than in the reference studies.

To illustrate the influence of the experimental data range, the measured and refined data for the PF-R 3000 are shown as a representative sample (Figure 8). Additionally, simulated WANS data using the microstructural parameters from Badaczewski et al. [37] (refined from WAXS data) are included. Hence, beyond the accessible data range, these simulated data are a projection calculated with the refined set of parameters based on WAXS data featuring a shorter s-range. It can be seen that the higher order (hk) reflections were broader compared to the actually measured WANS reflections. This deviation can be explained by the parameter σ_1, which has a higher influence at higher order reflections at a large s. The refinement of the WANS data reveals that σ_1 was substantially smaller than determined in our previous study, and, concomitantly, L_a was significantly smaller, too, which is further illustrated in Figure 9A. In detail, the sp^2-hybridized graphene sheets had markedly smaller extensions (L_a~16–40 Å for 1000 °C–3000 °C, compared to 7–87 Å), but possessed a higher degree of order (σ_1~0.065–0.05, compared to 0.18–0.08) compared to Badaczewski et al. [37]. An interpretation of different values for σ_1 is discussed in the SI in S6.

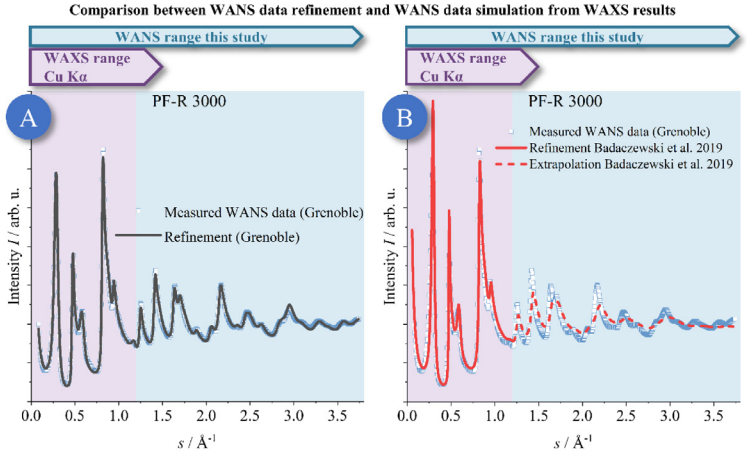

Figure 8. (**A**): Measured and refined WANS data of PF-R 3000. (**B**): Measured WANS data with simulated WANS data calculated from the WAXS refinement of Badaczewski et al. [37]. The dotted curve means an extrapolation in the range of large s, which was not measured in the reference.

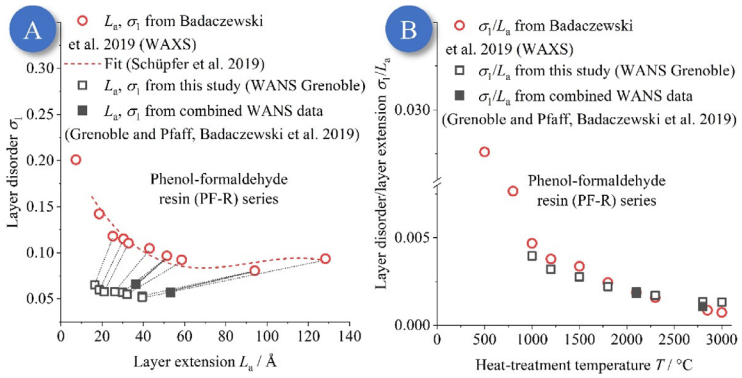

Figure 9. (**A**): Plot of σ_1 vs. L_a for the phenol-formaldehyde resin (PF-R) temperature series. determined by WANS and previous WAXS results from Pfaff et al. 2019 [43] and fitted by Schüpfer et al. 2019 [25]. This comparison illustrates that the σ_1 values were much smaller than previously assumed. (**B**): However, the ratio σ_1/L_a did not change, compared to our previous studies, over the whole temperature range. This agreement is due to the fact that it is these two parameters which determine the profile of the (*hk*) reflections, i.e., their widths, especially at large *s* values. A similar figure for the pitches can be found in the SI file as Figure S15.

Figure 8 thus demonstrates that the range of *s* values exerts a dramatic impact on the evaluation of WANS/WAXS data with regard to the extraction of structural parameters. While the qualitative progression of layer extent and disorder as a function of treatment temperature is correctly described by our previous studies on the same samples (Badaczewski et al. [37]), the cut-off at moderate *s* values resulted in erroneous values for L_a and σ_1. In other words, if the already-published parameters L_a and σ_1 described were correct, the simulated data in Figure 8 should fit the measured WANS data over the whole *s*-range and not only for small *s* values. We conclude that the intralayer parameters determined from the present WANS data are significantly more accurate and reliable than our previous analyses based on WAXS.

Figure 9B shows the quotient σ_1/L_a, which depends on the heat treatment temperature, for the different analyses. This quotient does not significantly alter for the whole temperature range, which is reasonable and not surprising, because the width of the (*hk*) reflections is mainly determined by L_a and σ_1. Also, the combination of the different WANS data did not influence the intralayer parameters significantly, since the experimental broadening in the WANS data from Grenoble was smaller for higher *s* values. The higher (*hk*) reflections did not suffer from this problem, i.e. L_a and σ_1 could be determined accurately.

3.3. NGCs from Mesophase (MP) and Low Softening-Point Pitch (LSPP)

In general, pitch-based carbon (MP and LSPP) possesses a higher order in the graphene microstructure than the resin-based carbons (PF-R) at the same heat treatment temperature. Additionally, the low softening-point pitch (LSPP) exhibits a more ordered graphene structure than the mesophase pitch. This general behavior is already well known and illustrated in Figure 6. The phenol-formaldehyde resin contains phenol and formaldehyde, which polymerizes under the release of water. Nevertheless, the resulting carbon structure still contains hydrogen and oxygen (see elemental analysis in Section 3.5 or Table S3), especially at lower temperatures. The pitches mainly consist of aromatic molecules, which can build sp^2-hybridized graphene layers more easily than resin. Therefore, the layer extension is much higher for the pitches, and, additionally, at very high heat treatment temperatures, a graphitic carbon is formed, i.e., one that shows three-dimensional order.

C 2023, 9, 27

Since the softening point of LSPP is much smaller than for the mesophase pitch (70 °C in contrast to 250 °C [40]) due to generally smaller polyaromatic molecules, the LSPP forms bigger graphene layers and stacks than MP. Contrary to PF-R-based carbon, the LSPP samples start forming graphitic carbon above temperatures of 2500 °C (see Figure S8), as is evidenced by the occurrence of reflections of the (*hkl*) type, i.e., a three-dimensional periodicity. Hence, for these samples, the model of Ruland and Smarsly [34] cannot be used. Thus, the LSPP 2800 and 3000 should be analyzed by a single-peak analysis. The LSPP 1800 and 2500 were borderline cases for both evaluation methods. Here, the LSPP 2500, LSPP 2800, and LSPP 3000 were included into the comparison of structural parameters (Figure 10) using a single-peak analysis, as they are not NGCs but graphitic carbons. This discussion should be kept in mind when dealing with the resulting absolute values.

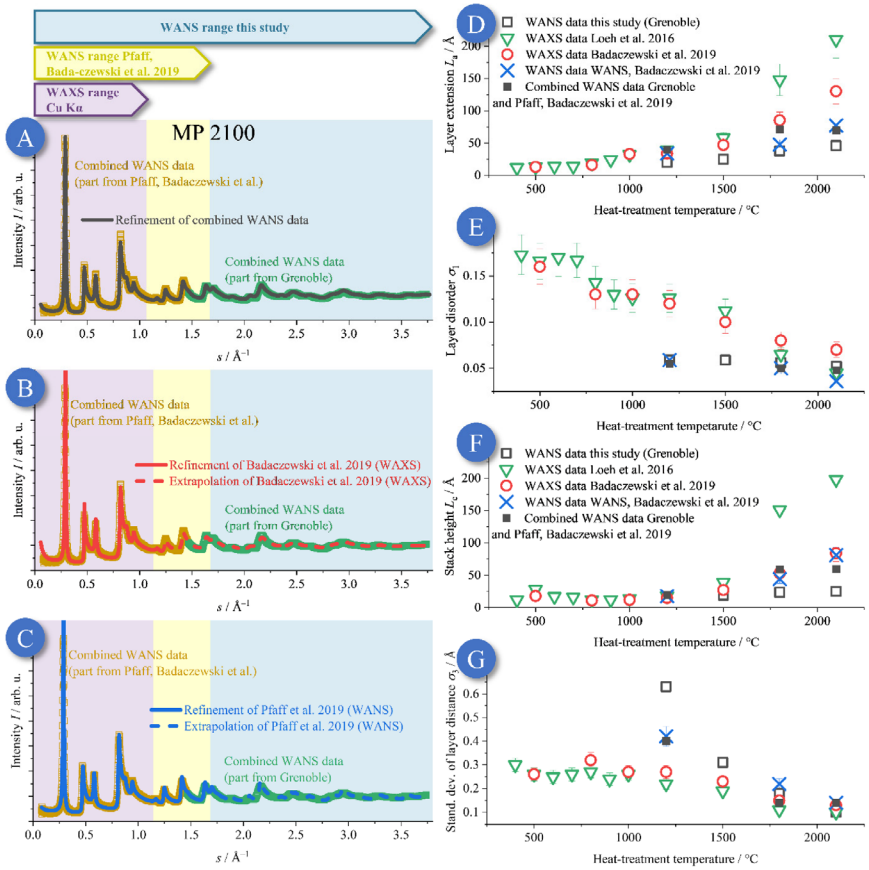

Figure 10. (**A–C**): Comparison of the mesophase pitch temperature series between the present WANS study, WAXS analysis of Badaczewski et al. [37], and WANS data from Pfaff et al. [43]. There are significant differences between the fits of this study (black border only) and the simulation using the WAXS results from Loeh et al. [40] (2016), Badaczewski et al. [37] (2019) and the WANS results from Pfaff

et al. [43] (2019). Especially for more highly ordered samples, i.e., higher heat treatment temperatures, the resulting structural parameters are quite different. These differences are caused by the different experimental accessible *s*-ranges, as well as by different experimental broadening of the WANS measurements [43]. Therefore, the WANS data from the two different WANS facilities (Grenoble, HZB) were merged to optimize the accuracy in the parameter determination. The results from the reference studies were used to simulate a WANS curve in their measurement range (filled) and to extrapolate them beyond the range (dotted curve). It can be seen that the intralayer parameters could not be determined precisely using the prior measured data, since the extrapolation based on the previous studies did not fit the current WANS data taken at Grenoble facility. (**D–G**): Importantly, previous WAXS measurements from Loeh et al. and Badaczewski et al. [40] overestimated the layer size and disorder when compared to the present results determined from the WANS data from the beamtime in Grenoble. Due to the higher amount of visible (*hk*) reflections, it can be assumed that the results from these WANS data are more accurate. On the other hand, the experimental broadening in this study (Grenoble) at small *s* values led to too high and disordered stacks compared to WANS measurements from from Pfaff et al. [43]. A zoom of the WAXS region (purple) can be found in the SI file (Figure S15).

Comparison to Previous WANS and WAXS Studies

The works of Pfaff et al. [43], Badaczewski et al. [37], Loeh et al. [40] had analyzed the very same mesophase pitch samples by WAXS [37] and WANS [43], the results of which we now compared with the present WANS analyses (Figure 10). The resulting values can be found in the SI file in Figures S6 and S8, as well as in Table S1. Compared to the previous WAXS analyses, the values for the average layer distance ($\overline{a_3}$) and C-C bond length (l_{cc}) were comparable. However, for most of the other important structural parameters (L_c, L_a, σ_1, ...) there were marked differences, especially compared to the WAXS study of Badaczewski et al. [37], thus again proving the benefit of using WANS data for large *s* values.

To illustrate the importance of a large *s*-range as shown in in Figure 10, we compared the refinement of the combined WANS data (Grenoble, HZB, Figure 10A) with simulated WANS data (Figure 10B,C) using the structural parameters taken from the previous WAXS and WANS measurements from Loeh et al., Badaczewski et al., and Pfaff et al. [37,40,43] for the MP 2100. Thus, in the case of Figure 10B,C, the curves are an extrapolation beyond the respective maximum accessible value of *s* for the respective instrument. These reflections were too broad in case of the extrapolation using the parameters from Badaczewski et al. [37] as determined by WAXS (Figure 10B). In contrast, for the simulation using the WANS results from Pfaff et al. [43] (Figure 10C), the simulated reflections at higher *s*-values were too sharp. In conclusion, too big and ordered layers were obtained in the WANS study of Pfaff et al. [43], and too disordered layers were proposed in the WAXS study of Badaczewski et al. [37], as shown in Figure 10D,E. Magnified figures further illustrating such comparisons are given in Figures S14 and S15.

Overall, it can be concluded that the presence of higher-ordered (*hk*) reflections is crucial to determine the intralayer parameters exactly, but a high *s*-space resolution over the entire *s*-range is crucial to determine the interlayer parameters exactly. Hence, ideally, a valid determination of all microstructural parameters can only be reached by using a combination of two different WANS measurements, for the small and large *s*-range, as described in Section 2.2.

Since WAXS study of Loeh et al. [40] published only results for lower heat treatment temperatures of LSPP, only a few LSPP samples could be compared with the results of the present WANS study (Figure 11). However, a detailed comparison was possible with the WAXS analysis from 2019 [37] and the WANS analysis of Pfaff et al. [43]. The differences for the microstructure data of the low softening-point pitch (LSPP) at a heat treatment temperature of 1200 °C (LSPP 1200) were only small (Figure 11). In contrast to this, the results for LSPP 1800 were very different. These differences can be explained by the

C 2023, 9, 27

experimental broadening from the WANS data collected in Grenoble. The combination with the WANS data from Berlin lead to more reliable and accurate results for the intralayer parameters.

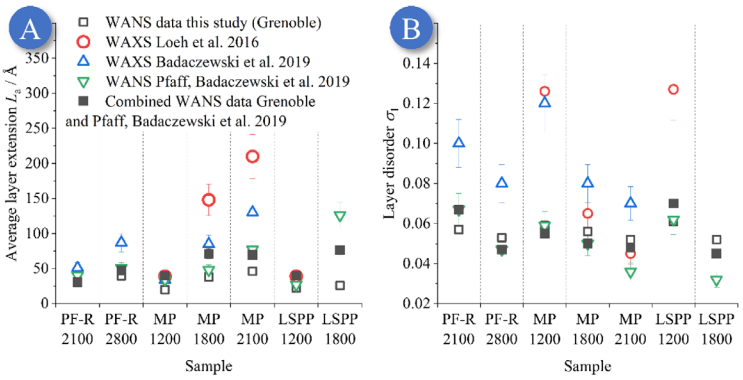

Figure 11. (**A**,**B**): Comparison of L_a (**A**) and σ_1 (**B**) values obtained from different scattering experiments using X-ray and neutron radiation for identical samples. Black border only: WANS results from WANS data collected in Grenoble. Red: WAXS results from Loeh et al. (2016) [40]. Blue: WAXS results from Badaczewski et al. (2019) [37]. Green: WANS results of Pfaff et al. (2019) [43]. Black filled: results from the combination of WANS data from Grenoble and Pfaff et al. [43]. In general, WANS measurements lead to more accurate results for the layer structure because of the larger accessible s-range and the absence of the atomic form factor.

For LSPP 2500/2800/3000, we only used the average stacking height L_c as determined by Scherrer analysis from the (002) reflection (Equation (2)) for comparing the samples (Figures S7 and S8, Table S1). As for the other samples and parameters, the overall tendency, i.e., an increase in L_c following an increase in heat treatment temperature, was identical to the previous studies, but the absolute values were different. These differences might have been caused by the different approaches according to the fit function (Gauss vs. Voigt) and the different resolution $\Delta s/s$, which both influenced the resulting parameters. However, the value for L_c determined from the WANS data from Grenoble seems to be too high for the LSPP 2500, which was caused by the degree of disorder in this sample. At this heat treatment temperature, no three-dimensional crystallographic order was present, and the resulting stack height L_c was intrinsically overestimated by the Scherrer equation. Additionally, the average layer distance ($\overline{a_3}$) showed a clear decreasing tendency down to 3.38 Å for the LSPP 3000, which is close to the theoretical value of perfect graphite (3.35–3.36 Å) and corresponds to a graphite-like microstructure [58,59].

3.4. Structural Differences between the Resin and the Pitches

Overall, there was a clear tendency of increasing domain sizes and decreasing disorder from the phenol-formaldehyde resin (PF-R) over the mesophase pitch (MP) to the low softening-point pitch (LSPP) carbons. For the interlayer structure, the parameters L_a (average layer extension) and σ_1 (layer disorder) are most relevant. For a treatment at 2100 °C, L_a increased from 16 to 40 Å for the PF-R in contrast to 20 to 45 Å for the MP, and even higher values that were found for the LSPP. Owing to the occurrence of general (*hkl*) reflections for the LSPP 2500/2800/3000, but not for the PF-R samples treated at such temperatures, L_a could not be calculated and compared for these samples in a consistent way. The observed differences were caused by the different precursors, as pitches contain a higher proportion of aromatic molecules in the precursor with a relatively low concentration

of foreign atoms. Thus, these polyaromatic hydrocarbons grow faster to extended sp^2-hybridized layers. For both the PF-R and MP, σ_1 significantly decreased upon treatment at 2100 °C, from σ_1 = 0.065 to 0.052 (PF-R) and σ_1 = 0.059 to 0.0482 (MP), which indicates higher-ordered graphenes.

In contrast to the interlayer structure, the parameters L_c (average stack height) and σ_3 (stacking disorder) are the most significant ones regarding the interlayer structure. Surprisingly, and contrary to expectation, our WANS analysis revealed that, for the MP and LSPP carbons, L_c remained quite small until reaching considerably high temperatures (see Figure 10, Figures S7 and S8), did not exceed ~60 Å at up to 2200 °C, and only increased up to ~70 Å for a heat treatment temperature of 3000 °C (LSPP). Yet, the L_c values for the MP/LSPP were significantly larger than for the PF-R carbons and rose moderately from 7 to 20 Å (3000 °C). Interestingly, the disorder of the stacks was still higher for the MP samples than for the LSPP carbons, which can be explained by the different softening points (250 °C for MP vs. 70 °C for LSPP). In general, the softening point influences the carbonization and pyrolysis at lower temperatures, as a lower thermal energy is needed to build sp^2-hybridized layers and small stacks, as is the case for materials with lower softening points [40]. In contrast to the pitches, PF-R-derived carbon contains more foreign atoms and less aromatic hybridized molecules, which is related to the larger degree of disorder and smaller stack dimensions. See the following section for more details. Additionally, these materials can contain nanoscaled porosity, implying that the resulting density is significantly lower than for the pitches or graphite [37].

3.5. Comparison of Structural and Chemical Analysis

Elemental analysis made it possible to determine the proportions (mass) of hydrogen, oxygen, nitrogen, and sulfur (the latter only for the LSPP). Overall, the amount of foreign atoms decreased with an increasing heat treatment temperature (Figure 12). In the case of the LSPP, sulfur was additionally detectable, which is caused by the precursor, but the amount was so small that it will not be considered in the further analysis. The elemental analysis data for the PF-R were already published by Badaczewski et al. [37], and those for the LSPP were only published for lower temperatures [40]. The other values were derived in the present study. The results for all samples are shown in Figure 8, Figures S1–S3, and Table S3. It should be emphasized that we focused on temperatures above 1000 °C, which pertain to quite low contents of foreign atoms below 1 wt.%. Still, even such small fractions seemed to exert a strong impact on the formation of the graphene layers, as is discussed in the following. Notably, a small amount of only 0.5 wt.% hydrogen impeded the analysis of WANS data due to the huge incoherent background.

As a first conclusion for the PF-R samples, there is a clear correlation between the graphene sizes/disorder and the concentration of hydrogen/oxygen/nitrogen (Figure 12): along a decreasing content of these impurities, the stacks/layers continuously become bigger and more ordered. Note that the hydrogen and oxygen fractions are not independent, as hydrogen is linked to oxygen-containing moieties such as hydroxyl or carbonyl groups, but it is also bound to carbon at the edges of the graphene sheets. Hence, the lateral growth of graphenes should go hand in hand with the removal of hydrogen.

In detail, the L_a values for the PF-R (Figure 12) were still quite small for a treatment at 1000 °C, being on the order of 1–2 nm only, as was already found in previous studies (Loeh et al., Badaczewski et al., Pfaff et al. [37,40,43]). At higher temperatures, the substantial growth of the layers, as well as a decrease in the disorder parameter σ_1, were observed, which corresponded to a decline in the fraction of hydrogen/oxygen below 0.5 wt.%. Our previous studies suggested that hydrogen and oxygen-containing molecules such as CO_2 and H_2O are released at temperatures up to 1000 °C [37].

C 2023, 9, 27

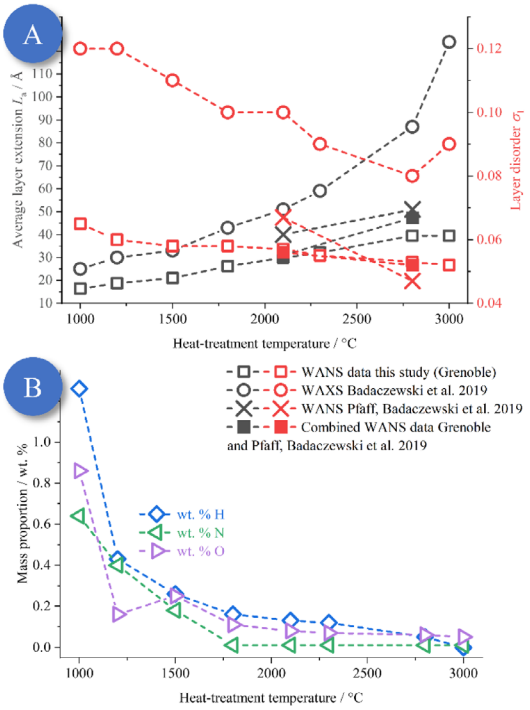

Figure 12. (**A**)**:** Comparison of the layer extension (L_a) and disorder (σ_1) with elemental analysis (**B**) for phenol-formaldehyde resin (PF-R) as precursor. Foreign atoms such as oxygen and nitrogen hinder the formation and lateral growth of graphenes (in the form of carbonyl groups, -OH groups, etc.). Therefore, a decreasing concentration of elements leads to bigger and more highly ordered graphene layers. The values of L_c and σ_3 are not shown here, because the trends were quite similar to (L_a) and disorder (σ_1). The corresponding figures for MP and LSPP can be found in the SI file (Figures S12 and S13). The data used can be found in the works of Badaczewski et al. (2019) [37] and Pfaff et al. (2019) [43].

For both pitches (Figures S12 and S13), similar trends were observed; thus, only a small number of samples were studied. For these pitch samples, the amount of foreign atoms decreased upon higher heat treatment temperatures, and the absolute amount was significantly smaller than for the PF-R samples at the same temperatures. This smaller content of foreign atoms was accompanied by larger stack/layer dimensions and higher order when compared to the resin-based carbon samples. Interestingly, nitrogen was still present at higher heat treatment temperatures for all samples, and a small residual amount remained, even at high T. In addition, only for the LSPP samples at 2500 °C and above, "mixed" (*hkl*) reflections occurred, which speaks to a graphitic structure. At this point, hydrogen was no longer detectable. For the pitches, a further parameter needed to be considered in the evolution of the microstructure next to the content in foreign atoms, which was the softening-point itself, as seen by the differences between MP and LSPP.

In contrast to this, the PF-R as a precursor led, in general, to glass-like carbon through to the pyrolysis process at lower temperatures. This process is caused by the significant amount of oxygen/nitrogen in the precursor even at higher temperature, as well as by

the lower proportion of aromatic/$sp^2$0hybridized species, thus hindering the formation of graphene layers [37]. Closer insight was obtained by comparing the structural parameters L_a and σ_1 with the composition (Figure 12): while σ_1 stayed almost constant up to high temperatures, L_a continuously rose, while the amount of foreign atoms declined slowly in the range of 2000 °C. Thus, the changes in composition seem primarily be related to the lateral growth of the graphenes, while, surprisingly, their order (σ_1) was already quite developed and high as for the pitch-based carbons (Figure 11) but was not further enhanced at very high treatment temperatures (above 2500 °C). Hence, the thermal energy seems to be decisive for removing foreign atoms from the graphenes' edges and for the conversion of sp^3 into sp^2 carbon.

Overall, based on the comparison of the elemental analysis of the determined microstructure data, the following can be concluded:

1. The stack height, stack disorder and the layer extension/disorder are strongly linked to the amount of foreign atoms, especially oxygen. Due to the very low amount of foreign atoms at this temperature, sp^3-hybridized domains probably cause this disorder.
2. A detailed comparison of composition and disorder, as described by the parameter σ_1, is only meaningful using valid microstructural data, which could not be obtained in previous studies, except for by using the high-quality WANS data in this study.
3. Oxygen or oxygen-containing functional groups are located on the edges as well as on the lower/upper side of the graphene layers; otherwise, either the layers or the stacks would have to grow faster at high temperatures, especially for the PF-R carbon.
4. Oxygen is believed to often be removed as water or other functional groups that contain hydrogen. While hydrogen is still required at the edges of the graphene layers to saturate the free electrons, the hydrogen content nonetheless decreases significantly. Therefore, oxygen and hydrogen are believed to be removed together. Similar trends for lower heat treatment temperatures have been shown and proven in previous studies [37,40].
5. Nitrogen has no direct correlation with the stack/layer size and order. Therefore, nitrogen must be mainly built in into the graphene structure. This is possible and plausible, since nitrogen can also make sp^2-hybridized structures.
6. For the formation of three-dimensional ordered graphite, the amount of foreign atoms must be small, close to zero. It seems that the absence of hydrogen (or a not-detectable amount) is a good indicator.
7. At very high temperatures (2500 °C and above for LSPP), it is not the foreign atoms, but the heat treatment temperature, i.e., the thermal energy, that causes the higher order of the graphite stacks.

3.6. Raman Spectroscopy

Raman spectroscopy analysis was performed using the procedure that was recently introduced by Schüpfer et al. in 2020 [25]. In that study, several of the samples had already been investigated, and an improved methodology was established for the interpretation of Raman spectroscopy data in terms of L_a and σ_1 by comparison with the WAXS analysis. Hence, here we used the advanced precision in the determination of the L_a and σ_1 by WANS analysis to check and validate the procedure of Schüpfer et al. [25]. For the PF-R and LSPP, the already published data were used, but for the MP series, Raman spectroscopy data were measured in this study. Overall, the used spectral range of 1000 cm^{-1}–3000 cm^{-1} shows the typical, most common D, G, D' and 2D bands (Figure 13 and Figure S18) [24,25,60–63]. As with most prominent signals, a broad and overlapping D (~1350 cm^{-1}) and G (~1850 cm^{-1}) band were observed for lower treatment temperatures for all samples. The absence of a 2D band up to this temperature indicated small and disordered graphene sheets, which matched the WAXS/WANS analysis [25,61,64]. For higher treatment temperatures, the D' and 2D bands appeared starting from ~1800 °C. At even higher temperatures, the signals became sharper, and, especially for the LSPP (Figure S18), the D and D' bands even

disappeared, which was due to a highly ordered microstructure in the pitch-based carbons, which coincided with the WANS analysis shown in the section above. A more detailed interpretation of the general trends for the temperature dependence of the Raman data of the PF-R and LSPP samples can be found in the work of Schüpfer et al., 2020/2021 [25].

In essence, Schüpfer et al. [25] correlated basic quantities of the Raman spectroscopic data of NGC, namely, the G- and D-band positions, the I_D/I_G ratio, and the widths of the D- and G-band positions, against L_a and σ_1. Owing to the large number of PF-R- and pitched-based carbon, a large range of L_a values provided a meaningful basis for such correlations. This present study achieved an improved accuracy in determining L_a and σ_1 and, thus, enabled a revision of the dependences established in ref. [25] when we recall that the WANS analysis on the Grenoble data yielded significantly smaller L_a values for the very same samples. In the case of the I_D/I_G ratio for the PF-R (Figure 13A), the general trend of an increase in I_D/I_G ratio with increasing L_a was confirmed. However, we observed a small, but significant shift of the overall dependence to smaller values of L_a when compared to ref. [25], while, for the LSPP and MP samples (Figures S6 and S8 in the SI), the new values lay well within the proposed relationship. Our study thus supports the relationship between the I_D/I_G ratio and L_a for small $L_a < 6$ nm, but unfortunately for $L_a > 6$ nm, further samples need to be studied to determine the course of this relationship.

For the PF-R, the I_D/I_G ratio (Figure 13A) increased up to a temperature of 1800 °C, and, additionally for the PF-R and LSPP, a clear blue shift was visible up to this temperature (Figure 13B). Additionally, the shape of the 2D signal was strongly symmetric and, therefore, a Lorentzian curve could be used to fit these data. The resulting full widths at half maximum (FWHM) were broader than in graphene, which indicates the turbostratic structure, thus independently confirming the WAXS and WANS analysis [25,34,65]. The asymmetrical shape of the 2D band for the LSPP at 3000 °C, where the right shoulder was higher than the left, is a clear indicator for a graphitized carbon structure [61,64].

Also, the measured D-band position depending on the average layer extension (L_a) was significant lower for the PF-R series when compared to the study of Schüpfer et al. [25], while for the LSPP, the measured values fit the theoretical values (Figure S18). However, for a highly graphitizable precursor (LSPP), the position of the D-band fit the theoretical values well, and the layer size could be determined from Raman measurements.

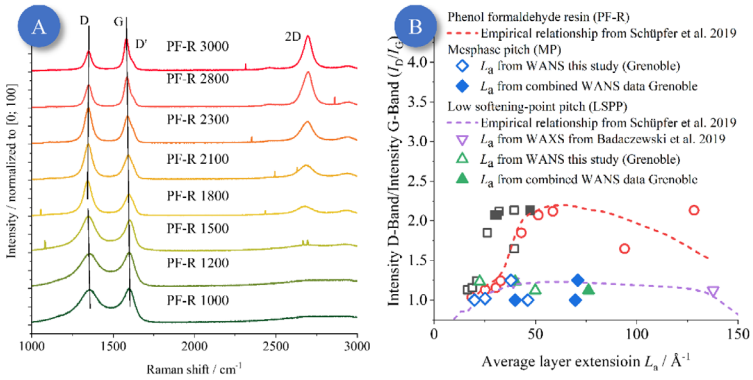

Figure 13. *Cont.*

C **2023**, *9*, 27

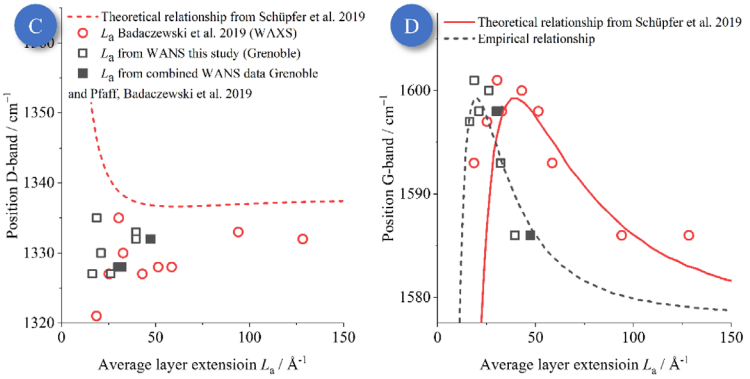

Figure 13. (**A**): Raman spectroscopy data for the phenol-formaldehyde resin-based carbons (PF-R) for different treatment temperatures, using an excitation wavelength of 633 nm. All samples showed increasing 2D and D′ bands and a higher G/D ratio at higher heat treatment temperatures, which are clear indicators for the increase in layer extension and decrease in disorder at higher temperatures [24,25]. (**B**): The intensity quotients I_D/I_G values were previously determined by Schüpfer et al. [25] and compared to the different L_a values determined in this present study and in the work of Badaczewski et al. [37]. (**C**): The position of the D-band was lower than the theoretical values for these resins as determined in ref. [25], indicating that, for (disordered) glass-like carbon, such a theory may not be applicable. (**D**): Position of the G-band related to the L_a values obtained from WAXS and WANS. Compared to the previous study of Schüpfer et al. [25], the G-band positions needed to be shifted to smaller L_a. In both cases, the Campbell–Fauchet approach was used to model the data, as described by Schüpfer et al. [25,66,67]. A similar figure for the pitches can be found in the SI as Figures S17 and S18.

For the G-band position, a similar shift of the entire relationship to smaller L_a was observed. (Figure 13C). Hence, this significant deviation compared to the study of Schüpfer et al. [25] implies that the underlying Campbell–Fauchet approach [66,67] might need to be modified or might not even be applicable. From Figure 13C, one can extract a shift in the L_a values by a factor of ca. two. Assuming that the Campbell–Fauchet approach is still valid, the constant in the exponent of the Fourier coefficient concomitantly would need to be changed by a factor of four, i.e., changing it formally to

$$C(\vec{k}_0, \vec{k}) \propto \exp\left(-\frac{1}{8} L_a^2 (\vec{k}_0 - \vec{k})\right) \text{ to } C(\vec{k}_0, \vec{k}) \propto \exp\left(-\frac{1}{32} (0.5\, L_a)^2 (\vec{k}_0 - \vec{k})\right).$$

Hence, the correction in the L_a values shown in Figure 13D might point to an interesting aspect in the interpretation of band positions for graphene-like materials. One major intrinsic shortcoming of the Campbell–Fauchet approach, if applied to such materials, is the assumption of spherical particles, which is not valid for graphenes. Thus, our study might serve as the basis for a reconsideration of the important relationship between band positions and graphene layer dimension in general.

4. Discussion/Outlook: Usage of Small-Wavelength-Radiation for X-ray Scattering vs. WANS

In spite of the large *s*-range and high quality of the Grenoble WANS data, the question remains as to whether the refinement with respect to the most relevant intralayer parameters L_a and σ_1 is accurate, or if an even lower wavelength is needed. Hence, we simulated WANS data, while varying L_a and σ_1, for a carbon corresponding to the PF-R 1800 (Figure 14).

C 2023, 9, 27

The refinement values for L_a and σ_1 were used, and simulations for different values of L_a and σ_1 were done, with the other parameters being kept constant (Figure 14A,B). Since σ_1 does not have a significant influence on the scattering data in the common WAXS range ($s < 1.2$ Å^{-1}), the layer disorder could be much overweighted or overestimated in WAXS measurements. For this reason, the average layer extension must be higher, otherwise the (10) and (11) reflections would not fit sufficiently. By using WANS data with a low radiation wavelength, a much higher range of s is available, and, therefore, the intralayer parameters can be refined more exactly. To be more precise, the refinement is now unique, which was not the case when using only WAXS data. Moreover, it is now possible to disentangle L_a and σ_1, i.e., the layer size and the layer disorder. Moreover, the Mo-Kα radiation having a small wavelength and, therefore, allowing a higher measurement range cannot lead to more exact results, since the damping of the atomic form factor is too strong.

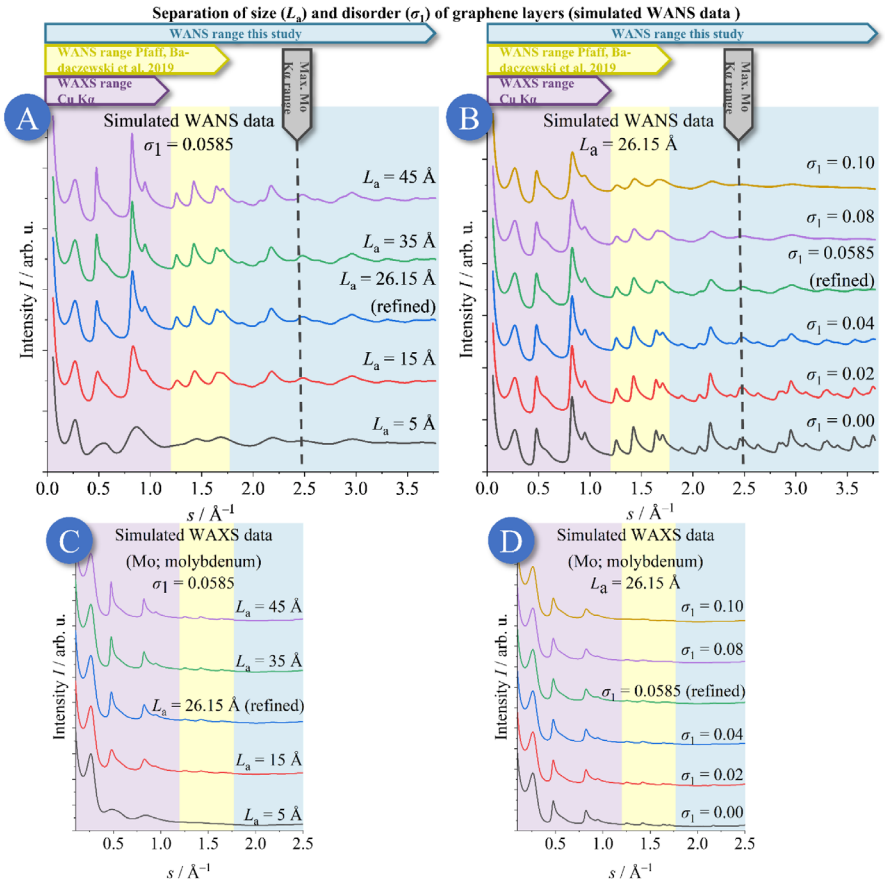

Figure 14. (**A–D**): Simulation of WANS and WAXS curves to assess the respective impact of different values of L_a and σ_1 with regard to the fundamental question as to whether size (L_a) and

disorder/strain (σ_1) can be validly disentangled at all. The refined values for PF-R 1800 were used to simulate scattering curves with higher/lower layer extension/order. (**A**): simulated WANS data (λ = 0.4975 Å) with constant σ_1 and variation of L_a. (**B**): simulated WANS data (λ = 0.4975 Å) with constant L_a and variation of σ_1 assuming typical values of σ_1. The layer disorder (σ_1) as well as the layer extension (L_a) were overestimated in previous WAXS studies, as the *s*-range was insufficient. By using WANS data presented here in this study, it is possible to differentiate between these parameters in their impact on the data and to quantify them reliably. Building on this leads to a new view of the NGCs, especially the resins: The graphene layers were much smaller but more ordered, as assumed before. (**C**,**D**): simulated WAXS curves using Mo-Kα radiation (λ = 0.71 Å), under variation of L_a and σ_1, analogue to (**A**) and (**B**). Using Mo-Kα radiation (λ = 0.71 Å) allows for WAXS data with a high *s*-range, but suffers from the damping of the atomic form factor, so the visible reflections will have only a low intensity. Hence, size (L_a) and disorder (σ_1) cannot be precisely determined, even when using a Mo-Kα radiation source. The measurement range of Pfaff et al. is related to reference [43].

In contrast to prior measurements and publications, these are the first measurements of such NGCs where the intralayer parameters could be determined validly and reproducibly. Since the layer disorder as well as the layer extension were overestimated in prior studies, the present analysis led to smaller, but higher-ordered graphene sheets.

5. Conclusions

This study was dedicated to the fundamental question of the magnitude of nanoscaled disorder in the abundant class of non-graphitic carbon (NGC) materials, which are composed of small-sized graphenes as building blocks. The basic structural make-up had already been described decades ago, based on X-ray scattering, by pioneers in the field, such as Rosalind Franklin and B. E. Warren: NGCs are made up of graphene stacks possessing finite, small dimensions, as well as rotational and translational disorder in the stacking of the graphenes. The substantial structural disorder of the graphenes themselves can be fundamentally quantified by analysis of the width of the (*hk*) reflections in wide-angle X-ray and neutron scattering (WAXS/WANS). However, as a finite dimension of the graphenes causes broadening of these reflections as well, the disentanglement of size and disorder from experimental WAXS/WANS data is a challenge.

The main strategy of this study was to merge WANS data from two facilities, HZB (Berlin) and ILL (Grenoble), that were acquired on the very same materials. Thus, the WANS data spanned a huge range of the modulus of the scattering vector *s* ($s = 2\sin(\theta)/\lambda$) and also profited from the different resolutions of the beamlines as small and large *s* values. We showed that WANS is superior to WAXS for several reasons, and that high-quality WANS data, obtained at the Grenoble facility, enabling a huge *s*-range, indeed allowed for disentangling size and disorder and, therefore, provided reliable values for the disorder in the form of the parameter σ_1. This led to a detailed and meaningful verification of the present view on the microstructure (especially the layer extension (L_a) and stack height (L_c), as well as their degree of disorder (mainly σ_1 and σ_3, respectively)) and their evolution at different heat treatment temperatures. We studied three different carbon materials from different carbon precursors, i.e., non-graphitizing glass-like carbon building (phenol-formaldehyde resin, PF-R) and two graphitizing pitch-based carbons (mesophase pitch and low softening-point pitch, MP and LSPP), which had been previously studied by WAXS and WANS [37,40,43].

Our study advances the characterization of graphene-based carbons and the view on their structural make-up in several aspects:

1. Only WANS data with a high *s*-range lead to a reliable and reproducible determination of the dimension and disorder of the graphene layers. Using WAXS data or WANS data with a small *s*-range, e.g., using typical XRD instruments using Cu-Kα radiation, leads e.g. to unreliable intralayer parameters L_a and σ_1.

2. The refinement approach of Ruland and Smarsly [34] allows for excellent fitting of WANS data, even up to quite large s values, which enables a precise determination of the microstructural parameters describing the graphene structure.
3. Raman spectroscopy studies by Schüpfer et al. [24,25] established and advanced methods for the correlation between signal width/height of the different bands and the microstructure, especially L_a, based on a validation with WANS/WAXS. While the present study showed that the previously determined values for L_a were too large, we demonstrated that the method by Schüpfer et al. is still usable to quantify the graphene structure and, in particular, to describe qualitative changes e.g., upon temperature treatment. Further theoretical work needs to be advanced in order to establish a quantitative relationship between band positions and the graphene dimension.
4. As a most relevant finding, apparently "disordered" carbons (especially prepared from phenol-formaldehyde resin; PF-R) are much less disordered as previously assumed, based on the σ_1 values. Concomitantly, the graphene layers in such PF-R carbon samples are smaller (on the order of a few nm at most) but are internally more highly ordered than predicted in prior studies (Figure 15) in which the layer extension and disorder were overestimated systematically. We think this insight represents a paradigmatic, fundamental advance in the view on the structure of these materials. They are by no means "amorphous", but, on the contrary, the graphenes in NGCs possess an order close to an ideal "graphene". This result might contribute to the understanding of graphitization in the formation of graphite in the future.

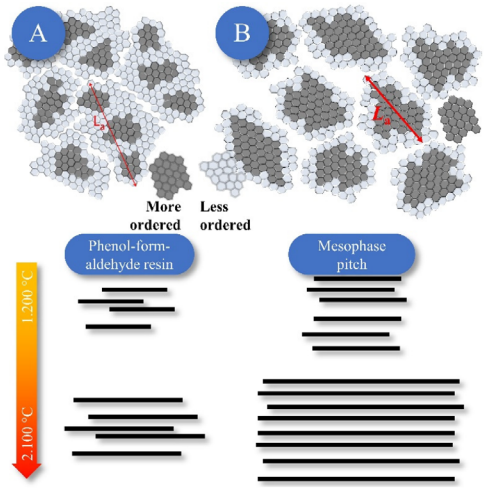

Figure 15. New insights into the microstructure of non-graphitic carbon: Compared to prior studies on the same materials [43] (**A**), the present analysis (**B**) suggests smaller, but highly ordered graphene-layers. Reprinted and adapted with permission from Ref. [43]. Copyright 2019 American Chemical Society.

Hence, our study stimulates further questions and further analysis e. For instance, the so-called pair distribution function (PDF) [49–53] will be calculated from the present WANS, but also from suitable WAXS data, for example, from an XPDF experiment performed at the Diamond light source. Additionally, WAXS measurements at similar wavelengths, as applied in this study (λ~0.5 Å), should be performed for samples containing a significant

amount of hydrogen, which impedes reliable WANS analysis. Tests should be performed as to whether the WAXS of such samples can be evaluated more accurately than at present and, additionally, if such measurements are as exact as WANS measurements.

In conclusion, we believe that the present study proposes an advanced methodology for studying graphene-based carbons, and also advances the view on the structure of important classes of non-graphitic carbon.

Supplementary Materials: The following supporting information can be downloaded at: https://www.mdpi.com/article/10.3390/c9010027/s1. SI—Additional Data and Mathematical Background. References [21,24,25,34,37,40,43,66,67] are cited in the supplementary mate-rials.

Author Contributions: Conceptualization, O.O. and B.M.S.; Data curation, H.E.F., A.F., J.-U.H. and M.R.; Formal analysis, O.O., M.O.L., F.M.B. and T.P.; Funding acquisition, P.J.K. and B.M.S.; Investigation, O.O., M.O.L., F.M.B. and T.P.; Methodology, O.O. and B.M.S.; Project administration, B.M.S.; Resources, P.J.K. and B.M.S.; Software, O.O.; Supervision, B.M.S.; Validation, O.O.; Visualization, O.O.; Writing—original draft, O.O.; Writing—review and editing, M.O.L., F.M.B., T.P., H.E.F., A.F., J.-U.H., M.R., P.J.K. and B.M.S. All authors have read and agreed to the published version of the manuscript.

Funding: Financial support was provided by the DFG via the GRK (Research Training Group) 2204 "Substitute Materials for Sustainable Energy Technologies."

Data Availability Statement: The WANS data from Grenoble presented in this study are openly available at https://doi.ill.fr/10.5291/ILL-DATA.5-26-218, reference number 10.5291/ILL-DATA.5-26-218, accessed on 17 February 2023. Restrictions apply to the availability of the WAXS data. The WANS data from Berlin was obtained from Torben Pfaff and Felix Badaczewski and are available from the authors.

Acknowledgments: The authors thank the ILL for the allocation of neutron radiation beamtime and also thankfully acknowledge the financial support from the ILL.

Conflicts of Interest: The authors declare no conflict of interest.

References

1. Doherty, C.M.; Caruso, R.A.; Smarsly, B.M.; Adelhelm, P.; Drummond, C.J. Hierarchically Porous Monolithic $LiFePO_4$/Carbon Composite Electrode Materials for High Power Lithium Ion Batteries. *Chem. Mater.* **2009**, *21*, 5300–5306. [CrossRef]
2. Kumar, R.; Dhakate, S.R.; Mathur, R.B. The role of ferrocene on the enhancement of the mechanical and electrochemical properties of coal tar pitch-based carbon foams. *J. Mater. Sci.* **2013**, *48*, 7071–7080. [CrossRef]
3. Oberlin, A. Carbonization and graphitization. *Carbon* **1984**, *22*, 521–541. [CrossRef]
4. Goel, C.; Bhunia, H.; Bajpai, P.K. Synthesis of nitrogen doped mesoporous carbons for carbon dioxide capture. *RSC Adv.* **2015**, *5*, 46568–46582. [CrossRef]
5. Oschatz, M.; Borchardt, L.; Thommes, M.; Cychosz, K.A.; Senkovska, I.; Klein, N.; Frind, R.; Leistner, M.; Presser, V.; Gogotsi, Y.; et al. Carbide-derived carbon monoliths with hierarchical pore architectures. *Angew. Chem. Int. Ed. Engl.* **2012**, *51*, 7577–7580. [CrossRef]
6. Oschatz, M.; Kockrick, E.; Rose, M.; Borchardt, L.; Klein, N.; Senkovska, I.; Freudenberg, T.; Korenblit, Y.; Yushin, G.; Kaskel, S. A cubic ordered, mesoporous carbide-derived carbon for gas and energy storage applications. *Carbon* **2010**, *48*, 3987–3992. [CrossRef]
7. Silvestre-Albero, A.; Rico-Francés, S.; Rodríguez-Reinoso, F.; Kern, A.M.; Klumpp, M.; Etzold, B.J.; Silvestre-Albero, J. High selectivity of TiC-CDC for CO_2/N_2 separation. *Carbon* **2013**, *59*, 221–228. [CrossRef]
8. Li, J.; Lu, R.; Dou, B.; Ma, C.; Hu, Q.; Liang, Y.; Wu, F.; Qiao, S.; Hao, Z. Porous graphitized carbon for adsorptive removal of benzene and the electrothermal regeneration. *Environ. Sci. Technol.* **2012**, *46*, 12648–12654. [CrossRef]
9. Manthiram, A.; Fu, Y.; Chung, S.-H.; Zu, C.; Su, Y.-S. Rechargeable lithium-sulfur batteries. *Chem. Rev.* **2014**, *114*, 11751–11787. [CrossRef]
10. Dash, R.; Chmiola, J.; Yushin, G.; Gogotsi, Y.; Laudisio, G.; Singer, J.; Fischer, J.; Kucheyev, S. Titanium carbide derived nanoporous carbon for energy-related applications. *Carbon* **2006**, *44*, 2489–2497. [CrossRef]
11. Inagaki, M.; Konno, H.; Tanaike, O. Carbon materials for electrochemical capacitors. *J. Power Sources* **2010**, *195*, 7880–7903. [CrossRef]
12. Oschatz, M.; Borchardt, L.; Pinkert, K.; Thieme, S.; Lohe, M.R.; Hoffmann, C.; Benusch, M.; Wisser, F.M.; Ziegler, C.; Giebeler, L.; et al. Hierarchical Carbide-Derived Carbon Foams with Advanced Mesostructure as a Versatile Electrochemical Energy-Storage Material. *Adv. Energy Mater.* **2014**, *4*, 1300645. [CrossRef]

13. Wang, J.; Sugita, S.; Nagayama, K.; Matsumoto, T. OS18-3 Spatiotemporal Dynamics of Actin during Adhesion Process of MC3T3-E1 Cells to Substrate (Cell and Tissue mechanics 1,OS18 Cell and tissue mechanics, BIOMECHANICS). *ATEM* **2015**, *2015*, 237. [CrossRef]
14. Kim, Y.-S.; Guo, X.-F.; Kim, G.-J. Synthesis of carbon monolith with bimodal meso/macroscopic pore structure and its application in asymmetric catalysis. *Catal. Today* **2010**, *150*, 91–99. [CrossRef]
15. Zhang, S.; Chen, L.; Zhou, S.; Zhao, D.; Wu, L. Facile Synthesis of Hierarchically Ordered Porous Carbon via in Situ Self-Assembly of Colloidal Polymer and Silica Spheres and Its Use as a Catalyst Support. *Chem. Mater.* **2010**, *22*, 3433–3440. [CrossRef]
16. Perret, R.; Ruland, W. X-ray small-angle scattering of glassy carbon. *J. Appl. Crystallogr.* **1972**, *5*, 183–187. [CrossRef]
17. Tzeng, S.-S.; Chr, Y.-G. Evolution of microstructure and properties of phenolic resin-based carbon/carbon composites during pyrolysis. *Mater. Chem. Phys.* **2002**, *73*, 162–169. [CrossRef]
18. Warren, B.E. X-ray Diffraction in Random Layer Lattices. *Phys. Rev.* **1941**, *59*, 693–698. [CrossRef]
19. Fitzer, E.; Kochling, K.-H.; Boehm, H.P.; Marsh, H. Recommended terminology for the description of carbon as a solid (IUPAC Recommendations 1995). *Pure Appl. Chem.* **1995**, *67*, 473–506. [CrossRef]
20. Faber, K.; Badaczewski, F.; Oschatz, M.; Mondin, G.; Nickel, W.; Kaskel, S.; Smarsly, B.M. In-Depth Investigation of the Carbon Microstructure of Silicon Carbide-Derived Carbons by Wide-Angle X-ray Scattering. *J. Phys. Chem. C* **2014**, *118*, 15705–15715. [CrossRef]
21. Osswald, O.; Smarsly, B.M. *OctCarb*—A GNU Octave Script for the Analysis and Evaluation of Wide-Angle Scattering Data of Non-Graphitic Carbons. *C* **2022**, *8*, 78. [CrossRef]
22. Sharma, A.; Kyotani, T.; Tomita, A. Comparison of structural parameters of PF carbon from XRD and HRTEM techniques. *Carbon* **2000**, *38*, 1977–1984. [CrossRef]
23. Kovalevski, V.; Buseck, P.R.; Cowley, J. Comparison of carbon in shungite rocks to other natural carbons: An X-ray and TEM study. *Carbon* **2001**, *39*, 243–256. [CrossRef]
24. Schüpfer, D.B.; Badaczewski, F.; Peilstöcker, J.; Guerra-Castro, J.M.; Shim, H.; Firoozabadi, S.; Beyer, A.; Volz, K.; Presser, V.; Heiliger, C.; et al. Monitoring the thermally induced transition from sp3-hybridized into sp2-hybridized carbons. *Carbon* **2021**, *172*, 214–227. [CrossRef]
25. Schüpfer, D.B.; Badaczewski, F.; Guerra-Castro, J.M.; Hofmann, D.M.; Heiliger, C.; Smarsly, B.M.; Klar, P.J. Assessing the structural properties of graphitic and non-graphitic carbons by Raman spectroscopy. *Carbon* **2020**, *161*, 359–372. [CrossRef]
26. Zickler, G.A.; Smarsly, B.M.; Gierlinger, N.; Peterlik, H.; Paris, O. A reconsideration of the relationship between the crystallite size La of carbons determined by X-ray diffraction and Raman spectroscopy. *Carbon* **2006**, *44*, 3239–3246. [CrossRef]
27. Biscoe, J.; Warren, B.E. An X-ray Study of Carbon Black. *J. Appl. Phys.* **1942**, *13*, 364–371. [CrossRef]
28. Diamond, R. X-ray studies of some carbonized coals. *Phil. Trans. R. Soc. Lond. A* **1960**, *252*, 193–223. [CrossRef]
29. Houska, C.R.; Warren, B.E. X-ray Study of the Graphitization of Carbon Black. *J. Appl. Phys.* **1954**, *25*, 1503–1509. [CrossRef]
30. Warren, B.E.; Bodenstein, P. The diffraction pattern of fine particle carbon blacks. *Acta Cryst.* **1965**, *18*, 282–286. [CrossRef]
31. Shi, H.; Reimers, J.N.; Dahn, J.R. Structure-refinement program for disordered carbons. *J. Appl. Crystallogr.* **1993**, *26*, 827–836. [CrossRef]
32. Azuma, H. A New Structural Model for Nongraphitic Carbons. *J. Appl. Crystallogr.* **1998**, *31*, 910–916. [CrossRef]
33. Fujimoto, H.; Shiraishi, M. Characterization of unordered carbon using Warren–Bodenstein's equation. *Carbon* **2001**, *39*, 1753–1761. [CrossRef]
34. Ruland, W.; Smarsly, B.M. X-ray scattering of non-graphitic carbon: An improved method of evaluation. *J. Appl. Crystallogr.* **2002**, *35*, 624–633. [CrossRef]
35. Krüner, B.; Schreiber, A.; Tolosa, A.; Quade, A.; Badaczewski, F.; Pfaff, T.; Smarsly, B.M.; Presser, V. Nitrogen-containing novolac-derived carbon beads as electrode material for supercapacitors. *Carbon* **2018**, *132*, 220–231. [CrossRef]
36. Wang, H.; Delacroix, S.; Osswald, O.; Anderson, M.; Heil, T.; Lepre, E.; Lopez-Salas, N.; Kaner, R.B.; Smarsly, B.M.; Strauss, V. Laser-carbonization: Peering into the formation of micro-thermally produced (N-doped) carbons. *Carbon* **2021**, *176*, 500–510. [CrossRef]
37. Badaczewski, F.; Loeh, M.O.; Pfaff, T.; Dobrotka, S.; Wallacher, D.; Clemens, D.; Metz, J.; Smarsly, B.M. Peering into the structural evolution of glass-like carbons derived from phenolic resin by combining small-angle neutron scattering with an advanced evaluation method for wide-angle X-ray scattering. *Carbon* **2019**, *141*, 169–181. [CrossRef]
38. Badaczewski, F.M.; Loeh, M.O.; Pfaff, T.; Wallacher, D.; Clemens, D.; Smarsly, B.M. An advanced structural characterization of templated meso-macroporous carbon monoliths by small- and wide-angle scattering techniques. *Beilstein J. Nanotechnol.* **2020**, *11*, 310–322. [CrossRef]
39. Faber, K.; Badaczewski, F.; Ruland, W.; Smarsly, B.M. Investigation of the Microstructure of Disordered, Non-graphitic Carbons by an Advanced Analysis Method for Wide-Angle X-ray Scattering. *Z. Anorg. Allg. Chem.* **2014**, *640*, 3107–3117. [CrossRef]
40. Loeh, M.O.; Badaczewski, F.; Faber, K.; Hintner, S.; Bertino, M.F.; Mueller, P.; Metz, J.; Smarsly, B.M. Analysis of thermally induced changes in the structure of coal tar pitches by an advanced evaluation method of X-ray scattering data. *Carbon* **2016**, *109*, 823–835. [CrossRef]
41. Loeh, M.O.; Badaczewski, F.; von der Lehr, M.; Ellinghaus, R.; Dobrotka, S.; Metz, J.; Smarsly, B.M. Hard-templating of carbon using porous SiO2 monoliths revisited—Quantitative impact of spatial confinement on the microstructure evolution. *Carbon* **2018**, *129*, 552–563. [CrossRef]

42. Pfaff, T.; Simmermacher, M.; Smarsly, B.M. CarbX: A program for the evaluation of wide-angle X-ray scattering data of non-graphitic carbons. *J. Appl. Crystallogr.* **2018**, *51*, 219–229. [CrossRef]
43. Pfaff, T.; Badaczewski, F.M.; Loeh, M.O.; Franz, A.; Hoffmann, J.-U.; Reehuis, M.; Zeier, W.G.; Smarsly, B.M. Comparative Microstructural Analysis of Nongraphitic Carbons by Wide-Angle X-ray and Neutron Scattering. *J. Phys. Chem. C* **2019**, *123*, 20532–20546. [CrossRef]
44. Hoffmann, J.-U.; Reehuis, M. E2: The Flat-Cone Diffractometer at BER II. *JLSRF* **2018**, *4*, A129. [CrossRef]
45. Smarsly, B.M.; Badaczewski, F.; Fischer, H.E.; Loeh, M.; Osswald, O.; Pfaff, T. *Analysis of the Wide-Angle Neutron Scattering of Non-Graphitic Carbon—Testing of an Advanced Evaluation Approach*; Institut Laue-Langevin (ILL): Grenoble, France, 2019. [CrossRef]
46. Fischer, H.E.; Cuello, G.J.; Palleau, P.; Feltin, D.; Barnes, A.C.; Badyal, Y.S.; Simonson, J.M. D4c: A very high precision diffractometer for disordered materials. *Appl. Phys. A Mater. Sci. Process.* **2002**, *74*, s160–s162. [CrossRef]
47. Fischer, H.E.; Barnes, A.C.; Salmon, P.S. Neutron and x-ray diffraction studies of liquids and glasses. *Rep. Prog. Phys.* **2006**, *69*, 233–299. [CrossRef]
48. Placzek, G. The Scattering of Neutrons by Systems of Heavy Nuclei. *Phys. Rev.* **1952**, *86*, 377–388. [CrossRef]
49. Masson, O.; Thomas, P. Exact and explicit expression of the atomic pair distribution function as obtained from X-ray total scattering experiments. *J. Appl. Crystallogr.* **2013**, *46*, 461–465. [CrossRef]
50. Olds, D.P.; Duxbury, P.M. Efficient algorithms for calculating small-angle scattering from large model structures. *J. Appl. Crystallogr.* **2014**, *47*, 1077–1086. [CrossRef]
51. Peterson, P.F.; Božin, E.S.; Proffen, T.; Billinge, S.J.L. Improved measures of quality for the atomic pair distribution function. *J. Appl. Crystallogr.* **2003**, *36*, 53–64. [CrossRef]
52. Weisbecker, P.; Leyssale, J.-M.; Fischer, H.E.; Honkimäki, V.; Lalanne, M.; Vignoles, G.L. Microstructure of pyrocarbons from pair distribution function analysis using neutron diffraction. *Carbon* **2012**, *50*, 1563–1573. [CrossRef]
53. Willinger, E. *Analysis of Local Structure by Atomic Pair Distribution Function*; Department of Inorganic Chemistry, Fritz Haber Institute: Berlin, Germany, 2017.
54. Scherrer, P. Bestimmung der inneren Struktur und der Größe von Kolloidteilchen mittels Röntgenstrahlen. In *Kolloidchemie Ein Lehrbuch*; Zsigmondy, R., Ed.; Springer: Berlin/Heidelberg, Germany, 1912; pp. 387–409. ISBN 978-3-662-33517-8.
55. Stephens, P.W. *International Tables for Crystallography 8v Set 4e (Updated Sept 2014)*; John Wiley & Sons Inc.: Hoboken, NJ, USA, 2014.
56. Putman, K.J.; Rowles, M.R.; Marks, N.A.; Suarez-Martinez, I. The role of the 2D-to-3D transition in X-ray diffraction analysis of crystallite size. *J. Phys. Condens. Matter* **2021**, *33*, 294002. [CrossRef] [PubMed]
57. Bragg, W.H.; Bragg, W.L. The reflection of X-rays by crystals. *Proc. R. Soc. Lond. A* **1913**, *88*, 428–438. [CrossRef]
58. Strunz, H.; Nickel, E.H. *Strunz Mineralogical Tables: Chemical-Structural Mineral Classification System*, 9th ed.; E. Schweizerbart'sche Verlagsbuchhandlung: Stuttgart, Germany, 2001; ISBN 351065188X.
59. Holleman, A.F.; Wiberg, N. *Anorganische Chemie, Aufl. 103*; De Gruyter: Berlin, Germany, 2016; ISBN 9783110269321.
60. Ferrari, A.C.; Basko, D.M. Raman spectroscopy as a versatile tool for studying the properties of graphene. *Nat. Nanotechnol.* **2013**, *8*, 235–246. [CrossRef] [PubMed]
61. Jorio, A.; Dresselhaus, M.S.; Saito, R.; Dresselhaus, G. *Raman Spectroscopy in Graphene Related Systems*; John Wiley & Sons: Hoboken, NJ, USA, 2011; ISBN 9783527643905.
62. Tuinstra, F.; Koenig, J.L. Raman Spectrum of Graphite. *J. Chem. Phys.* **1970**, *53*, 1126–1130. [CrossRef]
63. Vinado, R.; Fischbach, D.B. New Lines in the Raman Spectra of Carbons and Graphite. *J. Am. Ceram. Soc.* **1978**, *61*, 13–17. [CrossRef]
64. Ferrari, A.C.; Meyer, J.C.; Scardaci, V.; Casiraghi, C.; Lazzeri, M.; Mauri, F.; Piscanec, S.; Jiang, D.; Novoselov, K.S.; Roth, S.; et al. Raman spectrum of graphene and graphene layers. *Phys. Rev. Lett.* **2006**, *97*, 187401. [CrossRef]
65. Pimenta, M.A.; Dresselhaus, G.; Dresselhaus, M.S.; Cançado, L.G.; Jorio, A.; Saito, R. Studying disorder in graphite-based systems by Raman spectroscopy. *Phys. Chem. Chem. Phys.* **2007**, *9*, 1276–1291. [CrossRef]
66. Campbell, I.H.; Fauchet, P.M. The effects of microcrystal size and shape on the one phonon Raman spectra of crystalline semiconductors. *Solid State Commun.* **1986**, *58*, 739–741. [CrossRef]
67. Fauchet, P.M.; Campbell, I.H. Raman spectroscopy of low-dimensional semiconductors. *Crit. Rev. Solid State Mater. Sci.* **1988**, *14*, s79–s101. [CrossRef]

6.4. Publikationen – Anhänge

6.4.1. Anhang Publikation 1 – Teil A [1]

Reproduziert mit Genehmigung von Oliver Osswald; veröffentlicht bei MDPI, *C*, 2022.

OctCarb – A GNU *Octave* Script for the Analysis and Evaluation of Wide-Angle Scattering Data of Non-graphitic Carbons

Supporting information part A

***Octave* installation and examples**

Authors

Oliver Osswald[a]* and Bernd M. Smarsly[a]

[a]Institute of Physical Chemistry, Justus-Liebig-University Giessen, Heinrich-Buff-Ring 17, Giessen, 35392, Germany

Correspondence email: oliver.osswald@phys.chemie.uni-giessen.de

Funding information Financial support is provided by the DFG via the RTG (Research Training Group) 2204 "Substitute Materials for Sustainable Energy Technologies".

Supporting information part A – *Octave* installation and examples

S1. Overview of all used parameters

In addition to 2.2, not the microstructure parameters itself, but parameters of distribution functions are refined (μ and β for interlayer parameters, v and α for intralayer parameters) from which the microstructure parameters are calculated (equations (7) – (14)). Therefore, a brief overview of all parameters used for the refinement and the received microstructure parameters as well as some other important units is given here.

For the number deviation of the average number of layers per stacks the following equations were found [1]:

$$n(N) = \frac{\beta^{\mu}}{\Gamma(\mu)} N^{\mu-1} \exp(-\beta N) \tag{7}$$

$$\langle N \rangle = \frac{\mu}{\beta} \tag{8}$$

$$L_c = \bar{a}_3 \frac{\mu+1}{\beta} \tag{9}$$

$$\kappa_c = \frac{1}{\mu} \tag{10}$$

Table S1 Overview of all used parameters for a refinement using *Octave*. The column "influence on scattering data" describes, if the parameter has a large (+), medium (o) or small (-) influence on the theoretical intensity.

Parameter	Parameter in *Octave*	Parameter used for refinement	Description	Influence on scattering data
q	q	Measured	Modules of the scattering vector ($= 2 \cdot \pi \cdot s$)	
s	s	Measured	Modules of the scattering vector ($= 2/\lambda \cdot \sin(\theta)$)	
λ	wavelength	Given constant	Wavelength of used radiation	
θ	theta	Measured	Scattering angle, half „Bragg-angle"	
$\bar{a}_3$	a3	$a3$	Average layer distance	+
$a_{3\,min}$	a3min	$= \bar{a}_3 - da_3$	Minimal layer distance	+ (only for visible (004) reflection, else -)
σ_3	sig3	σ_3	Disorder of the stacks (standard deviation of a_3)	+
L_a	La	$= (v + 1)/\alpha$	Average graphene layer size	+ (calculated parameter)
l_m	lm	$= v/\alpha$	Average chord length	+ (calculated parameter)
κ_a	kapa	$= 1/v$	Polydispersity of chord length	Depends a lot on the experiment, see 2.3
l_{cc}	lcc	lcc	Average C-C bond length	+
σ_1	sig1	σ_1	Disorder of the layers (i.e. stress and strain)	+
ε_1	eps1	-	Disorder of graphene layers due to local strains	-- (not implemented)
κ_r	kapr	$= 3\pi2\ (1/v + 1)/32 - 1$	Polydispersity of the radius of the graphene layers	Currently not used

N	N	$= (\mu+1)/\beta$	Average number of graphene layers per stack	+ (calculated parameter)
L_c	Lc	$= \bar{a}_3 \cdot (\mu+1)/\beta = L_c \cdot \bar{a}_3$	Average stack height	+ (calculated parameter)
κ_c	kapc	$= 1/\mu$	Polydispersity of stack height	o (calculated parameter, but generally high error)
ε_3	eps3	$= a_3/a_{3\,min}$	Disorder of stacks due to local strains	o (calculated parameter, but generally high error)
q	q	q	Preferred orientation	+
c_H	cH	c_H (constant)	Concentration of unorganized hydrogen	-
c_N	cN	c_N (constant)	Concentration of unorganized nitrogen	o (depends on value)
c_O	cO	c_O (constant)	Concentration of unorganized oxygen	o (depends on value)
c_S	cS	c_S (constant)	Concentration of unorganized sulfur	+
Δ_{an}	dan	Δ_{an}	Anisotropy of atomic form factor of carbon	-
k	k	k	Normalization constant for log10(k · Ie.u. + const1) + const2	+
$const_1$	const1	$const_1$	Constant shift for log10(k · Ie.u. + const1) + const2	+
$const_2$	const2	$const_2$	Non-constant (linear) shift for log10(k · Ie.u. + const1) + const2	+
g	g	g	Factor for exponential damping of the scattering intensity with Ie.u. = exp(g · s) · Ie.u.	+
Q	b	Q	Additional parameter for incoherent background (Q ≠ b, see 2)	-
ρ	density	ρ (constant)	Density of the sample	o

d	sampleThickness	d (constant)	Thickness of the sample	o
μ_{ab}	mue_ab	μ_{ab} (constant)	Absorption factor, calculated from density, sample thickness and wavelength	o
-	polarizedBeam	constant	Is the beam polarized?	+
Φ	polarizationDegree	Φ (constant)	Polarization direction of beam in °	+
r	par_r	r (constant)	Radius of the goniometer (in cm; fixed due to experiment)	o
δ	par_delta	δ (constant)	Divergence angle (in °; to choose by user)	o
l	par_l	l (constant)	Irradiated length (in cm; fixed during measurement)	o
R	R	R (constant)	Parameter for position correction according to D2thtx	-- (not available)
t	t	t (constant)	Parameter for position correction according to D2thtx	-- (not available)

Influence on scattering data is just the personal meaning of the author based on the experience of several refinements.

S2. Implementation and calculation time consumption of *v*

The implementation of *v* as described in 3.1 in the main article

$$P_L(r) = \frac{1}{\Gamma(v+1)}[\Gamma(v+1, \alpha r) - \alpha r\Gamma(v, \alpha r)] \tag{11}$$

$$\langle l \rangle = \frac{v}{\alpha} \tag{12}$$

$$L_a = \frac{\langle l^2 \rangle}{\langle l \rangle} = \frac{v+1}{\alpha} \tag{13}$$

$$\kappa_a = \frac{1}{v} \tag{14}$$

is used to calculate the profile shape of the intralayer reflections and therefore the intralayer parameters (e.g. the average layer extension L_a). However, *v* is not refined, but fixed to a constant depending on the maximum measured modules of the scattering vector s_{max} (see Table S2). Several calculations showed that this implementation is very useful to improve the speed of the refinement, since the influence of *v* is only very small on a single reflection. Also, the parameters α (for the calculation of the layer extension L_a) and σ_1 (stress and strain of the layers ("disorder")) have a much higher influence on the profile shape. Hence, this usage of *v* does not degrade the physical assumptions and the resulting accuracy of the refinement. More precisely, it is not possible to determine ν and therefore the polydispersity of the graphene layers ($\kappa_a = 1/v$) in an experimental way.

In the following, an overview of the recommended minimal value of *v* for the *s*-value is given. Table S2 is just a recommendation and for some samples or more special experiments, e.g. WANS with a low wavelength, it might be useful to use a larger value of *v*. In general, $v < 4$ is not recommended. Additionally, the calculation time using *Octave* is about 4 times faster than using the algorithm from Pfaff et al. [3] for $v = 4$.

Table S2 Recommended value of v for a maximum measured modules of the scattering vector s_{max}, regarding maximum polydispersity and the average calculation times using the algorithm from Pfaff et al. [3] and the improved used in the present study, respectively. In general, $v < 4$ is not recommended.

			Duration for a single calculation	
v	s_{max} / Å^{-1}	$\kappa_{c,\,max}$	Pfaff et. al (2018)	*Octave*
4	1.4	0.250	21.6 s	5.9 s
5	1.85	0.200	30.1 s	13 s
6	2.35	0.167	39.3 s	25.2 s
7	2.8	0.143	49.9 s	44.2 s
8	3.1	0.125	61.6 s	75.1 s
9	3.5	0.111	74.5 s	114.3 s
10	3.85	0.100	88.6 s	166.7 s

S3. Determination of the error bars

Generally, in non-linear fitting procedures the initial values of the fitting parameters may exhibit an undesired strong impact on the final fitting result. In order to evaluate this possible issue, two automatic refinements were performed for the four samples by means of *Octave*, using different starting parameter values. In the first one, the refined microstructure values taken from Pfaff et al. [3] were used as initial parameters (*Octave data set* Pfaff et al. see Figure 6 in the main article and Figure S1). The second one takes our default starting parameters as described in Table S6 (*Octave data set default values* , see Figure 6 in the main article and Figure S1). First tests using the already refined microstructure from Pfaff et al. [3] were done to validate, if the general refinement works in principle and leads to comparable results. The second test using the default starting parameters as described in Figure 6 in the main article and Figure S1 was performed to validate if the numerical refinement/minimalization of *Octave* works well and leads to the same (or similar) results. These default starting values are in principle mean-values of the aforementioned structural parameters of common NGCs.

More precisely, *Octave* uses the Levenberg-Marquardt non-linear fitting algorithm to perform the refinement. Hence, the influence of each (microstructure) parameter on each simulated fit value is calculated, so the refinement time depends on multiple effects: First, the size of the matrix as described before, second, the direct calculation time of a theoretical scattering curve and third, the number of scattering curves, which must be calculated in each refinement step (two for each refinement parameter - one with a greater and one with a lesser value). In the following steps, a so-called singular-value-decomposition (SVD) is performed, which leads to a covariance matrix of all refinement parameters. The square of the individual values of the diagonals of the matrix is then the standard deviation (σ deviation) of the corresponding refinement parameters. A deviation of 1σ means the probability that the "real" value of the parameter is in the range of ["calculated value – σ deviation"; "calculated value + σ deviation"] is ~ 68 %. In the same way, the so called 2σ/3σ deviations can be calculated: The probability of the value of a refinement parameter lying in the 2σ range (["calculated value – 2 · σ deviation"; "calculated value + 2 · σ deviation"]) is ~ 96.5 % and for the 3σ range the probability is ~ 99.7 %. In other words, the refined parameter is the mean value of a Gaussian distribution and σ its standard deviation.

This quantification of the refinement error is completely different than in prior studies [2–6], where the uncertainty of the individual microstructural parameters was determined by variating a single parameter until a significant visual change of the calculated scattering curve was observable. Applying this procedure, the typical error for each parameter was in the range of 10 – 15 %. By contrast, using *OctCarb* the error is systematically calculated within the fitting procedure, thus the resulting error is usually much smaller using *Octave*. However, the user has to decide whether to use the 1σ, 2σ or 3σ range as the refinement error, which refers to the importance of how exactly the relative parameter uncertainty should be known (2σ or 3σ).

We found that the uncertainties of the individual structural parameters defined in this way strongly depend on the number of data points in one scattering curve, which can now be nicely demonstrated by the samples used (Table S3): For example, the errors for the PIL WAXS data are small, because the data possess about 10-times more measurement points than the other samples. For the same reason, the calculated errors for AC Type H are quite high, because the WAXS data of this sample consist of only a low amount of measurement points (258 compared to 2392 of PIL) (for more information about the influence of the number of data points see S11).

S4. Results of the refined samples for the verification of the *OctCarb* (plots)

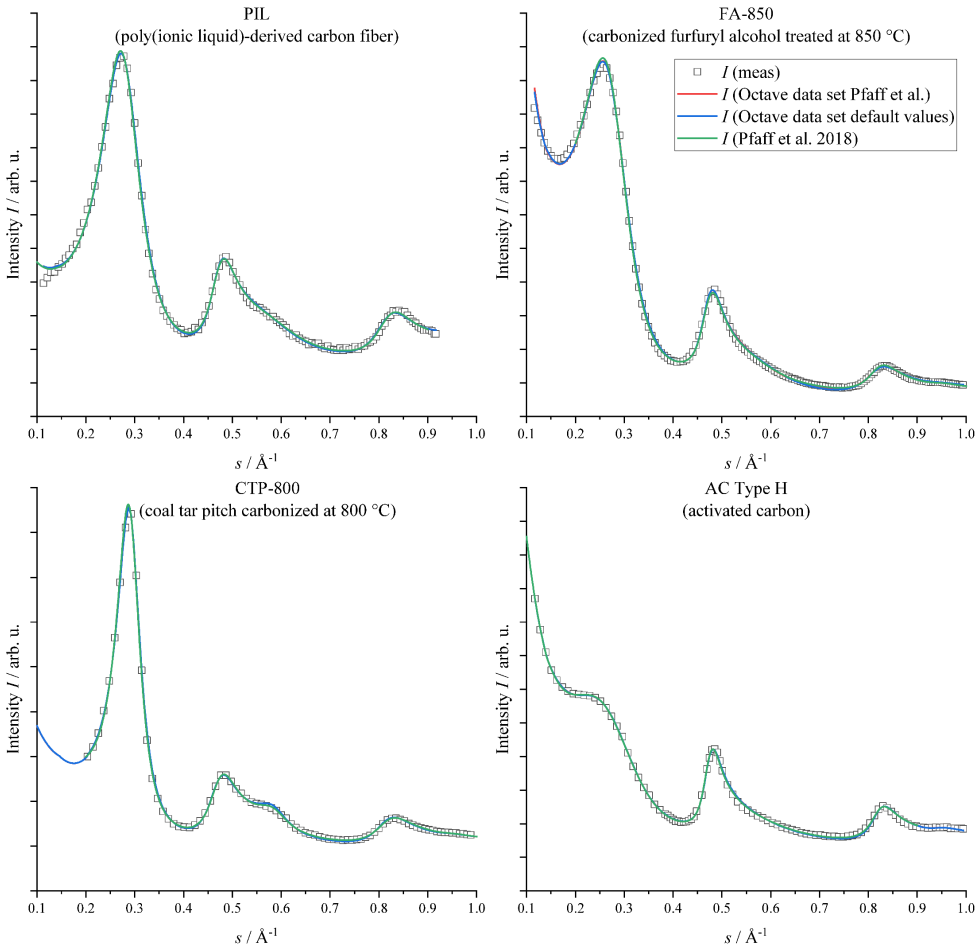

Figure S1 Validation of *CarbOct* using WAXS data of different well-evaluated samples (PIL = poly(ionic liquid)-derived carbon fiber, FA-850 = carbonized furfuryl alcohol treated at 850 °C, CTP-800 = coal tar pitch carbonized at 800 °C, AC Type H = an activated carbon). All three methods (automatic fits using *Octave* with the values of Pfaff et al. [3] as start values (red) and the recommended standard values as start values (blue) and the fit from Pfaff et al. [3]) lead to a similarly acceptable fitting and comparable structural parameters as reported in Pfaff et al. [3]. For improved visualization, for PIL only every 20th point and for all other samples only every 2nd point is shown. The evaluations of sample FA-850 by the different approaches are compared in further detail in Figure 6.

S5. Results of the refined samples for the verification *OctCarb* including the calculation times for the WAXS refinements

Table S3 Overview of the microstructure parameters of CTP-800 (carbonized coal tar pitch), AC Type H (activated carbon), FA-850 (carbonized furfuryl alcohol) and PIL (poly(ionic liquid) carbon fiber).

The parameters were rounded to the same number of digits as the values given in the original publications. v was fixed to 4, i.e. $\kappa_a = 1/v$ was fixed to 0.25. In Faber et al. [5] and Pfaff et al. [3], the errors of the other parameters were estimated by the influence of changing the parameter on the quality of the fit. For *Octave manual* and *Octave fitted* the error was calculated inside the fitting process. For this refinement, the error is a mathematical calculated error and more accurate than in the references.

Parameter	AC Type H [5]	AC Type H [3]	AC Type H (*Octave* manual)	AC Type H (*Octave* fitted)
L_a / Å	32 ± 4	31 ± 3.9	30 ± 7.3	30 ± 7.1
l_m / Å	26 ± 3.3	24 ± 3	24 ± 11.7	24 ± 11.4
σ_1	0.12 ± 0.014	0.12 ± 0.014 [1]	0.11 ± 0.006	0.11 ± 0.006
κ_a / Å	0.25	0.25	0.25	0.25
N_m	1.8 ± 0.23	1.8 ± 0.23	1.7 ± 0.37	2 ± 0.4
N	2.7 ± 0.27	2 ± 0.25	2 ± 0.2	2 ± 0.2
L_c / Å	7 ± 0.9	7 ± 0.9	7 ± 0.6	7 ± 0.6
κ_c / Å	0.15 ± 0.02	0.12 ± 0.02	0.15 ± 0.02	0.15 ± 0.02
$\overline{a_3}$ / Å	3.6 ± 0.054	3.56 ± 0.053	3.51 ± 0.057	3.52 ± 0.056
σ_3 / Å	0.57 ± 0.057	0.5 ± 0.05	0.45 ± 0.058	0.46 ± 0.058

[1] Not published but known due to personal contact to the author.

Parameter	CTP-800 [5]	CTP-800 [3]	CTP-800 (*Octave* manual)	CTP-800 (*Octave* fitted)
L_a / Å	19 ± 2.4	19 ± 2.4	18 ± 1.3	18 ± 1.3
l_m / Å	16 ± 2	15 ± 1.9	15 ± 2.1	15 ± 2.1
σ_1	0.14 ± 0.016	0.13 ± 0.016 [2]	0.12 ± 0.02	0.12 ± 0.02
κ_a / Å	0.25	0.25	0.25	0.25
N_m	2 ± 0.25	2.2 ± 0.28	1.5 ± 0.59	1 ± 0.6
N	3.9 ± 0.49	3.8 ± 0.48	3.4 ± 0.39	3.4 ± 0.39
L_c / Å	13 ± 1.6	13 ± 1.6	12 ± 0.8	12 ± 0.8
κ_c / Å	0.96 ± 0.12	0.76 ± 0.1	1.27 ± 0.38	1.27 ± 0.38
$\overline{a_3}$ / Å	3.44 ± 0.052	3.44 ± 0.052	3.43 ± 0.006	3.43 ± 0.006
σ_3 / Å	0.26 ± 0.026	0.23 ± 0.023	0.2 ± 0.025	0.2 ± 0.025

Parameter	FA-850 [5]	FA-850 [3]	FA-850 (*Octave* manual)	FA-850 (*Octave* fitted)
L_a / Å	25 ± 3.1	23 ± 2.9	28 ± 1.6	28 ± 1.7
l_m / Å	20 ± 2.5	19 ± 2.4	23 ± 2.5	23 ± 2.8
σ_1	0.13 ± 0.016	0.13 ± 0.016 3	0.15 ± 0.012	0.16 ± 0.013
κ_a / Å	0.25	0.25	0.25	0.25
N_m	1.5 ± 0.19	1.6 ± 0.2	1.6 ± 0.28	2 ± 0.7
N	2.3 ± 0.29	2.3 ± 0.29	2.3 ± 0.17	2.8 ± 0.4
L_c / Å	8 ± 1	8 ± 1	8 ± 0.5	10 ± 1.3
κ_c / Å	0.51 ± 0.06	0.42 ± 0.05	0.44 ± 0.05	0.44 ± 0.1
$\overline{a_3}$ / Å	3.6 ± 0.054	3.61 ± 0.054	3.6 ± 0.025	3.74 ± 0.13
σ_3 / Å	0.43 ± 0.043	0.44 ± 0.044	0.44 ± 0.052	0.69 ± 0.217

[2] Not published but known due to personal contact to the author.
[3] Not published but known due to personal contact to the author.

Parameter	PIL [7]	PIL [3]	PIL (*Octave* manual)	PIL (*Octave* fitted)
L_a / Å	20 ± 2.5	20 ± 2.5	22 ± 0.5	22 ± 0.5
l_m / Å	16 ± 1.9	16 ± 2	18 ± 0.8	18 ± 0.9
σ_l	0.25	0.13 ± 0.016 [4]	0.15 ± 0.005	0.14 ± 0.005
κ_a / Å	1.7 ± 0.21	0.25	0.25	0.25
N_m	3 ± 0.36	1.7 ± 0.21	1.5 ± 0.14	1 ± 0.1
N	11 ± 1.4	3 ± 0.38	2.6 ± 0.09	2.6 ± 0.09
L_c / Å	11 ± 1.4	11 ± 1.4	9 ± 0.3	9 ± 0.2
κ_c / Å	0.77 ± 0.1	0.77 ± 0.1	0.79 ± 0.05	0.78 ± 0.05
$\bar{a_3}$ / Å	3.63 ± 0.054	3.64 ± 0.055	3.57 ± 0.008	3.56 ± 0.007
σ_3 / Å	0.54 ± 0.054	0.56 ± 0.056	0.47 ± 0.015	0.46 ± 0.014

Table S4 Calculation times for the different samples and a different amount of measurement points.

HPC means high-performance computing cluster (JustHPC at the Justus Liebig University Giessen [8] using CentOS 7, typical node parameters are 2 x 12 sockets x cores/socket, 192 GB memory, 54.4 GFlops/Core and Intel Xeon Skylake 6126 or 6226 (1.7 Ghz or 1.9 Ghz) processors), *common PC* is a Windows computer using an Intel® Core™ i5-8400 CPU (4x 2.8 GHz) and 16 GB RAM *Raspberry Pi* is a Raspberry PI 4B Rev. 1.1 using an ARM v7 processor (4x 1.5 GHz) and 4 GB RAM running at Raspbian 11 (bullseye).. The main influence on the calculation time has the amount of measurement points and not the processor, due to the missing availability of parallel computing. Of course, a high-performance computing cluster is faster, if one want to refine multiple samples at once, because on these systems a high number of different programs can run simultaneously. All values are just examples and might vary due to different background processes on the different systems. The calculation time is given in minutes.

Sample	Measurement points	Calc. time HPC	Calc. time common PC	Calc. time Raspberry Pi
AC Type H	258	05:14	03:42	11:49
CTP-800	163	01:50	02:13	04:08
FA-850	300	04:36	07:56	05:13
PIL	2392	22:17	15:55	50:54

[4] Not published but known due to personal contact to the author.

Table S5 Overview of the microstructure parameters of H-2100/H-2800 (phenol formaldehyde resorcinol) and LSPP-1200 (low softening point pitch) measured by wide-angle neutron scattering (WANS).

The parameters were rounded to the same number of digits as the values given in the original publications. v was fixed to 4, i.e. $\kappa_a = 1/v$ was fixed to 0.25. The error for each parameter for the references and the manual fitting is about 10-15 %.

	H-2100	H-2100	H-2800	H-2800
Parameter	2	*Octave* automatic	2	*Octave* automatic
L_a / Å	40	34 ± 0.3	51	51 ± 1.2
l_m / Å	32	27 ± 0.5	43	41 ± 1.9
l_{cc} / Å	1.413	1.418 ± 0.0002	1.419	1.421 ± 0.0002
σ_1	0.067	0.056 ± 0.0025	0.047	0.052 ± 0.0024
L_c / Å	14	11 ± 0.4	23	19 ± 1
N_m / Å	3	2 ± 0.3	5	3 ± 0.7
N	4	3 ± 0.2	7	6 ± 0.4
κ_c / Å	0.37	0.43 ± 0.029	0.49	0.79 ± 0.032
$\overline{a_3}$ / Å	3.56	3.49 ± 0.005	3.48	3.46 ± 0.003
$a_{3,\,min}$ / Å	3.16	2.49 ± 0.076	3.3	2.87 ± 0.037
σ_3 / Å	0.44	0.34 ± 0.009	0.25	0.2 ± 0.008
η	0.86	0.89 ± 0.003	0.93	0.96 ± 0.002

Parameter	LSPP-1200 2	LSPP-1200 *Octave* automatic	LSPP-1200 *Octave* manual
L_a / Å	27	23 ± 0.1	23
l_m / Å	22	18 ± 0.2	18
l_{cc} / Å	1.418	1.42 ± 0.0003	1.420
σ_1	0.062	0.066 ± 0.0037	0.066
L_c / Å	17	31 ± 3.3	15
N_m / Å	3	0 ± 0.7	3
N	5	9 ± 1.2	4
κ_c / Å	0.63	100 ± 559.241	0.67
$\overline{a_3}$ / Å	3.48	3.51 ± 0.006	3.51
$a_{3,\,min}$ / Å	3.00	2.51 ± 0.1	3.21
σ_3 / Å	0.30	0.45 ± 0.009	0.33
η	1.00	1 ± 0.002	1

S6. Tests for fitting the (004)-region of the LSPP-1200 WANS-data

In section 4.2.3 of the main article, the problem of fitting the (004)-region of the WANS data of the sample LSPP-1200 was discussed. The main problem is the poor fitting of the (004)-region using the automatic fit from *OctCarb*. Hence, an automatic refinement using the whole data range must be adjusted manually afterwards (Figure 7 of the main article). To get deeper insights and a more detailed understanding of this issue, some other refinements were performed using only a smaller range of the measured data (Figure S2 - Figure S4).

First, only the refinement range was reduced, and the resulting scattering curve was extrapolated over the entire range (red). Second, the normalization parameters were fixed, and the other microstructure parameter were refined and the result extrapolated (blue). In the next step, only the interlayer parameters with (green) and without the normalization parameters (purple) were refined and the result extrapolated. Since at higher values of s, only intralayer reflections are visible, a smaller range is sufficient to determine the interlayer structure parameters. Data at higher s-values do not lead to more accurate results regarding the interlayer structure parameters.

Three main conclusions can be drawn from these tests:

1. Looking at the refinements including the normalization parameters, it becomes evident that the normalization parameters were calculated wrong using only the smaller data range. On the other hand, the scattering data in this area including the (004)-region can be refined well. Overall, this indicates that the incoherent background of the scattering data was not subtracted properly.
2. Even if the measured data are hardly influenced by noise and the fitted curve lies almost perfectly on the data, the intralayer parameters cannot be determined exactly. For the higher order reflections ($s > 1.2$ Å^{-1}), slight differences are visible between the "without normalization" and "only interlayer" fits. This means, that *Octave* tries to use the overlapping intralayer reflections as small background correction to refine all data as best as possible. This results in slightly calculated intralayer reflections and therefore other intralayer parameters.
3. Another explanation for 2 can be found by the influence of the layer disorder on the scattering data: In general, a stronger layer disorder causes broader reflections, with higher order reflections becoming broader [1]. So the used range for the refinement might be too small to determine this disorder correctly, since the influence is too small on these lower ordered reflections. On the other hand, with higher values of s, no more interlayer reflections are visible, so an extension of the measurement range would not solve this problem.

However, overall the main problem for the automatic refinement regarding the (004)-reflection is its shape: It is too much a shoulder rather than a clearly visible reflection and therefore, it is too "insignificant" for the *Octave* fitting routine compared to the whole scattering curve, especially to the neighboring valleys/feet which makes the manual adjustment necessary.

As another test, in the ranges of 0.33 $Å^{-1} < s < 0.44$ $Å^{-1}$ and 0.63 $Å^{-1} < s < 0.77$ $Å^{-1}$ not all measured points were refined. Instead, some points were left out during the refinement and extrapolated afterwards (Figure S5 - Figure S7). This test confirms that for *Octave* the feet/valleys besides the (004) and (11) reflection are more relevant in the fitting algorithm as the (004) reflection itself. Figure S7 shows, that only every 30th point (in the *s*-ranges 0.33-0.44 & 0.63-0.77 $Å^{-1}$) should be considered in this case, while more points would still influence the results. Nevertheless, the results from the automatic refinement are different compared to the manual refinement, especially the stacks are now significant higher (L_c). At first glance, this sounds like a significant intrinsic flaw between these two methods. However, this difference can be explained on closer inspection of the individual parameters: With the manual fit, both the difference between a_3 and $a_{3\,min}$ and the absolute value for σ_3 are smaller. This higher order results in sharper interlayer reflections in WAXS/WANS data. To compensate for this effect, the crystallite size, i.e. the stack height, has to be smaller, which in turn leads to broader reflections. Overall, these effects balance each other out, so that both fits and both results are plausible.

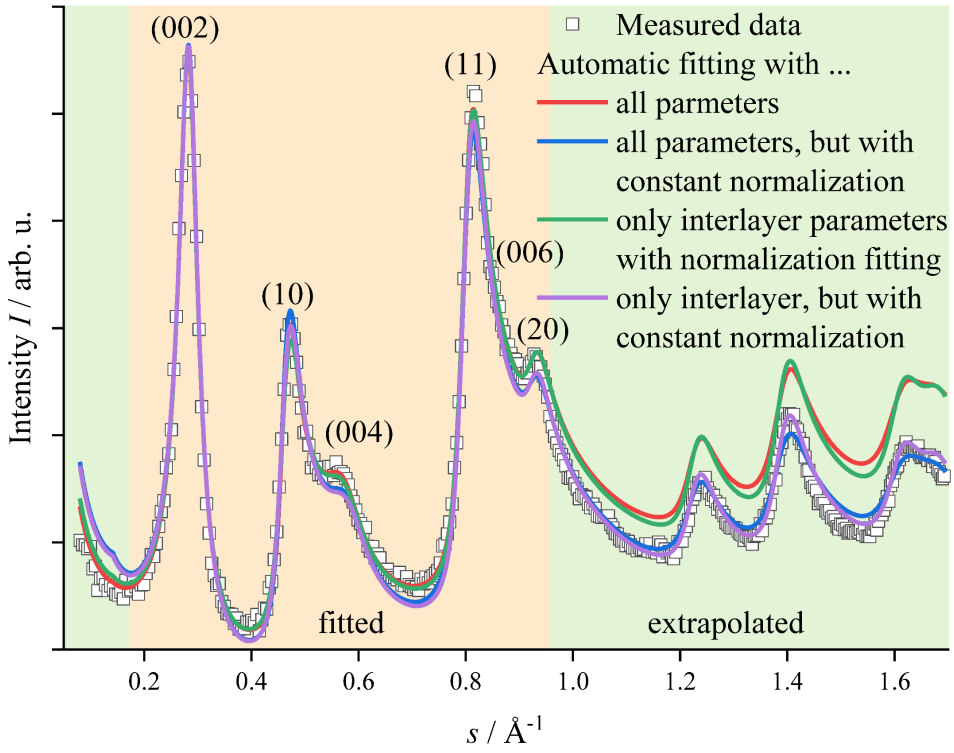

Figure S2 Tests for the automatic *Octave* refinement with special attention to the (004)-region of WANS data from LSPP-1200 (low softening-point pitch). For all tests, only the orange area was fitted, and the green areas extrapolated. Tests were performed with all parameters (red), the interlayer and intralayer parameters without the normalization (blue), the interlayer parameters with the normalization (green) and only with the interlayer parameters (purple). Only every 5th data point is shown.

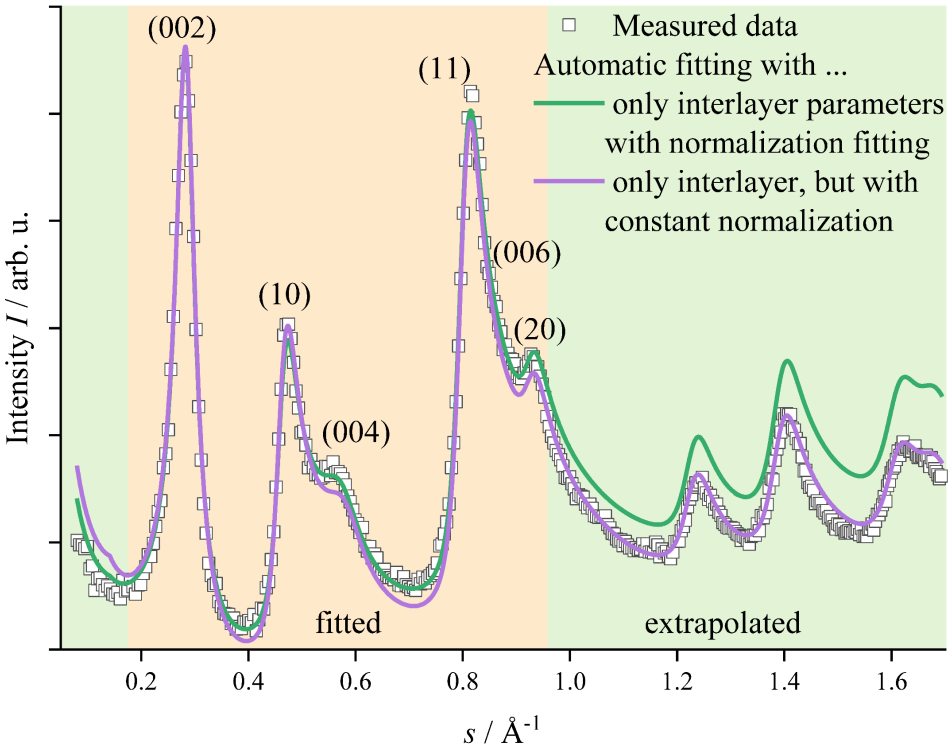

Figure S3 Tests for the automatic *Octave* refinement with special attention to the (004)-region of WANS data from LSPP-1200 (low softening-point pitch). For all tests, only the orange area was fitted, and the green parts extrapolated. Tests were performed with all parameters (red), the interlayer and intralayer parameters without the normalization (blue), the interlayer parameters with the normalization (green) and only with the interlayer parameters (purple).

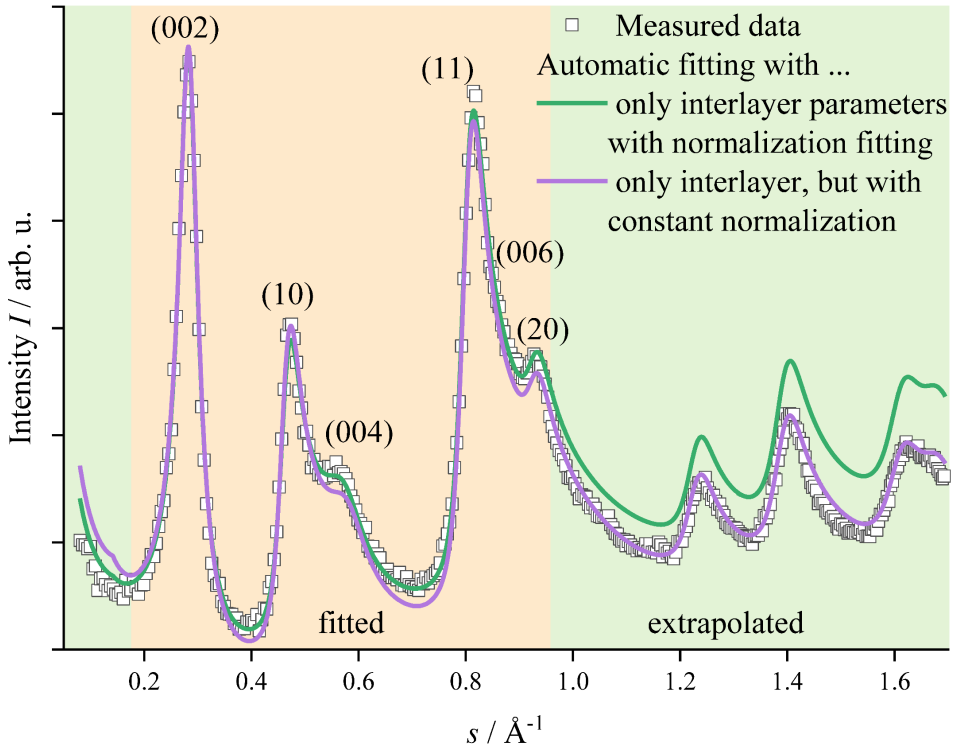

Figure S4 Tests for the automatic *Octave* refinement with special attention to the (004)-region of WANS data from LSPP-1200 (low softening-point pitch). For all tests, only the orange area was fitted, and the green parts extrapolated. Tests were performed with all parameters (red), the interlayer and intralayer parameters without the normalization (blue), the interlayer parameters with the normalization (green) and only with the interlayer parameters (purple).

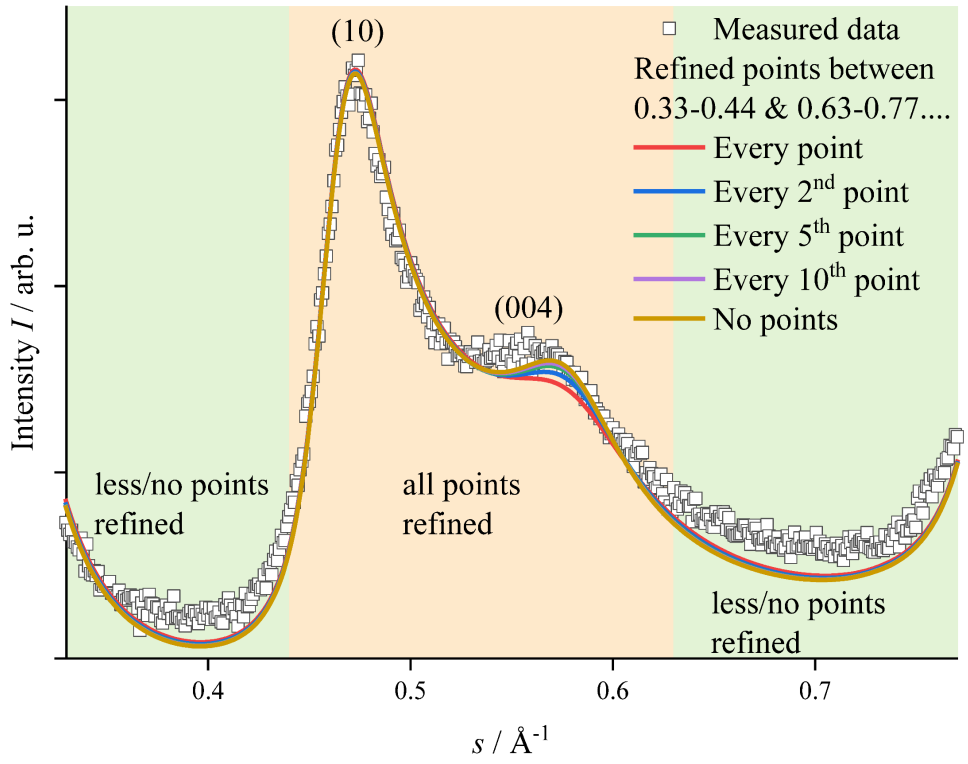

Figure S5 Tests for the automatic *Octave* refinement with special attention to the (004)-region of WANS data from LSPP-1200 (low softening-point pitch). For all tests, only the orange area was fitted, and the green parts extrapolated. In order to determine the influence of the feet/valleys on the (004)-reflection, first all (red) and then only every 2nd (blue), every 5th (green), every 10th (purple) and at last no point (brown) were used for the refinement. For more details, take a look at Figure S6. It becomes clearly, that the high number of data points in the feet/valleys influence the refinement. Compared to the (004)-reflection, these green areas are in mathematical terms more important. Less refined points in the green areas lead to a higher accuracy in the (004)-reflection.

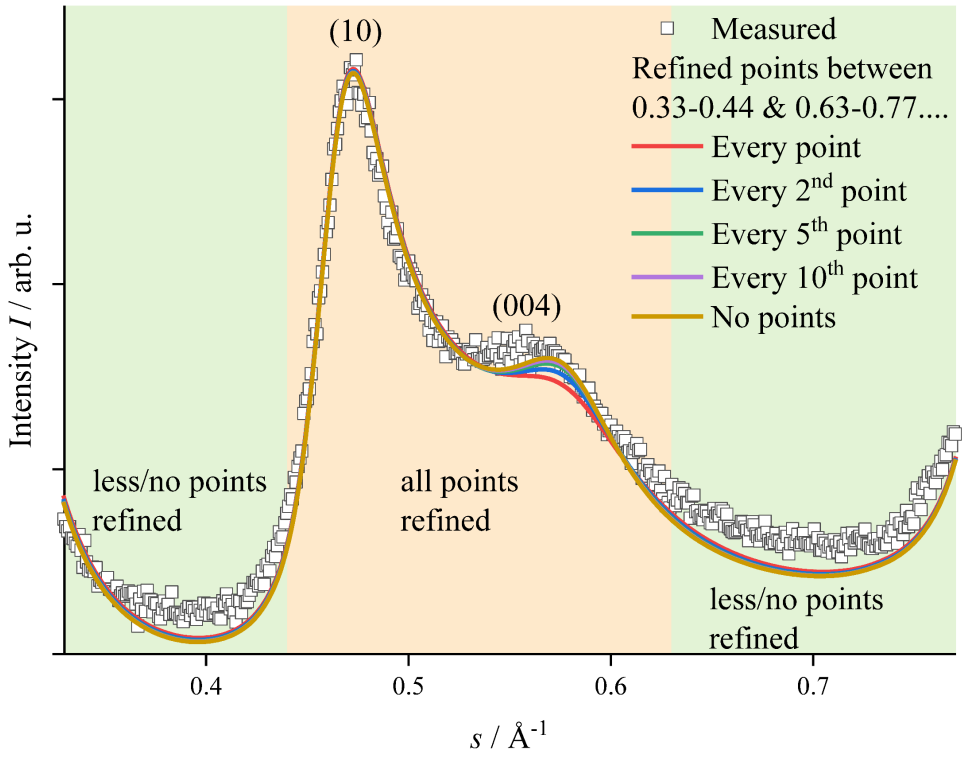

Figure S6 Tests for the automatic *Octave* refinement with special attention to the (004)-region of WANS data from LSPP-1200 (low softening-point pitch). For all tests, in the orange area all points and in the green area less points were fitted. Hence, in the ranges of 0.33 $Å^{-1} < s < 0.44$ $Å^{-1}$ and 0.63 $Å^{-1} < s < 0.77$ $Å^{-1}$, not all points were used. In order to determine the influence of the feet/valleys on the (004)-reflection, first all (red) and then only every 2nd (blue), every 5th (green), every 10th (purple) and at last no point (brown) were used for the refinement. It becomes clearly, that the high number of data points in the feet/valleys influence the refinement. Compared to the (004)-reflection, these green areas are in mathematical terms more important. Less refined points in the green areas lead to a higher accuracy in the (004)-reflection.

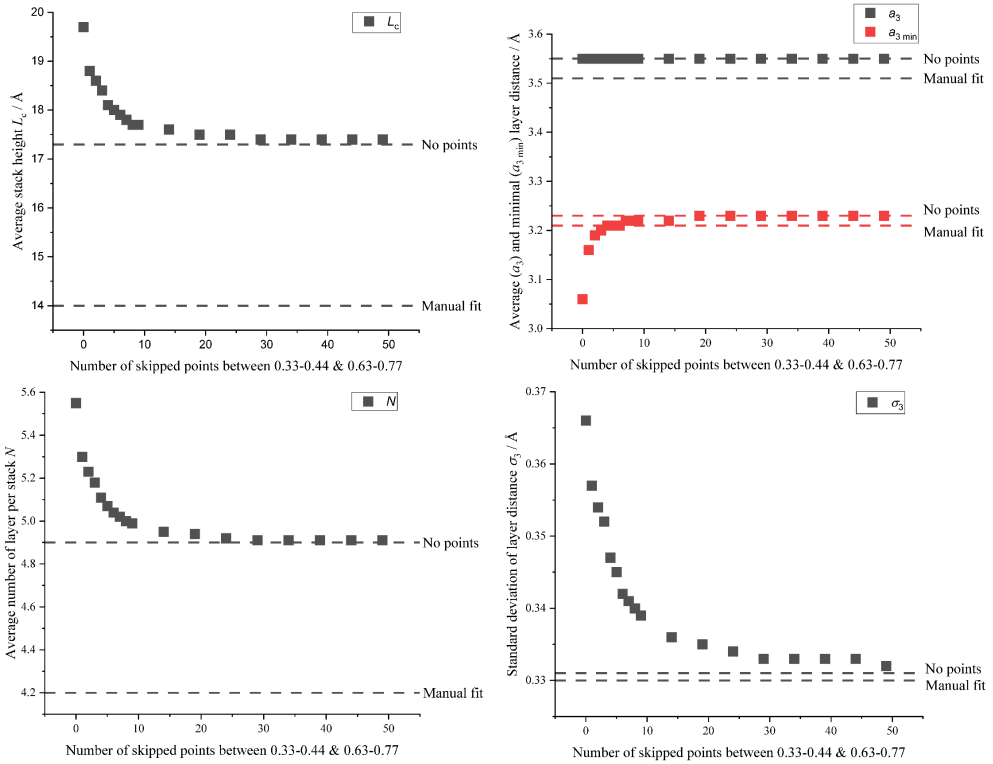

Figure S7 Tests for the automatic *Octave* refinement with special attention to the (004)-region of WANS data from LSPP-1200 (low softening-point pitch). For all tests, only the green range in Figure S5 was fitted. Hence, in the range of 0.33 $Å^{-1} < s < 0.44$ $Å^{-1}$ and 0.63 $Å^{-1} < s < 0.77$ $Å^{-1}$, not all points were used. In order to determine the influence of the feet/valleys on the (004)-reflection, some points were skipped. Evidently, a high number of data points in the feet/valleys influence the refinement. Compared to the (004)-reflection, these regions of the scattering curve (green domains in the figures above) are in mathematical terms more important. Less refined points in the green areas lead to a higher accuracy in the (004)-reflection and therefore, the interlayer microstructure parameters are different.

S7. Download and usage of *iObs*

The currently used C++ code for calculating *iObs* including some auxiliary files for compiling an *.oct file for *Octave* is available in the GitHub. [5]

S7.1. Compilation of an *.oct file for using *iObs* with *Octave*

An alternative way to use the calculations code in C++ is to compile it in an *.oct file, which can be used from *Octave*. A video describing the next step is available in the GitHub [6] and at YouTube [7] [8].The basic idea is, that *Octave* uses some code, which is precompiled for different operating systems. This code can be used as an additional library for C++, so the algorithm of calculating I_{obs} can be converted in an *.oct file on the currently used operating system. This *.oct file in turn can be opened and used by *Octave* to calculate I_{obs} inside *Octave*. This method allows to calculate I_{obs} and therefore to refine measured WAXS/WANS data without the directly usage of any C++ code. Hence, the command *mkoctfile* implemented in *Octave* is used to perform this compilation. In principle, beside the pure calculation file, an additional file performing the in- and output operations, which is basically a "connector" between *Octave* and C++ code, is needed (*iObs.cpp*).

Since the compilation is unique for each operating system, it is highly recommended to compile the file on every different operating system. While the compilation is different for each operating system, only a brief overview of the command and its usage can be given. A more detailed instruction how to build an *.oct file explaining these steps as well as some example files are available in the GitHub. [9]

For Microsoft Windows, two commands must be executed, whereas the paths must be adjusted, obviously:

cd C:\Octave\Octave-5.2.0\mingw64\bin

C:\Octave\Octave-5.2.0\mingw64\bin\mkoctfile -LC:\Octave\Octave-5.2.0\mingw64\lib\Octave\5.2.0 -IC:\Octave\Octave-5.2.0\mingw64\include\Octave-5.2.0\Octave 'C:\iObsOct\iObs.cpp'

For MacOS and Linux, only one command must be executed:

MacOS: mkoctfile -I/usr/local/bin/Octave ~//iObsOct/iObs.cpp

Linux: mkoctfile -I/usr/include/Octave-5.2.0/octave ~/iObsOct/iObs.cpp

The exact path for the include files can be found out using the following command:

which Octave

[5] https://github.com/osswaldo/NGCs/blob/master/Octave/oct-files/Self-compilation/iObsOct/calculations.cpp
[6] https://github.com/osswaldo/NGCs/tree/master/Instruction%20Videos
[7] English: https://www.youtube.com/playlist?list=PLTlnYDX5g1FylWfH8cSM_ZQUQpn3dSp6M
[8] German: https://www.youtube.com/playlist?list=PLTlnYDX5g1FwaOQkLXTxrpvHW9CRUwBrk
[9] https://github.com/osswaldo/NGCs/tree/master/Octave/oct-files

S8. Installation and updates

A video describing the next step is available in the GitHub [10] and at YouTube [11, 12].

S8.1. Installation under *Microsoft Windows*

For Microsoft Windows, an executable installation package can be downloaded directly from the developer website [13]. Afterwards the *optim* package including all needed dependencies can be installed using "pkg install -forge optim".

S8.2. Installation under *MacOS*

For MacOS, no official-maintained installer or bundle is available, but, however, there are some *.app builds available from the developer [14], for newer versions, an installation guide can be found in the developer instructions. [15]

S8.3. Installation under *GNU/Linux*, *BSD* and other systems

For all other operating systems like *Linux*, *BSD* and distribution independent approaches like *Docker* it is impossible to give a brief installation guide due to the high number of different systems. In general, all guides can be found in the developer instructions. [16]

S8.4. Installation of *optim* for non-*Windows* builds

For some operating systems/installations (if *pkg install -forge optim* fails) the *optim* package and its dependencies must be installed manually using console commands. First the optim package and its dependencies (*structs*, *statistics* and *io*) must be downloaded from *sourceforge* [17]. Second, open *Octave* and navigate to the download directory, e.g. "cd C:\Users\<*Username*>\Downloads". In the last step, install optim and its dependencies (order as followed):

pkg install io-<*version*>.tar.gz

pkg install statistics-<*version*>.tar.gz

pkg install struct-<*version*>.tar.gz

pkg install optim-<*version*>.tar.gz

[10] https://github.com/osswaldo/NGCs/tree/master/Instruction%20Videos
[11] English: https://www.youtube.com/playlist?list=PLTlnYDX5g1FylWfH8cSM_ZQUQpn3dSp6M
[12] German: https://www.youtube.com/playlist?list=PLTlnYDX5g1FwaOQkLXTxrpvHW9CRUwBrk
[13] https://www.gnu.org/software/octave/download
[14] https://octave-app.org/
[15] https://wiki.octave.org/Octave_for_MacOS
[16] https://wiki.octave.org/Category:Installation and https://wiki.octave.org/Octave_for_GNU/Linux
[17] https://octave.sourceforge.io/packages.php

S8.5. Links and updates

Due to the number of different programs, extensions and scripts that are used and the resulting update frequency that can be expected from them, it does not make sense to describe the update process in this static work. Current links, installation files can be found in the file “Useful links.txt” and scripts can be found in the GitHub. [18]

[18] https://github.com/osswaldo/NGCs

S9. Usage of *Octave*

After loading the refinement script (*OctCarb*), only a few adjustments are necessary to perform the first fit. Stepwise, consecutive files for the next steps below can be found in the other SI files. A video explaining these steps is available in the in the GitHub [19] and at YouTube [20, 21].

0. Download and install *Octave*, *iObs* and the *CarbOct* (see above).
1. First, some initial parameters like the sample name, data path, radiation type, wavelength etc. must be adjusted (Figure S8). Additionally, a meaningful for the parameter *nSkip* should be set. *nSkip* = *5* means, that only every 5th point will be calculated to make the calculations much faster, less accurate at the same time. The value should be higher the more measurement points are available. Also, a constant v must be chosen. For a common XRD measurement using Cu-K_α radiation in a range of 10 ° < 2θ < 140 °, a value of $v = 4$ is sufficient for most of the samples (see Table S2).
2. As the first real refinement step, the normalization parameters (k, $const_1$, $const_2$) and the concentrations of foreign atoms (c_H, c_N, c_O, c_S) should be refined. While the last ones are known exactly form elemental analysis, the normalization parameters must be refined by hand. For the automatic adjustment, it can be done only roughly, but for the manual adjustment, it should be done more exactly. The normalization constants should be adjusted at every of the following steps.

Manual refinement:

3a. Generally, the manual refinement is divided into 3 parts: refinement of the interlayer structure, refinement of the intralayer structure and a final step with all parameters including the normalization. For the interlayer parameters, first μ or β can be left constant and only one of it should be variated. Also, $a_{3\ min}$ should not be lower than 3 Å, otherwise it will dominate the whole curve too much, because the set value is no longer physically meaningful. σ_3 can be used to refine the broadness of the (002) and (004) reflections and has a high influence on the damping of the (004) reflection. If the (002) reflection is refined approximately, both μ and β should be further refined. It should be noted that the stack height $L_c \sim (\mu+1)/\beta$ should no longer vary too much. In this step, η (homogeneity of the stacks) can be refined by taking the left side of the (002) reflection and lower values of the modules of the scattering vector/scattering angle into account. q (preferred orientation) should be left constant in this step, because without a refinement of the intralayer structure, it is not possible to refine this parameter meaningfully.

[19] https://github.com/osswaldo/NGCs/tree/master/Instruction%20Videos
[20] English: https://www.youtube.com/playlist?list=PLTlnYDX5g1FylWfH8cSM_ZQUQpn3dSp6M
[21] German: https://www.youtube.com/playlist?list=PLTlnYDX5g1FwaOQkLXTxrpvHW9CRUwBrk

Figure 5 in the main article shows an exemplary WAXS pattern and a manually adjusted result that contains the priority of the various regions.

4a. For the most samples, this step is easier to perform than the refinement of the interlayer parameters due to the lower number of parameters. Since v is chosen as a constant, only α, σ_1 and l_{cc} must be refined. α influences both, the height and the broadness of the (10) and the (11) reflection, σ_1 influences more the (11) reflection. Using l_{cc}, the exactly position of both reflections can be refined. For some samples, the preferred orientation q must be refined at this step.

5a. As the last step for the manual refinement, all microstructural parameters including the normalization should be adjusted. The exact procedure depends strongly on the sample and can therefore not be described in general here. In general, the accuracy should focus on the valley between the (002) and the (10) reflection rather than on the values that lie left to the (002) reflection. For the (10) and (11) reflections it is important to assure that the ratio of the size and shape in relation to the background is correct. The (004) reflection needs to be adjusted precisely, even if it sometimes just becomes like a shoulder. The accuracy of the refinement of this reflection significantly influences the accuracy of the resulting disorder parameters of the stack structure (see Figure 5 in the main article).

Automatic refinement:

3b. For the basic automatic refinement, the default values from Table S6 can be used. These values are in principle mean values from the common range of these values. Of course, if other suitable start values are known, they should be used (i.e., for measurements from a temperature series). To start the automatic refinement, the switch *plotOnly* must be set to *false*. For some samples or measurements, the upper and lower bonds for the preferred orientation (q) must be adjusted to a range from 0 to 1 (ub3 & lb3), otherwise, a preferred orientation will not be refined.

4b. As a final refinement step, the parameter *nSkip* should set to 1. Now, every measured point will be refined, and the fitting result might improve. As start values, the values from the 3rd step (3a or 3b) should be used. In addition, the calculated error for the microstructure parameters will become a little bit lower.

5b. As a last step, an additional manual adjustment can be performed. This step is often necessary for more disordered samples, where the (004) reflection is damped and broad.

Table S6 Overview about the default starting values for the refinement with *Octave*.

These values are in principle mean values of the common range of the fitting values and can be regarded as recommendations. Of course, every additional information like results from an elemental analysis should be used to choose as best start values as possible. The *microstructural parameters* are partly calculated from the *parameter for Octave*.

Parameter for *Octave*	Value
μ	4
β	0.5
$\overline{a_3}$ / Å	3.5
da_3 / Å	0.4
σ_3 / Å	0.25
u_3	0
η	1
v	4
α	0.2
l_{cc} / Å	1.412
σ_1	0.1
q	0
Δ_{an}	0
k	500
$const_1$	0
$const_2$	0

Microstructural parameter	Value
L_a / Å (= (v + 1)/ α)	25
l_m / Å (=v /α)	20
κ_a / Å (= 1/v)	0.25
l_{cc} / Å	1.412
σ_1	0.1
L_c / Å (= (μ + 1)/β · $\overline{a_3}$ = N · $\overline{a_3}$)	35
κ_c / Å (= 1/β)	0.25
$\overline{a_3}$ / Å	3.5
$a_{3\,min}$ / Å	3.1
σ_3 / Å	0.25
N (= (μ + 1)/β = N)	10
u_3	0
η	1
q	0
Δ_{an}	0

```
cno = 0.0; #Concentration of disordered sp3 carbon
cH  = 0.0; #Concentration of hydrogen
cN  = 0.0; #Concentration of nitrogen
cO  = 0.0; #Concentration of oxygen
cS  = 0.0; #Concentration of sulfur

#Name of the series and id of the sample, filename of current used file
name = "WAXS example";
global id = "WAXS example Step 1";
filename = "WAXS Step 1 - path and data adjustments.m";
path = 'D:/OneDrive/Uni/PhD/Paper Octave/Github/NGCs/examples/WAXS Steps';
cd 'D:/OneDrive/Uni/PhD/Paper Octave/Github/NGCs/examples/WAXS Steps';
#Measurement data file
measFile = 'D:/OneDrive/Uni/PhD/Paper Octave/Github/NGCs/examples/WAXS Steps/WAXS example data.xy';

neutronCorrection = false; #Corrections for Wide-Angle Neutron Scattering (WANS) experiments.
neutronCorrectionVoigt = false; #Useful for samples containing hydrogen.

#Wavelength and type of radiation (0 = X-ray, 1 = neutrons)
wavelength = 1.5418;
radiation = 0;

#Type of x-values: theta, thetaRad, twoTheta, twoThetaRad, scatS, scatQ
type = "twoTheta";

useQ    = false; #Use Additional Deby-Waller-factor
b       = 0.002; #Deby-Waller-factor Factor
useA                 = true;    #Absorption correction
density              = 2.2;     #Density of sample in g/cm^3
sampleThickness      = 0.3;     #Sample thickness in cm
transmission         = false;   #Transmission geometry (if false, reflection geometry is assumed)
absorptionCorrection = 1;       #Correction factor for absorption coefficient (multiplicator)
useP                 = true;    #Polarization correction
polarizedBeam        = false;   #Do you use a polarized beam?
polarizationDegree   = 0;       #Polarization direction of beam in °.
useCorrAutoColl = false;  #Slit-correction
par_r           = 14;     #Radius of the diffractometer (Debye-Scherrer) in cm
par_delta       = 4;      #Divergence angle in ° (it is converted as if this fixed slit were inside)
par_l           = 5;      #Irradiated length in cm
```

Figure S8 Overview about the basic instrumental parameters, which should be checked and changed for every different measurement.

S10. Example refinement

All files described in this section are also available under in the GitHub [22] and in the file "Example refinement.zip".

S10.1. Step 0 – initial situation

First, you have to download and install *Octave* and an *iObs* file as described below. Depending on your system, you might have to compile the *iObs* file by your own. For this case, the Numerical Recipes for C must be downloaded [23]. Generally, the lines 89 – 134 should be checked for each measurement or measurement group. In these lines, some parameters like the polarization or absorption as well as mathematical fit parameters like the function tolerance, upper and lower bounds and the weight can be tweaked. The initial (downloaded) refinement script (WAXS Fit-Routine-IUCr.m) can be found in the "Excerpt from Github.zip" file. In general, all other lines from 136 onwards should not be changed. The final modified script is also shown in S10.11.

S10.2. Step 1 – path and data adjustments

As first steps, v (line 14) must be tweaked. In general, for a common XRD using Copper-radiation (1.54 Å), $v = 4$ is sufficient. If you use another wavelength, you can look at Table S2 to get a suitable value for v. Additionally, the lines 41 – 87 must be checked. "name" means the name of your sample series or the current date or whatever you want to choose. The resulting refinements will be saved in this directory. The "global id" is a unique name for your current sample or step. You can also use a consecutive number to not override old refinements. "filename" must be the name of the currently used refinement scripts and can be found on top of the editor. "<path_to_filename>" must be replaced by the path, where the "filename" AND the *iObs.oct* file is placed. The *iObs.oct* file must be in the same directory as the refinement script. The complete path of your measurement file (x, y without headers) is stored in the variable "measFile". If you use neutron scattering or another wavelength, you must check the lines 54, 57, 60 and 61, otherwise you can skip these lines. If you want to plot only the coherent or incoherent scattering, you can change the values in the lines 64 and 65. Line 74 ("type") is important if you are not using 2 θ in ° as x-values. The parameters "nStart", "nEnd", "nSkip" and "nUp" can be used to skip some points at the beginning or the end or to plot only every n^{th} point ("nSkip"). To prevent negative values of the intensity, you can use "nUp" to add a constant background to move the WAXS/WANS pattern up.

Regarding the measurement geometry, there are some correction terms, you can use (absorption, polarization and variable slit, lines 121 – 134). These parameters are set to Bragg-Brentano geometry using a unpolarized incidence beam and absorption correction for a 3 mm graphite sample. You should

[22] https://github.com/osswaldo/NGCs/tree/master/Example%20refinement/WAXS%20Steps
[23] http://numerical.recipes/com/storefront.html

check the parameters “density” and “sampleThickness” in lines 122 and 123 and change it to the values of your samples. It is not necessary to know the exact values, but you should put in the correct tendency.

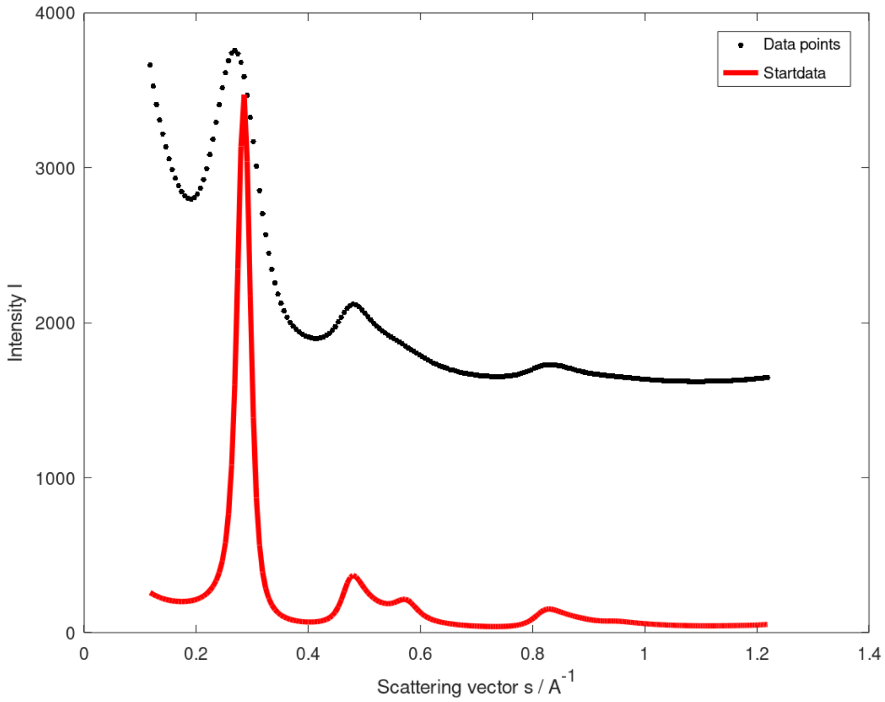

Figure S9 Step 1 - path and data adjustments without any refinements of the normalization or the microstructure.

S10.3. Step 2 – manual background

Second, the background must be corrected in order to start to refine the microstructure. “k” is a normalization constant depending on the amount of the sample, intensity of the radiation etc. and “const1” is used a constant offset of the scattering intensity caused by several effects like cosmic background radiation, incoherent scattering by your sample holder and other general measurement effects. The concentrations of foreign atoms (in atomic %) of hydrogen, nitrogen, oxygen and sulfur known from an elemental analysis can be considered in the lines 29 – 32 (parameters “cH”, “cN”, “cO” and “cS”).

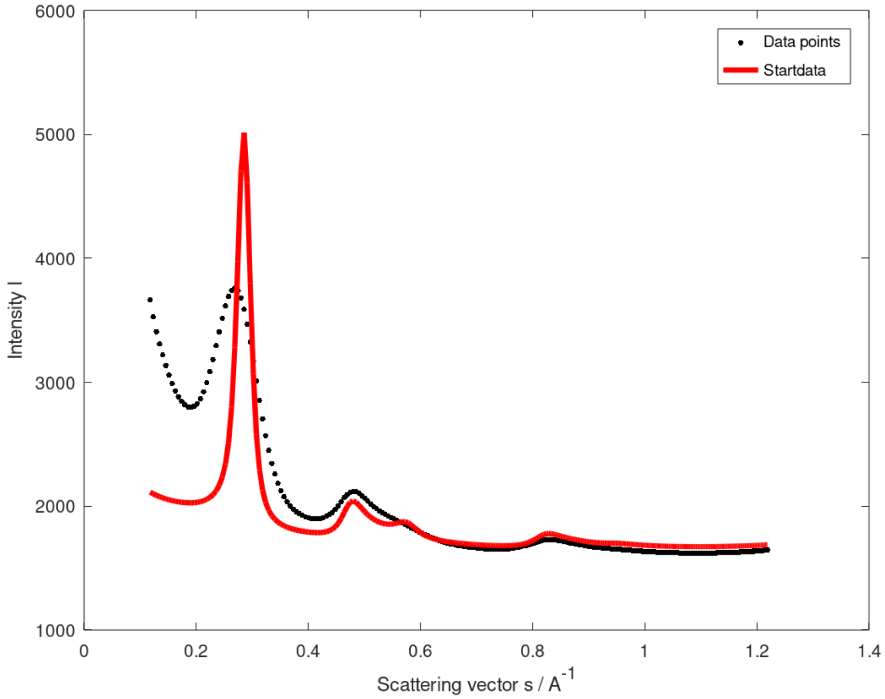

Figure S10 Step 2 – manual background. Only “k” and “const1” are refined.

S10.4. Step 3a – manual fitting – interlayer

To start the refinement of the microstructure, you should start with the interlayer scattering, but you can also start with the intralayer scattering (Step 4a). For the interlayer scattering, the parameters "mu", "beta", "a3", "da3", "sig3" and "eta" must be refined. In addition, "q" (preferred orientation), "k" and "const1" must be refined parallel (lines 7 – 22). The important and significant parts of the WAXS data are shown in Figure 5 in the main article. "mu" and "beta" are parameters to refine the stack height (L_c = $(\mu+1)/\beta \cdot \bar{a_3}$) and polydispersity ($\kappa_c$ = $1/\mu$), "a3" is the average layer distance ($\bar{a_3}$), "da3" is the difference between the average and the minimal layer distance ($a_{3\,min} = \bar{a_3} - da_3$), "sig3" the standard deviation of it (σ_3) and eta means the homogeneity of the stacks (η).

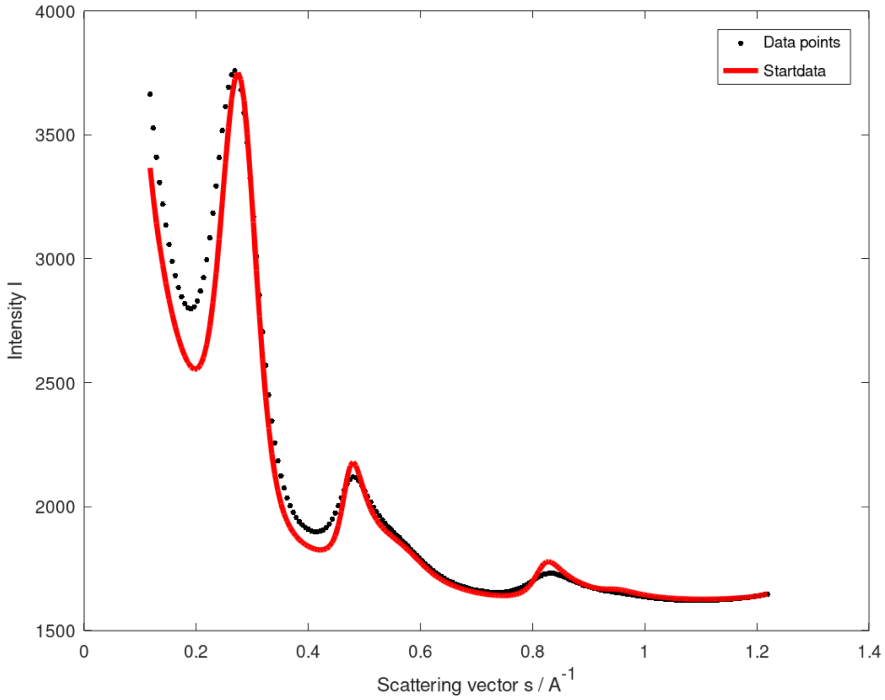

Figure S11 Step 3a – manual fitting – interlayer. The microstructure parameters for the interlayer scattering ("mu", "beta", "a3", "da3", "sig3" and "eta") and "q" (preferred orientation) as well as "k" and "const1" were refined.

S10.5. Step 4a – manual fitting – intralayer

Beside the normalization, the parameters “alpha”, “lcc” and “sig1” (lines 15 – 17) must be refined in this step. Analogous to the interlayer scattering, “alpha” is used to calculate the average layer extension ($L_a = (v+1)/\alpha$), l_{cc} is the average bond length and σ_1 the disorder of the layers (i.e. stress and strain).

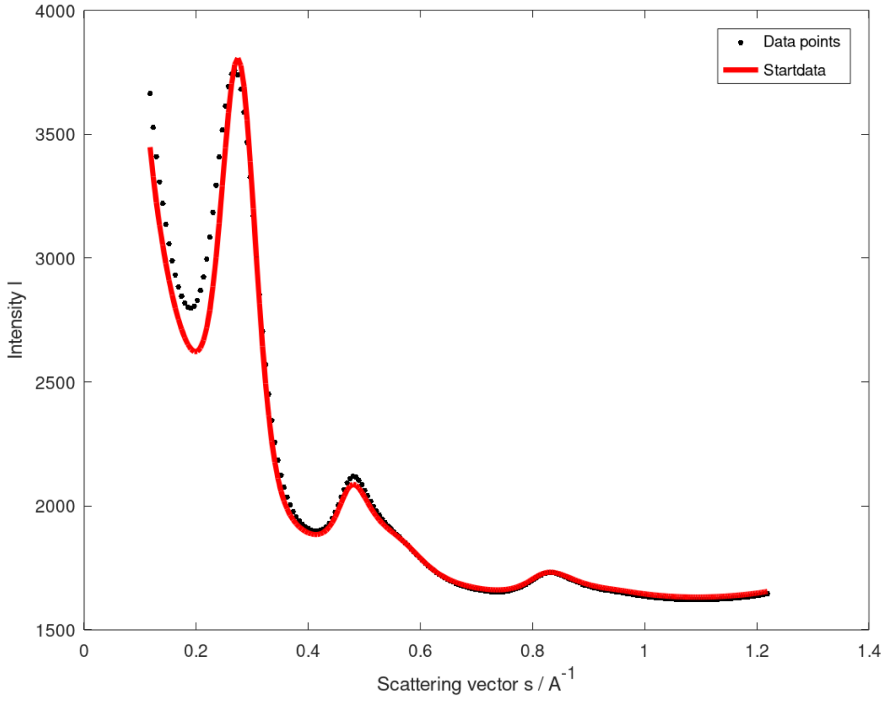

Figure S12 Step 4a – manual fitting – interlayer. The microstructure parameters for the intralayer scattering (“alpha”, “lcc”, “sig1”) and “*q*” (preferred orientation) as well as “*k*” and “const1” were refined.

S10.6. Step 5a – manual fitting – all

For the final step of the manual fitting, you should set "nSkip" to 0 (line 84). Afterwards, try to refine all parameters as described above. You should start with the normalization constants, q and η. As an alternative, you can use these parameters as new start parameters for step 2. In principle, you should repeat the steps 2 – 5 multiple times to get a result, which is as good as possible.

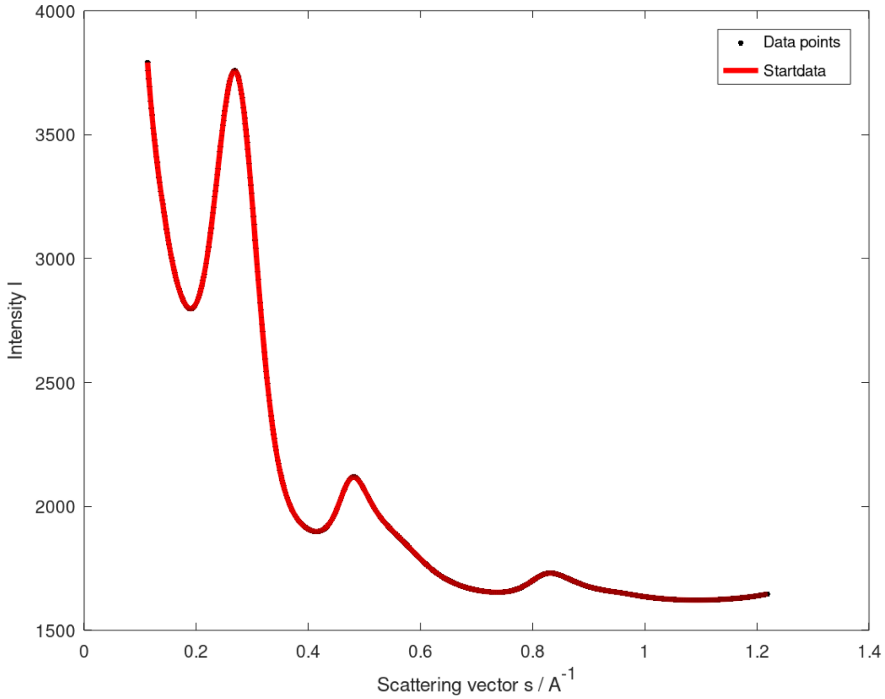

Figure S13 Step 5a - manual fitting – all. In this step, all microstructure and normalization parameters were refined at once.

S10.7. Step 3b – automatic fitting – initialization

To make things easier, you do not have to refine the scattering data manually. There is an automatically fitting routine, which can fit the scattering data and give out the microstructure data. To use this method, you need to roughly refine the background (step 2) set "plotOnly" to "false" (line 35). Basically, that is all what you have to do (of course, you have to press the "run" button on top of the *Octave* GUI). Beside this, you can set the lower and upper bonds for the different microstructure parameters (89 – 104). This might be useful, if you have a temperature series and some parameters have to increase or decrease, but in general, it is not necessary to use it.

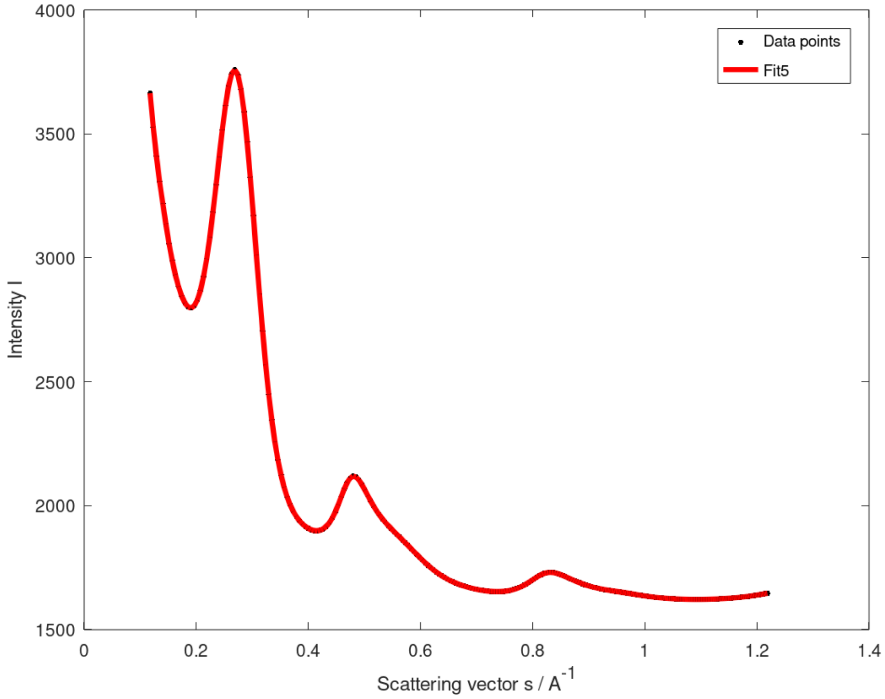

Figure S14 Step 3b – result of the automatic refinement. No further refinement must be done.

S10.8. Step 4b – automatic fitting - fine adjustment

If everything works well, you do not need this step (like in this example). For other samples or insufficient start values or a too bad refinement of the normalization in step 2, you have to make a manual refinement after the automatically fit. To do so, change “plotOnly” back to “true” and perform the steps 3a – 5a. As an alternative, use the resulting parameters as new start parameters and repeat step 3b.

S10.9. Common warnings/errors during the refinement and how to fix them

A list of common errors and their solutions can be found in the GitHub [24] and in the SI under Octave/README.pdf.

[24] https://github.com/osswaldo/NGCs

S11. General influence of the amount/noise of data points and start parameters on the fitting routine

The influence of the number of data points and the noise must be considered in a differentiated manner. Evidently, data noise should be as low as possible, especially for the parts of low scattering intensities in a WAXS/WANS curve.

We find that the number of points and the spread of the measurement data influence the time required for the refinement (Table S4), which is notably also dependent on the computing hardware used. In general, *Octave* uses only one core for computing, especially on Microsoft Windows. For Linux distributions, parallel computing can be performed using *OpenBLAS*, it is thus sufficient to use a cheap Raspberry Pi running on Linux. For high-performance computing clusters (HPCs), the option to perform several refinements simultaneously is a main advantage, which can decrease the refinement time for one WAXS/WANS data set. For a single refinement, the HPC might not even be faster than a commonly used desktop computer, since *Octave* mainly performs computation only with one CPU core. HPCs are mainly built to perform multiple parallel computations, and they might have slower cores than other commercially available PCs. On the other hand, HPCs can run 50 or more *Octave* scripts (*OctCarb* instances) at once, so that the overall time requirement is lower for a high number of samples/data sets.

Another point is the available RAM, which is needed to save and perform the huge matrices calculations (covariance and correlation matrices). The N x N matrix dimension increases quadratically with the number of data points (N), thus HPCs are advantageous for data sets with a high number of measured points (10.000 and above). Another important point is the range of the measured data. For maximum values of the modules of the scattering vector $s_{max} > 4$ Å^{-1}, a lot of (*hk*) reflections must be calculated and saved in between (in the RAM), here HPCs offer a clear benefit.

Last but not least, we found that the start parameters used as input for launching the refinement are not that relevant with regard to attaining a decent fitting, with the exception of the normalization parameters *k*, $const_1$ and $const_2$ (see eq. (6) from the main article). These scaling parameters need to be refined first, prior to the microstructure parameters, aiming at a reasonable match between the fit function and the WAXS/WANS curve with respect to the global scaling. For all parameters, the standard input parameters from Table S6 can be used for the automatically refinement. Using the automatic refinement, first a refinement of the normalization parameters is done, and afterwards the physical microstructure parameters will be refined. Hence, the interlayer and intralayer parameters were refined separately, so these steps need only a short computation time, due to the only small number of simultaneously refined parameters. Only the last step, in which all parameters are refined altogether, takes a long time, because the calculation time is roughly proportional to the square of the number of the number of parameters to be refined.

S12. *Octave* cannot always calculate parameter errors – what to do

The following issue is important for determining the error range of the refinement parameters: In some cases, *Octave* is not able to calculate the correlation and covariation matrices correctly, generating "NaN" as output values for the errors. However, this does not disturb the quality of the fitting, i.e. the resulting structural parameters themselves are still reasonable. If the errors are, however, relevant, in such cases there are basically 2 ways to work around the problem, described in the SI this section and Figure S15. First, the resulting parameters obtained from the fitting can be used as input parameters for another automatic refinement (variant 1 in Figure S15). This procedure might already allow *Octave* to calculate the matrices and therefore the errors correctly. If not, the errors from the intralayer- and interlayer-refinement (steps 1 and 2 of the refinement script) can be used as errors. Second, the "NaN" error often occurs for the normalization parameters k and $const_1$. Hence, the influence of the variation of these parameters on the resulting scattering curve is negligible (< 0.1 %). Second, another possibility to avoid the NaN problem and to obtain error bars is to add an additional refinement step after all other steps, in which all microstructure parameters except for the normalization parameters are refined and therefore the errors of the parameters are calculated (variant 2 in Figure S15). To do so, some other changes are necessary and already implemented in the file "WAXS Fit-Routine-IUCr with additional step all-without-normalization.m".

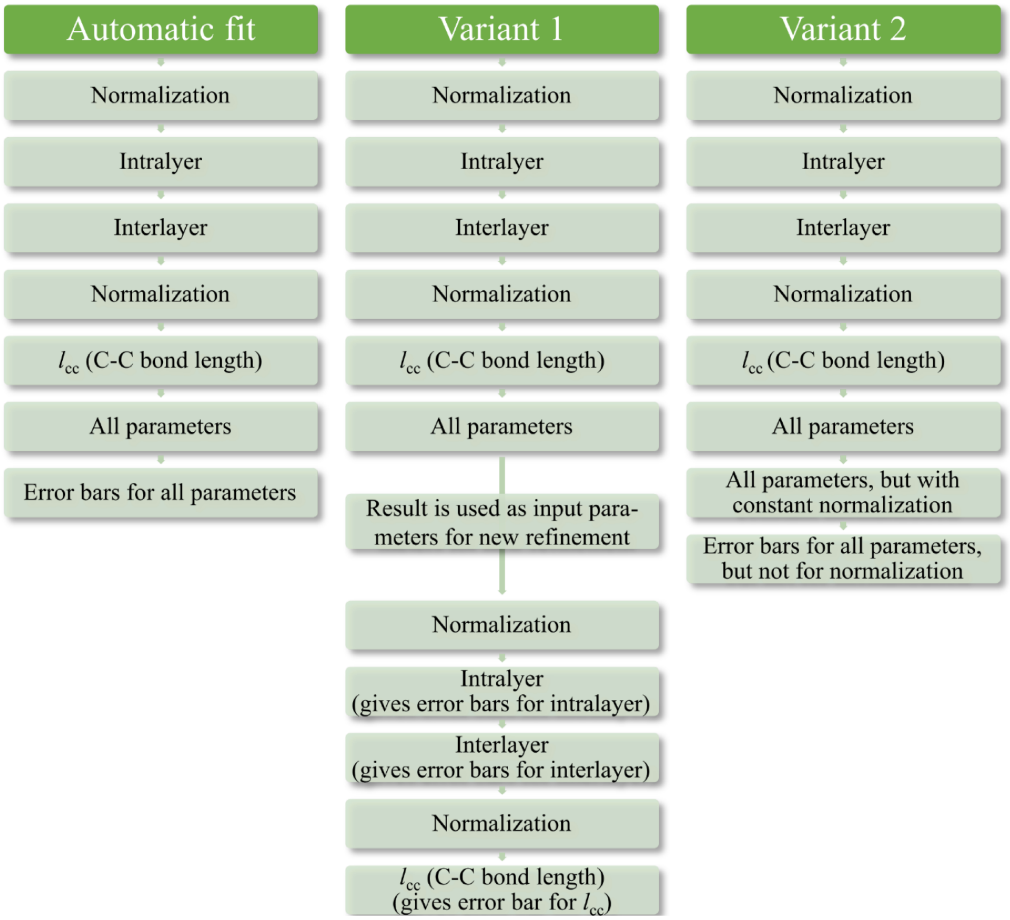

Figure S15 Schematic representation for calculating the error bars for the refined parameters. If the automatic fit cannot calculate the errors, there are basically 2 options for how to proceed: Variant 1 can be used with the existing script. The result of the fit is used there as input parameters for a new fit. In this new fit, the error from the individual steps for the intralayer and interlayer parameters can be determined individually. For mathematical reasons, the error here is generally higher than if all parameters were calculated at the same time. Variant 2 describes the procedure with a modified script. In this case, after the automatic fit, a fit of intra- and interlayer parameters is performed while the now known normalization parameters are kept constant. This allows the error bars to be calculated, but it is possible that the structure parameters will change very slightly as a result.

S13. Whole refinement script (*OctCarb*)

The final refinement scripts (*OctCarb*), which can used with *Octave* are in the SI in the directory "Example refinement". In principle, the file "WAXS Fit-Routine-IUCr.m" should be used to perform the whole refinement. In some cases, it might happen, that the errors of the refined parameters cannot be calculated (see S11). This is often caused by the refinement of the normalization parameters (which one could not be determined so far). In this case and if the error values of the refined parameters needed to be known (and only in this case), the file "WAXS Fit-Routine-IUCr with additional step all-without-normalization.m" should be used. Hence, an additional refinement step including the intralayer and interlayer but without the normalization parameters will be performed. This will reduce a bit the quality of the whole fit, but *Octave* will calculate the parameter errors correctly.

References

1. Ruland, W.; Smarsly, B.M. X-ray scattering of non-graphitic carbon: an improved method of evaluation. *J Appl Crystallogr* **2002**, *35*, 624–633, doi:10.1107/S0021889802011007.
2. Pfaff, T.; Badaczewski, F.M.; Loeh, M.O.; Franz, A.; Hoffmann, J.-U.; Reehuis, M.; Zeier, W.G.; Smarsly, B.M. Comparative Microstructural Analysis of Nongraphitic Carbons by Wide-Angle X-ray and Neutron Scattering. *J. Phys. Chem. C* **2019**, *123*, 20532–20546, doi:10.1021/acs.jpcc.9b03590.
3. Pfaff, T.; Simmermacher, M.; Smarsly, B.M. CarbX : a program for the evaluation of wide-angle X-ray scattering data of non-graphitic carbons. *J Appl Crystallogr* **2018**, *51*, 219–229, doi:10.1107/S1600576718000195.
4. Badaczewski, F.M.; Loeh, M.O.; Pfaff, T.; Dobrotka, S.; Wallacher, D.; Clemens, D.; Metz, J.; Smarsly, B.M. Peering into the structural evolution of glass-like carbons derived from phenolic resin by combining small-angle neutron scattering with an advanced evaluation method for wide-angle X-ray scattering. *Carbon* **2019**, *141*, 169–181, doi:10.1016/j.carbon.2018.09.025.
5. Faber, K.; Badaczewski, F.M.; Ruland, W.; Smarsly, B.M. Investigation of the Microstructure of Disordered, Non-graphitic Carbons by an Advanced Analysis Method for Wide-Angle X-ray Scattering. *Z. anorg. allg. Chem.* **2014**, *640*, 3107–3117, doi:10.1002/zaac.201400210.
6. Loeh, M.O.; Badaczewski, F.M.; Faber, K.; Hintner, S.; Bertino, M.F.; Mueller, P.; Metz, J.; Smarsly, B.M. Analysis of thermally induced changes in the structure of coal tar pitches by an advanced evaluation method of X-ray scattering data. *Carbon* **2016**, *109*, 823–835, doi:10.1016/j.carbon.2016.08.031.
7. Einert, M.; Wessel, C.; Badaczewski, F.; Leichtweiß, T.; Eufinger, C.; Janek, J.; Yuan, J.; Antonietti, M.; Smarsly, B.M. Nitrogen-Doped Carbon Electrodes: Influence of Microstructure and Nitrogen Configuration on the Electrical Conductivity of Carbonized Polyacrylonitrile and Poly(ionic liquid) Blends. *Macromol. Chem. Phys.* **2015**, *216*, 1930–1944, doi:10.1002/macp.201500169.
8. HKHLR - HPC Hessen. justHPC Gießen. Available online: https://www.hkhlr.de/de/cluster/justhpc-giessen (accessed on 21 July 2022).

6.4.2. Anhang Publikation 1 – Teil B [1]

Reproduziert mit Genehmigung von Oliver Osswald; veröffentlicht bei MDPI, *C*, 2022.

OctCarb – A GNU *Octave* Script for the Analysis and Evaluation of Wide-Angle Scattering Data of Non-graphitic Carbons

Supporting information part B

Correction/fine treatment of WAXS/WANS data

Mathematical background

Authors

Oliver Osswald[a]* and Bernd M. Smarsly[a]

[a]Institute of Physical Chemistry, Justus-Liebig-University Giessen, Heinrich-Buff-Ring 17, Giessen, 35392, Germany

Correspondence email: oliver.osswald@phys.chemie.uni-giessen.de

Funding information Financial support is provided by the DFG via the RTG (Research Training Group) 2204 "Substitute Materials for Sustainable Energy Technologies".

Supporting information part B – Correction/fine treatment of WAXS/WANS data and mathematical background

S14. Incoherent scattering and correction terms for WAXS

I_{incoh} is modified by different specific correlation factors for primary/secondary monochromatizating, e.g. Q_{abs} (specific absorption of Compton scattering), Q (secondary-monochromator) and the Breit-Dirac *recoil* factor. However, equation (15) is only valid for X-ray radiation and not for neutrons:

$$I_{incoh,\,c} = I_{com,\,c} \cdot recoil \cdot Q_{abs} \cdot Q \tag{15}$$

The influence of the different correction terms for incoherent x-ray scattering of NGCs is described in Figure S16. Further details about the incoherent scattering can be found in following parts. For WANS, in principle a similar equation like eq. (3) of the main article holds true, but it is not meaningful to calculate the inelastic scattering in an analytical way due to possible nuclear absorption resonance and possible similar values of the energy exchange and the incident energy. In essence, the possibly huge non-linear background of hydrogen, even present for small hydrogen contents of NGC, cannot be evaluated analytically. Hence, we treat WANS data in a different way, namely by fitting the incoherent background either by a polynomial or a Pseudo-Voigt function, depending on the amount of hydrogen in the sample as described in the works of Placzek [1] and Fischer et al. [2] as shown in S19. Thus, the pristine WANS data are corrected by subtraction of $I_{incoh,c}$ from the pristine WANS data prior to further evaluation, i.e. $I_{incoh,\,c}$ is not evaluated simultaneously together with the structural parameters, as performed for WAXS analysis.

Besides this description of the scattering of carbon, the scattering of foreign atoms (currently only H, N, O, S) can be considered if present in the sample. Since these foreign atoms cause an incoherent background, the following equations (16) and (17) are only valid for WAXS and not for WANS data. For the foreign atoms, the scattering intensity is given by (X = H, N, O, S)

$$I_{e.u.,\,X} = I_{coh,\,X} + I_{incoh,\,X} = f^2_X + I_{com,\,X} \cdot recoil \cdot Q_{abs} \tag{16}$$

In this case, the intensity $I_{e.u.,\,X}$ for every element is weighted by its concentration (c_H, c_O, c_N, c_S and $c_C = 1 - c_H - c_O - c_N - c_S$). Therefore, the overall resulting scattering of all atoms $I_{e.u.,}$ is calculated by

$$I_{e.u.} = c_C \cdot I_{e.u.,\,c} + c_H \cdot I_{e.u.,\,H} + c_N \cdot I_{e.u.,\,N} + c_O \cdot I_{e.u.,\,O} + c_S \cdot I_{e.u.,\,S} \tag{17}$$

A detailed description about the calculation of the scattering intensity of the foreign atoms as well as the calculation of the atomic form factors including fits is given in S17.

S14.1. Compton scattering

The theoretical data for the atomic form factor of carbon is given in Milberg and Brailsford [3] for $s \leq 1.4$ Å^{-1} (which is also used in Pfaff et al. [4]). A more detailed description is in Keating and Vineyard

[5]. For $s > 1.4$ Å^{-1} the data from Prince et al. [6] is used. Using a spline interpolation (5 parts, 3rd order polynomial), the intensity of Compton scattering of carbon is given by

$$I_{com,c}(s) = \begin{cases} -33.525 \cdot s^3 + 26.296 \cdot s^2 + 2.160 \cdot s - 0.025, 0 < s \leq 0.4 \\ 11.179 \cdot (s-0.4)^3 - 13.935 \cdot (s-0.4)^2 + 7.104 \cdot (s-0.4) - 2.901, 0.4 < s \leq 0.8 \\ 0.222 \cdot (s-0.4)^3 - 0.520 \cdot (s-0.4)^2 + 1.322 \cdot (s-0.4) + 4.228, 0.8 < s \leq 1.2 \\ 0.013 \cdot (s-0.4)^3 - 0.254 \cdot (s-0.4)^2 + 1.013 \cdot (s-0.4) + 4.688, 1.2 < s \leq 1.8 \\ 0.023 \cdot (s-0.4)^3 - 0.230 \cdot (s-0.4)^2 + 0.722 \cdot (s-0.4) + 5.207, 1.8 < s \leq 4 \end{cases} \quad (18)$$

S14.2. Breit-Dirac correction

The correction factor for the recoil effect as used in Ruland [7] and described in Pfaff et al. [4] is given by using the Breit-Dirac equation intensity of Compton scattering of carbon is given by

$$recoil = \left(\frac{1}{1 + 0.0485262 \cdot \lambda_A \cdot \frac{1}{4} \cdot s^2} \right)^3 \quad (19)$$

which can be reached using James [8] (20) and the Bragg's law (21) and the physical constants

$$B = 1 + \frac{2 \cdot h \cdot \lambda}{m \cdot c} \cdot \left(\frac{\sin(\theta)}{\lambda_m} \right)^2 \quad (20)$$

$$\lambda_A = 2 \cdot d \cdot \sin(\theta) \quad (21)$$

λ_m = Wavelength in m

λ_A = Wavelength in Å

B = Total scattered radiation ($recoil = B^3$)

h = Planck constant ($6.62607015 \cdot 10^{-37}$ J s) [1]

c = Speed of Light ($299792458 \cdot 10^{-37}$ m/s) [2]

m = Mass of electron ($9.1093837015(28) \cdot 10^{-31}$ kg) [3]

d = Lattice distance in Å ($d = 1/s$)

[1] https://physics.nist.gov/cgi-bin/cuu/Value?me
[2] https://physics.nist.gov/cgi-bin/cuu/Value?c
[3] https://physics.nist.gov/cgi-bin/cuu/Value?h

S14.3. Absorption correction

The absorption correction of the incoherent scattering of the sample is given in Ruland [7] as

$$Q_{\mathrm{abs}} = 1 + \frac{3 \cdot h}{m \cdot c \cdot \lambda_{\mathrm{m}}} \cdot (\sin(\theta))^2 \tag{22}$$

and can be transformed into [4]

$$Q_{\mathrm{abs}} = \frac{1}{1 + 0.0485262 \cdot \lambda_{\mathrm{A}} \cdot \frac{3}{8} \cdot s^2} \tag{23}$$

S14.3.1. Secondary monochromator correction

While the recoil and absorption correction must be considered for each measurement, a secondary monochromator and the corresponding correction is optional. It is given by Ruland [9] as

$$Q = \frac{1}{\left(1 + \frac{\Delta\lambda}{b}\right) \cdot \left(1 + \frac{\pi^2}{(\Delta\lambda + b)^2} \Delta\lambda_{\mathrm{C}}^2\right)} \tag{24}$$

(b = pass-band). For carbon $\Delta\lambda$ and $\Delta\lambda_{\mathrm{C}}$ can be calculated using the following expressions

$$\Delta\lambda = \frac{\lambda_{\mathrm{A}}^2}{c} \cdot s \cdot \Delta q(s) \tag{25}$$

$$\Delta q(s) = \Delta q_{\max} \frac{s^2}{a^2 + s^2} \tag{26}$$

For graphite: $\Delta q_{\max} = 3.05$, a = 0.53

$$\Delta\lambda_{\mathrm{C}} = \frac{2 \cdot h}{m \cdot c} \cdot (\sin(\theta))^2 - D \cdot \lambda_{\mathrm{A}}^2 \tag{27}$$

In this case, c is the velocity of light given in astronomical unit (c = 137) and $D = 1.5 \cdot 10^{-3}$ for carbon. Since this equation is only valid for high Compton energies, it must be corrected for low energies, especially for copper radiation, where the $\Delta\lambda_{\mathrm{c}}$ would be negative for $\theta < 23$ °. It can be assumed, that D correlates with $\Delta q(s)$ for low energies. In this way, an additional term like equation (26) can be used to consider this effect. Finally, the correction term for the secondary monochromator is [4]:

$$Q = \frac{1}{\left(1 + \frac{\frac{\lambda_A^2 \cdot s}{137} \cdot \left(\frac{3.05 \cdot s^2}{0.53^2 + s^2}\right)}{b}\right) \cdot \left(1 + \frac{\pi^2 \cdot \left(\frac{0.0485262}{4} \cdot s^2 \cdot \lambda_A^2 - \frac{1.5 \cdot 10^{-3} \cdot \lambda^2 \cdot s^4}{(0.53^2 + s^2)^2}\right)^2}{\left(\frac{{\lambda_A}^2 \cdot s}{137} \cdot \left(\frac{3.05 \cdot s^2}{0.53^2 + s^2}\right) + b\right)^2}\right)} \quad (28)$$

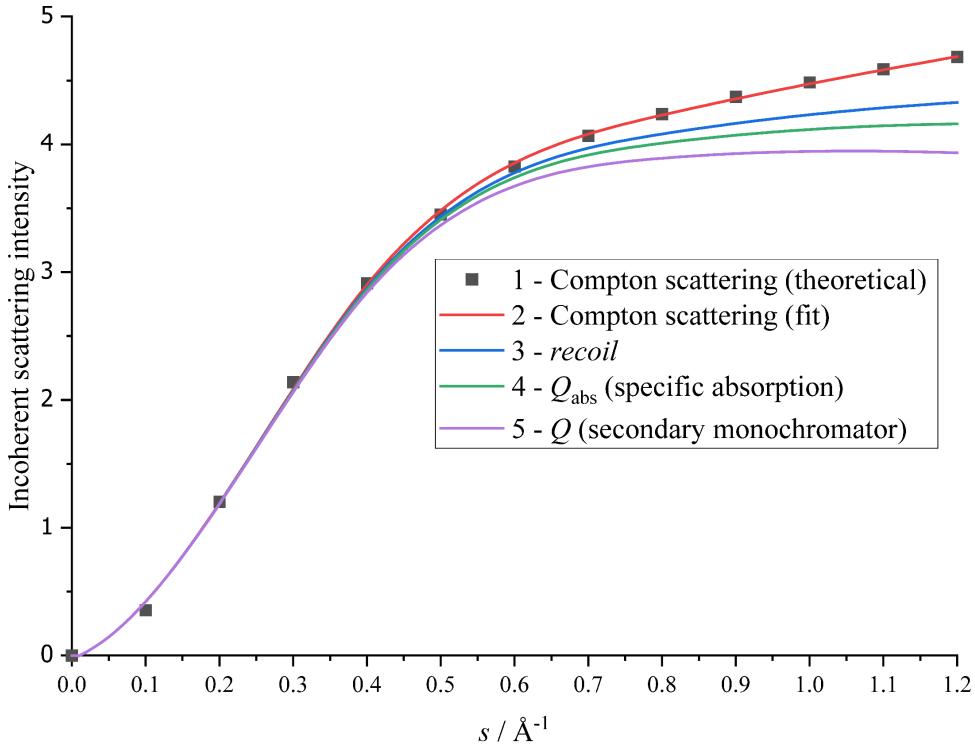

Figure S17 Theoretical (1) intensity and spline interpolation (2) of the Compton scattering of carbon. This scattering must be corrected with the Breit-Dirac recoil factor (*recoil*) and the specific absorption (Q_{abs}). In addition, the absorption of a possible secondary monochromator can also be considered (Q).

S15. Implementation of *v*

The last difference in the code used in this study compared to Pfaff et al. [4] is the implementation of v, which together with α serves for modelling the intralayer scattering I_{intra}. Since this is a very special feature, it is not handled in the main text, but in the SI in part … v is used to calculate a polydispersity parameter for the chord-length distribution of the graphene layers (κ_a).

In Ruland and Smarsly's model [10], the correlation function $P_L(r)$ of the intralayer scattering is calculated as a gamma function Γ with the parameters v and α:

$$P_L(r) = \frac{1}{\Gamma(v+1)}[\Gamma(v+1, \alpha r) - \alpha r\Gamma(v, \alpha r)] \tag{29}$$

$\Gamma(x)$ is the complete, and $\Gamma(a, x)$ the incomplete gamma function. v and α are related to the layer size (L_a) and its polydispersity (κ_a) as follows:

$$L_a = (v+1)/\alpha \tag{30}$$

$$\kappa_a = 1/v \tag{31}$$

Thus, both parameters v and α are needed to calculate the resulting intralayer parameters by this approach. Equation (32) is used to calculate the shape profile of the intralayer reflections (J_{hk}):

$$J_{hk}(s) = \frac{1}{s}\mathrm{Im}\left[\int_0^\infty P_L(r) J_0(2\pi r s_{hk}) \exp(2\pi i r s)\, dr\right] \tag{32}$$

It should be noted that equation (32) does NOT include the disorder of the layers. s_{hk} is the position of the hk reflection, which should be calculated and J_0 the Bessel function of the first kind of order zero. We found that a numerical calculation of J_{hk} by eq. (32) takes inacceptable time. Since equation (32) cannot be solved analytically for real values of v, but for whole numbers, v is set to a fixed whole number for one particular fit in our approach.

Since v generally has also only a very small influence on the resulting WAXS pattern for the same layer sizes (Figure S17), it is not meaningful to refine this parameter. Note that we had already proposed in a previous study (Faber et al. [11]) that the value of κ_a (v) cannot be reliably determined. We found the average layer extension (L_a) is predominantly determined by α, and the disorder of the layers (σ_1) has a much higher influence on the profile shape than v. Hence, setting *v constant* does not compromise the accuracy of the refinement and the physical assumptions in the model at the same time.

The parameter is now rather used as empirical limit for the number of (hk) reflections to be calculated and based on eq. (32) indirectly specify an upper limit for the polydispersity:

$$k \leq h \leq v \text{ and } h^2 + h \cdot k + k^2 < (v+1)^2 \tag{33}$$

$$\kappa_a \leq 1/v \tag{34}$$

This implementation and the relationships (33) and (34) have no direct physical basis, rather it is a practical implementation for a better software-handling based on empirical knowledge. Yet, this procedure is also justified with respect to the NGC structure, as a high amount of observable (*hk*) reflections means a small layer disorder (κ_a) and therefore a high value of *v*. More details about the implementation and calculation times for different values of *v* can be found in the SI file under S2.

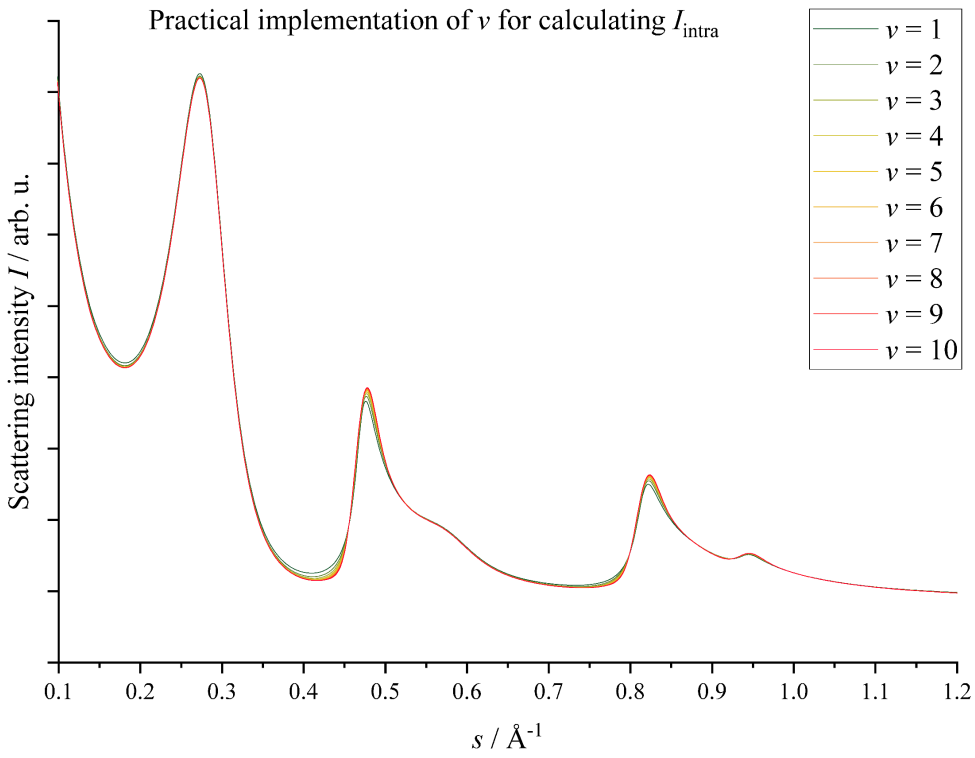

Figure S18 Influence of *v* on a typical WAXS scattering pattern. *v* is one of the two parameters used for defined a chord-length distribution of the graphene layers, according to [10]. Since this parameter influences only the intralayer scattering, the (002) and (004) reflections are not affected. The calculations are done for a constant L_a = 30 Å. Hence, it is seen that *v* only minor affects the shape of "classic" scattering patterns of NGCs. It is thus sufficient to use a fixed value of *v* in the fitting routine.

S16. General intensity correction terms

S16.1. General remarks

The following correction terms are dependent on the sample and the measurement geometry. There is no generally applicable guideline which corrections must be used and which not. All correction terms except the experimental broadening widening are implemented in *OctCarb* and can be optionally used. Overall, the correction for the fixed irradiated length (if used), the polarization and the Polarization correction must be used for every measurement, but note that these corrections might already be performed by the measurement software of the device. *gFact* is a general scaling correction term and is not directly related to a physical phenomenon, so it should be used in the refinement only, if refining the structural parameters does not result in a reasonable fitting. The absorption correction can be used, but in many of the cases studied, the correction is comparably small in its effect on the refinement. Only for very thin samples in reflection geometry using X-ray radiation, e.g. for thin film measurement, the absorption correction has a significant to the measured intensity.

S16.2. Experimental device broadening

For the instrumental broadening, no generally applicable procedure can be given. The best way is to measure the instrumental broadening using a reference sample and then to correct the measured data before refining it. However, there are some approaches for such data correction, which are explained in the SI file of Pfaff et al. [4]. However, the influence of the device broadening is only very small for materials with broad reflections, i.e. for quite disordered carbons (see Figure S18). The black dots are a typical (002) reflection profile, which can be roughly fitted through a Gaussian profile (red, standard deviation is 0.01 $Å^{-1}$). For a XRD instrument with a medium resolution of ca. 100 nm (domain size), which means a standard deviation of 0.0007413 $Å^{-1}$ for an integral width of 0.001 $Å^{-1}$, the resulting reflection broadening is shown in the blue line. The resulting corrected gauss profile of the (002) reflection is included as green line. The difference is evidently small and therefore, the device broadening can be ignored for most of the cases.

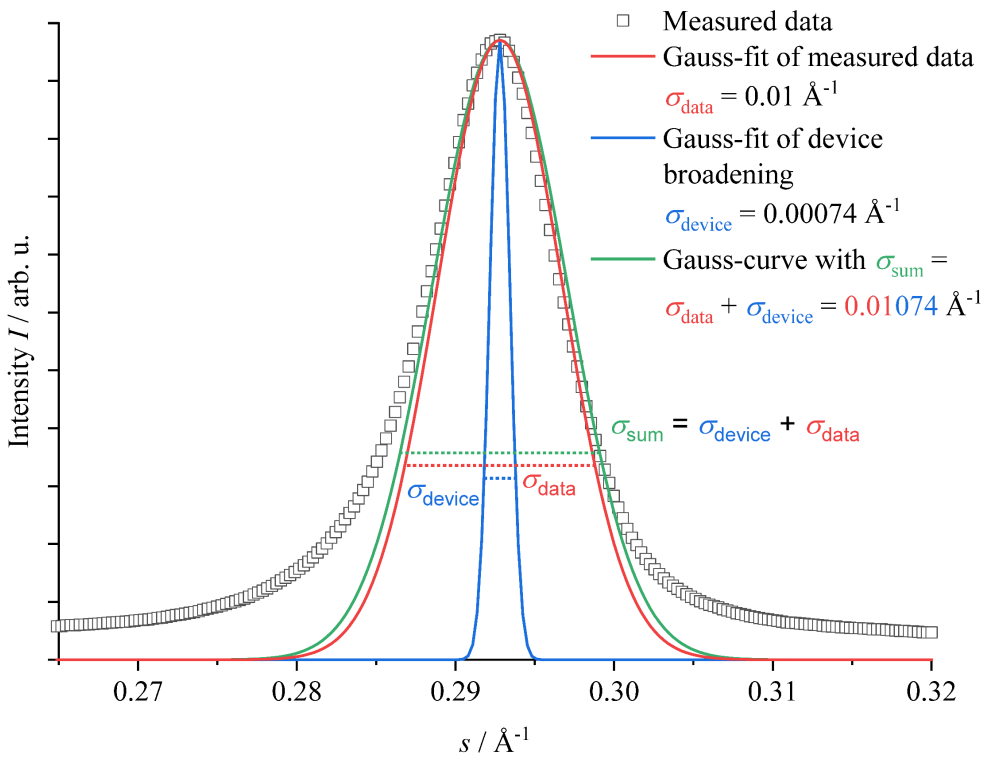

Figure S19 Overview of the influence of the device broadening effect. The (002) reflection is so wide that the device broadening does not have to be considered.

S16.3. AutoColl

The correction term *AutoColl* can convert scattering data from Bragg-Brentano geometry at the scattering angle θ using a fixed irradiated length to a fixed slit geometry with the divergence angle δ. The goniometer radius r and the irradiated length l must have the same dimension [4].

$$AutoColl = \frac{r \cdot \sin(\theta) \cdot \sin^2(\delta)}{l \cdot \left(\sin^2(\theta) - \sin^2\left(\frac{\delta}{2}\right)\right)} \tag{35}$$

S16.4. gFact

gFact can be used to perform an exponential damping or increasing of the overall scattering curve due to scattering effects which we have not considered so far, e.g. for a possible influence of a small-angle X-ray/neutron (SAXS/WANS) intensity contribution at low s values choosing a meaningful parameter g [4]. Since it does not have any physical meaning, the factor should only be used for special reasons and not by default.

$$gFact = \exp(g \cdot s) \tag{36}$$

S16.5. Lorentz-factor

The Lorentz factor as described in [12,13] is considered in the model of Ruland and Smarsly [10] and therefore, there is no need to consider a further Lorentz factor as an additional correction term.

S16.6. Polarization

In general, the polarization correction can only be used for X-rays, but not for neutron radiation due to the different orientated electron orbitals. For a polarized radiation source with the polarization direction Φ, the following equation can be used [14]:

$$P(\theta, \Phi) = 1 - \sin^2(2\theta)\cos^2(\Phi) \tag{37}$$

For a non-polarized radiation, the polarization factor can be calculated using the average of Φ from 0 to 2π [4,14]:

$$P(\theta) = \frac{1}{2\pi}\int_0^{2\pi} P(\theta, \Phi)\, d\Phi = \frac{1}{2}(1+\cos^2(2\theta)) \tag{38}$$

S16.7. Absorption

For the absorption correction, both, the measurement geometry as well as the type of radiation (X-ray or neutrons) must be considered. The most common cases for wide-angle powder scattering are the reflection geometry for X-rays and transmission geometry for neutrons and therefore, this will be discussed here. The discussion and formulars are based on scripts from W. Ruland (1995) and the work of Sivia [14].

S16.7.1. Absorption coefficients

For X-ray radiation, μ_{ab} is the mass attenuation coefficient, which can be fitted using the data from [15]:

$$\mu_{ab} = \lambda^{-3.089} \cdot 10^{1.081} \cdot \rho \tag{39}$$

ρ is the density of the sample in g/cm^3. For neutron radiation, the absorption coefficient is given by

$$\mu_{ab} = n \cdot \sigma_{abs} \tag{40}$$

n is the number of atoms per unit cell:

$$n = \rho \cdot N_A/m = \rho \cdot 6.02214076 \cdot 10^{23}/12.011 \text{ cm}^3/\text{g} \tag{41}$$

σ_{abs} can be calculated using the wave vector ω (in Å^{-1}) and the incoherent neutron cross section σ_{inc}:

$$\sigma_{abs} = 4\pi/\omega \cdot \sigma_{inc} \tag{42}$$

$$\omega = 2\pi/\lambda \tag{43}$$

For carbon, $\sigma_{inc} = 0.001 \cdot 10^{-24}$ cm^2 [16]. Per definition, σ_{abs} is measured and tabulated for neutrons with a velocity of $v = 2200$ m/s, i.e. a wavelength of $\lambda = 1.8$ Å, but in most of the cases, σ_{abs} must be calculated for the used wavelength.

S16.7.2. Reflection geometry

For reflection geometry, i.e. Bragg-Brentano geometry, the case of an infinitely thick sample with a thickness smaller than the maximum depth of penetration of X-ray radiation in a carbon sample can be used. The covered track of the X-ray radiation in the sample with a thickness d in cm is not constant. Therefore, also the absorption correction is not constant:

$$I(\theta, \mu_{ab}, d) = I_0(\theta) \cdot \frac{1}{2 \cdot \mu_{ab}} \cdot \left(1 - \exp\left(\frac{-2 \cdot d \cdot \mu_{ab}}{\sin(\theta)}\right)\right) \tag{44}$$

S16.7.3. Transmission geometry

The average way of a neutron through a cylindric sample is not the diameter but smaller, so it must be calculated. For a beam bigger than the sample diameter, die average length is

$$l = \frac{\int_0^d \sqrt{d^2 - 4x^2}\,\mathrm{d}x}{d} = \frac{\pi}{4} d \tag{45}$$

where $\sqrt{d^2 - 4x^2}$ is the chord length of a circle with the diameter d with a distance x to the center. For a beam smaller than the diameter of the cylindric sample ($a < d$), the average length is

$$l = \frac{\int_0^{\frac{a}{2}} \sqrt{d^2 - 4x^2}\,\mathrm{d}x}{\frac{a}{2}} = \frac{a\sqrt{-a^2 + d^2} + d^2 \mathrm{ArcTan}\left[\frac{a}{\sqrt{-a^2 + d^2}}\right]}{2a} \tag{46}$$

In *Octave*, only the mainly used first case is considered, so if you want to use an endless beam width smaller than the diameter, you have to calculate the resulting irradiated length by your own using

$$d = \frac{4}{\pi} l \tag{47}$$

The resulting absorption can be calculated by

$$I(\theta, \mu_{ab}, l) = I_0(\theta) \cdot \frac{l}{\cos(\theta)} \cdot \exp\left(\frac{-l \cdot \mu_{ab}}{\cos(\theta)}\right) \tag{48}$$

S17. Atomic form factors

In general, the atomic form factor can be calculated solving the Schrödinger equation or relativistic wavefunction for heavier atoms than hydrogen. As this is procedure very complex and time-consuming to calculate, these values have already been calculated and tabulated [6]. In addition, the atomic form factors can be fitted using

$$f(s) = \sum_{i=1}^{4} a_i \cdot \exp\left(-b_i \cdot s^2\right) + c \tag{49}$$

s = modules of the scattering vector (in Å)

Since this equation diverges to *c* instead to 0, Fox et al. [17] proofed the following formular as more accurate for higher values of *s*, which correspondences to relativistic Hartree-Fock wavefunctions:

$$f(s) = \exp\left(\sum_{i=0}^{3} a_i \cdot \left(\frac{s}{2}\right)^i\right) \tag{50}$$

S17.1. Atomic form factor of carbon

Regarding equation (49) and (50) and Prince et al. [6], the atomic form factor of carbon is given by

$$f_{\mathrm{c,perp}}(s) = \begin{cases} 2.31 \cdot \exp(-20.84339 \cdot s^2) + 1.02 \cdot \exp(-10.2075 \cdot s^2) \\ +1.5886 \cdot \exp(0.5687 \cdot s^2) + 0.865 \cdot \exp(-51.6512 \cdot s^2) + 0.2156, s < 3.74 \\ \exp\left(1.7056 - 1.5676 \cdot \frac{s}{2} + \frac{1.1893}{10}\left(\frac{s}{2}\right)^2 - \frac{0.42715}{100}\left(\frac{s}{2}\right)^3\right), \text{else} \end{cases} \tag{51}$$

This equation is a little bit different to Pfaff et al. [4] because of the introduction of the 4th exponential term and the correction for high *s*-values, which make the fit a little bit more accurate

S17.1.1. Anisotropy

For the anisotropy of the atomic form factor, i.e. the anisotropy in the interlayer scattering caused of the parallel stacking of the graphene layers, the parameter Δ_{an} is used. While the parameter itself is physically meaningful, the implementation is done only in an empirical mathematical way. Therefore and because of the generally small influence, it is recommended to fix this parameter to 0. However, the resulting atomic form factor for the parallel graphene sheets can be calculated through:

$$f_{c,para}(s) = \begin{cases} 2.31 \cdot \exp(-(20.84339 + \Delta_{an}) \cdot s^2) + 1.02 \cdot \exp(-10.2075 \cdot s^2) \\ +1.5886 \cdot \exp(0.5687 \cdot s^2) + 0.865 \cdot \exp(-51.6512 \cdot s^2) + 0.2156, s < 3.74 \\ \exp\left(1.7056 - 1.5676 \cdot \frac{s}{2} + \frac{1.1893}{10}\left(\frac{s}{2}\right)^2 - \frac{0.42715}{100}\left(\frac{s}{2}\right)^3\right), \text{else} \end{cases} \quad (52)$$

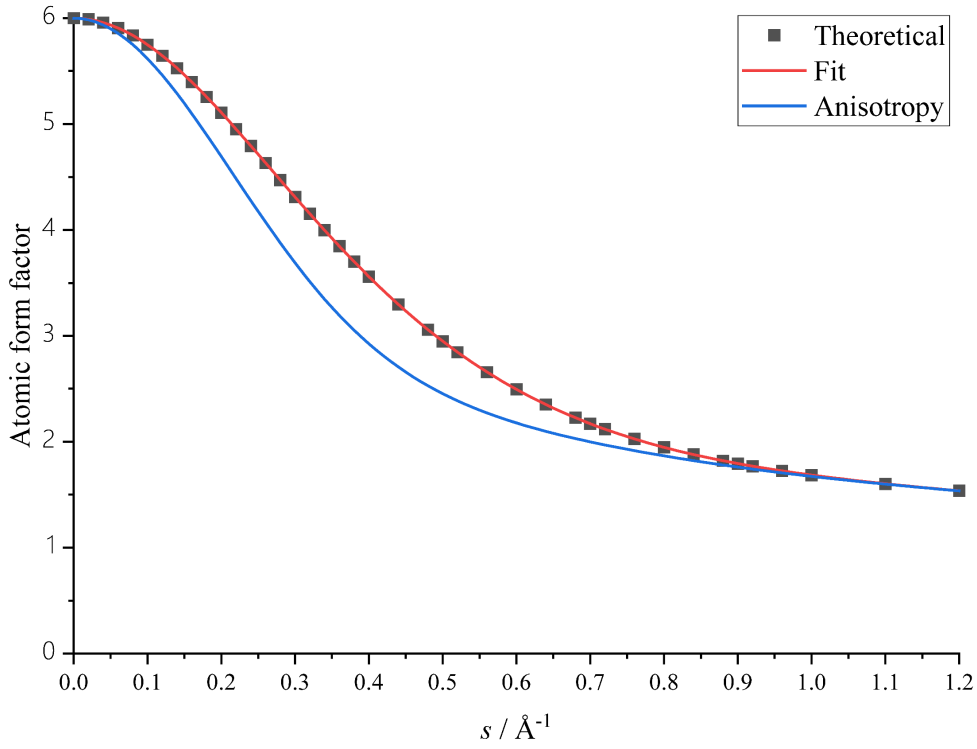

Figure S20 Theoretical and fitted atomic form factor and the influence of the anisotropy (Δ_{an} = 25).

S17.2. Atomic form factor of foreign atoms (H, N, O, S)

The atomic form factor of hydrogen, nitrogen, oxygen and sulfur can be calculated like the atomic form factor of carbon. All data is taken from Prince et al. [6].

S17.2.1. Hydrogen

$$f_{\mathrm{c,perp}}(s) = \begin{cases} 0.493002 \cdot \exp(-10.5109 \cdot s^2) + 0.322912 \cdot \exp(-26.1257 \cdot s^2) \\ +0.140191 \cdot \exp(3.14236 \cdot s^2) + 0.04081 \cdot \exp(-57.7997 \cdot s^2) + 0.003038, s < 3.81 \\ 0, \text{else} \end{cases} \quad (53)$$

S17.2.2. Nitrogen

$$f_{\mathrm{c,perp}}(s) = \begin{cases} 12.2126 \cdot \exp(-0.0057 \cdot s^2) + 3.1322 \cdot \exp(-9.8933 \cdot s^2) \\ +2.0125 \cdot \exp(28.9975 \cdot s^2) + 1.1663 \cdot \exp(-0.5826 \cdot s^2) - 11.529, s < 3.88 \\ \exp\left(1.5494 - 1.2019 \cdot \frac{s}{2} + \frac{0.51064}{10}\left(\frac{s}{2}\right)^2 + \frac{0.2472}{100}\left(\frac{s}{2}\right)^3\right), \text{else} \end{cases} \quad (54)$$

S17.2.3. Oxygen

$$f_{\mathrm{c,perp}}(s) = \begin{cases} 3.0485 \cdot \exp(-13.2771 \cdot s^2) + 2.2868 \cdot \exp(-5.7011 \cdot s^2) \\ +1.5463 \cdot \exp(0.3239 \cdot s^2) + 0.867 \cdot \exp(-32.9089 \cdot s^2) + 0.2508, s < 3.79 \\ \exp\left(1.3053 - 0.83742 \cdot \frac{s}{2} + \frac{-0.16738}{10}\left(\frac{s}{2}\right)^2 + \frac{0.475}{100}\left(\frac{s}{2}\right)^3\right), \text{else} \end{cases} \quad (55)$$

S17.2.4. Sulfur

$$f_{\mathrm{c,perp}}(s) = \begin{cases} 6.9053 \cdot \exp(-1.4679 \cdot s^2) + 5.2034 \cdot \exp(-22.2151 \cdot s^2) \\ +1.4379 \cdot \exp(0.2536 \cdot s^2) + 1.5863 \cdot \exp(-56.172 \cdot s^2) + 0.2156, s < 5.86 \\ \exp\left(1.104 - 0.40325 \cdot \frac{s}{2} + \frac{0.20094}{10}\left(\frac{s}{2}\right)^2 + \frac{-0.26058}{100}\left(\frac{s}{2}\right)^3\right), \text{else} \end{cases} \quad (56)$$

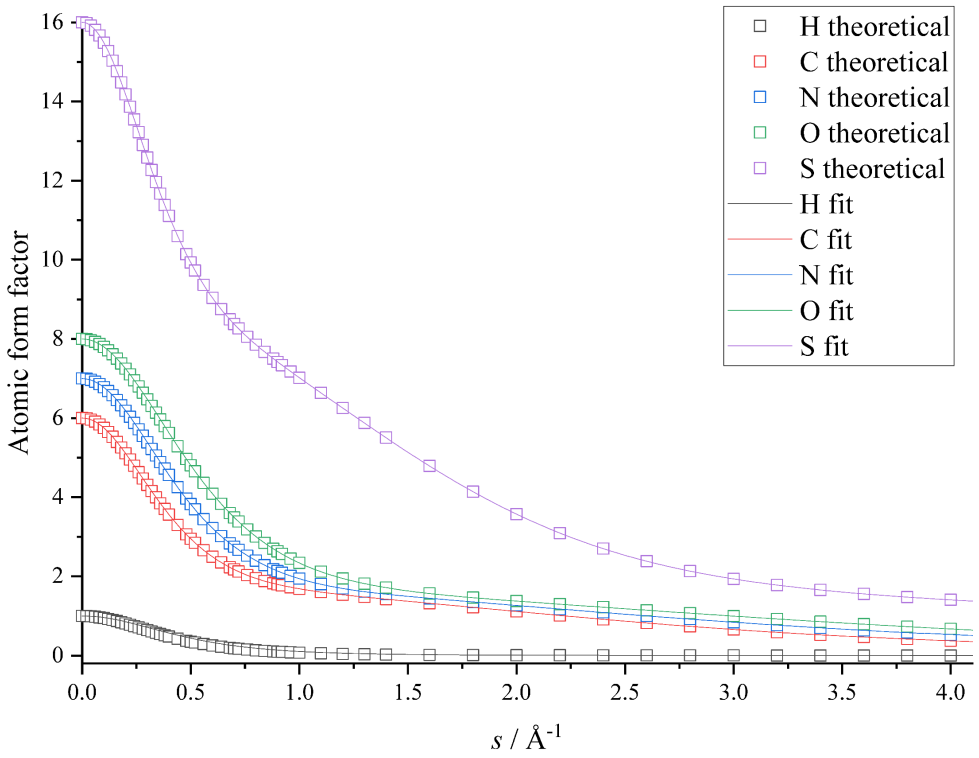

Figure S21 Theoretical and fitted atomic form factors of carbon and the most common (hydrogen, nitrogen, oxygen, sulfur).

S17.3. Atomic form factor for neutron scattering

For wide-angle neutron scattering (WANS), the atomic form factor is directly related to the coherent nuclear scattering length b_{coh} [14]:

$$f(\lambda, \theta) = - b_{coh} \tag{57}$$

For b_{coh}, the values are tabulated in Table S7 [18] and online available under [16]. The scattering length densities required for the purpose here are taken from the NIST center.

Table S7 Coherent nuclear scattering lengths for C, H, N, O, S. The values are mean values from the natural isotopes.

Atom	Coherent scattering length / fm
C	6.6460
H	-3.7390
N	9.36
O	5.803
S	2.847

S18. Incoherent scattering – theoretical and calculated data

Analogous to S14, the Compton scattering for carbon and the foreign atoms (hydrogen, nitrogen, oxygen, sulfur) can be fitted through spline interpolation. Since the commonly lowest used wavelength is $\lambda = 0.72$ Å (Mo K-α) and therefore, the maximum scattering vector is about $s = 2.75$ Å^{-1}, the tabulated theoretical values for the Compton scattering up to $s = 4$ Å^{-1} are more than sufficient [6] for atoms with only a few amount of electrons (C, H, N, O). For sulfur, the data from Cromer [19] up to $s = 16$ Å^{-1} were used to get more accurate data for possible synchrotron measurements.

S18.1. Carbon

$$I_{com,c}(s) = \begin{cases} -33.525 \cdot s^3 + 26.296 \cdot s^2 + 2.160 \cdot s - 0.025, 0 < s \leq 0.4 \\ 11.179 \cdot (s-0.4)^3 - 13.935 \cdot (s-0.4)^2 + 7.104 \cdot (s-0.4) - 2.901, 0.4 < s \leq 0.8 \\ 0.222 \cdot (s-0.8)^3 - 0.520 \cdot (s-0.8)^2 + 1.322 \cdot (s-0.8) + 4.228, 0.8 < s \leq 1.2 \\ 0.013 \cdot (s-1.2)^3 - 0.254 \cdot (s-1.2)^2 + 1.013 \cdot (s-1.2) + 4.688, 1.2 < s \leq 1.8 \\ 0.023 \cdot (s-1.8)^3 - 0.230 \cdot (s-1.8)^2 + 0.722 \cdot (s-1.8) + 5.207, 1.8 < s \leq 5 \\ 6, 5 < s \end{cases} \quad (58)$$

S18.2. Hydrogen

$$I_{com,H}(s) = \begin{cases} -8.009 \cdot s^3 + 5.645 \cdot s^2 + 0.925 \cdot s, 0 < s \leq 0.4 \\ 3.378 \cdot (s-0.4)^3 - 3.966 \cdot (s-0.4)^2 + 1.596 \cdot (s-0.4) + 0.760, 0.4 < s \leq 0.8 \\ -0.202 \cdot (s-0.8)^3 + 0.088 \cdot (s-0.8)^2 + 0.045 \cdot (s-0.8) + 0.980, 0.8 < s \leq 1.2 \\ 0.217 \cdot (s-1.2)^3 - 0.155 \cdot (s-1.2)^2 + 0.018 \cdot (s-1.2) + 0.999, 1.2 < s \leq 1.8 \\ 1, 1.8 < s \end{cases} \quad (59)$$

S18.3. Nitrogen

$$I_{com,N}(s) = \begin{cases} -31.81 \cdot s^3 + 764.875 \cdot s^2 + 1.124 \cdot s, 0 < s \leq 0.4 \\ 5.846 \cdot (s-0.4)^3 - 10.409 \cdot (s-0.4)^2 + 8.066 \cdot (s-0.4) + 2.856, 0.4 < s \leq 0.8 \\ 2.573 \cdot (s-0.8)^3 - 3.393 \cdot (s-0.8)^2 + 2.545 \cdot (s-0.8) + 4.791, 0.8 < s \leq 1.2 \\ 0.055 \cdot (s-1.2)^3 - 0.305 \cdot (s-1.2)^2 + 1.066 \cdot (s-1.2) + 5.431, 1.2 < s \leq 1.8 \\ 0.020 \cdot (s-1.8)^3 - 0.206 \cdot (s-1.8)^2 + 0.759 \cdot (s-1.8) + 5.972, 1.8 < s \leq 5.5 \\ 7, 5.5 < s \end{cases} \quad (60)$$

S18.4. Oxygen

$$I_{com,O}(s) = \begin{cases} -30.697 \cdot s^3 + 29.263 \cdot s^2 + 0.183 \cdot s - 0.002, 0 < s \leq 0.4 \\ 2.011 \cdot (s-0.4)^3 - 7.570 \cdot (s-0.4)^2 + 8.860 \cdot (s-0.4) + 2.789, 0.4 < s \leq 0.8 \\ 3.591 \cdot (s-0.8)^3 - 5.157 \cdot (s-0.8)^2 + 3.769 \cdot (s-0.8) + 5.251, 0.8 < s \leq 1.2 \\ 0.379 \cdot (s-1.2)^3 - 0.849 \cdot (s-1.2)^2 + 1.367 \cdot (s-1.2) + 6.163, 1.2 < s \leq 1.8 \\ 0.013 \cdot (s-1.8)^3 - 0.166 \cdot (s-1.8)^2 + 0.759 \cdot (s-1.8) + 6.960, 1.8 < s \leq 6 \\ 8, 6 < s \end{cases} \quad (61)$$

S18.5. Sulfur

$$I_{com,S}(s) = \begin{cases} -47.563 \cdot s^3 + 37.813 \cdot s^2 + 5.116 \cdot s - 0.058, 0 < s \leq 0.4 \\ 16.192 \cdot (s-0.4)^3 - 19.262 \cdot (s-0.4)^2 + 12.536 \cdot (s-0.4) + 4.963, 0.4 < s \leq 0.8 \\ -1.502 \cdot (s-0.8)^3 + 0.168 \cdot (s-0.8)^2 + 4.898 \cdot (s-0.8) + 7.989, 0.8 < s \leq 1.2 \\ 0.355 \cdot (s-1.2)^3 - 0.168 \cdot (s-1.2)^2 + 4.311 \cdot (s-1.2) + 9.853, 1.2 < s \leq 1.8 \\ 0.143 \cdot (s-1.8)^3 - 0.996 \cdot (s-1.8)^2 + 2.733 \cdot (s-1.8) + 11.928, 1.8 < s \leq 4 \\ 0.00186 \cdot (s-4)^3 - 0.04921 \cdot (s-4)^2 + 43412 \cdot (s-4) + 14.64861, 4 < s \leq 16 \\ 16, 16 < s \end{cases} \quad (62)$$

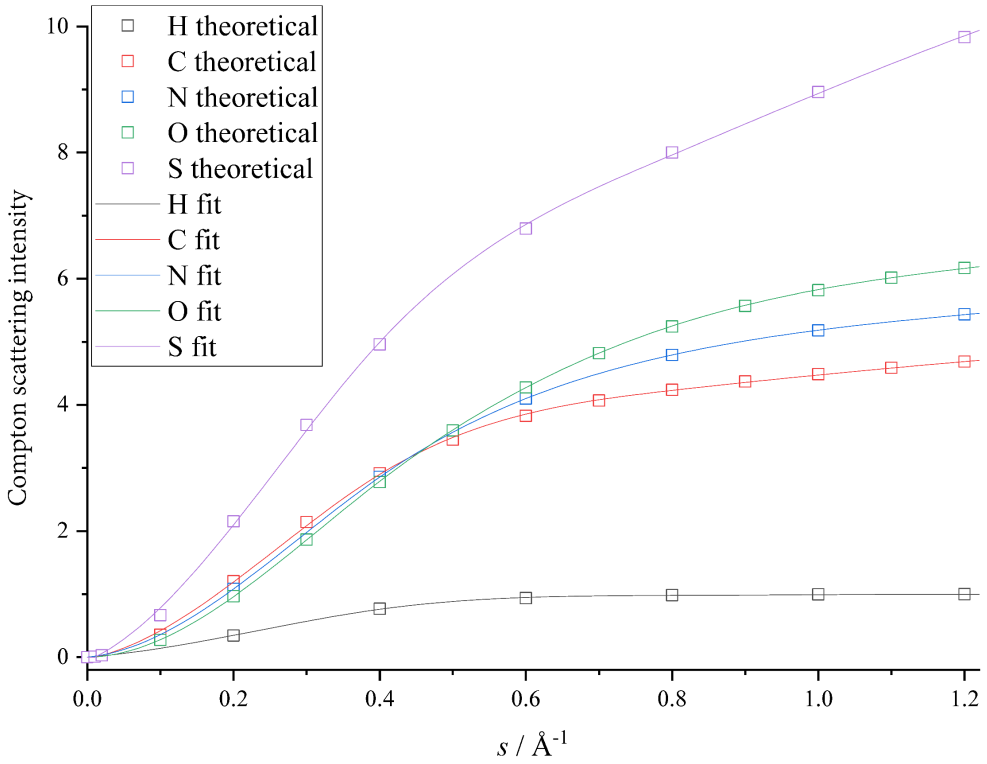

Figure S22 Theoretical and fitted Compton scattering intensity of carbon and the most common foreign atoms (hydrogen, nitrogen, oxygen, sulfur).

S18.6. Incoherent neutron scattering

For the incoherent, i.e. the inelastic scattering, of neutrons with the nucleus, is related to the spin of the nucleus [14]. For ^{1}H (i.e. a proton), the scattering lengths for the triplet and singlet states are $b^+ = 10.85$ fm and $b^- = -4.750$ fm, respectively. Therefore, a hydrogen nucleus has an average scattering length of

$$\langle b \rangle = \frac{3}{4} b^+ + \frac{1}{4} b^- = -3.738 \text{ fm} \tag{63}$$

The standard, i.e. the root mean square, deviation Δb of it is the so-called incoherent scattering length:

$$b_{inc} = \Delta b = \sqrt{\langle b^2 \rangle - \langle b \rangle^2} = 25.266 \text{ fm} \tag{64}$$

using

$$\langle b^2 \rangle = \frac{3}{4}(b^+)^2 + \frac{1}{4}(b^-)^2 = 652.354 \text{ fm} \quad (65)$$

The value measured in [18] are close similar to the value calculated above and therefore, they can be used for the present calculations. The data in Table S9 is also available in [16].

Table S8 Incoherent nuclear scattering lengths for C, H, N, O, S. The values are mean values from the natural isotopes.

Atom	Incoherent scattering length / fm
C	-0.00572
H	25.271
N	1.99
O	0.000068
S	0.011

For the calculation of the incoherent scattering, a superposition of the coherent and incoherent scattering lengths is assumed:

$$I_{\text{incoh, x}} = c_X \cdot (b_{\text{coh}} + b_{\text{inc}})^2 \quad (66)$$

for X = C, H, N, O, S

However, since these values are constants, it is not necessary to use exact values of the concentrations or the scattering lengths. Furthermore, it is possible to set I_{incoh} to 0 since a constant offset is applied and refined using the normalization constants in equation (6). Nevertheless, this approach of a constant background is only applicable for an energy exchange, $\hbar\omega$, is NOT comparable to the incidence E_0, otherwise, the self-scattering will "fall off" with an increasing value of s and a non-constant correction is necessary. Additionally, neutron absorption resonances can lead to a non-constant background [2]. For these reasons, there are different models for taking these into account [1,20]. The finally used corrections are described in the following chapter.

S19. Background correction for wide-angle neutron scattering

As described in the chapter before, the case of constant inelastic scattering is only applicable, there as the $\hbar\omega$, is comparable to the incidence E_0. Especially for hydrogen (^{1}H, i.e. a proton), the a huge damping of the incoherent scattering is measured, whereas for ^{113}Cd there are strong neutron absorption resonance effects in the commonly used wavelength, range around 0.5 to 1 Å [2].

Overall, the measured data is "fitted" over the whole q range (NOT θ) using two different equations. The resulting data oscillates around 1 for high values of q, so in principle $S(q)$ data, which can also be used for a pair-distribution-function calculation, is generated (without a correct normalization) [21,22].

For samples containing significant amounts of hydrogen (^{1}H), either deuterium (^{2}H) must be used or a pseudo-Voigt function, i.e. a linear combination of a Gaussian and a Lorentzian function with equal full-with at half-maximum (FWHM) values, must be applied (equation (67)). For all other cases, a correction using the method of the Placzek falloff, i.e. a quadratic equation with only even powers is sufficient [1,2] (equation (68)).

$$S(q) = I_{obs}(q) - k \cdot (\eta \cdot L(q, \omega) + (1 - \eta) \cdot G(q, \omega)) + 1 \tag{67}$$

$$S(q) = I_{obs}(q) - (a \cdot q^2 + b) + 1 \tag{68}$$

$$L(q, \omega) = \frac{1}{1 + \left(\frac{q}{\omega}\right)^2} \tag{69}$$

$$G(q, \omega) = \exp^{-\ln(2) \cdot \left(\frac{q}{\omega}\right)^2} = 2^{-\left(\frac{q}{\omega}\right)^2} \tag{70}$$

I_{obs} = observed (measured) intensity

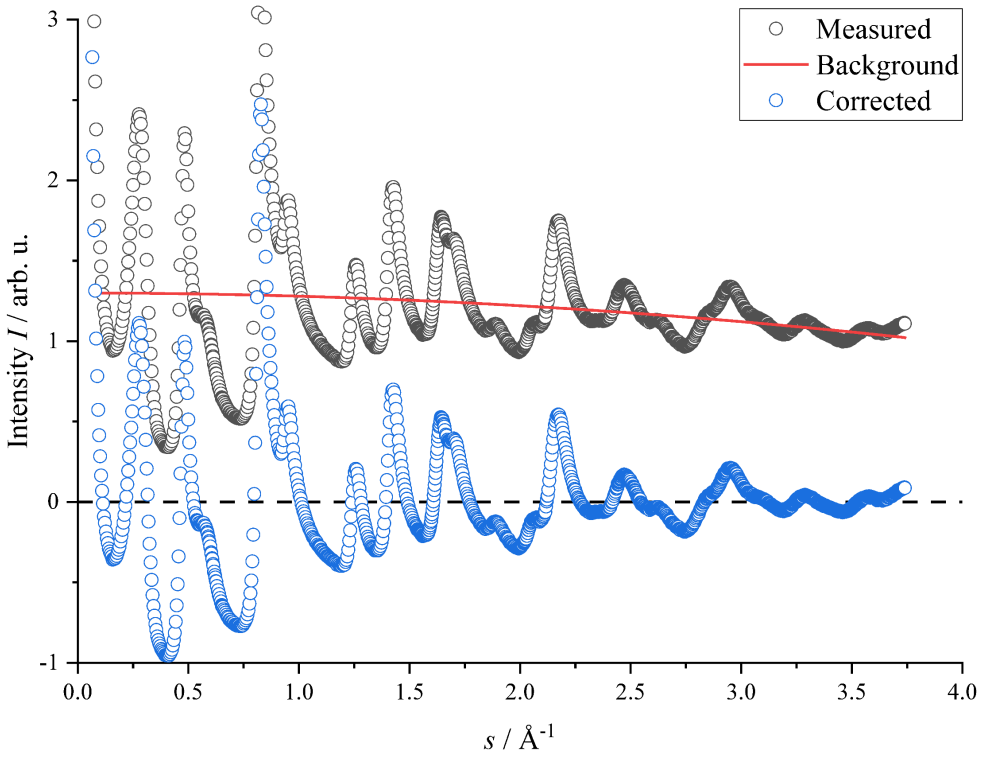

Figure S23 Example for a background correction of WANS data using the method from sufficient [1,2] (equation (68)). Black: measured data. Red: Assumed background. Blue: Corrected data.

References

1. Placzek, G. The Scattering of Neutrons by Systems of Heavy Nuclei. *Phys. Rev.* **1952**, *86*, 377–388, doi:10.1103/PhysRev.86.377.
2. Fischer, H.E.; Barnes, A.C.; Salmon, P.S. Neutron and x-ray diffraction studies of liquids and glasses. *Rep. Prog. Phys.* **2006**, *69*, 233–299, doi:10.1088/0034-4885/69/1/R05.
3. Milberg, M.E.; Brailsford, A.D. The atomic incoherent scattering intensities of boron, oxygen and carbon. *Acta Cryst* **1958**, *11*, 672–673, doi:10.1107/S0365110X58001808.
4. Pfaff, T.; Simmermacher, M.; Smarsly, B.M. CarbX : a program for the evaluation of wide-angle X-ray scattering data of non-graphitic carbons. *J Appl Crystallogr* **2018**, *51*, 219–229, doi:10.1107/S1600576718000195.
5. Keating, D.T.; Vineyard, G.H. The complete incoherent scattering function for carbon. *Acta Cryst* **1956**, *9*, 895–896, doi:10.1107/S0365110X56002539.
6. Prince, E.; Fuess, H.; Hahn, T.; Wondratschek, H.; Müller, U.; Shmueli, U.; Authier, A.; Kopský, V.; Litvin, D.B.; Rossmann, M.G.; et al. *International Tables for Crystallography;* International Union of Crystallography: Chester, England, 2006, ISBN 978-1-4020-5259-0.
7. Ruland, W. X-ray determination of crystallinity and diffuse disorder scattering. *Acta Cryst* **1961**, *14*, 1180–1185, doi:10.1107/S0365110X61003429.
8. James, R.W. *The optical principles of the diffraction of X-rays*, Repr. with addendum; London, 1962, *2*.
9. Ruland, W. The separation of coherent and incoherent Compton X-ray scattering. *Br. J. Appl. Phys.* **1964**, *15*, 1301–1307, doi:10.1088/0508-3443/15/11/306.
10. Ruland, W.; Smarsly, B.M. X-ray scattering of non-graphitic carbon: an improved method of evaluation. *J Appl Crystallogr* **2002**, *35*, 624–633, doi:10.1107/S0021889802011007.
11. Faber, K.; Badaczewski, F.M.; Ruland, W.; Smarsly, B.M. Investigation of the Microstructure of Disordered, Non-graphitic Carbons by an Advanced Analysis Method for Wide-Angle X-ray Scattering. *Z. anorg. allg. Chem.* **2014**, *640*, 3107–3117, doi:10.1002/zaac.201400210.
12. Buerger, M.J. The Correction of X-Ray Diffraction Intensities for Lorentz and Polarization Factors. *Proc. Natl. Acad. Sci. U. S. A.* **1940**, *26*, 637–642, doi:10.1073/pnas.26.11.637.
13. Schulz, L.G. A Direct Method of Determining Preferred Orientation of a Flat Reflection Sample Using a Geiger Counter X-Ray Spectrometer. *Journal of Applied Physics* **1949**, *20*, 1030–1033, doi:10.1063/1.1698268.
14. Sivia, D.S. *Elementary scattering theory*: *For X-ray and neutron users*, Reprinted.; Oxford University Press: Oxford [etc.], 2017, ISBN 9780199228683.
15. Seltzer, S. *Tables of X-Ray Mass Attenuation Coefficients and Mass Energy-Absorption Coefficients, NIST Standard Reference Database 126*, 1995.

16. NIST Center for Neutron Research. Neutron scattering lengths and cross sections. Available online: https://www.ncnr.nist.gov/resources/n-lengths/ (accessed on 22 December 2020).
17. Fox, A.G.; O'Keefe, M.A.; Tabbernor, M.A. Relativistic Hartree–Fock X-ray and electron atomic scattering factors at high angles. *Acta Crystallogr A Found Crystallogr* **1989**, *45*, 786–793, doi:10.1107/S0108767389007567.
18. Sears, V.F. Neutron scattering lengths and cross sections. *Neutron News* **1992**, *3*, 26–37, doi:10.1080/10448639208218770.
19. Cromer, D.T. Compton Scattering Factors for Aspherical Free Atoms. *The Journal of Chemical Physics* **1969**, *50*, 4857–4859, doi:10.1063/1.1670980.
20. Salmon, P.S.; Petri, I. Structure of glassy and liquid GeSe 2. *J. Phys.: Condens. Matter* **2003**, *15*, S1509-S1528, doi:10.1088/0953-8984/15/16/301.
21. Masson, O.; Thomas, P. Exact and explicit expression of the atomic pair distribution function as obtained from X-ray total scattering experiments. *J Appl Crystallogr* **2013**, *46*, 461–465, doi:10.1107/S0021889812051357.
22. Olds, D.P.; Duxbury, P.M. Efficient algorithms for calculating small-angle scattering from large model structures. *J Appl Crystallogr* **2014**, *47*, 1077–1086, doi:10.1107/S1600576714005925.

6.4.3. Anhang Publikation 2 [209]

Reproduziert mit Genehmigung von Oliver Osswald; veröffentlicht bei MDPI, *C*, 2023.

On the highly ordered graphene structure of Non-Graphitic Carbons (NGCs) – a Wide-Angle Neutron Scattering (WANS) study

Supporting information

Authors

Oliver Osswald[1*], Marc O Loeh[2], Felix M Badaczewski[2], Torben Pfaff[3], Henry E Fischer[4], Alexandra Franz[5], Jens-Uwe Hoffmann[5], Manfred Reehuis[5], Peter J Klar[6] and Bernd M Smarsly[1*]

1 Institute of Physical Chemistry, Justus-Liebig-University Giessen, Heinrich-Buff-Ring 17, Giessen, 35392, Germany
2 Schunk Kohlenstofftechnik GmbH, Rodheimer Strasse 59, 35452 Heuchelheim, Germany
3 Lang GmbH & Co. KG, Dillstraße 4, 35625 Hüttenberg, Germany
4 Institut Laue-Langevin, 71 avenue des Martyrs, CS 20156, 38042 Grenoble cedex 9, France
5 Helmholtz-Zentrum Berlin für Materialien und Energie, Hahn-Meitner-Platz 1, 14109 Berlin, Germany
6 Institute of Experimental Physics I, Justus-Liebig-University Giessen, Heinrich-Buff-Ring 16, Giessen, 35392, Germany

* Correspondence: carbon@oss-wald.de; bernd.smarsly@pyhs.chemie.uni-giessen.de

Funding information Financial support is provided by the DFG via the GRK (Research Training Group) 2204 "Substitute Materials for Sustainable Energy Technologies".

Supporting information

S1. Data treatment and background correction

S1.1. Refinement by Ruland and Smarsly's algorithm

In principle, the theoretical scattering intensity of the material ($I_{e.u.}$) is a superposition of the coherent scattering (I_{coh}) and the incoherent scattering (I_{incoh}), where the coherent scattering can be calculated by the interlayer and intralayer scattering intensity (I_{inter} and I_{intra}, respectively) and the atomic form-factor of carbon (f_c):

$$I_{e.u.} = I_{coh} + I_{incoh} \tag{1}$$

$$I_{coh,\,c} = f_c^2 \cdot (I_{inter} + I_{intra}) \tag{2}$$

Beside these structural influences, the calculated theoretical intensity without any experimental influences (I_{calc}) can be calculated by:

$$I_{calc} = k \cdot A \cdot P \cdot I_{e.u.} \tag{3}$$

Hence, k is a normalization constant, which is needed through the different intensities of the incoming radiation and the amount of irradiated material, A is the absorption parameter and P describes the polarization. The Lorentz factor is already considered in the calculation of the coherent scattering intensity and therefore, this parameter does not have to and must not be considered further. Additional information of these correction parameters can be found the work of Osswald and Smarsly [1].

However, a factor considering a fixed irradiated length instead a fixed divergence slit (*AutoColl*), an exponential damping factor (*gFact*) for taking the possibility of a small angle scattering contribution at low scattering vector values as well as two constants ($const_1$, $const_2$) for considering a linear and a non-linear background, can be used to obtain the full observed intensity (I_{obs}):

$$I_{obs} = 10\text{^}[\log_{10}((1/AutoColl) \cdot gFact \cdot k \cdot A \cdot P \cdot (I_{coh} + I_{incoh})) + const_1) + const_2] \tag{4}$$

Since the parameters *AutoColl*, A, P, I_{coh} and I_{incoh} are clearly and unique to calculate and use, in this study, the parameters k, *gFact*, $const_1$ and $const_2$ are from more interest. Hence, k is just a normalization constant, which must be used every time due to the different intensity of the incoming radiation and the different amounts and densities of the used samples. The parameter $const_1$ causes a constant shift of the whole scattering curve, which is caused by cosmical background radiation, incoherent scattering, sample holder or other general influences during the experiment. $const_2$ describes a non-linear background, which may be caused by the incoherent scattering due to the incoherent cross section of the atoms. Further information about these parameters and their influence is given in the next section.

S1.2. Background correction

The previous described background correction is very simple and cannot cover the entire background in WANS measurements. Instead, the models of Placzek [2] or Fischer et al. [3] should be used, where the background scattering can be calculated by fitted by a cubic polynomial or a Pseudo-Voigt function with the normalization constant k, the proportion of the Lorentzian/Gaussian function η and the half with at full maximum (FWHM) 2ω (equation (5) and (6), respectively):

$$S(s) = I_{Obs}(s) - (a \cdot s^2 + b) + 1 \tag{5}$$

$$S(s) = I_{Obs}(s) - k \cdot (\eta \cdot L(s, \omega) + (1 - \eta) \cdot G(s, \omega)) + 1 \tag{6}$$

$$L(s, \omega) = \frac{1}{1 + \left(\frac{s}{\omega}\right)^2} \tag{7}$$

$$G(s, \omega) = \exp^{-\ln(2) \cdot \left(\frac{s}{\omega}\right)^2} = 2^{-\left(\frac{s}{\omega}\right)^2} \tag{8}$$

Hence, equation (8) should be used for samples containing only a very small of hydrogen, otherwise equation (8) should be used. In Figure S1, the background correction for PF-R 1000 and PF-R 1500 is shown. Since PF-R 1000 consists of a very high amount of hydrogen and therefore, a Pseudo-Voigt background correction is necessary. On the other hand, PF-R 1500 consists of less hydrogen and therefore, the difference is much smaller and for higher heat-treated samples, a Placzek instead of Pseudo-Voigt correction is sufficient. For a hydrogen amount > 0.3 wt. %, a Pseudo-Voigt function should be used to determine the background (Figure S1). For all other samples, a Placzek correction is sufficient. More detailed information about the background correction can be found in the work of Osswald & Smarsly [1].

Using equation (4), the influences of the different parameters can be determined easily. Now, the measured scattering intensity can be turned into a theoretical calculated intensity, which corresponds to the model of Ruland and Smarsly [4]. Hence, k is just a normalization constant, which must be used every time due to the different intensity of the incoming radiation and the different amounts and densities of the used samples. The parameter $const_1$ causes a constant shift of the whole scattering curve, which is caused by cosmical background radiation, incoherent scattering, sample holder or other general influences during the experiment. For the parameter $const_2$, it must be differentiated into two cases: If $const_1 = 0$, then $const_2$ is nothing else than the normalization constant with $const_2 = -\log(k)$.

Additionally, also the parameter $gFact = \exp(g\ s)$ is not that easily to understand. In principle, this parameter should describe a possible influence of a small-angle scattering intensity on the WAXS or WANS data [5]. However, this intensity falls with Porod's law ($I \sim P/s^4$) and the influence of the fluctuation of the graphene sheets in the stacking structure ($I \sim B_{fl}/s^2$) and overall, the damping of can

be described as a superposition of them as described in the works of Porod, Ruland, Smarsly and coworkers [6–8]. Since, both influences are only small in bulk materials, it can be described by the factor *gFact* well as already done in the references [9–11]. Additionally, the theoretical calculated scattering intensity assumes a hexagonal layer structure, which might not be the case for very disordered structures. Also, resin as precursor results in a porous structure [9,12], which can also interpretated as a degree of disorder in the stacking structure. These different types of additionally disorders causes some damping of the intensity, where the damping is higher at higher values of *s*.

To proof these assumptions, data refinements using *gFact* and $const_2$ and refinements fixing them to 0 were performed. Overall, there is a significant difference in the refinements for the samples PF-R 1000/1200/1500/1800/2100 and MP 1200/1500, respectively, for all other samples, the values are generally nearly identical. Additionally, the resulting refinements for the refinements $g = 0/const_2 =$ fitted and $g = 0/const_2 = 0$ are also very similar, only for $g \neq 0$, there is a significant difference (Figure S2). This behavior is directly related to the amount of hydrogen of the sample (Figure 12, Table S2). It seems, that the amount of hydrogen has a direct or indirect influence on the resulting microstructure parameters, even if this incoherent background scattering was subtracted.

However, this differences in the ways of determining the background can be balanced by the additional normalization parameters $const_2$ and *g*. In the resulting refinements, both parameters are only small and therefore, they can be seen as “smoothing parameters”. Therefore, the parameters $const_2$ and *g* are needed for samples containing hydrogen, since these influences the refinement result directly through the incoherent background indirectly through a higher degree of disorder, which can be described through the additional normalization parameters. These theoretical considerations can also be proofed looking at the refinements. In Figure S2, the refinements for PF-R 1200 and PF-R 3000 are shown. Since PF-R 1000 consists of high amount of hydrogen, the different refinements are slightly different, but overall, $const_2$ and *g* must be used to get the best result as possible. In contrast, PF-R 3000 is much more ordered and does not consist of any hydrogen and therefore, the refinements are nearly identical. It does not matter, whether $const_2$ and *g* was used or not and both parameters do not have an influence on the resulting microstructure parameters. Therefore, they can also be used for these samples, since they will be fitted near to 0 in this case.

To conclude this discussion about the background correction and the usage of the normalization constants, the following two points should be considered:

1. For a hydrogen amount > 0.2 %, a Pseudo-Voigt function should be used to determine the background. For all other samples, a Placzek correction is sufficient.
2. The parameters *g* and $const_2$ should be refined for every sample, since it leads to more exact results for less ordered samples it does not influence higher ordered samples.

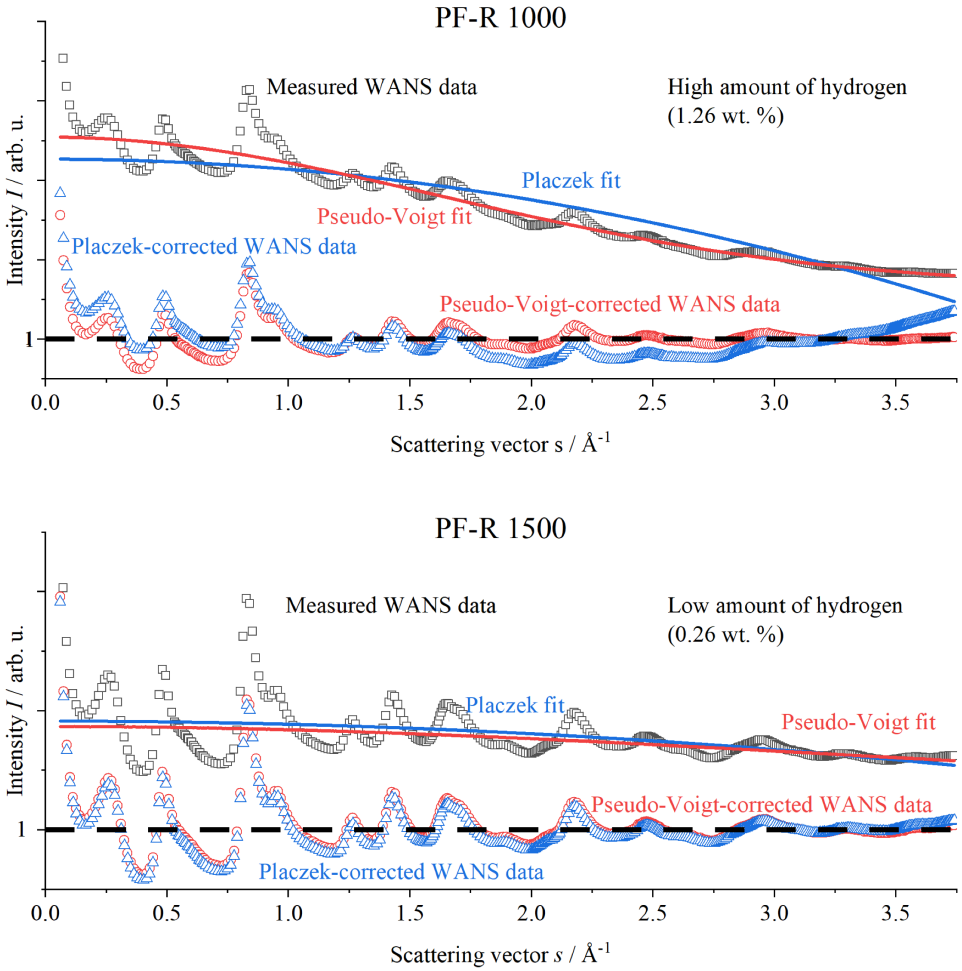

Figure S1 Background correction using a Pseudo-Voigt function (red) for PF-R 1000, which contains a significant amount of hydrogen in contrast du a Placzek correction (blue), which is used for samples consist of only a few hydrogen (< 0.2 %). For PF-R 1500, the difference is only small and therefore, the Placzek correction is sufficient for temperatures with less hydrogen (= higher heat-treatment temperatures). Only every 3rd measured point is shown.

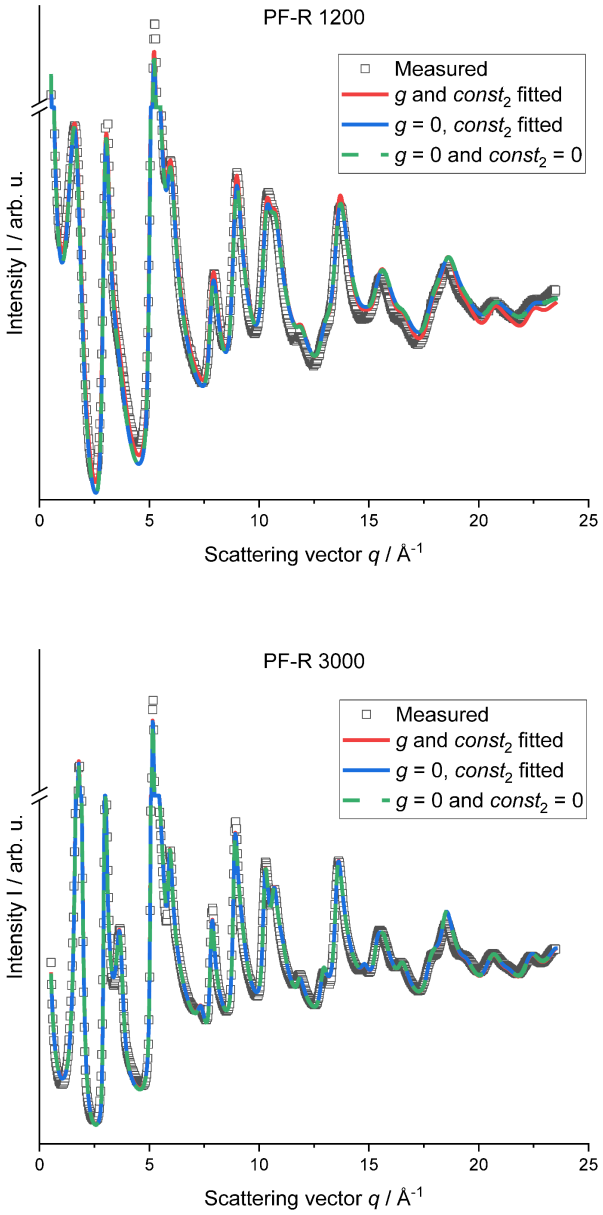

Figure S2 Example refinements for PF-R 1200 and PF-R 3000 using three different types of normalization correction (red: g and $const_2$ fitted, blue: $g = 0$, $const_2$ fitted, green: $g = 0$ and $const_2 = 0$). Overall, the differences are only very small and therefore, it is recommended to use g and $const_2$ during the refinement, since it leads to more comparable and exact results.

S2. Overview about the refined microstructure

S2.1. Results for the phenol-formaldehyde resin (PF-R) temperature series

S2.1.1. WANS-data refinement for the phenol-formaldehyde resin (PF-R) temperature series

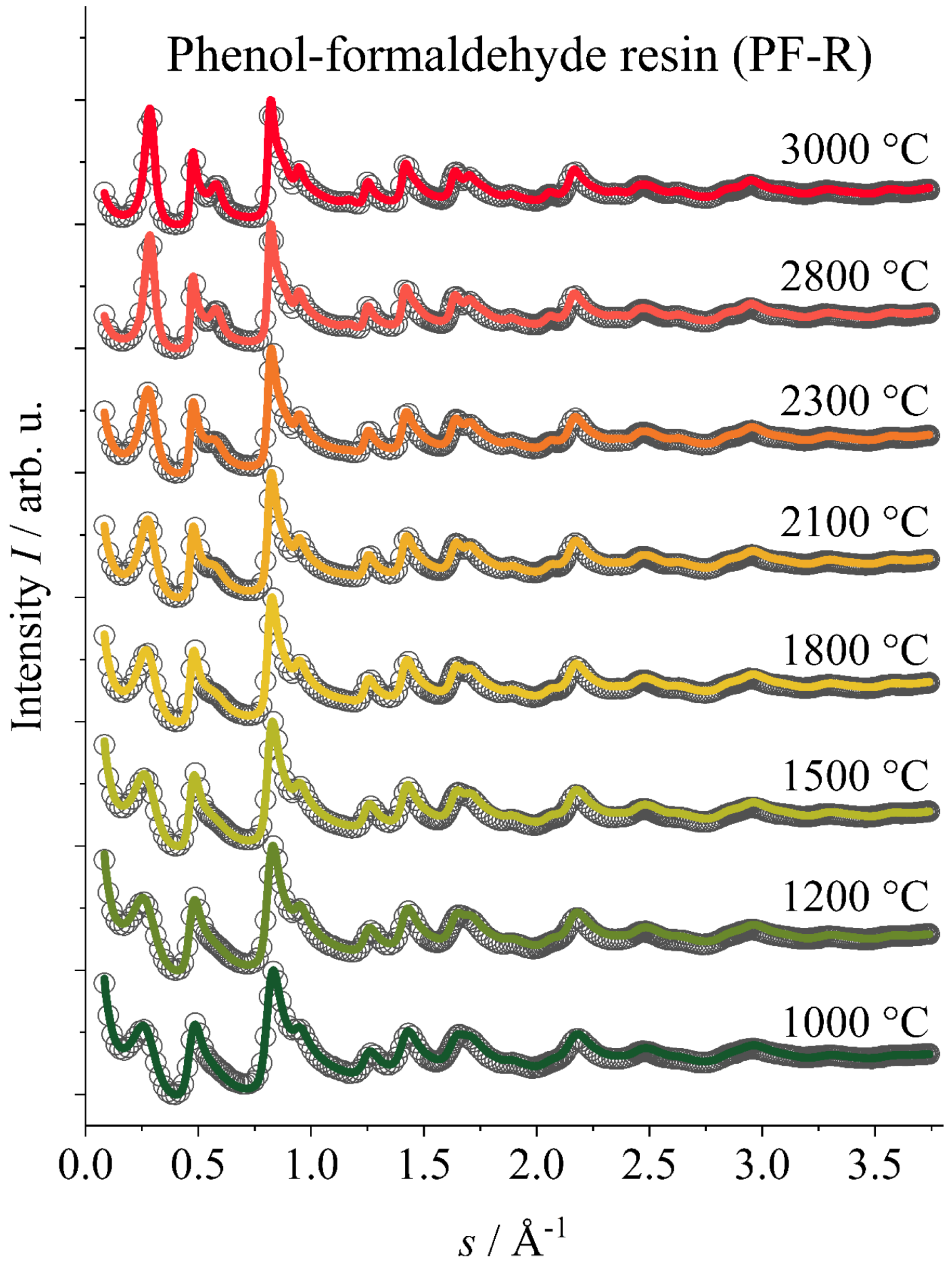

Figure S3 WANS-data refinement for the phenol-formaldehyde resin (PF-R) temperature series.

S2.1.2. Microstructure parameters for the phenol-formaldehyde resin (PF-R) temperature series

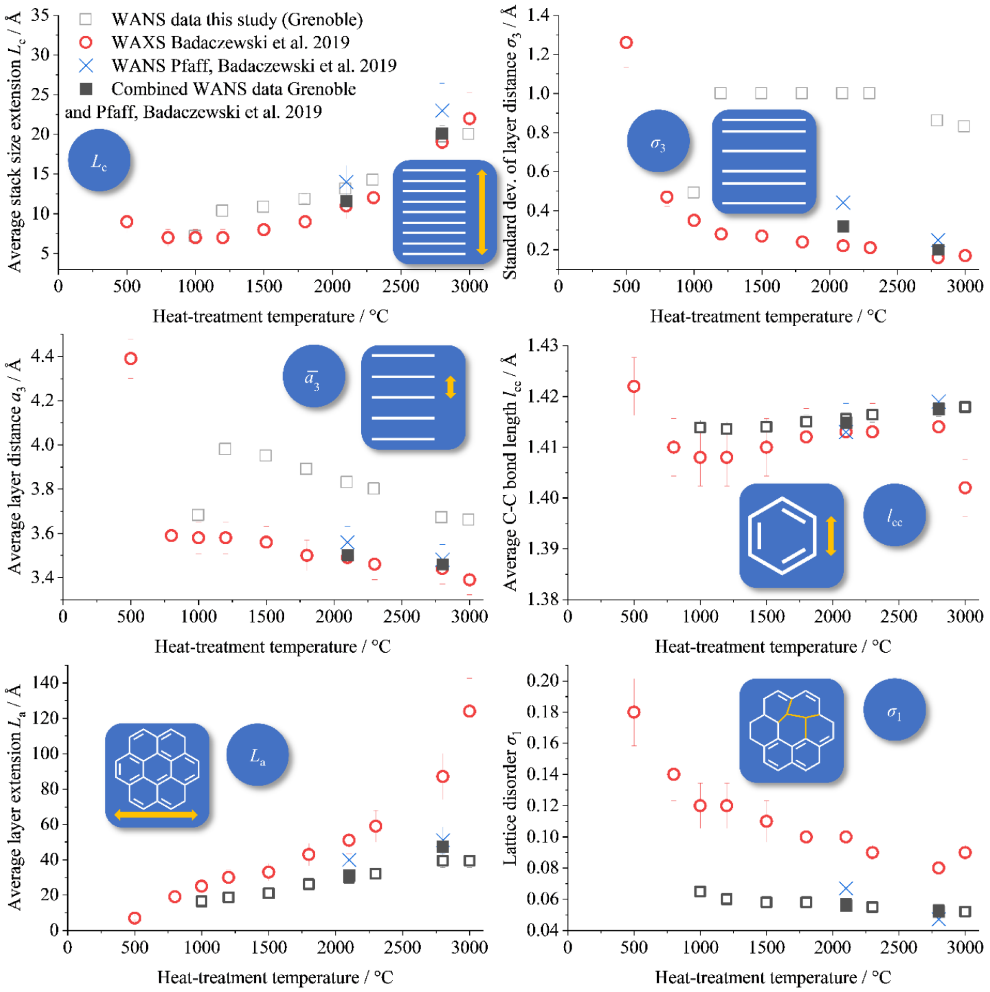

Figure S4 Refined microstructure data for phenol-formaldehyde resin (PF-R) as precursor (black border-only: this study (WANS Grenoble), red: Badaczewski et al. (WAXS) [1], blue: Pfaff, Badaczewski et al. (WANS Berlin) [2], black filled: combined WANS data from Grenoble and Berlin).

S2.1.3. Stack structure of the phenol-formaldehyde resin (PF-R) temperature series

Regarding to 3.2.1 in the main article, another important point to analyze and determine the disorder of the stacking structure is the parameter κ_c, which describes the polydispersity of the stack height. In the work of Badaczewski et al. [1], these parameter does not have any clear tendency, but they are spread between 0.1 and 1, where 0 means no and 1 a high polydispersity of the stack height. Since this parameter has only a very small influence on the scattering curve, it is nearly impossible to refine this parameter in a meaningful way using wide-angle X-ray scattering at a common copper radiation wavelength (λ = 1.54 Å). Using neutron scattering at a lower wavelength, higher ordered reflections without any damping from the atomic form factor become visible. Therefore, it is possible to also refine the polydispersity of the stack height. In the case of the phenol-formaldehyde resin, this value decreases from 0.45 at 1000 °C to 0.35 at 3000 °C, which means, the stack height become more unique at higher heat treatment temperatures.

The last parameter describing the order of the stacks is the homogeneity η. This parameter describes, if the sheets are completely parallel and perfectly stacked on each other (η = 1) or not (η < 1). The homogeneity is increasing from 0.94 to 1 (perfectly homogeneous), which means an increasing degree of order in the stacking structure. These values are higher than in the reference, where the homogeneity also does not have a clear dependent tendency of the heat treatment, but overall, the order of magnitudes of all parameters are in a good agreement with the WAXS data measured by of Badaczewski et al. [1]. Therefore, also the tendency for the average stack height (L_c) is comparable to the reference, even if the absolute values are a little bit higher. A higher stack height, which means nothing else than a bigger crystallite size, causes higher and sharper reflections in the scattering pattern, while a higher disorder causes smaller and broader reflections, so also bigger stack height balances the high values of σ_3 and the evaluation of the WANS data of this study is comparable and the results consistent with the reference, even if the absolute values are different.

S2.2. Results for the mesophase pitch (MP) temperature series

S2.2.1. WANS-data refinement for the mesophase pitch (MP) temperature series

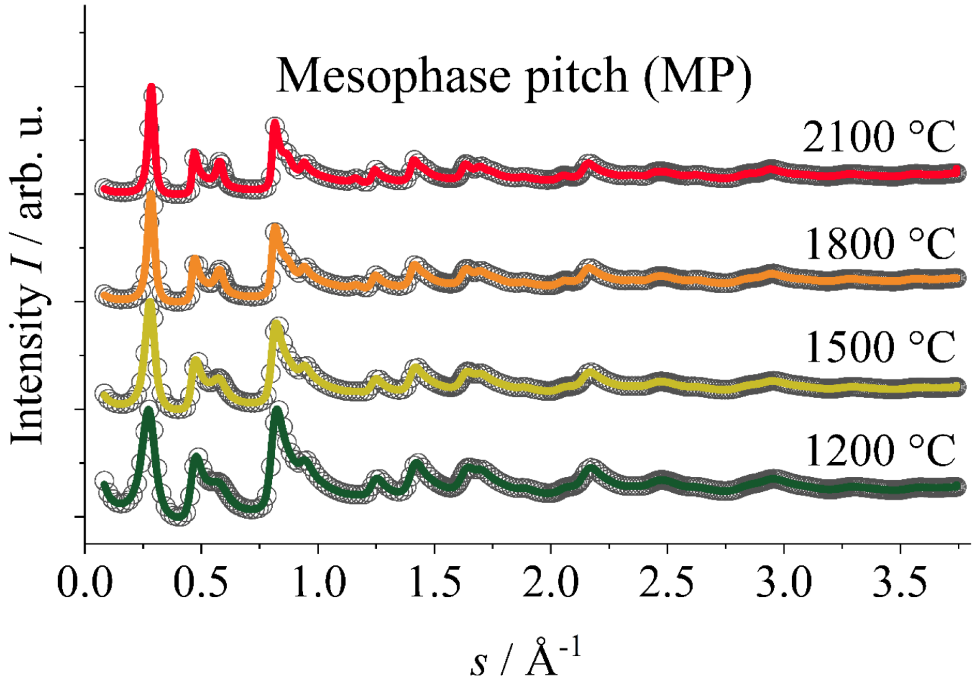

Figure S5 WANS-data refinement for the mesophase pitch (MP) temperature series.

S2.2.2. Microstructure parameters for the mesophase pitch (MP) temperature series

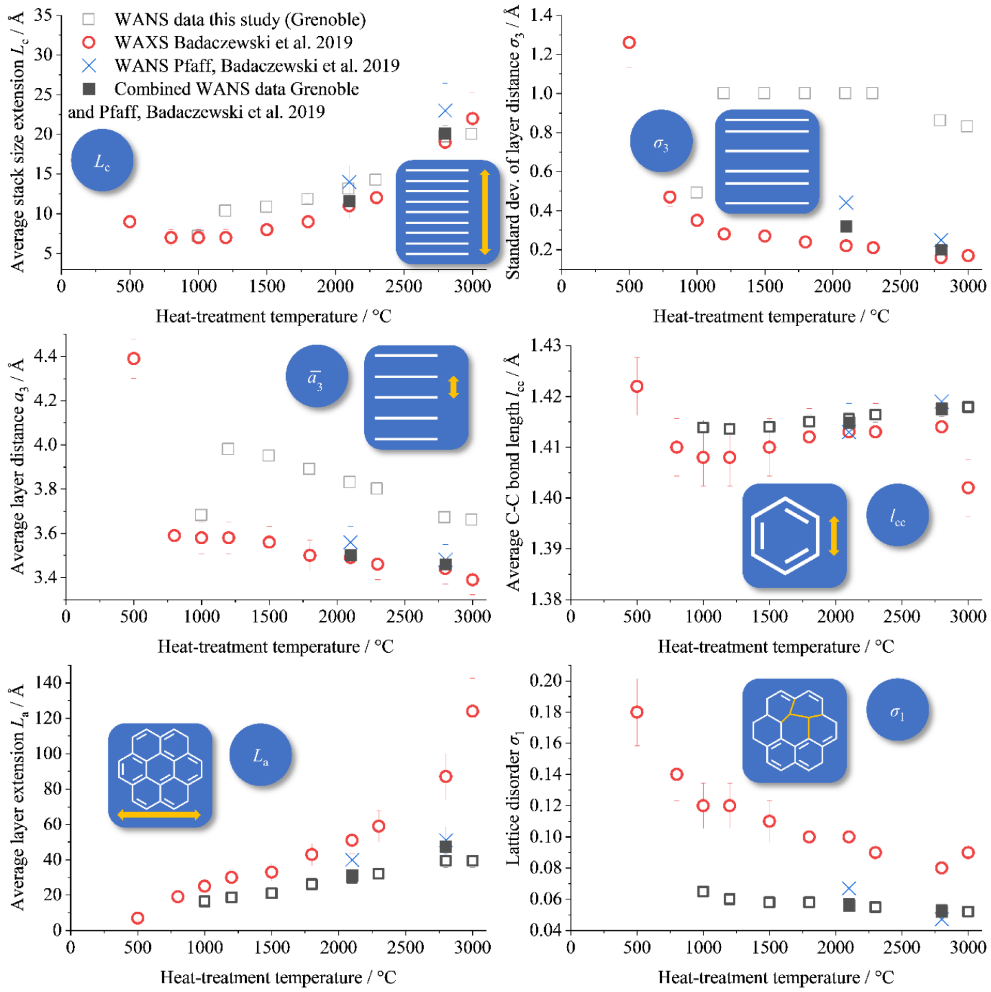

Figure S6 Refined microstructure data for a mesophase pitch (MP) as precursor (black border-only: this study (WANS Grenoble), green: Loeh et al. (WAXS) [3], red: Badaczewski et al. (WAXS) [1], blue: Pfaff, Badaczewski et al. (WANS Berlin) [2], black filled: combined WANS data from Grenoble and Berlin).

S2.3. Results for the low softening-point pitch (LSPP) temperature series

S2.3.1. WANS-data refinement for the low softening-point pitch (LSPP) temperature series

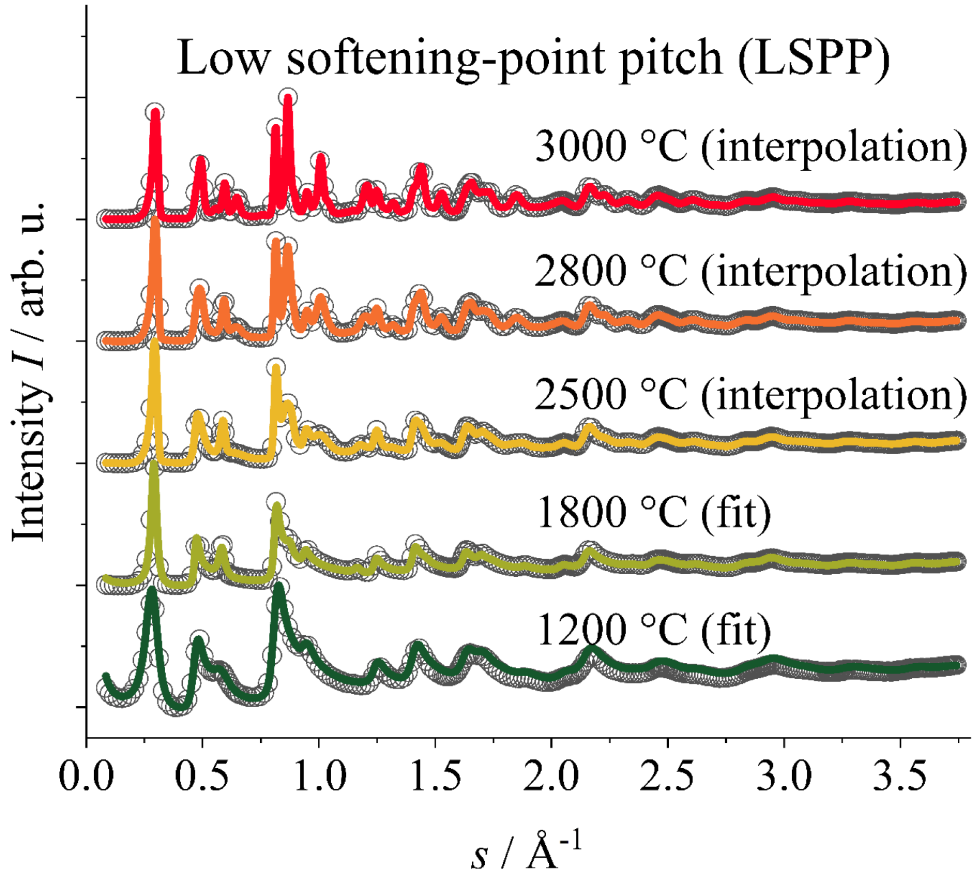

Figure S7 WANS-data refinement (1200 °C and 1800 °C) for the low softening-point pitch (LSPP) temperature series. For 2500 °C, 2800 °C and 3000 °C, the data could not be refined using the model of Ruland & Smarsly [4] due to the "mixed" (*hkl*)-reflections. Therefore, the data was just interpolated.

S2.3.2. Microstructure parameters for the low softening-point pitch (LSPP) temperature series

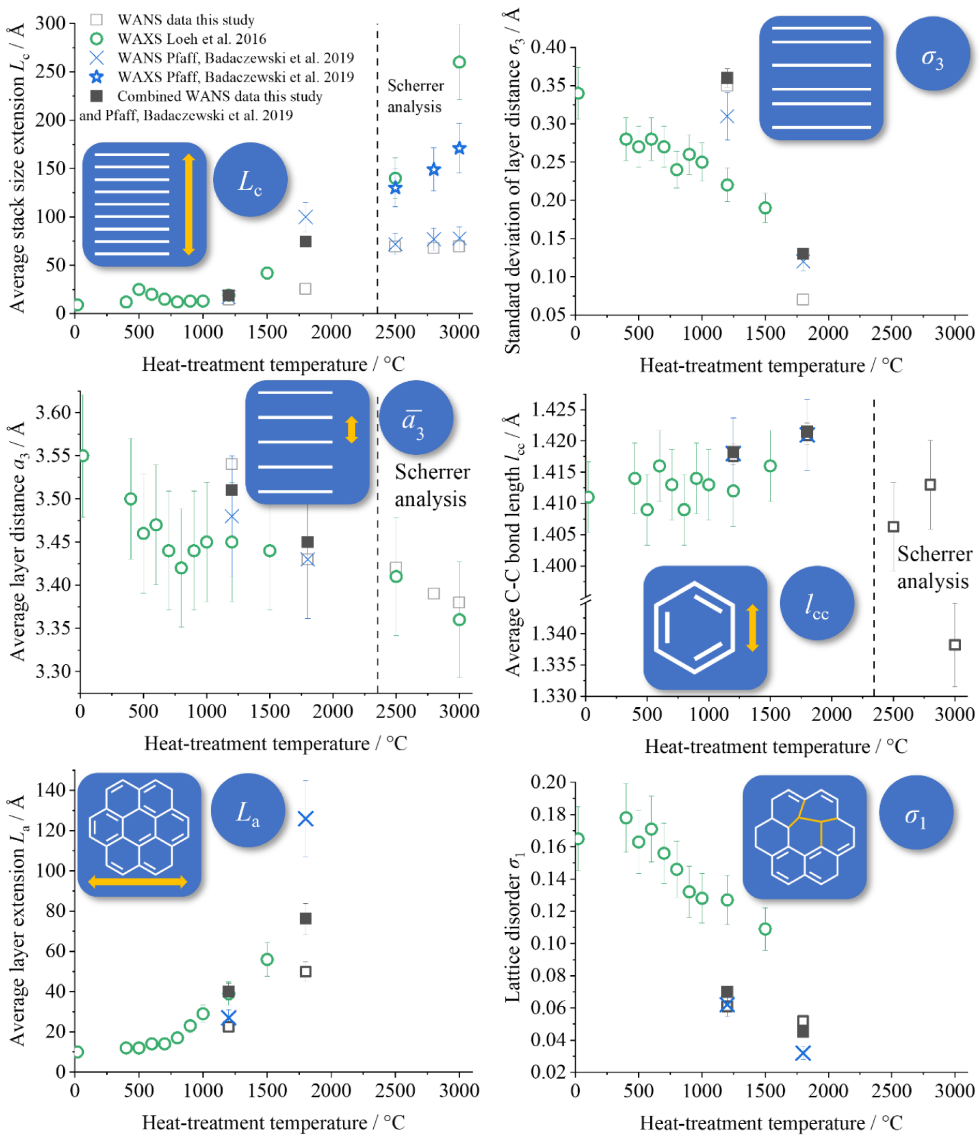

Figure S8 Refined microstructure data for a low softening-point pitch (LSPP) as precursor (black border-only: this study (WANS Grenoble), green: Loeh et al. (WAXS) [3], blue: Pfaff, Badaczewski et al. (WANS Berlin) [2], black filled: combined WANS data from Grenoble and Berlin).

S2.4. Comparison between measured wide-angle neutron scattering data of this study to wide-angle X-ray and neutron (WAXS/WANS) to works of Badaczewski, Loeh, Pfaff et al. [1–3]

- Grenoble WANS data PF-R
- Grenoble WANS data MP
- Grenoble WANS data LSPP
- Combined Grenoble/Berlin WANS data PF-R
- Combined Grenoble/Berlin WANS data MP
- Combined Grenoble/Berlin WANS data LSPP

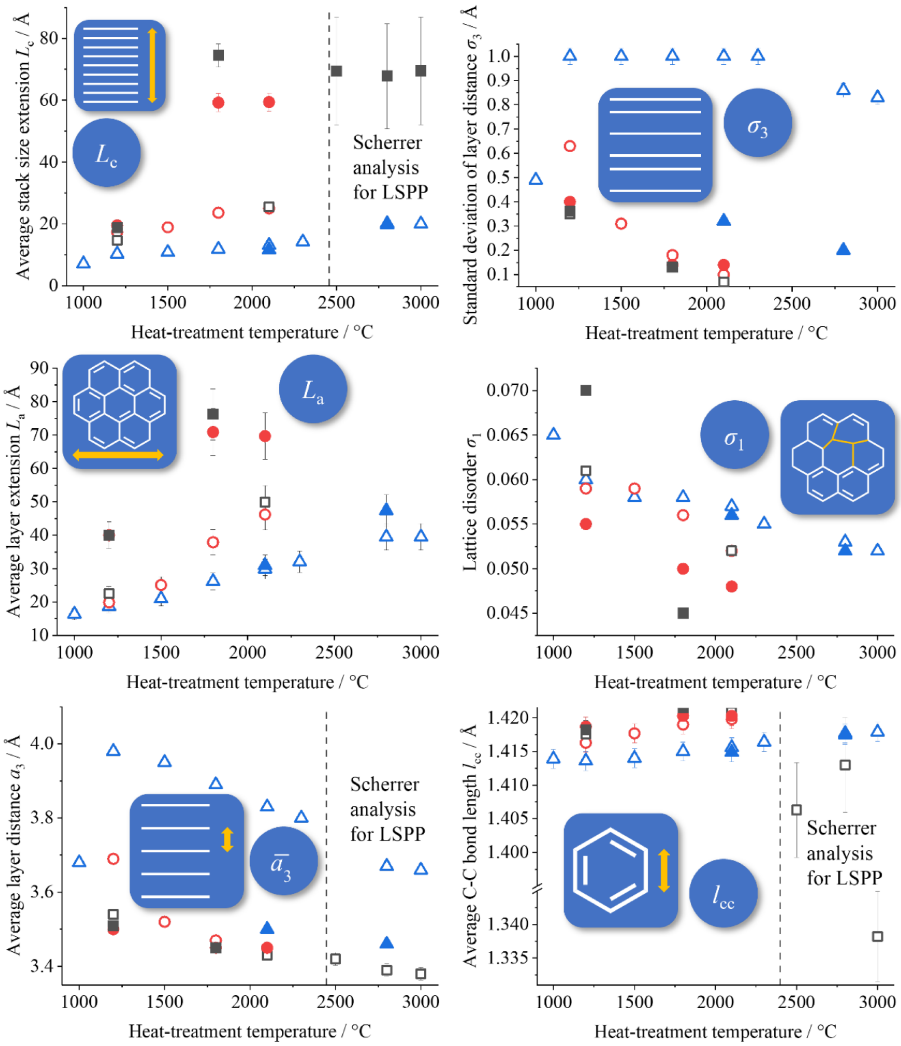

Figure S9 Refined microstructure data comparison between the different precursors (black: phenol-formaldehyde resin (PF-R), red: mesophase pitch (MP), blue: low softening-point pitch (LSPP)). Border-only: Refinement from WANS data from Grenoble (this study); filled: combined WANS data from Grenoble and Berlin (Pfaff, Badaczewski et al. 2019 [2])).

Table S1 Overview about final resulting microstructure parameters. Since phenol-formaldehyde resin (PF-R) is non-graphitizable, the samples still consist of a certain degree of disorder, even hat high heat-treatment temperatures. In contrast, the mesophase pitch (MP) and the low softening-point pitch (LSPP) consist of more ordered aromatic systems in the precursor, so the resulting microstructure is more graphite like at high heat-treatment temperatures. Since the softening-point is lower for LSPP, it is better graphitizable than MP. A detailed description as well as a figure of the meaning of it, can be found in the work of Osswald and Smarsly [5]. The numbers in brackets are the results from the combination of the WANS data from Grenoble and Berlin.

	Phenol-formaldehyde resin (PF-R)								
	L_c / Å	N	$\overline{a_3}$ / Å	a_{3min} / Å	σ_3 / Å	η	L_a / Å	l_{cc} / Å	σ_1
									
Max. error	5 %	7.5 %	0.1 %	3.3 %	3.3 %	5 %	10 %	0.1 %	2 %
PF-R 1000	7.1	1.9	3.68	3.12	0.49	0.94	16.4	1.4139	0.065
PF-R 1200	10.3	2.6	3.98	3.21	1	0.95	18.7	1.4136	0.060
PF-R 1500	10.8	2.7	3.95	3.24	1	0.96	21.0	1.4140	0.058
PF-R 1800	11.8	3.0	3.89	3.32	1	0.95	26.2	1.4150	0.058
PF-R 2100	13.1 (11.6)	3.4 (3.3)	3.83 (3.5)	3.36 (2.74)	1 (0.32)	0.96 (0.87)	29.9 (31)	1.4156 (1.4149)	0.057 (0.056)
PF-R 2300	14.2	3.7	3.80	3.38	1	0.98	32.1	1.4164	0.055
PF-R 2800	19.7 (20.1)	5.4 (5.8)	3.67 (3.46)	3.39 (3.08)	0.86 (0.20)	1 (0.94)	39.5 (47.4)	1.4177 (1.4175)	0.053 (0.052)
PF-R 3000	20	5.5	3.66	3.39	0.83	1.00	39.5	1.4179	0.052

	Mesophase pitch (MP)								
	L_c / Å	N	$\bar{a}_3$ / Å	a_{3min} / Å	σ_3 / Å	η	L_a / Å	l_{cc} / Å	σ_1
									
Max. error	5 %	7.5 %	0.1 %	3.3 %	3.3 %	5 %	10 %	0.1 %	2 %
MP 1200	17.3 (19.5)	4.7 (5.6)	3.69 (3.5)	3.28 (3.3)	0.63 (0.40)	1 (1)	19.9 (40)	1.4163 (1.4187)	0.059 (0.055)
MP 1500	18.9	5.4	3.52	3.27	0.31	1	25.1	1.4177	0.059
MP 1800	23.6 (59.2)	6.8 (17.1)	3.47 (3.45)	3.37 (3.33)	0.18 (0.14)	1 (0.99)	37.9 (70.9)	1.4190 (1.4203)	0.056 (0.050)
MP 2100	25.0 (59.4)	7.3 (17.2)	3.45 (3.45)	3.39 (3.34)	0.10 (0.14)	1 (0.99)	46.2 (69.7)	1.4198 (1.4203)	0.052 (0.048)

Low softening-point pitch (LSPP) (2500 °C and higher only evaluated by Scherrer analysis)

	L_c / Å	N	$\overline{a_3}$ / Å	a_{3min} / Å	σ_3 / Å	η	L_a / Å	l_{cc} / Å	σ_1
									
Max. error	5 %	7.5 %	0.1 %	3.3 %	3.3 %	5 %	10 %	0.1 %	2 %
LSPP 1200	14.6 (18.7)	4.1 (5.3)	3.54 (3.51)	3.21 (3.11)	0.35 (0.36)	1.00 (1.00)	22.5 (40.0)	1.4176 (1.4182)	0.061 (0.07)
LSPP 1800	25.5 (74.5)	7.4 (21.6)	3.43 (3.45)	2.76 (3.36)	0.07 (0.13)	1.00 (0.99)	49.9 (76.2)	1.4209 (1.4215)	0.052 (0.045)

Scherrer analysis (higher error bars)

LSPP 2500	69.4 (72)	20.3	3.42					1.4063	
LSPP 2800	67.8 (77)	20.0	3.39					1.4130	
LSPP 3000	69.5 (78)	20.6	3.38					1.3382	

S3. Combination of WANS-data

For 7 samples, WANS data from two different experiments were measured and can be combined (PF-R 2100/2800, MP 1200/1800/2100, LSPP 1200/1800). The advantages of the combination have already been discussed in the main article, so only the practical implementation is shown here (Figures S10 and S11).

In principle, the raw data (part A) from Berlin was adjusted to fit the raw data from Grenoble using a linear function (only stretching and moving) in the range from 1.4 $Å^{-1} < s < 1.5$ $Å^{-1}$. Afterwards, the already known background correction determined from the WANS data from Grenoble was used to correct both, the WANS data from Grenoble and from Berlin. For the combined data, for $s < 1.45$ $Å^{-1}$, the part from Berlin, and for $s > 1.45$ $Å^{-1}$ the part from Grenoble was used.

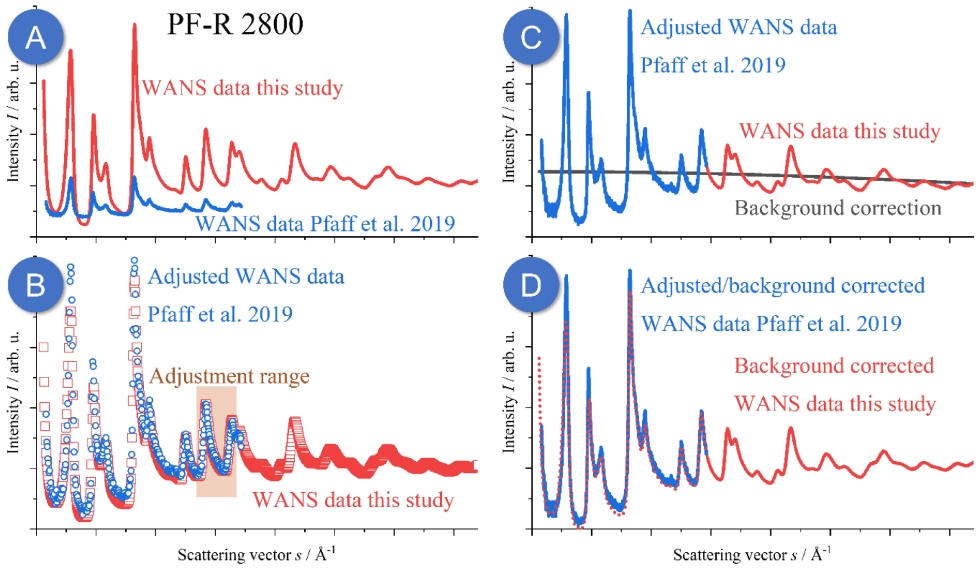

Figure S10 Combination of WANS data for the phenol-formaldehyde heat-treated at 2800 °C measured for this study in Grenoble and already measured by Pfaff, Badaczewski et al. in Berlin [2].

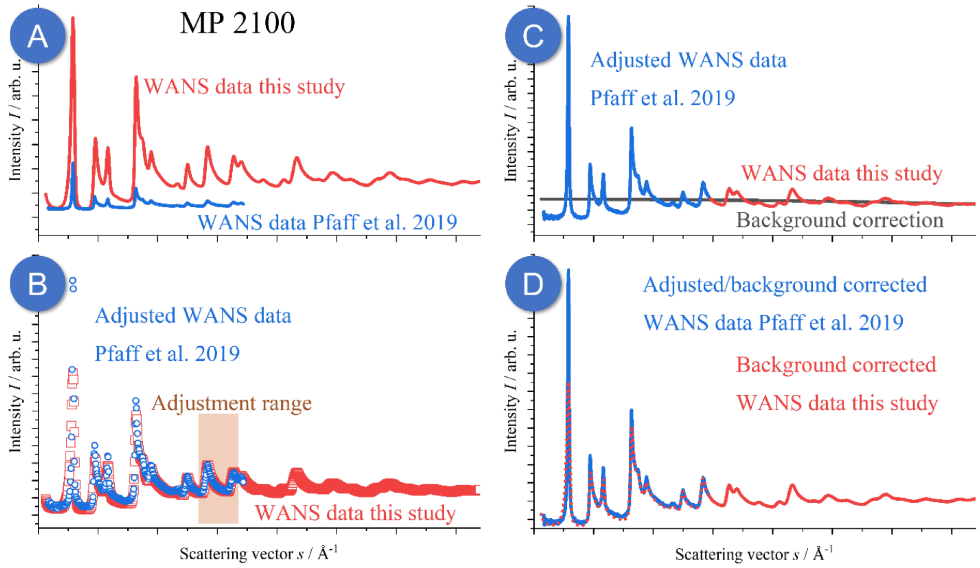

Figure S11 Combination of WANS data for the mesophase pitch heat-treated at 2100 °C measured for this study in Grenoble and already measured by Pfaff, Badaczewski et al. in Berlin [2].

S4. Elemental analysis

Table S2 Overview of the elemental analysis of all measured samples. PF-R = phenol-formaldehyde resin, MP = mesophase pitch, LSPP = low softening-point pitch. Sulfur was only measured for the LSPP series.

Precursor	Heat treatment temperature	Carbon (C)	Hydrogen (H)	Nitrogen (N)	Oxygen (O)	Sulfur (S)
PF-R	1000 °C	95.90%	1.26%	0.64%	0.86%	
PF-R	1200 °C	99.20%	0.43%	0.40%	0.16%	
PF-R	1500 °C	99.50%	0.26%	0.18%	0.25%	
PF-R	1800 °C	99.70%	0.16%	0.01%	0.11%	
PF-R	2100 °C	99.80%	0.13%	0.01%	0.08%	
PF-R	2300 °C	99.80%	0.12%	0.01%	0.07%	
PF-R	2800 °C	99.90%	0.05%	0.01%	0.06%	
PF-R	3000 °C	100.00%	0.00%	0.01%	0.05%	
MP	1200 °C	98.70%	0.40%	0.78%	0.15%	
MP	1500 °C	99.40%	0.24%	0.34%	0.07%	
MP	1800 °C	100.00%	0.15%	0.01%	0.04%	
MP	2100 °C	99.80%	0.15%	0.01%	0.04%	
LSPP	1200 °C	96.20%	0.19%	1.01%	0.17%	0.40%
LSPP	1800 °C	97.80%	0.00%	0.96%	0.05%	0.10%
LSPP	2500 °C	97.10%	0.00%	0.92%	0.06%	0.10%
LSPP	2800 °C	97.20%	0.00%	0.85%	0.04%	0.00%
LSPP	3000 °C	97.50%	0.00%	0.81%	0.06%	0.00%

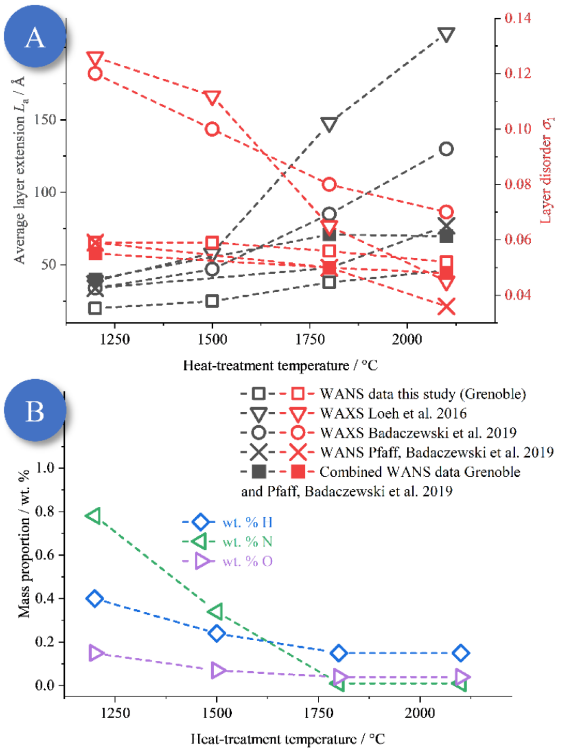

Figure S12 Comparison of the layer extension (L_a) und disorder (σ_1) and stack height (L_c) und disorder (σ_3) to the elemental analysis for a mesophase pitch (MP) as precursor. Since foreign atoms as oxygen and nitrogen cannot build perfect sp^2-hybridizes layers, the presence of it hinders the formation of such layers. Therefore, with a decreasing amount of such atoms leads to bigger and higher ordered layers. The values of L_c and σ_3 are not shown here, because their determination does not possess sufficient accuracy.

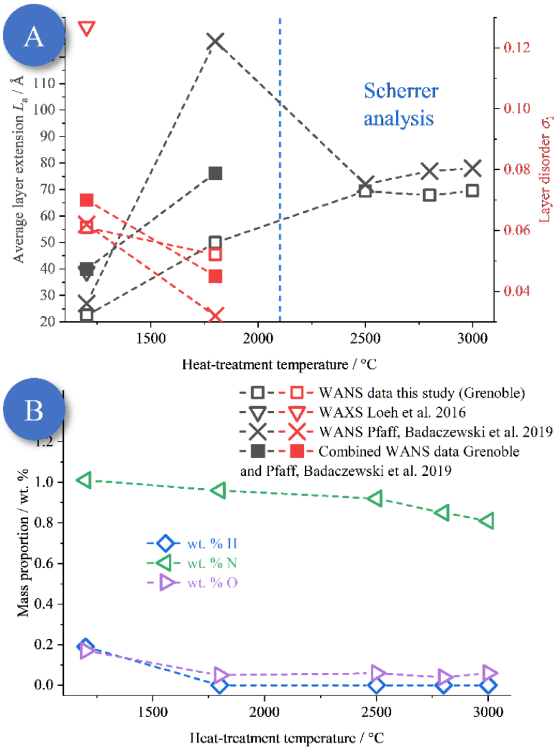

Figure S13 Comparison of the layer extension (L_a) und disorder (σ_1) and stack height (L_c) und disorder (σ_3) to the elemental analysis for the low softening-point pitch (LSPP) as precursor. Since foreign atoms as oxygen and nitrogen cannot build perfect sp^2-hybridizes layers, the presence of it hinders the formation of such layers. Therefore, a decreasing amount of such atoms leads to bigger and higher ordered layers. Additionally, the complete absence of oxygen seems to be a good indicator for the presence of a three-dimensionally ordered graphite-like structure (LSPP 2800/3000). The values of L_c and σ_3 are not shown here, because their determination does not possess sufficient accuracy.

S5. Results, microstructure parameters and comparison to literature

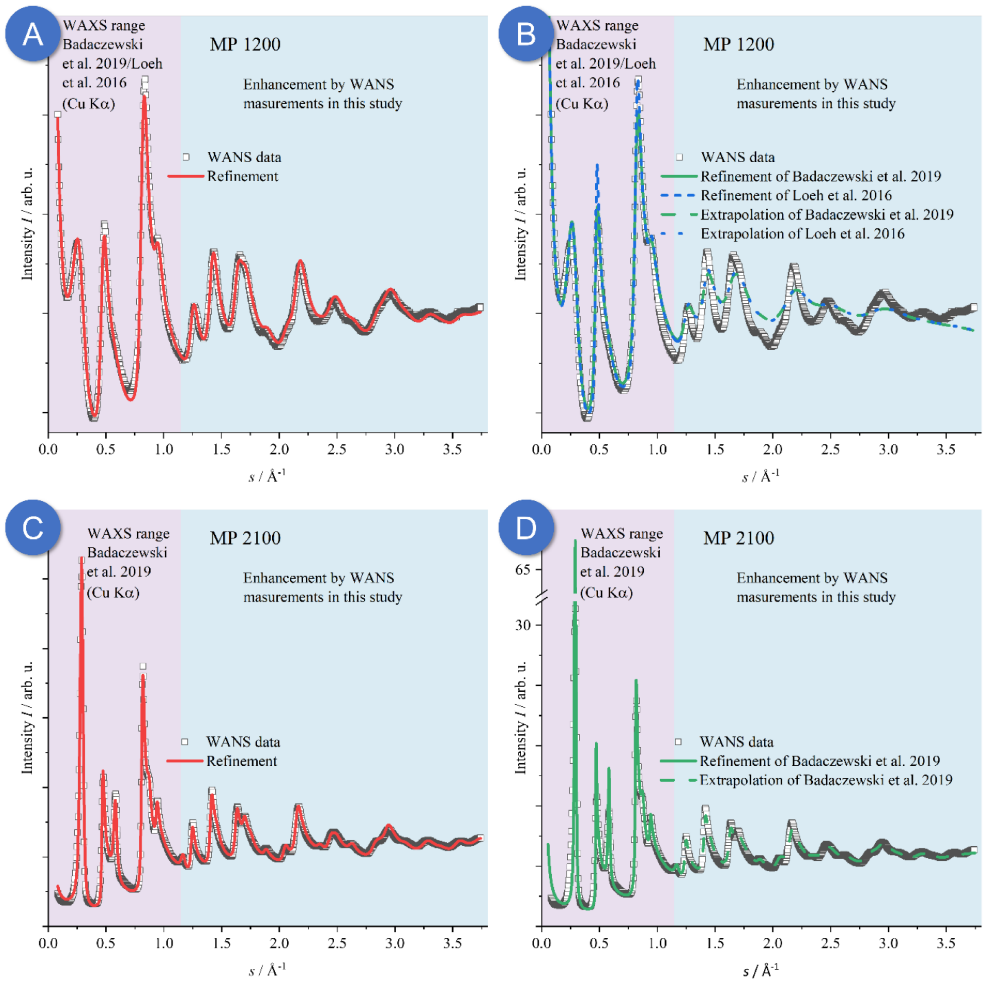

Figure S14 Refinement for MP 1200 and MP 2100 (mesophase pitch heat-treated at 1200 °C/2100 °C). In this figure, only WANS data collected in Grenoble and not the combined WANS data are shown. Red: Refinement of the WANS data. Green/blue: Simulated WANS data using the results from previous WAXS refinements. Especially for MP 2100, the simulated (002)-reflection at $s \sim 0.25$ Å is too small compared to the measured data. The reason is the bad s-space resolution ($\Delta s/s$), which causes a broadening in the WANS data at lower values of s.

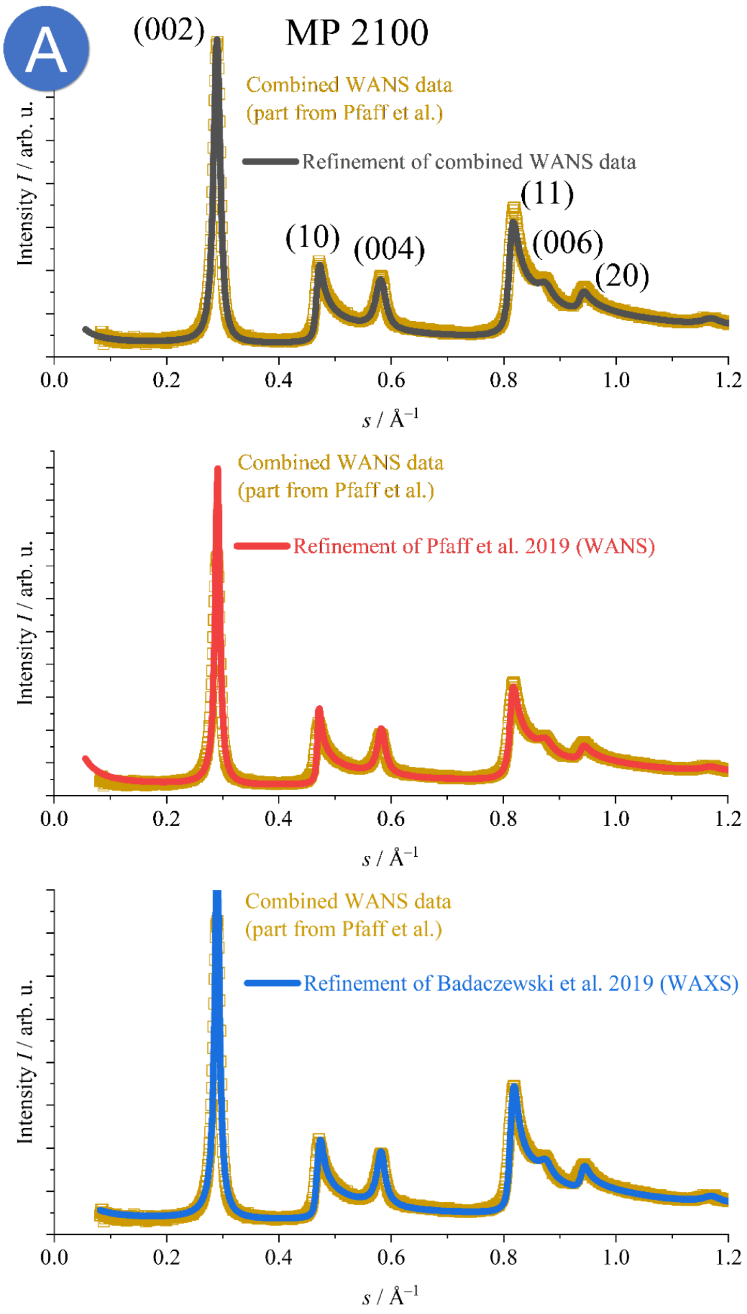
A
MP 2100
(002)
(10)
(004)
(11)
(006)
(20)
Combined WANS data
(part from Pfaff et al.)
Refinement of combined WANS data
Intensity I / arb. u.
s / Å⁻¹
Combined WANS data
(part from Pfaff et al.)
Refinement of Pfaff et al. 2019 (WANS)
Intensity I / arb. u.
s / Å⁻¹
Combined WANS data
(part from Pfaff et al.)
Refinement of Badaczewski et al. 2019 (WAXS)
Intensity I / arb. u.
s / Å⁻¹

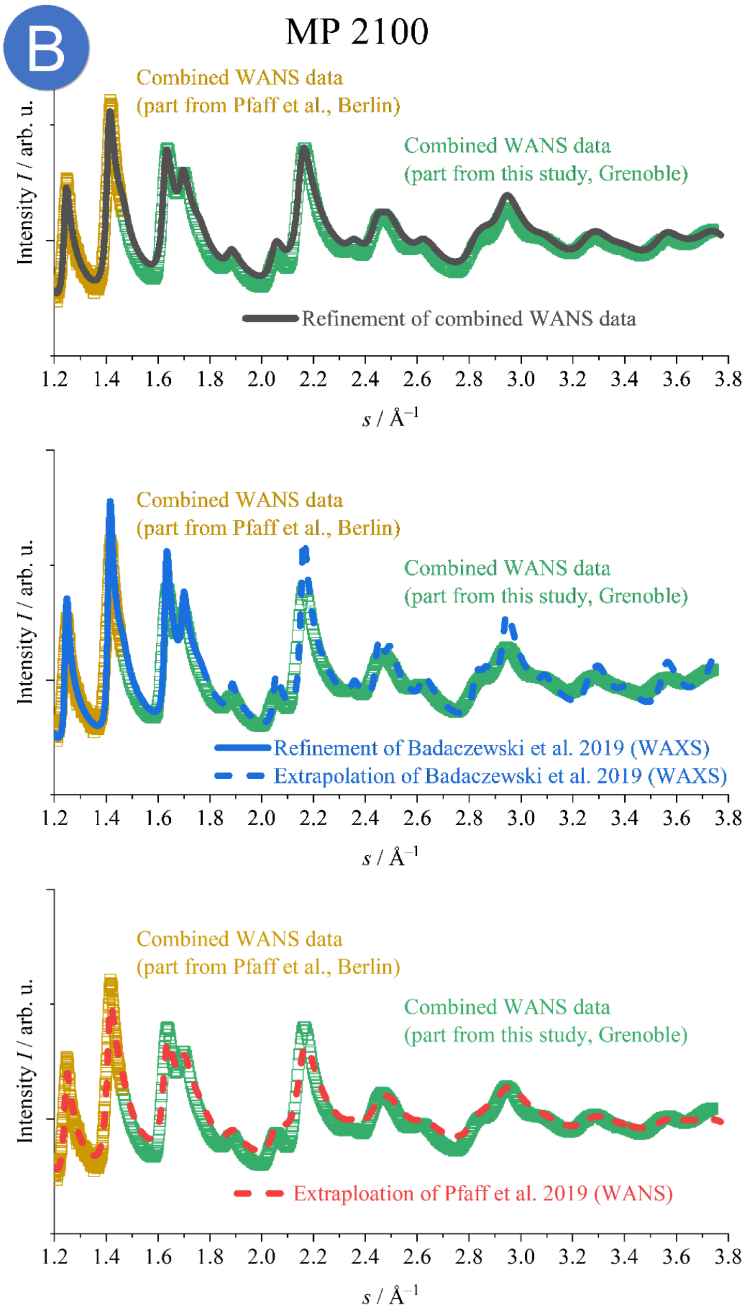

Figure S15 A: Zoom in the WAXS region ($s < 1.2$ Å^{-1}) of Figure 10 of the main article. It is seen that the fitting in the WANS study from 2019 deviates at small s, due to the different resolutions of the setups as HZB and ILL beamlines. B: Zoom in the WANS region ($s > 1.2$ Å^{-1}) of Figure 10 of the main article. It is seen that the fitting in the WANS study from 2019 deviates at large s, due to the different results for the intralayer structure, which is caused by the limited measurement range in this prior study.

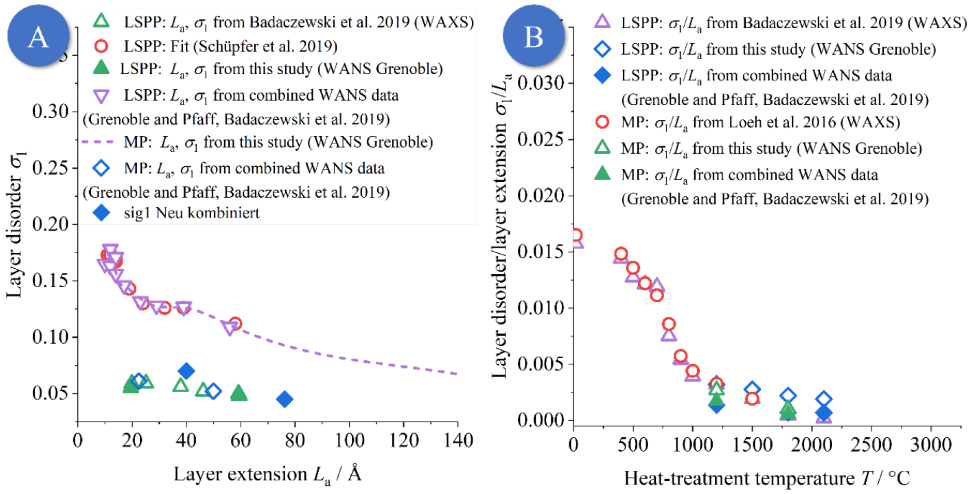

Figure S16 Even if both, σ_1 and L_a for the mesophase pitch (MP) and low softening-point pitch (LSPP) temperature series determined by WANS are much smaller compared to WAXS results, the ratio of σ_1/L_a does not change over the whole temperature range. A similar figure for the resins can be found in the main article as Figure 9.

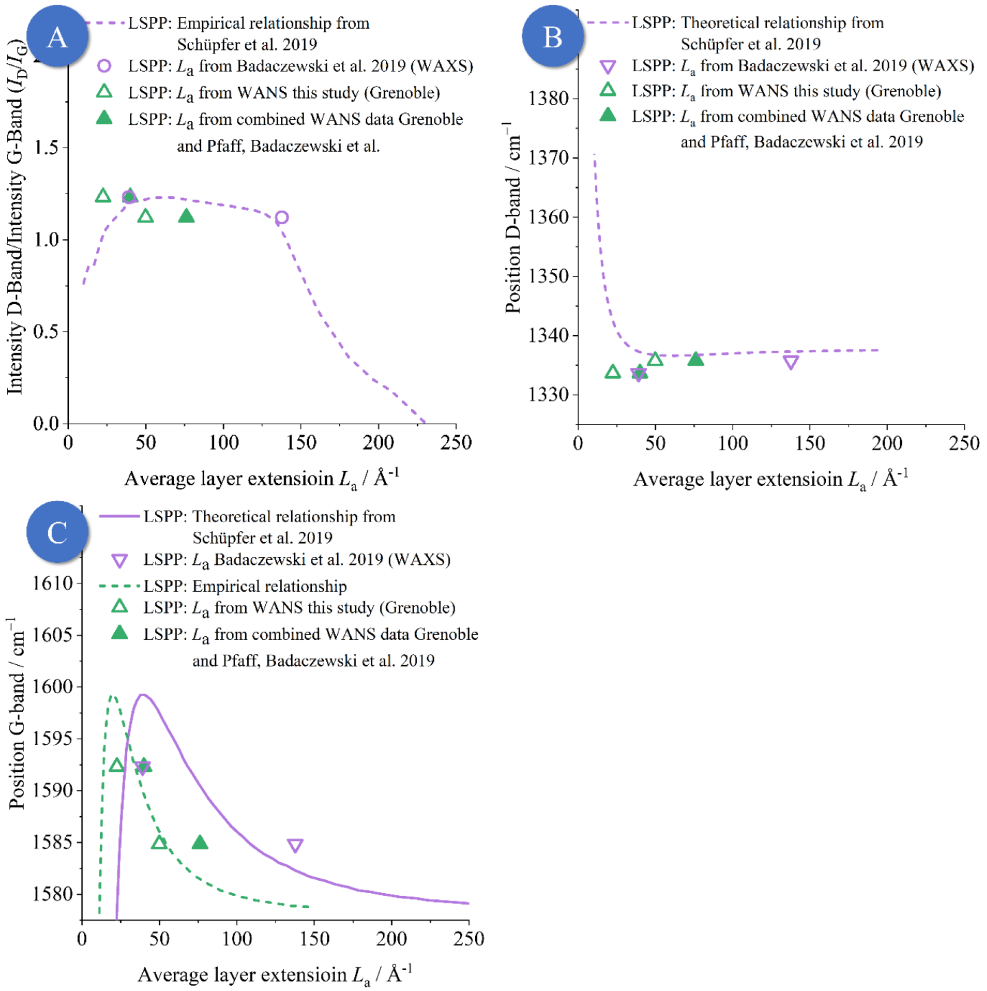

Figure S17 A: The intensity quotient between the D- and G-band (I_D/I_G) for the low softening-point pitch (LSPP) were fitted by Schüpfer et al. using L_a determined from data from Badaczewski et al. [1] Even if L_a is now different, the results from the WANS measurements still fits the fit. B: The position of the D-band is still lower than the theoretical value for these resins. It seems, that in general the theoretical calculations are not valid for (disordered) glassy carbon. C: The theoretical position of the G-band does fit the measured values for both, WAXS and WANS measurements. Even if the layer extension alters, it still fits the theoretical position. Both positions were calculated using the Campbell-Fauchet modelling as described by Schüpfer et al. [6–8] A similar figure for the resins can be found in the main article as Figure 13.

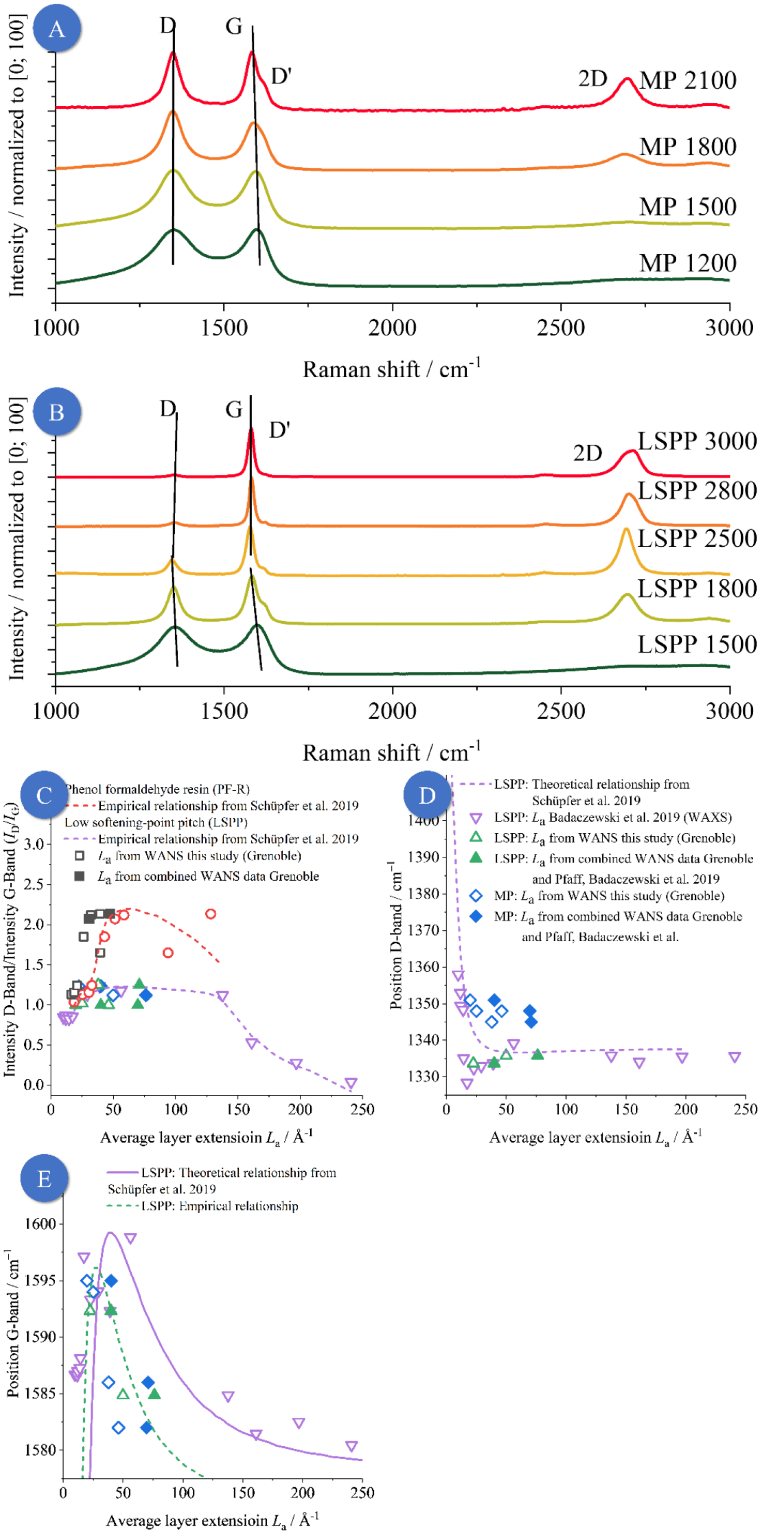
A
D
G
D'
2D
MP 2100
MP 1800
MP 1500
MP 1200
Intensity / normalized to [0; 100]
Raman shift / cm-1
B
LSPP 3000
LSPP 2800
LSPP 2500
LSPP 1800
LSPP 1500
C
Phenol formaldehyde resin (PF-R)
Empirical relationship from Schüpfer et al. 2019
Low softening-point pitch (LSPP)
Empirical relationship from Schüpfer et al. 2019
La from WANS this study (Grenoble)
La from combined WANS data Grenoble
Intensity D-Band/Intensity G-Band (ID/IG)
Average layer extensioin La / Å-1
D
LSPP: Theoretical relationship from Schüpfer et al. 2019
LSPP: La Badaczewski et al. 2019 (WAXS)
LSPP: La from WANS this study (Grenoble)
LSPP: La from combined WANS data Grenoble and Pfaff, Badaczewski et al. 2019
MP: La from WANS this study (Grenoble)
MP: La from combined WANS data Grenoble and Pfaff, Badaczewski et al.
Position D-band / cm-1
E
LSPP: Theoretical relationship from Schüpfer et al. 2019
LSPP: Empirical relationship
Position G-band / cm-1

Figure S18 A/B: Measured Raman data for the mesophase and low softening-point pitch (MP/LSPP) temperature series. All samples show increasing 2D and D' bands and a higher G/D ratio at higher heat-treatment temperature, which are clear indicators for a higher degree of graphitization [6,9]. C: The intensity quotient between the D- and G-band (I_D/I_G) for the low softening-point pitch (LSPP) were fitted by Schüpfer et al. using L_a determined from data from Badaczewski et al. [1] from the MP-series. Even if L_a is now different, the results from the WANS measurements still fits the fit. D: The position of the D-band is still lower than the theoretical value for these resins. It seems, that in general the theoretical calculations are not valid for (disordered) glassy carbon. E: The theoretical position of the G-band does fit the measured values for both, WAXS and WANS measurements. Even if the layer extension alters, it still fits the theoretical position. Both positions were calculated using the Campbell-Fauchet modelling as described by Schüpfer et al. [6–8] A similar figure for the resins can be found in the main article as Figure 13.

S6. Calculation of the correlation function $P(r)$ from the layer size (L_a) and disorder (σ_1)

In order to obtain a simpler phenomenological understanding of the layer disorder parameter σ_1 (also in relation to the layer extension L_a), the layer correlation function $P(r)$ from Ruland & Smarsly [4] can be considered. This function describes the probability that an atom at a distance r (in real space) is exactly in the same position as in a graphene layer. The resulting function $P(r)$ is the multiplication of the influence through the finite layer size ($P_L(r)$) and the layer disorder ($P_D(r)$):

$$P(r) = P_L(r) \cdot P_D(r) \tag{9}$$

The correlation function for the finite layer size $P_L(r)$ can be calculated by

$$P_L(r) = \Gamma(v+1)^{-1} \cdot [\Gamma(v+1, \alpha \cdot r) - \alpha \cdot r \cdot \Gamma(v, \alpha \cdot r)] \tag{10}$$

using the complete ($\Gamma(x)$) and the incomplete ($\Gamma(a, x)$) gamma functions and the parameters v and α, which are related to the average layer size by $L_a = (v+1)/\alpha$.

For the disorder, $P_D(r)$ can be calculated using the standard deviation of the next-neighbor-distribution (σ_1) and the average C-C bond for a given (hk)-reflection:

$$P_D(r) = \exp[-2 \cdot \pi^2 \cdot 2/(3 \cdot l_{cc}) \cdot r \cdot s_{hk}^2] \tag{11}$$

$$s_{hk} = \sqrt{h^2 + k^2 + h \cdot k} \cdot \frac{2}{3 \cdot l_{cc}} \tag{12}$$

In Figure S19, different plots for $P_D(r)$, $P_L(r)$ and $P(r)$ are shown. In A, the $P_D(r)$ for the phenol-formaldehyde resin (PF-R) temperature series shows a clear tendency for increasing heat-treatment temperatures, in particular $P_D(r)$ becomes higher for higher temperatures, which means a higher ordered structure. Nevertheless, the function is continuous decreasing for higher values of r, which indicates, that some disorder is present in the graphene layers. But however, even for high distances of 100 Å (= 10 nm), $P_D(r) > 0.75$, which indicates, that the layer structure is very similar to graphene and a high degree of long-range order is present even for lower heat-treatment temperatures. Additionally, a comparison of $P_D(r)$ calculated from the results of the WANS data from Grenoble in this study (filled) to the one based on the WAXS-results from Badaczewski et al. [1] can be performed. Hence, the results for $P_D(r)$ based on the WANS-results are much higher than the one based on the WAXS-results. Moreover, the results based on the WAXS-data lead more to the assumption, that the layers are highly disordered and especially for higher distances not graphene like ($P_D(r) < 0.5$). For the more accurate results based on the WANS-data, the opposite is the case: The layers are graphene like over their whole extension and the disorder is only small.

C and D in Figure S19 compare the different precursors (phenol-formaldehyde resin (PF-R), mesophase pitch (MP) and low softening-point pitch (LSPP)) for the same temperatures. It becomes clearly, that the pitches are in general higher ordered than the resin, especially for lower heat-treatment temperatures. For higher temperatures, the differences are much smaller, which means, that the layer-order is very

similar for the pitches and the resin for 1800 °C. But even if the difference for 1200 °C is higher, it is only ~ 0.05 for r = 100 Å, which means, that the probability, that the atom position at 100 Å differs from the perfect graphene one is only ~ 5% higher for the resin precursor compared to the low softening-point pitch precursor. Additionally to $P_D(r)$, also $P_L(r)$ and $P(r)$ are shown in B for PF-R heat-treated at 1200 °C, 1800 °C and 3000 °C. Interestingly, the influence of $P_L(r)$ is much higher as the one for $P_D(r)$ for all temperatures and therefore, the resulting $P(r)$ function is mainly dominated from the finite-layer size ($P_L(r)$) and not from the layer disorder ($P_D(r)$).

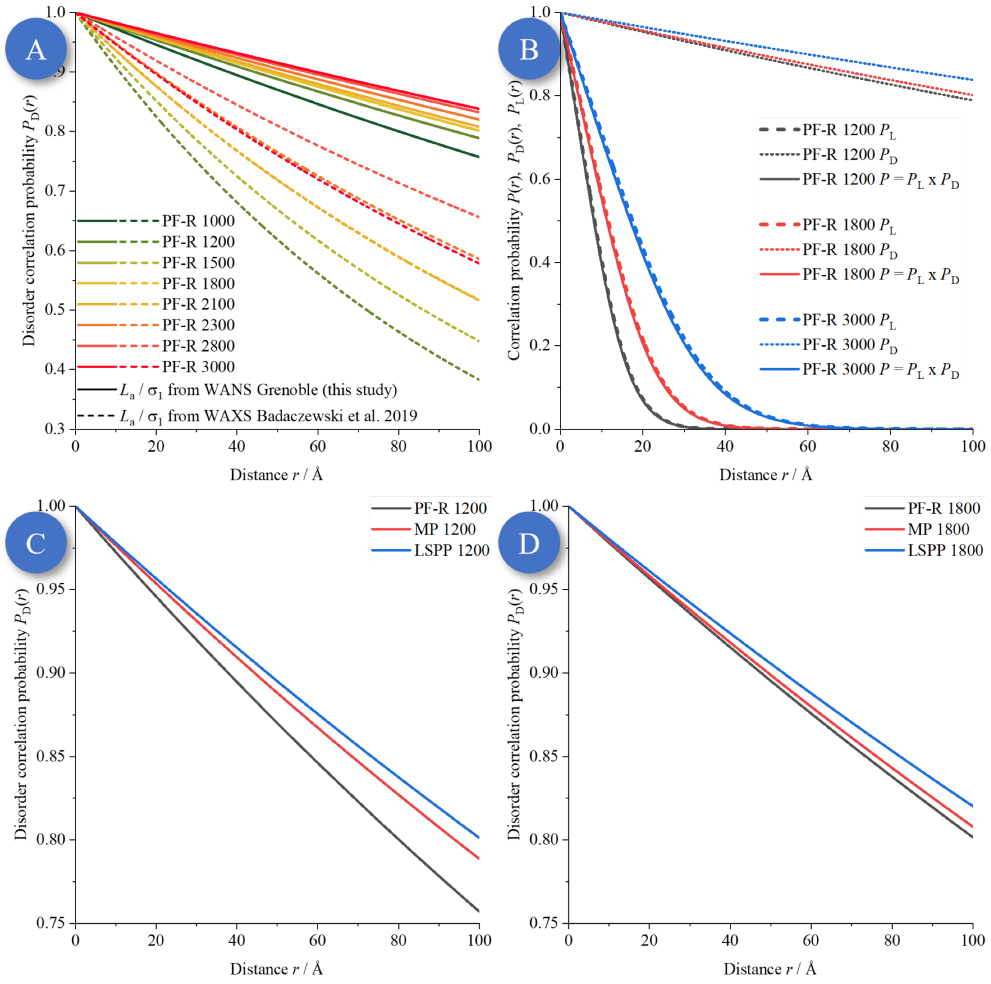

Figure S19 Plot of the layer structure correlation function ($P(r)$) based on the extension ($P_L(r)$) and disorder ($P_D(r)$). The comparison between the function based on the results from the WANS-data analysed in this study and the WAXS-data from Badaczewski et al. [1] (A) lead to the conclusion, that the layers are much more ordered as assumed and graphene like over their whole extension.

S7. Refined microstructure data

S7.1. Microstructure parameters for the phenol-formaldehyde resin (PF-R) temperature series

Table S3 Comparison of the average stack height L_c in Å for WANS data for the phenol-formaldehyde resin temperature series measured in this study, WAXS data measured by Badaczewski et al. (WAXS) [1] and WANS data measured by Pfaff, Badaczewski et al. (WANS) [2]. Additionally, the WANS data from this study from Grenoble were combined with WANS data from Pfaff, Badaczewski et al. [2]

	This study Grenoble (WANS)	Badaczewski et al. (WAXS) [1]	Pfaff, Badaczewski et al. (WANS) [2]	Combined WANS data Grenoble & Pfaff, Badaczewski et al. (WANS) [2]
Max Error	5 %	15 %	15 %	5 %
PF-R 500		9 Å		
PF-R 800		7 Å		
PF-R 1000	7.1 Å	7 Å		
PF-R 1200	10.3 Å	7 Å		
PF-R 1500	10.8 Å	8 Å		
PF-R 1800	11.8 Å	9 Å		
PF-R 2100	13.1 Å	11 Å	14 Å	11.6 Å
PF-R 2300	14.2 Å	12 Å		
PF-R 2800	19.7 Å	19 Å	23 Å	20.1 Å
PF-R 3000	20.0 Å	22 Å		

Table S4 Comparison of the average number of layers per stack *N* for WANS data for the phenol-formaldehyde resin temperature series measured in this study, WAXS data measured by Badaczewski et al. (WAXS) [1] and WANS data measured by Pfaff, Badaczewski et al. (WANS) [2]. Additionally, the WANS data from this study from Grenoble were combined with WANS data from Pfaff, Badaczewski et al. [2]

	This study Grenoble (WANS)	Badaczewski et al. (WAXS) [1]	Pfaff, Badaczewski et al. (WANS) [2]	Combined WANS data Grenoble & Pfaff, Badaczewski et al. (WANS) [2]
Max Error	7.5 %	15 %	15 %	7.5 %
PF-R 500		2.0		
PF-R 800		2.0		
PF-R 1000	1.9	2.0		
PF-R 1200	2.6	2.0		
PF-R 1500	2.7	2.2		
PF-R 1800	3.0	2.4		
PF-R 2100	3.4	3.0	4	3.3
PF-R 2300	3.7	3.4		
PF-R 2800	5.4	5.6	7	5.8
PF-R 3000	5.5	6.8		

Table S5 Comparison of the average stack height $\overline{a_3}$ in Å for WANS data for the phenol-formaldehyde resin temperature series measured in this study, WAXS data measured by Badaczewski et al. (WAXS) [1] and WANS data measured by Pfaff, Badaczewski et al. (WANS) [2]. Additionally, the WANS data from this study from Grenoble were combined with WANS data from Pfaff, Badaczewski et al. [2]

	This study Grenoble (WANS)	Badaczewski et al. (WAXS) [1]	Pfaff, Badaczewski et al. (WANS) [2]	Combined WANS data Grenoble & Pfaff, Badaczewski et al. (WANS) [2]
Max Error	0.1 %	2 %	2 %	0.1 %
PF-R 500		4.39 Å		
PF-R 800		3.59 Å		
PF-R 1000	3.68 Å	3.58 Å		
PF-R 1200	3.98 Å	3.58 Å		
PF-R 1500	3.95 Å	3.56 Å		
PF-R 1800	3.89 Å	3.50 Å		
PF-R 2100	3.83 Å	3.49 Å	3.56 Å	3.05 Å
PF-R 2300	3.80 Å	3.46 Å		
PF-R 2800	3.67 Å	3.44 Å	3.48 Å	3.46 Å
PF-R 3000	3.66 Å	3.39 Å		

Table S6 Comparison of the minimal stack height $a_{3\ min}$ in Å in Å for WANS data for the phenol-formaldehyde resin temperature series measured in this study, WAXS data measured by Badaczewski et al. (WAXS) [1] and WANS data measured by Pfaff, Badaczewski et al. (WANS) [2]. Additionally, the WANS data from this study from Grenoble were combined with WANS data from Pfaff, Badaczewski et al. [2]

	This study Grenoble (WANS)	Badaczewski et al. (WAXS) [1] **Not given**	Pfaff, Badaczewski et al. (WANS) [2]	Combined WANS data Grenoble & Pfaff, Badaczewski et al. (WANS) [2]
Max Error	2 %		12 %	2 %
PF-R 500				
PF-R 800				
PF-R 1000	3.12 Å			
PF-R 1200	3.21 Å			
PF-R 1500	3.24 Å			
PF-R 1800	3.32 Å			
PF-R 2100	3.36 Å		3.16 Å	2.74 Å
PF-R 2300	3.38 Å			
PF-R 2800	3.39 Å		3.30 Å	3.08 Å
PF-R 3000	3.39 Å			

Table S7 Comparison of the standard deviation of the layer distance σ_3 in Å for WANS data for the phenol-formaldehyde resin temperature series measured in this study, WAXS data measured by Badaczewski et al. (WAXS) [1] and WANS data measured by Pfaff, Badaczewski et al. (WANS) [2]. Additionally, the WANS data from this study from Grenoble were combined with WANS data from Pfaff, Badaczewski et al. [2]

	This study Grenoble (WANS)	Badaczewski et al. (WAXS) [1]	Pfaff, Badaczewski et al. (WANS) [2]	Combined WANS data Grenoble & Pfaff, Badaczewski et al. (WANS) [2]
Max Error	3.3 %	10 %	10 %	3.3 %
PF-R 500		1.26 Å		
PF-R 800		0.47 Å		
PF-R 1000	0.49 Å (fitting problem, 1 Å assumed)	0.35 Å		
PF-R 1200	1 Å (max fit value)	0.28 Å		
PF-R 1500	1 Å (max fit value)	0.27 Å		
PF-R 1800	1 Å (max fit value)	0.24 Å		
PF-R 2100	1 Å (max fit value)	0.22 Å	0.44 Å	0.32 Å
PF-R 2300	1 Å (max fit value)	0.21 Å		
PF-R 2800	0.86 Å	0.16 Å	0.25 Å	0.2 Å
PF-R 3000	0.83 Å	0.17 Å		

Table S8 Comparison of the homogeneity of the stacks η for WANS data for the phenol-formaldehyde resin temperature series measured in this study, WAXS data measured by Badaczewski et al. (WAXS) [1] and WANS data measured by Pfaff, Badaczewski et al. (WANS) [2]. Additionally, the WANS data from this study from Grenoble were combined with WANS data from Pfaff, Badaczewski et al. [2]

	This study Grenoble (WANS)	Badaczewski et al. (WAXS) [1]	Pfaff, Badaczewski et al. (WANS) [2]	Combined WANS data Grenoble & Pfaff, Badaczewski et al. (WANS) [2]
Max Error	0.3 %	5 %	5 %	0.3 %
PF-R 500		1 (max value)		
PF-R 800		0.90		
PF-R 1000	0.94	0.95		
PF-R 1200	0.95	0.89		
PF-R 1500	0.96	0.82		
PF-R 1800	0.95	0.92		
PF-R 2100	0.96	0.89	0.86	0.87
PF-R 2300	0.98	0.93		
PF-R 2800	1 (max value)	0.95	0.93	0.94
PF-R 3000	1 (max value)	0.94		

Table S9 Comparison of the average layer extension L_a in Å for WANS data for the phenol-formaldehyde resin temperature series measured in this study, WAXS data measured by Badaczewski et al. (WAXS) [1] and WANS data measured by Pfaff, Badaczewski et al. (WANS) [2].

	This study Grenoble (WANS)	Badaczewski et al. (WAXS) [1]	Pfaff, Badaczewski et al. (WANS) [2]	Combined WANS data Grenoble & Pfaff, Badaczewski et al. (WANS) [2]
Max Error	10 %	15 %	15 %	10 %
PF-R 500		7 Å		
PF-R 800		19 Å		
PF-R 1000	16.4 Å	25 Å		
PF-R 1200	18.7 Å	30 Å		
PF-R 1500	21.0 Å	33 Å		
PF-R 1800	26.2 Å	43 Å		
PF-R 2100	29.9 Å	51 Å	40 Å	31.0 Å
PF-R 2300	32.1 Å	59 Å		
PF-R 2800	39.5 Å	87 Å	51 Å	47.4 Å
PF-R 3000	39.5 Å	124 Å		

Table S10 Comparison of the average C-C bond length l_{cc} for WANS data for the phenol-formaldehyde resin temperature series measured in this study, WAXS data measured by Badaczewski et al. (WAXS) [1] and WANS data measured by Pfaff, Badaczewski et al. (WANS) [2]. Additionally, the WANS data from this study from Grenoble were combined with WANS data from Pfaff, Badaczewski et al. [2]

	This study Grenoble (WANS)	Badaczewski et al. (WAXS) [1]	Pfaff, Badaczewski et al. (WANS) [2]	Combined WANS data Grenoble & Pfaff, Badaczewski et al. (WANS) [2]
Max Error	0.1 %	0.4 %	0.4 %	0.1 %
PF-R 500		1.422 Å		
PF-R 800		1.410 Å		
PF-R 1000	1.4139 Å	1.408 Å		
PF-R 1200	1.4136 Å	1.408 Å		
PF-R 1500	1.4140 Å	1.410 Å		
PF-R 1800	1.4150 Å	1.412 Å		
PF-R 2100	1.4156 Å	1.413 Å	1.413 Å	1.4149 Å
PF-R 2300	1.4164 Å	1.413 Å		
PF-R 2800	1.4177 Å	1.414 Å	1.419 Å	1.4175 Å
PF-R 3000	1.4179 Å	1.402 Å		

Table S11 Comparison of the layer disorder σ_1 for WANS data for the phenol-formaldehyde resin temperature series measured in this study, WAXS data measured by Badaczewski et al. (WAXS) [1] and WANS data measured by Pfaff, Badaczewski et al. (WANS) [2]. Additionally, the WANS data from this study from Grenoble were combined with WANS data from Pfaff, Badaczewski et al. [2]

	This study Grenoble (WANS)	Badaczewski et al. (WAXS) [1]	Pfaff, Badaczewski et al. (WANS) [2]	Combined WANS data Grenoble & Pfaff, Badaczewski et al. (WANS) [2]
Max Error	2 %	12 %	12 %	2 %
PF-R 500		0.18		
PF-R 800		0.14		
PF-R 1000	0.065	0.12		
PF-R 1200	0.060	0.12		
PF-R 1500	0.058	0.11		
PF-R 1800	0.058	0.10		
PF-R 2100	0.057	0.10	0.067	0.056
PF-R 2300	0.055	0.09		
PF-R 2800	0.053	0.08	0.047	0.052
PF-R 3000	0.052	0.09		

Table S12 Comparison of the polydispersity of the layer extension stack height κ_a for WANS data for the phenol-formaldehyde resin temperature series measured in this study, WAXS data measured by Badaczewski et al. (WAXS) [1] and WANS data measured by Pfaff, Badaczewski et al. (WANS) [2]. In general, is κ_a fixed to a fixed value $\kappa_a = 1/v$. Additionally, the WANS data from this study from Grenoble were combined with WANS data from Pfaff, Badaczewski et al. [2]

	This study Grenoble (WANS)	Badaczewski et al. (WAXS) [1]	Pfaff, Badaczewski et al. (WANS) [2]	Combined WANS data Grenoble & Pfaff, Badaczewski et al. (WANS) [2]
Max Error	0 % ($v = 7$)	0 % ($v = 4$)	0 % ($v = 4$)	0 % ($v = 7$)
PF-R 500		0.25		
PF-R 800		0.25		
PF-R 1000	0.14	0.25		
PF-R 1200	0.14	0.25		
PF-R 1500	0.14	0.25		
PF-R 1800	0.14	0.25		
PF-R 2100	0.14	0.25	0.25	0.14
PF-R 2300	0.14	0.25		
PF-R 2800	0.14	0.25	0.25	0.14
PF-R 3000	0.14	0.25		

Table S13 Comparison of the polydispersity of the stack height κ_c for WANS data for the phenol-formaldehyde resin temperature series measured in this study, WAXS data measured by Badaczewski et al. (WAXS) [1] and WANS data measured by Pfaff, Badaczewski et al. (WANS) [2]. Additionally, the WANS data from this study from Grenoble were combined with WANS data from Pfaff, Badaczewski et al. [2]

	This study Grenoble (WANS)	Badaczewski et al. (WAXS) [1]	Pfaff, Badaczewski et al. (WANS) [2]	Combined WANS data Grenoble & Pfaff, Badaczewski et al. (WANS) [2]
Max Error	15 %	15 %	15 %	15 %
PF-R 500		0.45		
PF-R 800		0.39		
PF-R 1000	0.45	0.39		
PF-R 1200	0.39	0.38		
PF-R 1500	0.39	0.38		
PF-R 1800	0.38	0.37		
PF-R 2100	0.38	0.39	0.37	0.36
PF-R 2300	0.37	0.37		
PF-R 2800	0.39		0.49	0.55
PF-R 3000	0.37			

S7.2. Microstructure parameters for the mesophase pitch (MP) temperature series

Table S14 Comparison of the average stack height L_c in Å for WANS data for the phenol-formaldehyde resin temperature series measured in this study, WAXS data measured by Badaczewski et al. (WAXS) [1] and WANS data measured by Pfaff, Badaczewski et al. (WANS) [2]. Additionally, the WANS data from this study from Grenoble were combined with WANS data from Pfaff, Badaczewski et al. [2]

	This study Grenoble (WANS)	Loeh et al. (WAXS) [3]	Badaczewski et al. (WAXS) [1]	Pfaff, Badaczewski et al. (WANS) [2]	Combined WANS data Grenoble & Pfaff, Badaczewski et al. (WANS) [2]
Max Error	5 %	15 %	15 %	15 %	5 %
MP 20		11 Å			
MP 400		12 Å			
MP 500		28 Å	18 Å		
MP 600		17 Å			
MP 700		16 Å			
MP 800		12 Å	11 Å		
MP 900		12 Å			
MP 1000		14 Å	12 Å		
MP 1200	17.3 Å	18 Å	15 Å	18 Å	19.5 Å
MP 1500	18.9 Å	39 Å	27 Å		
MP 1800	23.6 Å	151 Å	53 Å	44 Å	59.2 Å
MP 2100	25.0 Å	198 Å	84 Å	81 Å	59.4 Å

Table S15 Comparison of the average number of layers per stack *N* for WANS data for the phenol-formaldehyde resin temperature series measured in this study, WAXS data measured by Badaczewski et al. (WAXS) [1] and WANS data measured by Pfaff, Badaczewski et al. (WANS) [2]. Additionally, the WANS data from this study from Grenoble were combined with WANS data from Pfaff, Badaczewski et al. [2]

	This study Grenoble (WANS)	Loeh et al. (WAXS) [3]	Badaczewski et al. (WAXS) [1]	Pfaff, Badaczewski et al. (WANS) [2]	Combined WANS data Grenoble & Pfaff, Badaczewski et al. (WANS) [2]
Max Error	5 %	15 %	15 %	15 %	5 %
MP 20		3			
MP 400		4			
MP 500		8	5.1		
MP 600		5			
MP 700		5			
MP 800		4	3.3		
MP 900		4			
MP 1000		4	3.5		
MP 1200	4.7	5	4.4	5.1	5.6
MP 1500	5.4	11	7.7		
MP 1800	6.8	44	15.5	12.7	17.1
MP 2100	7.3	58	24.5	23.0	17.2

Table S16 Comparison of the average stack height $\overline{a_3}$ in Å for WANS data for the phenol-formaldehyde resin temperature series measured in this study, WAXS data measured by Badaczewski et al. (WAXS) [1] and WANS data measured by Pfaff, Badaczewski et al. (WANS) [2]. Additionally, the WANS data from this study from Grenoble were combined with WANS data from Pfaff, Badaczewski et al. [2]

	This study Grenoble (WANS)	Loeh et al. (WAXS) [3]	Badaczewski et al. (WAXS) [1]	Pfaff, Badaczewski et al. (WANS) [2]	Combined WANS data Grenoble & Pfaff, Badaczewski et al. (WANS) [2]
Max Error	5 %	15 %	15 %	15 %	5 %
MP 20		3.52 Å			
MP 400		3.51 Å			
MP 500		3.46 Å	3.46 Å		
MP 600		3.46 Å			
MP 700		3.45 Å			
MP 800		3.44 Å	3.46 Å		
MP 900		3.44 Å			
MP 1000		3.46 Å	3.47 Å		
MP 1200	3.69 Å	3.46 Å	3.49 Å	3.53 Å	3.5 Å
MP 1500	3.52 Å	3.44 Å	3.47 Å		
MP 1800	3.47 Å	3.42 Å	3.44 Å	3.47 Å	3.45 Å
MP 2100	3.45 Å	3.41 Å	3.44 Å	3.45 Å	3.45 Å

Table S17 Comparison of the minimal stack height $a_{3\ min}$ in Å in Å for WANS data for the phenol-formaldehyde resin temperature series measured in this study, WAXS data measured by Badaczewski et al. (WAXS) [1] and WANS data measured by Pfaff, Badaczewski et al. (WANS) [2]. Additionally, the WANS data from this study from Grenoble were combined with WANS data from Pfaff, Badaczewski et al. [2]

	This study Grenoble (WANS)	Loeh et al. (WAXS) [3]	Badaczewski et al. (WAXS) [1]	Pfaff, Bada-czewski et al. (WANS) [2]	Combined WANS data Grenoble & Pfaff, Badaczewski et al. (WANS) [2]
Max Error	5 %	15 %	15 %	15 %	5 %
MP 20		3.52 Å			
MP 400		3.51 Å			
MP 500		3.46 Å	3 Å (min fit value)		
MP 600		3.46 Å			
MP 700		3.45 Å			
MP 800		3.44 Å	3 Å (min fit value)		
MP 900		3.44 Å			
MP 1000		3.46 Å	3.24 Å		
MP 1200	3.28 Å	3.46 Å	3.08 Å		3.30 Å
MP 1500	3.27 Å	3.44 Å	3.11 Å		
MP 1800	3.37 Å	3.42 Å	3.05 Å		3.33 Å
MP 2100	3.39 Å	3.41 Å	3.19 Å	3.34	3.34 Å

Table S18 Comparison of the standard deviation of the layer distance σ_3 in Å for WANS data for the phenol-formaldehyde resin temperature series measured in this study, WAXS data measured by Badaczewski et al. (WAXS) [1] and WANS data measured by Pfaff, Badaczewski et al. (WANS) [2]. Additionally, the WANS data from this study from Grenoble were combined with WANS data from Pfaff, Badaczewski et al. [2]

	This study Grenoble (WANS)	Loeh et al. (WAXS) [3]	Badaczewski et al. (WAXS) [1]	Pfaff, Badaczewski et al. (WANS) [2]	Combined WANS data Grenoble & Pfaff, Badaczewski et al. (WANS) [2]
Max Error	5 %	15 %	15 %	15 %	5 %
MP 20		0.32 Å			
MP 400		0.30 Å			
MP 500		0.26 Å	0.26 Å		
MP 600		0.25 Å			
MP 700		0.26 Å			
MP 800		0.27 Å	0.32 Å		
MP 900		0.24 Å			
MP 1000		0.26 Å	0.27 Å		
MP 1200	0.63 Å	0.22 Å	0.27 Å	0.42 Å	0.4 Å
MP 1500	0.31 Å	0.19 Å	0.23 Å		
MP 1800	0.18 Å	0.11 Å	0.15 Å	0.22 Å	0.14 Å
MP 2100	0.10 Å	0.10 Å	0.13 Å	0.14 Å	0.14 Å

Table S19 Comparison of the homogeneity of the stacks η for WANS data for the phenol-formaldehyde resin temperature series measured in this study, WAXS data measured by Badaczewski et al. (WAXS) [1] and WANS data measured by Pfaff, Badaczewski et al. (WANS) [2]. Additionally, the WANS data from this study from Grenoble were combined with WANS data from Pfaff, Badaczewski et al. [2]

	This study Grenoble (WANS)	Loeh et al. (WAXS) [3]	Badaczewski et al. (WAXS) [1]	Pfaff, Badaczewski et al. (WANS) [2]	Combined WANS data Grenoble & Pfaff, Badaczewski et al. (WANS) [2]
Max Error	5 %	15 %	15 %	15 %	5 %
MP 20		0.77			
MP 400		0.71			
MP 500		0.70	0.68		
MP 600		0.75			
MP 700		0.76			
MP 800		0.96	1 (max value)		
MP 900		0.97	1 (max value)		
MP 1000		1 (max value)	1 (max value)		
MP 1200	1 (max value)	1 (max value)	1 (max value)		1 (max value)
MP 1500	1 (max value)	1 (max value)	0.97		
MP 1800	1 (max value)	0.97	0.97		0.99
MP 2100	1 (max value)	0.99	0.96	0.99	0.99

Table S20 Comparison of the average layer extension L_a in Å for WANS data for the phenol-formaldehyde resin temperature series measured in this study, WAXS data measured by Badaczewski et al. (WAXS) [1] and WANS data measured by Pfaff, Badaczewski et al. (WANS) [2]. Additionally, the WANS data from this study from Grenoble were combined with WANS data from Pfaff, Badaczewski et al. [2]

	This study Grenoble (WANS)	Loeh et al. (WAXS) [3]	Badaczewski et al. (WAXS) [1]	Pfaff, Badaczewski et al. (WANS) [2]	Combined WANS data Grenoble & Pfaff, Badaczewski et al. (WANS) [2]
Max Error	5 %	15 %	15 %	15 %	5 %
MP 20		11 Å			
MP 400		12 Å			
MP 500		13 Å	13 Å		
MP 600		14 Å			
MP 700		14 Å			
MP 800		19 Å	16 Å		
MP 900		24 Å			
MP 1000		32 Å	33 Å		
MP 1200	19.9 Å	39 Å	34 Å	34 Å	19.5 Å
MP 1500	25.1 Å	58 Å	47 Å		
MP 1800	37.9 Å	148 Å	85 Å	48 Å	59.2 Å
MP 2100	46.2 Å	210 Å	130 Å	77 Å	59.4 Å

Table S21 Comparison of the average C-C bond length l_{cc} for WANS data for the phenol-formaldehyde resin temperature series measured in this study, WAXS data measured by Badaczewski et al. (WAXS) [1] and WANS data measured by Pfaff, Badaczewski et al. (WANS) [2]. Additionally, the WANS data from this study from Grenoble were combined with WANS data from Pfaff, Badaczewski et al. [2]

	This study Grenoble (WANS)	Loeh et al. (WAXS) [3]	Badaczewski et al. (WAXS) [1]	Pfaff, Badaczewski et al. (WANS) [2]	Combined WANS data Grenoble & Pfaff, Badaczewski et al. (WANS) [2]
Max Error	5 %	15 %	15 %	15 %	5 %
MP 20		1.414 Å			
MP 400		1.417 Å			
MP 500		1.412 Å	1.413 Å		
MP 600		1.413 Å			
MP 700		1.412 Å			
MP 800		1.412 Å	1.409 Å		
MP 900		1.411 Å			
MP 1000		1.413 Å	1.413 Å		
MP 1200	1.4163 Å	1.413 Å	1.413 Å	1.417 Å	1.4187 Å
MP 1500	1.4177 Å	1.415 Å	1.414 Å		
MP 1800	1.4190 Å	1.420 Å	1.416 Å	1.420 Å	1.4203 Å
MP 2100	1.4198 Å	1.421 Å	1.417 Å	1.417 Å	1.4203 Å

Table S22 Comparison of the layer disorder σ_1 for WANS data for the phenol-formaldehyde resin temperature series measured in this study, WAXS data measured by Badaczewski et al. (WAXS) [1] and WANS data measured by Pfaff, Badaczewski et al. (WANS) [2]. Additionally, the WANS data from this study from Grenoble were combined with WANS data from Pfaff, Badaczewski et al. [2]

	This study Grenoble (WANS)	Loeh et al. (WAXS) [3]	Badaczewski et al. (WAXS) [1]	Pfaff, Badaczewski et al. (WANS) [2]	Combined WANS data Grenoble & Pfaff, Badaczewski et al. (WANS) [2]
Max Error	5 %	15 %	15 %	15 %	5 %
MP 20		0.173			
MP 400		0.173			
MP 500		0.166	0.16		
MP 600		0.170			
MP 700		0.167			
MP 800		0.143	0.13		
MP 900		0.130			
MP 1000		0.126	0.13		
MP 1200	0.059	0.126	0.12	0.059	0.055
MP 1500	0.059	0.112	0.10		
MP 1800	0.056	0.065	0.08	0.050	0.050
MP 2100	0.052	0.045	0.07	0.036	0.048

Table S23 Comparison of the polydispersity of the layer extension stack height κ_a for WANS data for the phenol-formaldehyde resin temperature series measured in this study, WAXS data measured by Badaczewski et al. (WAXS) [1] and WANS data measured by Pfaff, Badaczewski et al. (WANS) [2]. In general, is κ_a fixed to a fixed value $\kappa_a = 1/v$. Additionally, the WANS data from this study from Grenoble were combined with WANS data from Pfaff, Badaczewski et al. [2]

	This study Grenoble (WANS)	Loeh et al. (WAXS) [3]	Badaczewski et al. (WAXS) [1]	Pfaff, Badaczewski et al. (WANS) [2]	Combined WANS data Grenoble & Pfaff, Badaczewski et al. (WANS) [2]
Max Error	5 %	15 %	15 %	15 %	5 %
MP 20		0.25			
MP 400		0.25			
MP 500		0.25	0.25		
MP 600		0.25			
MP 700		0.25			
MP 800		0.25	0.25		
MP 900		0.25			
MP 1000		0.25	0.25		
MP 1200	0.14	0.25	0.25		0.14
MP 1500	0.14	0.25	0.25		
MP 1800	0.14	0.25	0.25		0.14
MP 2100	0.14	0.25	0.25	0.25	0.14

Table S24 Comparison of the polydispersity of the stack height κ_c for WANS data for the phenol-formaldehyde resin temperature series measured in this study, WAXS data measured by Badaczewski et al. (WAXS) [1] and WANS data measured by Pfaff, Badaczewski et al. (WANS) [2]. Additionally, the WANS data from this study from Grenoble were combined with WANS data from Pfaff, Badaczewski et al. [2]

	This study Grenoble (WANS)	Loeh et al. (WAXS) [3]	Badaczewski et al. (WAXS) [1]	Pfaff, Badaczewski et al. (WANS) [2]	Combined WANS data Grenoble & Pfaff, Badaczewski et al. (WANS) [2]
Max Error	5 %	15 %	15 %	15 %	5 %
MP 20		1.24			
MP 400		1.46			
MP 500		4.05	2.22		
MP 600		4.48			
MP 700		1.74			
MP 800		1.04	1.92		
MP 900		0.66			
MP 1000		0.51	0.85		
MP 1200	0.39	0.46	0.94		0.4
MP 1500	0.4	0.53	0.46		
MP 1800	0.37	0.54	0.86		0.57
MP 2100	0.39	0.04	1	2.23	0.57

S7.3. Microstructure parameters for the low softening-point pitch (LSPP) temperature series

Table S25 Comparison of the average stack height L_c in Å for WANS data for the low softening-point pitch temperature series measured in this study, WAXS data measured by Badaczewski et al. (WAXS) [1] and WANS data measured by Pfaff, Badaczewski et al. (WANS) [2]. Additionally, the WANS data from this study from Grenoble were combined with WANS data from Pfaff, Badaczewski et al. [2]

	This study Grenoble (WANS)	Loeh et al. (WAXS) [1]	Pfaff, Badaczewski et al. (WANS) [2]	Combined WANS data Grenoble & Pfaff, Badaczewski et al. (WANS) [2]
Max Error	5 %	15 %	15 %	5 %
LSSP 20		9 Å		
LSSP 400		12 Å		
LSSP 500		25 Å		
LSSP 600		20 Å		
LSSP 700		15 Å		
LSSP 800		12 Å		
LSSP 900		13 Å		
LSSP 1000		13 Å		
LSSP 1200	14.6 Å	19 Å	17 Å	18.7 Å
LSSP 1500		42 Å		
LSSP 1800	25.5 Å		100 Å	74.5 Å
LSSP 2500 (Scherrer)	69.4 Å (25 % error)	140 Å	72 Å (WAXS: 130 Å)	
LSSP 2800 (Scherrer)	67.8 Å (25 % error)		77 Å (WAXS: 149 Å)	
LSSP 3000 (Scherrer)	69.5 Å (25 % error)	260 Å	78 Å (WAXS: 171 Å)	

Table S26 Comparison of the average number of layers per stack *N* for WANS data for the low softening-point pitch temperature series measured in this study, WAXS data measured by Badaczewski et al. (WAXS) [1] and WANS data measured by Pfaff, Badaczewski et al. (WANS) [2]. Additionally, the WANS data from this study from Grenoble were combined with WANS data from Pfaff, Badaczewski et al. [2]

	This study Grenoble (WANS)	Loeh et al. (WAXS) [1]	Pfaff, Badaczewski et al. (WANS) [2]	Combined WANS data Grenoble & Pfaff, Badaczewski et al. (WANS) [2]
Max Error	7.5 %	15 %	15 %	7.5 %
LSSP 20		3		
LSSP 400		3		
LSSP 500		7		
LSSP 600		6		
LSSP 700		4		
LSSP 800		4		
LSSP 900		4		
LSSP 1000		4		
LSSP 1200	4.1	5	5	5.3
LSSP 1500		12		
LSSP 1800	7.4		29	21.6
LSSP 2500 (Scherrer)	20.3 (25 % error)	41		
LSSP 2800 (Scherrer)	20.0 (25 % error)			
LSSP 3000 (Scherrer)	20.6 (25 % error)	77		

Table S27 Comparison of the average stack height $\overline{a_3}$ in Å for WANS data for the low softening-point pitch temperature series measured in this study, WAXS data measured by Badaczewski et al. (WAXS) [1] and WANS data measured by Pfaff, Badaczewski et al. (WANS) [2]. Additionally, the WANS data from this study from Grenoble were combined with WANS data from Pfaff, Badaczewski et al. [2]

	This study Grenoble (WANS)	Loeh et al. (WAXS) [1]	Pfaff, Badaczewski et al. (WANS) [2]	Combined WANS data Grenoble & Pfaff, Badaczewski et al. (WANS) [2]
Max Error	0.1 %	2 %	2 %	0.1 %
LSSP 20		3.55 Å		
LSSP 400		3.50 Å		
LSSP 500		3.46 Å		
LSSP 600		3.47 Å		
LSSP 700		3.44 Å		
LSSP 800		3.42 Å		
LSSP 900		3.44 Å		
LSSP 1000		3.45 Å		
LSSP 1200	3.54 Å	3.45 Å	3.48 Å	3.51 Å
LSSP 1500		3.44 Å		
LSSP 1800	3.43 Å		3.43 Å	3.45 Å
LSSP 2500 (Scherrer)	3.42 Å (2 % error)	3.41 Å		
LSSP 2800 (Scherrer)	3.39 Å (2 % error)			
LSSP 3000 (Scherrer)	3.38 Å (2 % error)	3.36 Å		

Table S28 Comparison of the minimal stack height $a_{3\ min}$ in Å in Å for WANS data for the low softening-point pitch temperature series measured in this study, WAXS data measured by Badaczewski et al. (WAXS) [1] and WANS data measured by Pfaff, Badaczewski et al. (WANS) [2]. Additionally, the WANS data from this study from Grenoble were combined with WANS data from Pfaff, Badaczewski et al. [2]

	This study Grenoble (WANS)	Loeh et al. (WAXS) [1]	Pfaff, Badaczewski et al. (WANS) [2]	Combined WANS data Grenoble & Pfaff, Badaczewski et al. (WANS) [2]
Max Error	2 %	12 %	12 %	2 %
LSSP 20		3 Å (min fit value)		
LSSP 400		3 Å (min fit value)		
LSSP 500		3 Å (min fit value)		
LSSP 600		3 Å (min fit value)		
LSSP 700		3 Å (min fit value)		
LSSP 800		3 Å (min fit value)		
LSSP 900		3 Å (min fit value)		
LSSP 1000		3 Å (min fit value)		
LSSP 1200	3.21 Å	3 Å (min fit value)	3 Å (min fit value)	3.11 Å
LSSP 1500		3 Å (min fit value)		
LSSP 1800	2.76 Å		3 Å (min fit value)	3.36 Å
LSSP 2500 (Scherrer)				
LSSP 2800 (Scherrer)				
LSSP 3000 (Scherrer)				

Table S29 Comparison of the standard deviation of the layer distance σ_3 in Å for WANS data for the low softening-point pitch temperature series measured in this study, WAXS data measured by Badaczewski et al. (WAXS) [1] and WANS data measured by Pfaff, Badaczewski et al. (WANS) [2]. Additionally, the WANS data from this study from Grenoble were combined with WANS data from Pfaff, Badaczewski et al. [2]

	This study Grenoble (WANS)	Loeh et al. (WAXS) [1]	Pfaff, Badaczewski et al. (WANS) [2]	Combined WANS data Grenoble & Pfaff, Badaczewski et al. (WANS) [2]
Max Error	3.3 %	10 %	10 %	3.3 %
LSSP 20		0.34 Å		
LSSP 400		0.28 Å		
LSSP 500		0.27 Å		
LSSP 600		0.28 Å		
LSSP 700		0.27 Å		
LSSP 800		0.24 Å		
LSSP 900		0.26 Å		
LSSP 1000		0.25 Å		
LSSP 1200	0.35 Å	0.22 Å	0.31 Å	0.36 Å
LSSP 1500		0.19 Å		
LSSP 1800	0.07 Å		0.12 Å	0.13 Å
LSSP 2500 (Scherrer)				
LSSP 2800 (Scherrer)				
LSSP 3000 (Scherrer)				

Table S30 Comparison of the homogeneity of the stacks η for WANS data for the low softening-point pitch temperature series measured in this study, WAXS data measured by Badaczewski et al. (WAXS) [1] and WANS data measured by Pfaff, Badaczewski et al. (WANS) [2]. Additionally, the WANS data from this study from Grenoble were combined with WANS data from Pfaff, Badaczewski et al. [2]

	This study Grenoble (WANS)	Loeh et al. (WAXS) [1]	Pfaff, Badaczewski et al. (WANS) [2]	Combined WANS data Grenoble & Pfaff, Badaczewski et al. (WANS) [2]
Max Error	0.3 %	5 %	5 %	0.3 %
LSSP 20		0.78		
LSSP 400		0.71		
LSSP 500		0.67		
LSSP 600		0.68		
LSSP 700		0.81		
LSSP 800		0.96		
LSSP 900		0.97		
LSSP 1000		1 (max value)		
LSSP 1200	1 (max value)	1 (max value)	1 (max value)	1 (max value)
LSSP 1500		1 (max value)		
LSSP 1800	1 (max value)		1 (max value)	0.99
LSSP 2500 (Scherrer)				
LSSP 2800 (Scherrer)				
LSSP 3000 (Scherrer)				

Table S31 Comparison of the average layer extension L_a in Å for WANS data for the low softening-point pitch temperature series measured in this study, WAXS data measured by Badaczewski et al. (WAXS) [1] and WANS data measured by Pfaff, Badaczewski et al. (WANS) [2]. Additionally, the WANS data from this study from Grenoble were combined with WANS data from Pfaff, Badaczewski et al. [2]

	This study Grenoble (WANS)	Loeh et al. (WAXS) [1]	Pfaff, Badaczewski et al. (WANS) [2]	Combined WANS data Grenoble & Pfaff, Badaczewski et al. (WANS) [2]
Max Error	10 %	15 %	15 %	10 %
LSSP 20		10 Å		
LSSP 400		12 Å		
LSSP 500		12 Å		
LSSP 600		14 Å		
LSSP 700		14 Å		
LSSP 800		17 Å		
LSSP 900		23 Å		
LSSP 1000		29 Å		
LSSP 1200	22.5 Å	39 Å	27 Å	40.0 Å
LSSP 1500		56 Å		
LSSP 1800	49.9 Å		126 Å	76.2 Å
LSSP 2500 (Scherrer)				
LSSP 2800 (Scherrer)				
LSSP 3000 (Scherrer)				

Table S32 Comparison of the average C-C bond length l_{cc} for WANS data for the low softening-point pitch temperature series measured in this study, WAXS data measured by Badaczewski et al. (WAXS) [1] and WANS data measured by Pfaff, Badaczewski et al. (WANS) [2]. Additionally, the WANS data from this study from Grenoble were combined with WANS data from Pfaff, Badaczewski et al. [2]

	This study Grenoble (WANS)	Loeh et al. (WAXS) [1]	Pfaff, Badaczewski et al. (WANS) [2]	Combined WANS data Grenoble & Pfaff, Badaczewski et al. (WANS) [2]
Max Error	0.1 %	0.4 %	0.4 %	0.1 %
LSSP 20		1.411 Å		
LSSP 400		1.414 Å		
LSSP 500		1.409 Å		
LSSP 600		1.416 Å		
LSSP 700		1.413 Å		
LSSP 800		1.409 Å		
LSSP 900		1.414 Å		
LSSP 1000		1.413 Å		
LSSP 1200	1.4176 Å	1.412 Å	1.418 Å	1.4182 Å
LSSP 1500		1.416 Å		
LSSP 1800	1.4209 Å		1.421 Å	1.4215 Å
LSSP 2500 (Scherrer)	1.4063 Å			
LSSP 2800 (Scherrer)	1.413 Å			
LSSP 3000 (Scherrer)	1.3382 Å			

Table S33 Comparison of the layer disorder σ_1 for WANS data for the low softening-point pitch temperature series measured in this study, WAXS data measured by Badaczewski et al. (WAXS) [1] and WANS data measured by Pfaff, Badaczewski et al. (WANS) [2]. Additionally, the WANS data from this study from Grenoble were combined with WANS data from Pfaff, Badaczewski et al. [2]

	This study Grenoble (WANS)	Loeh et al. (WAXS) [1]	Pfaff, Badaczewski et al. (WANS) [2]	Combined WANS data Grenoble & Pfaff, Badaczewski et al. (WANS) [2]
Max Error	2 %	12 %	12 %	2 %
LSSP 20		0.165		
LSSP 400		0.178		
LSSP 500		0.163		
LSSP 600		0.171		
LSSP 700		0.156		
LSSP 800		0.146		
LSSP 900		0.132		
LSSP 1000		0.128		
LSSP 1200	0.061	0.127	0.062	0.07
LSSP 1500		0.109		
LSSP 1800	0.052		0.032	0.045
LSSP 2500 (Scherrer)				
LSSP 2800 (Scherrer)				
LSSP 3000 (Scherrer)				

Table S34 Comparison of the polydispersity of the layer extension stack height κ_a for WANS data for the low softening-point pitch temperature series measured in this study, WAXS data measured by Badaczewski et al. (WAXS) [1] and WANS data measured by Pfaff, Badaczewski et al. (WANS) [2]. In general, is κ_a fixed to a fixed value $\kappa_a = 1/v$. Additionally, the WANS data from this study from Grenoble were combined with WANS data from Pfaff, Badaczewski et al. [2]

	This study Grenoble (WANS)	Loeh et al. (WAXS) [1]	Pfaff, Badaczewski et al. (WANS) [2]	Combined WANS data Grenoble & Pfaff, Badaczewski et al. (WANS) [2]
Max Error	0 % ($v = 7$)	0 % ($v = 4$)	0 % ($v = 4$)	0 % ($v = 7$)
LSSP 20		0.25		
LSSP 400		0.25		
LSSP 500		0.25		
LSSP 600		0.25		
LSSP 700		0.25		
LSSP 800		0.25		
LSSP 900		0.25		
LSSP 1000		0.25		
LSSP 1200	0.14	0.25	0.25	0.14
LSSP 1500		0.25		
LSSP 1800	0.14		0.25	0.14
LSSP 2500 (Scherrer)				
LSSP 2800 (Scherrer)				
LSSP 3000 (Scherrer)				

Table S35 Comparison of the polydispersity of the stack height κ_c for WANS data for the low softening-point pitch temperature series measured in this study, WAXS data measured by Badaczewski et al. (WAXS) [1] and WANS data measured by Pfaff, Badaczewski et al. (WANS) [2]. Additionally, the WANS data from this study from Grenoble were combined with WANS data from Pfaff, Badaczewski et al. [2]

	This study Grenoble (WANS)	Loeh et al. (WAXS) [1]	Pfaff, Badaczewski et al. (WANS) [2]	Combined WANS data Grenoble & Pfaff, Badaczewski et al. (WANS) [2]
Max Error	15 %	15 %	15 %	15 %
LSSP 20		1.24		
LSSP 400		1.25		
LSSP 500		3.78		
LSSP 600		2.55		
LSSP 700		1.38		
LSSP 800		1.13		
LSSP 900		0.7		
LSSP 1000		0.52		
LSSP 1200	0.44	0.43	0.63	1.67
LSSP 1500		0.46		
LSSP 1800	0.58		0.11	0.27
LSSP 2500 (Scherrer)				
LSSP 2800 (Scherrer)				
LSSP 3000 (Scherrer)				

1. Badaczewski, F.; Loeh, M.O.; Pfaff, T.; Dobrotka, S.; Wallacher, D.; Clemens, D.; Metz, J.; Smarsly, B.M. Peering into the structural evolution of glass-like carbons derived from phenolic resin by combining small-angle neutron scattering with an advanced evaluation method for wide-angle X-ray scattering. *Carbon* **2019**, *141*, 169–181, doi:10.1016/j.carbon.2018.09.025.
2. Pfaff, T.; Badaczewski, F.M.; Loeh, M.O.; Franz, A.; Hoffmann, J.-U.; Reehuis, M.; Zeier, W.G.; Smarsly, B.M. Comparative Microstructural Analysis of Nongraphitic Carbons by Wide-Angle X-ray and Neutron Scattering. *J. Phys. Chem. C* **2019**, *123*, 20532–20546, doi:10.1021/acs.jpcc.9b03590.
3. Loeh, M.O.; Badaczewski, F.; Faber, K.; Hintner, S.; Bertino, M.F.; Mueller, P.; Metz, J.; Smarsly, B.M. Analysis of thermally induced changes in the structure of coal tar pitches by an advanced evaluation method of X-ray scattering data. *Carbon* **2016**, *109*, 823–835, doi:10.1016/j.carbon.2016.08.031.
4. Ruland, W.; Smarsly, B.M. X-ray scattering of non-graphitic carbon: an improved method of evaluation. *J Appl Crystallogr* **2002**, *35*, 624–633, doi:10.1107/S0021889802011007.
5. Osswald, O.; Smarsly, B.M. OctCarb - A GNU Octave Script for the Analysis and Evaluation of Wide-Angle Scattering Data of Non-Graphitic Carbons. *C* **2022**, *8(4)*, doi:10.3390/c8040078.
6. Schüpfer, D.B.; Badaczewski, F.; Guerra-Castro, J.M.; Hofmann, D.M.; Heiliger, C.; Smarsly, B.M.; Klar, P.J. Assessing the structural properties of graphitic and non-graphitic carbons by Raman spectroscopy. *Carbon* **2020**, *161*, 359–372, doi:10.1016/j.carbon.2019.12.094.
7. Campbell, I.H.; Fauchet, P.M. The effects of microcrystal size and shape on the one phonon Raman spectra of crystalline semiconductors. *Solid State Communications* **1986**, *58*, 739–741, doi:10.1016/0038-1098(86)90513-2.
8. Fauchet, P.M.; Campbell, I.H. Raman spectroscopy of low-dimensional semiconductors. *Critical Reviews in Solid State and Materials Sciences* **1988**, *14*, s79-s101, doi:10.1080/10408438808244783.
9. Schüpfer, D.B.; Badaczewski, F.; Peilstöcker, J.; Guerra-Castro, J.M.; Shim, H.; Firoozabadi, S.; Beyer, A.; Volz, K.; Presser, V.; Heiliger, C.; et al. Monitoring the thermally induced transition from sp3-hybridized into sp2-hybridized carbons. *Carbon* **2021**, *172*, 214–227, doi:10.1016/j.carbon.2020.09.063.

6.5. Bildnachweise

6.5.1. Abbildungen 6, 9, 12

Open Access Article

On the Highly Ordered Graphene Structure of Non-Graphitic Carbons (NGCs)—A Wide-Angle Neutron Scattering (WANS) Study

by
Oliver Osswald (https://sciprofiles.com/profile/2561843) [1,*] (mailto:carbon@oss-wald.de) (https://orcid.org/0000-0002-4497-4048),
Marc O. Loeh (https://sciprofiles.com/profile/author/ZlFndDhJdHVwcVgyaWVUaXNxRyt[illegible]) [2],

66. Pimenta, M.A.; Dresselhaus, G.; Dresselhaus, M.S.; Cançado, L.G.; Jorio, A.; Saito, R. Studying disorder in graphite-based systems by Raman spectroscopy. *Phys. Chem. Chem. Phys.* **2007**, *9*, 1276–1291. [**Google Scholar (https://scholar.google.com/scholar_lookup?title=Studying+disorder+in+graphite-based+systems+by+Raman+spectroscopy&author=Pimenta,+M.A.&author=Dresselhaus,+G.&author=Dresselhaus,+M.S.&author=Cançado,+L.G.&author=Jorio,+A.&author=Saito,+R.&publication_year=2007&journal=Phys.+Chem.+Chem.+Phys.&volume=9&pages=1276%E2%80%931291&doi=10.1039/B613962K)**] [**CrossRef (https://doi.org/10.1039/B613962K)**]

67. Fauchet, P.M. The effects of microcrystal size and shape on the one phonon Raman spectra of crystalline semiconductors. *Solid State Commun.* **1986**, *58*, 739–741. [**Google Scholar (https://scholar.google.com/scholar_lookup?title=The+effects+of+microcrystal+size+and+shape+on+the+one+phonon+Raman+spectra+of+crystalline+semiconductors&author=Campbell,+I.H.&author=Fauchet,+P.M.&publication_year=1986&journal=Solid+State+Commun.&volume=58&pages=739%E2%80%93741&doi=10.1016/0038-1098(86)90513-2)**] [**CrossRef (https://doi.org/10.1016/0038-1098(86)90513-2)**]

68. Fauchet, P.M.; Campbell, I.H. Raman spectroscopy of low-dimensional semiconductors. *Crit. Rev. Solid State Mater. Sci.* **1988**, *14*, s79–s101. [**Google Scholar (https://scholar.google.com/scholar_lookup?title=Raman+spectroscopy+of+low-dimensional+semiconductors&author=Fauchet,+P.M.&author=Campbell,+I.H.&publication_year=1988&journal=Crit.+Rev.+Solid+State+Mater.+Sci.&volume=14&pages=s79%E2%80%93s101&doi=10.1080/10408438808244783)**] [**CrossRef (https://doi.org/10.1080/10408438808244783)**]

Share and Cite

Back to TopTop

6.5.2. Abbildung 7

CCC Marketplace

This is a License Agreement between Oliver Osswald ("User") and Copyright Clearance Center, Inc. ("CCC") on behalf of the Rightsholder identified in the order details below. The license consists of the order details, the Marketplace Order General Terms and Conditions below, and any Rightsholder Terms and Conditions which are included below.

All payments must be made in full to CCC in accordance with the Marketplace Order General Terms and Conditions below.

Order Date	01-Dec-2022	Type of Use	Republish in a thesis/dissertation
Order License ID	1295864-1		
ISSN	2053-9169	Publisher	Royal Society of London
		Portion	Image/photo/illustration

LICENSED CONTENT

Publication Title	Proceedings of the Royal Society of London. Series A, Mathematical and physical sciences	Country	United Kingdom of Great Britain and Northern Ireland
		Rightsholder	The Royal Society (U.K.)
Author/Editor	Royal Society (Great Britain)	Publication Type	e-Journal
Date	01/01/1934	URL	https://royalsociety.org/journals/
Language	English		

REQUEST DETAILS

Portion Type	Image/photo/illustration	Distribution	Worldwide
Number of Images / Photos / Illustrations	2	Translation	Original language of publication
Format (select all that apply)	Print, Electronic	Copies for the Disabled?	No
		Minor Editing Privileges?	No
Who Will Republish the Content?	Publisher, not-for-profit	Incidental Promotional Use?	No
Duration of Use	Life of current and all future editions	Currency	EUR
Lifetime Unit Quantity	Up to 2,000,000		
Rights Requested	Main product		

NEW WORK DETAILS

Title	Quantitative Mikrostrukturanalyse nicht-graphitischer Kohlenstoffe – Durchführung und Auswertung von Weitwinkelneutronenstreuung	Institution Name	Justus-Liebig-Universität Gießen
		Expected Presentation Date	2022-12-01
Instructor Name	Oliver Osswald		

ADDITIONAL DETAILS

Order Reference Number	N/A	The Requesting Person/Organization to Appear on the License	Oliver Osswald

REUSE CONTENT DETAILS

Title, Description or Numeric Reference of the Portion(s)	Figure 7. Schematic representation of the structure of a graphitizing (but non-graphitic) carbon. Figure 7. Schematic representation of the structure of a non-graphitizing carbon.	Title of the Article/Chapter the Portion Is From	Crystallite growth in graphitizing and non-graphitizing carbons
		Author of Portion(s)	Royal Society (Great Britain)
		Issue, if Republishing an Article From a Serial	Volume 209, Issue 1097
Editor of Portion(s)	Rsolaind E. Franklin	Publication Date of Portion	1951-10-01
Volume of Serial or Monograph	Volume 209, Issue 1097		
Page or Page Range of Portion	213		

RIGHTSHOLDER TERMS AND CONDITIONS

Out of Copyright - any journal requested with a Publication date older than 70 years.

Marketplace Order General Terms and Conditions

The following terms and conditions ("General Terms"), together with any applicable Publisher Terms and Conditions, govern User's use of Works pursuant to the Licenses granted by Copyright Clearance Center, Inc. ("CCC") on behalf of the applicable Rightsholders of such Works through CCC's applicable Marketplace transactional licensing services (each, a "Service").

1) Definitions. For purposes of these General Terms, the following definitions apply:

"License" is the licensed use the User obtains via the Marketplace platform in a particular licensing transaction, as set forth in the Order Confirmation.

"Order Confirmation" is the confirmation CCC provides to the User at the conclusion of each Marketplace transaction. "Order Confirmation Terms" are additional terms set forth on specific Order Confirmations not set forth in the General Terms that can include terms applicable to a particular CCC transactional licensing service and/or any Rightsholder-specific terms.

"Rightsholder(s)" are the holders of copyright rights in the Works for which a User obtains licenses via the Marketplace platform, which are displayed on specific Order Confirmations.

"Terms" means the terms and conditions set forth in these General Terms and any additional Order Confirmation Terms collectively.

"User" or "you" is the person or entity making the use granted under the relevant License. Where the person accepting the Terms on behalf of a User is a freelancer or other third party who the User authorized to accept the General Terms on the User's behalf, such person shall be deemed jointly a User for purposes of such Terms.

"Work(s)" are the copyright protected works described in relevant Order Confirmations.

2) Description of Service. CCC's Marketplace enables Users to obtain Licenses to use one or more Works in accordance with all relevant Terms. CCC grants Licenses as an agent on behalf of the copyright rightsholder identified in the relevant Order Confirmation.

3) Applicability of Terms. The Terms govern User's use of Works in connection with the relevant License. In the event of any conflict between General Terms and Order Confirmation Terms, the latter shall govern. User acknowledges that Rightsholders have complete discretion whether to grant any permission, and whether to place any limitations on any grant, and that CCC has no right to supersede or to modify any such discretionary act by a Rightsholder.

4) Representations; Acceptance. By using the Service, User represents and warrants that User has been duly authorized by the User to accept, and hereby does accept, all Terms.

5) Scope of License; Limitations and Obligations. All Works and all rights therein, including copyright rights, remain the sole and exclusive property of the Rightsholder. The License provides only those rights expressly set forth in the terms and conveys no other rights in any Works

6) General Payment Terms. User may pay at time of checkout by credit card or choose to be invoiced. If the User chooses to be invoiced, the User shall: (i) remit payments in the manner identified on specific invoices, (ii) unless otherwise specifically stated in an Order Confirmation or separate written agreement, Users shall remit payments upon receipt of

6.5.3. Abbildung 8

Download PDF

Article | Open Access | Published: 29 November 2017

Graphitizing Non-graphitizable Carbons by Stress-induced Routes

Maziar Ghazinejad, Sunshine Holmberg, Oscar Pilloni, Laura Oropeza-Ramos & Marc Madou

Scientific Reports **7**, Article number: 16551 (2017)

Abstract

Graphitic carbons' unique attributes have attracted worldwide interest towards their development and application. Carbon pyrolysis is a widespread method for synthesizing carbon materials. However, our understanding of the factors that cause differences in graphitization of various pyrolyzed carbon precursors is inadequate. We demonstrate how electro-mechanical aspects of the synthesis process influence molecular alignment in a polymer precursor to enhance its graphitization. Electrohydrodynamic forces are applied via electrospinning to unwind and orient the molecular chains of a non-graphitizing carbon precursor, polyacrylonitrile. Subsequently, exerting mechanical stresses further enhances the molecular alignment of the polymer chains during the formative crosslinking phase. The stabilized polymer precursor is then pyrolyzed at 1000 °C and characterized to evaluate its graphitization. The final carbon exhibits a uniformly graphitized structure, abundant in edge planes, which translates into its electrochemical kinetics. The results highlight the significance of physical synthesis conditions in defining the structure and properties of pyrolytic carbons.

Download PDF

62. Zhong, J. *et al.* Quantitative Correlation between Defect Density and Heterogeneous Electron Transfer Rate of Single Layer Graphene. *J. Am. Chem. Soc.* **136**, 16609–16617 (2014).

63. Stoller, M. D., Park, S., Zhu, Y., An, J. & Ruoff, R. S. Graphene-Based Ultracapacitors. *Nano Lett.* **8**, 3498–3502 (2008).

Acknowledgements

The authors appreciate the National Science Foundation (NSF) grant #1449397 for financial support. The authors thank the UCI's Chemistry Department Laser Spectroscopy Facility and the Fuel Cell Research Center (FCRC) for the access to their facilities, equipment and materials. The third author would like to thank the CONACYT mixed scholarship (487698) and the UNAM CEP mobility scholarship for aiding in his participation in this project. The authors gratefully acknowledge Mr. Joshua Razink and University of Oregon CAMCOR Spectroscopy Lab for the assistance with TEM imaging. The first author appreciate the support of Fresno State's Lyles College of Engineering. The authors would also like to thank Mr. Derosh George and Mr. Brandon Pollack for helpful discussions and technical support.

Author information

Authors and Affiliations

Department of Mechanical Engineering, California State University, Fresno, USA
Maziar Ghazinejad

Department of Mechanical and Aerospace Engineering, University of California, Irvine, USA
Maziar Ghazinejad, Sunshine Holmberg & Marc Madou

Programa de Maestría y Doctorado en Ingeniería, Universidad Nacional Autónoma de México, CDMX, Mexico
Oscar Pilloni

Download PDF

Contributions

M.G. and S.H. Contributed equally to this work. M.G., S.H. and M.M. jointly conceived the study. M.G. and S.H. designed and performed the experiments and analyzed the results. S.H. performed HRTEM analysis and Raman spectroscopy. M.G. wrote the manuscripts with contributions from S.H. and O.P. L.O.-R. provided technical support on dielectrophoresis phenomenon. M.M. and M.G. supervised the research team. All authors reviewed the manuscript.

Corresponding author

Correspondence to Marc Madou.

Ethics declarations

Competing Interests

The authors declare that they have no competing interests.

Additional information

Publisher's note: Springer Nature remains neutral with regard to jurisdictional claims in published maps and institutional affiliations.

Electronic supplementary material

Supplementary Information

Rights and permissions

6.5.4. Abbildung 13

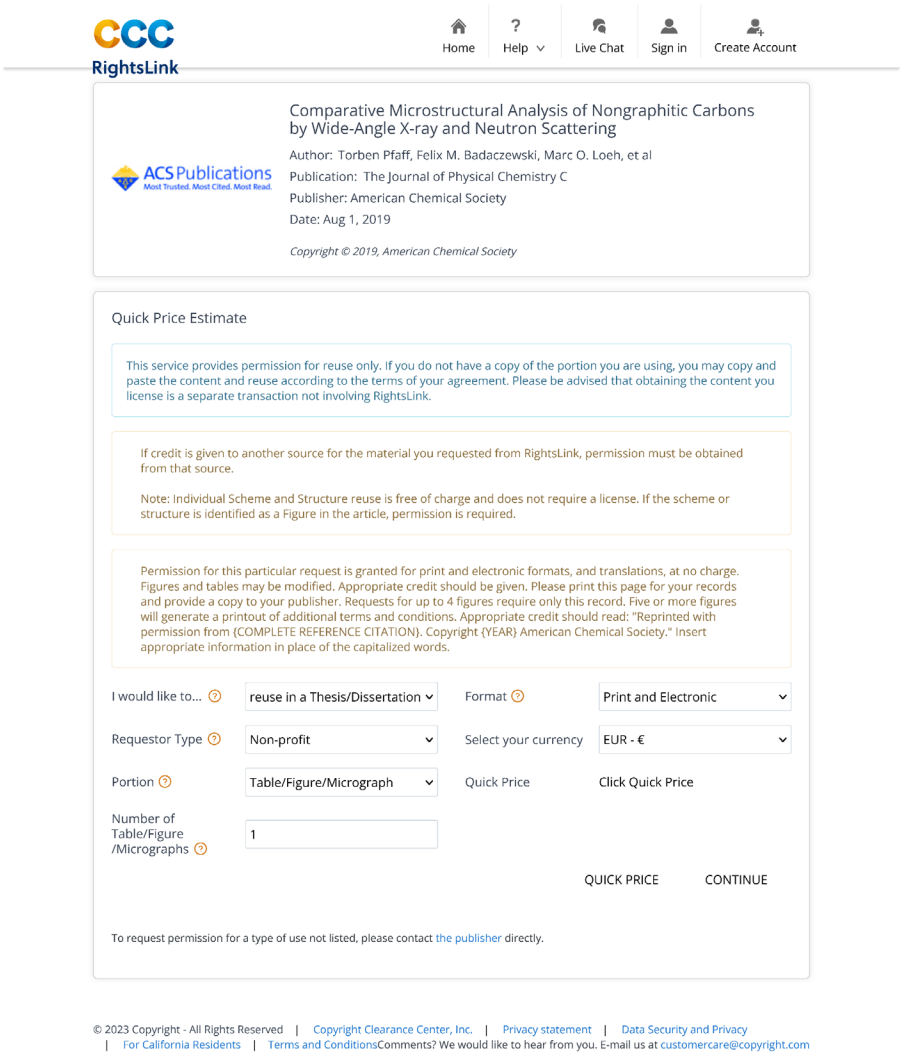

RightsLink

Home | Help | Live Chat | Sign in | Create Account

ACS Publications
Most Trusted. Most Cited. Most Read.

Comparative Microstructural Analysis of Nongraphitic Carbons by Wide-Angle X-ray and Neutron Scattering

Author: Torben Pfaff, Felix M. Badaczewski, Marc O. Loeh, et al
Publication: The Journal of Physical Chemistry C
Publisher: American Chemical Society
Date: Aug 1, 2019

Copyright © 2019, American Chemical Society

Quick Price Estimate

This service provides permission for reuse only. If you do not have a copy of the portion you are using, you may copy and paste the content and reuse according to the terms of your agreement. Please be advised that obtaining the content you license is a separate transaction not involving RightsLink.

If credit is given to another source for the material you requested from RightsLink, permission must be obtained from that source.

Note: Individual Scheme and Structure reuse is free of charge and does not require a license. If the scheme or structure is identified as a Figure in the article, permission is required.

Permission for this particular request is granted for print and electronic formats, and translations, at no charge. Figures and tables may be modified. Appropriate credit should be given. Please print this page for your records and provide a copy to your publisher. Requests for up to 4 figures require only this record. Five or more figures will generate a printout of additional terms and conditions. Appropriate credit should read: "Reprinted with permission from {COMPLETE REFERENCE CITATION}. Copyright {YEAR} American Chemical Society." Insert appropriate information in place of the capitalized words.

I would like to...	reuse in a Thesis/Dissertation	Format	Print and Electronic
Requestor Type	Non-profit	Select your currency	EUR - €
Portion	Table/Figure/Micrograph	Quick Price	Click Quick Price
Number of Table/Figure /Micrographs	1		

QUICK PRICE CONTINUE

To request permission for a type of use not listed, please contact the publisher directly.

7. Eidesstattliche Erklärung

Die vorliegende Arbeit und die ihr zu Grunde liegenden praktischen Arbeiten wurden in der Zeit von Mai 2018 bis Dezember 2022 am Physikalisch-Chemischen Institut der Justus-Liebig-Universität Gießen in der Arbeitsgruppe von Prof. Dr. Bernd Michael Smarsly angefertigt.

Ich erkläre: Ich habe die vorgelegte Dissertation selbstständig und ohne unerlaubte fremde Hilfe und nur mit den Hilfen angefertigt, die ich in der Dissertation angegeben habe. Alle Textstellen, die wörtlich oder sinngemäß aus veröffentlichten Schriften entnommen sind, und alle Angaben, die auf mündlichen Auskünften beruhen, sind als solche kenntlich gemacht. Ich stimme einer evtl. Überprüfung meiner Dissertation durch eine Antiplagiat-Software zu. Bei den von mir durchgeführten und in der Dissertation erwähnten Untersuchungen habe ich die Grundsätze guter wissenschaftlicher Praxis, wie sie in der „Satzung der Justus-Liebig-Universität Gießen zur Sicherung guter wissenschaftlicher Praxis“ niedergelegt sind, eingehalten. [b]

Gießen, April 2023

(Oliver Osswald)

[b] Entnommen aus: Promotionsordnung der Naturwissenschaftlichen Fachbereiche: Fachbereich 07 – Mathematik und Informatik, Physik, Geographie sowie Fachbereich 08 – Biologie und Chemie der Justus-Liebig-Universität Gießen vom 21.06.2021. Zugriff am 18.05.2022. https://www.uni-giessen.de/mug/7/pdf/7_40/7_40_12_1_2ae